5-2013

Device Characterization and Compact Modeling of the SiGe HBT in Extreme Temperature Environments

Beth Olivia Woods
University of Arkansas, Fayetteville

Device Characterization and Compact Modeling of the SiGe HBT in Extreme Temperature Environments

Device Characterization and Compact Modeling of the SiGe HBT in Extreme Temperature Environments

A dissertation submitted in partial fulfillment
of the requirements for the degree of
Doctor of Philosophy in Engineering

By

Beth Olivia Woods
University of Oklahoma
Bachelor of Science in Engineering Physics, 1985
University of Arkansas
Master of Science in Electrical Engineering, 1988

May 2013
University of Arkansas

Abstract

The silicon germanium heterojunction bipolar transistor, SiGe HBT, has very high frequency response but limited voltage range. Commercial communication applications in wireless and system integration have driven the development of the SiGe HBT. However, the device's excellent electrical performance goes beyond the commercial environment. The SiGe HBT performs exceptionally at low temperatures. The device DC current gain and AC small-signal gain significantly increase in the cryogenic temperature range. Applications at low temperatures with expansive temperature range specifications need an HBT compact model to accurately represent the device's performance.

In this work, a compact model referenced at 300K was developed to accurately represent both DC and AC electrical performance of the SiGe HBT over an extended temperature range, down to 93K. This single expansive temperature, SET, model supports all functions of circuit simulation; DC quiescent operation and AC frequency response. The SET model was developed from the Mextram 504.7 bipolar model and accurately represents full transistor operation over an extreme temperature environment. The model correctly simulates SiGe HBT DC output performance from saturation, through quasi-saturation and the linear region including impact ionization effects. This model was developed through a combination of physical calculations based on doping profiles and optimization techniques for modeling fitting. The SET model of this dissertation added 32 parameters to the original Mextram 504.7 model's 78 parameters. The device's static and dynamic performance over the full temperature range down to 93K was fitted with a single group of SET model parameters. The model results show excellent correlation with measured data over the entire temperature range.

This dissertation is approved for recommendation
to the Graduate Council.

Co-Dissertation Directors:

____
Dr. Simon S. Ang

____
Dr. Randy L. Brown

Dissertation Committee:

____
Mr. G. Wayne Dietrich

____
Dr. H. Alan Mantooth

____
Dr. Jerry R. Yeargan

Dissertation Duplication Release

I hereby authorize the University of Arkansas Libraries to duplicate this dissertation when needed for research and/or scholarship.

Agreed____________________________________
Beth Olivia Woods

Refused____________________________________
Beth Olivia Woods

Acknowledgements

The contributions of my advisors, Dr. Simon Ang and Dr. Randy Brown were invaluable. Their influence and suggestions are clearly present in this dissertation. I am so very grateful for their technical strategies and in-depth knowledge. Many times the limits of a current approach were reached in modeling an HBT over such a wide range temperature range. Their support was essential and I truly thank them.

I would like to express my deep gratitude to Wayne Dietrich for his never-ending contributions and brilliant ideas. I have encountered very few engineers in my long career who are as gifted or as humble as he. I do appreciate his help.

Dr. Yeargan, Dr. Brown, and Dr. Ang were my professors many years ago. During the following years I have been appreciative of the level of education I received from them as I compared my knowledge to colleagues in the semiconductor industry. During this return to the University of Arkansas to further my education I have found the standards are still the same.

I would like to thank Dr. John Cressler and Dr. Alan Mantooth and their students for the work done on the NASA sponsored extreme temperature project. The SiGe BiCMOS material and measurements were applied to this research.

Next, this research was conducted with Agilent Technologies Inc's modeling and measurement software, IC-CAP, and simulation software, ADS, as part of their University Donation program. Their tools were invaluable and exceptionally adjustable to the model development approach needed. I would like to express my gratitude to Agilent for supporting the university.

I would like to express my deep appreciation to all the students, professors and members of the university community that have helped me reach each level of achievement in the program. I would like to thank Dr. Samir El-Ghazaly, our Electrical Engineering Department Head. The professors let me sit in on their undergraduate classes as I prepared for the qualifying exams. They were outstanding. I would like to express my appreciation to the late George Tatge and recognize all his help and encouragement. Also, I sincerely appreciate the help and professionalism of Connie Howard. I would like to thank Admiral Jack Buffington for his years of mentoring, encouragement and straight-shooter approach. The graduate school at the University of Arkansas and those committed to its excellence are outstanding.

My family is very caring. I thank each of them for their support, faith in me and their prayers. They kept believing, even though the phrase, “just a little bit longer,” was getting old.

Table of Contents

List of Figures

List of Tables

1 Introduction

The SiGe heterojunction bipolar transistor, HBT, is an advanced bipolar device that is formed by adding germanium (Ge) during the growth of the base region. Ge introduces an energy bandgap reduction, which reduces the transit time. SiGe heterojunction bipolar transistors have the advantage of very high frequency response, but are limited to lower voltages. The HBT was designed for use in the commercial temperature range, however SiGe transistors were also found to perform exceptionally well in low temperature environment [1].

The high frequency response and low voltage range of this device requires an accurate simulation model. Industry standard HBT models do not adequately represent the SiGe HBT behavior in the low temperature cryogenic environment, 27 ^{o}C (300K) to -180 ^{o}C (93K). The main purpose of this dissertation is to modify an existing industry bipolar transistor model and parameter extractions to obtain accurate simulation performance at cryogenic temperatures. The Mextram bipolar model is an industry standard SiGe bipolar model that was found to be well suited for equation modifications and parameter extractions [2]. The SiGe HBT device models developed in the following work for cryogenic temperature conditions will be based on the Mextram model equations.

The SiGe HBT devices characterized and modeled in the cryogenic temperature environment in this work are first generation SiGe HBT's. There have been several generations of commercial HBT. Each generation has higher frequency response and lower breakdown voltage than the previous one. First generation SiGe HBT's have a frequency response of 45 GHz and operating voltage limit of 3.3V, while the most recent generation of commercial SiGe HBT's have a frequency response of 200 GHz and operating voltage limit of 1.8V [3], [4].

A principle cryogenic temperature application for SiGe HBT's is SiGe BiCMOS space electronics. The ability to operate at cryogenic temperatures makes the use of warm boxes unnecessary, saving considerable weight and space [5].

1.1 Scope of dissertation

Analog and mixed-signal integrated circuit designs in commercial and cryogenic temperature environments require very accurate representation of the HBT's behavior. Hand analysis is essential for the circuit designer, but it cannot provide enough information to meet circuit specifications. Therefore, advanced compact models are used by commercial simulator software to represent the HBT's electrical behavior over the simulated temperature range. The advanced bipolar models currently used are focused on performance in the military temperature range, 125^{o}C to -55^{o}C, and not at lower temperatures.

An initial investigation of several bipolar models found that non-convergence and inaccuracy were present in the standard bipolar models at cryogenic temperatures [6]. The industry standard advanced bipolar models each have their unique approaches to bipolar effects. All of the bipolar models support temperature simulations. In each model there is a model temperature parameter, such as TREF or TNOM, that defines the temperature applicable to all other model parameters. The simulation temperature is defined by the circuit level parameter, TEMP. The models include temperature effect equations that shift the parameter values to the simulation temperature. Parameter extraction/optimization was unable to create a model parameter set that accurately simulated the cryo temperature DC and AC data. Therefore, the bipolar model needed for accurate cryogenic temperature simulation would have to be developed.

The objective of this work was to develop a single model and a single set of model parameters, as depicted in Figure 1.1 which would accurately represent the DC and AC electrical behaviors from room temperature to the cryogenic temperature of 93K. The single model developed will be referred to as a SET, Single Expansive Temperature model.

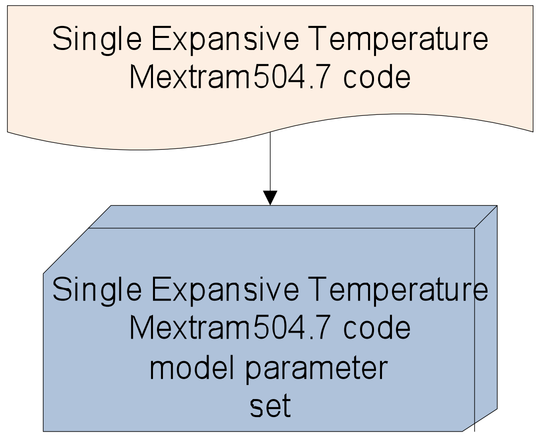

Figure 1.1 Components for DC and AC HBT simulation in the temperature environment of 300K to 93K

A key element in the development of a single expansive model was to utilize an advanced bipolar model to its full capability. Then, modify the standard model only as needed for cryogenic temperature functionality and expansive temperature ranges. The Mextram, an industry standard bipolar model, was selected for modification [2]. Mextram's strengths were needed in the cryogenic temperature region: advanced bipolar process features, a current description with the SiGe bandgap reduction effects, and several approaches to reducing convergence problems. The Mextram 504.7 release was the basis on which the SET model approach was applied [2].

The development of the SET Mextram 504.7 model required two steps. The first step was to modify the standard Mextram 504.7 to function at each of the measured cryogenic temperature points using a model parameter set specific to the corresponding measured temperature. The model temperature reference parameter, TREF, would be equal to the simulated ambient temperature, TEMP. The modified Mextram model for TREF=TEMP conditions will be referred to as Cryo Mextram504.7 model. There were four different temperature points at which DC and AC data were measured: 27°C, -50°C, -111°C and -180°C. For simplicity, the temperature points of data will be identified by their equivalent Kelvin temperatures: 300K, 223K, 162K, and 93K. The Cryo Mextram504.7 model was used to extract/optimize a corresponding model parameter set for each of the four temperature points as shown in Figure 1.2.

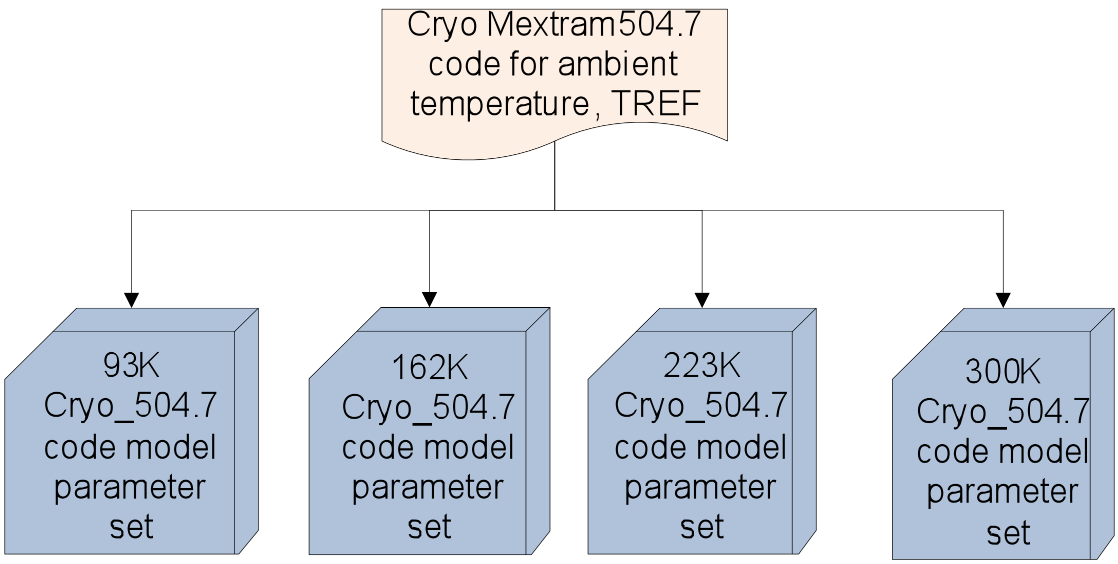

Figure 1.2 Modified Mextram 504.7 model code

The second step was to create the SET Mextram 504.7 model from the combination of the Cryo Mextram 504.7 models described above and the multiple temperature point model parameter sets. Model parameter temperature equations were developed based on the parameter values and this wide temperature range. The new temperature equations are placed into the Cryo Mextram 504.7 model to create the single expansive temperature, SET Mextram 504.7 model. The final component was to define the model parameter set that corresponds to the SET Mextram 504.7 model.

The overall flow of the model development process is summarized in Figure 1.3.

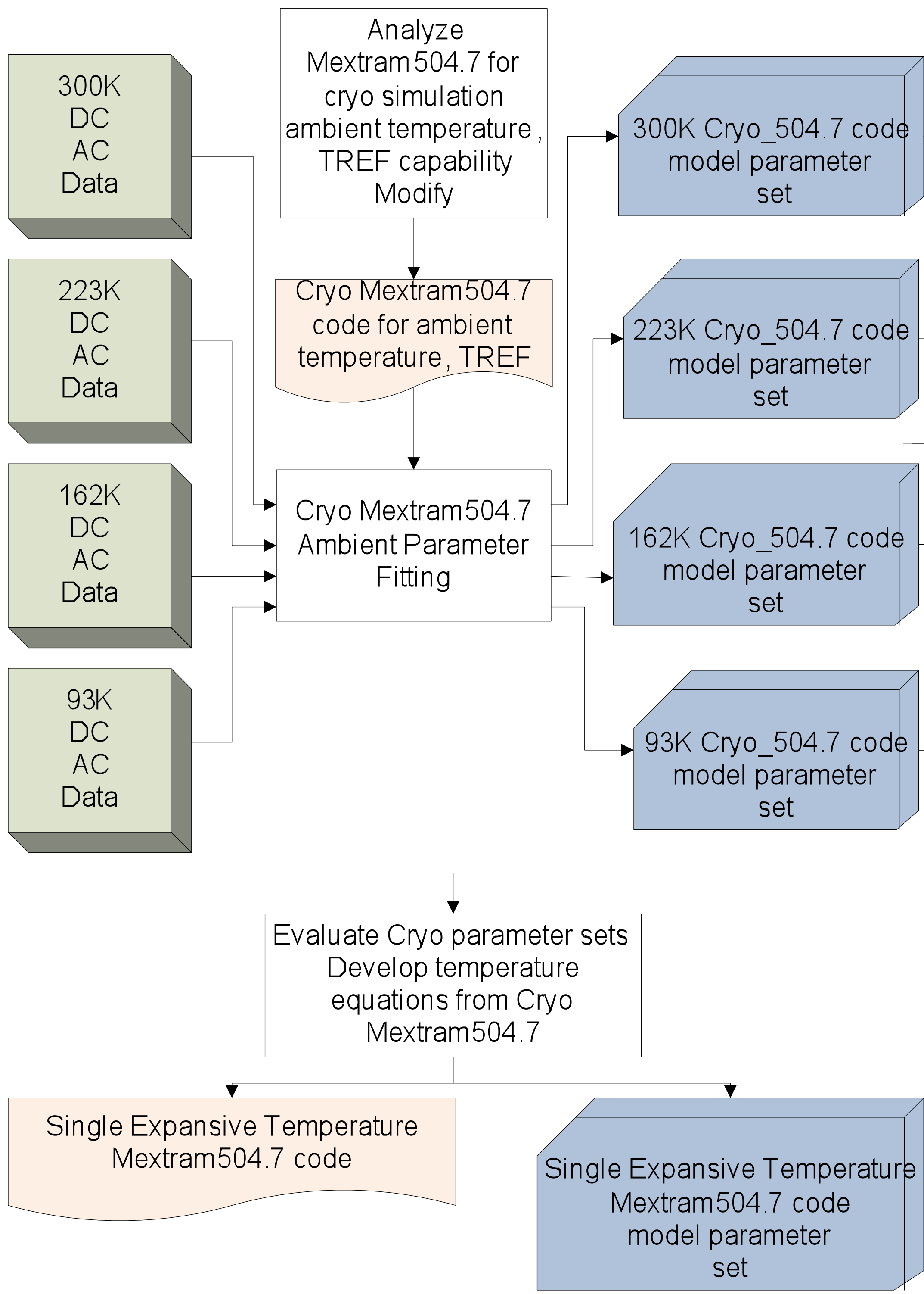

Figure 1.3 Development of Single Expansive Temperature, SET, Mextram 504.7 model equations and model parameter set

1.2 Characterization of the SiGe HBT

An introduction to the device structure and electrical performance at extremely cold ambient temperatures will focus the modeling issues of an expansive temperature range model. The following top level assessment highlights the challenges faced in developing a single expansive temperature model.

1.2.1 Device technology features

The SiGe HBT vertical NPN characterized and modeled over a very wide temperature environment was fabricated in the commercial IBM5AM BiCMOS standard process [7]. This device has a drawn emitter feature size of 0.5μm x 2.5μm. The minimum active area of the transistor structure reduces parasitic capacitance, but increases parasitic resistance. The largest parasitics are typically the depletion capacitance and extrinsic resistance. The base-emitter and base collector depletion capacitance decreases as the active area decreases. The extrinsic access resistance of both the base and the emitter increase as active area decreases. The modeled device is small as compared to other HBT's that are typically larger and used for RF power applications.

The SiGe HBT device is an advanced type of bipolar structure. A cross-section of the modeling SiGe bipolar device is shown in Figure 1.4. The device has the following features:

Polysilicon N^+ emitter
Thin N^+ Si emitter epilayer
Polysilicon extrinsic P^+ base
P^+ epitaxial SiGe intrinsic base
N^- epitaxial collector region
N^+ buried collector
N^+ plug collector for surface contact
Shallow trench oxide isolation
Deep trench isolation of sidewall oxide and poly-fill

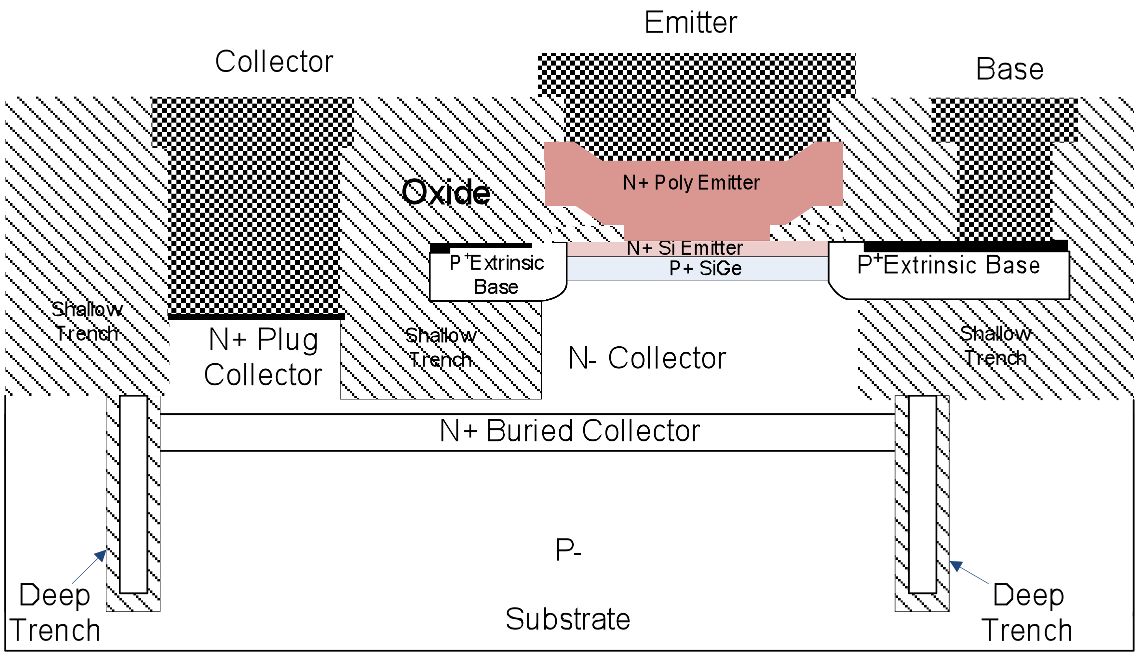

Figure 1.4 SiGe HBT cross-section [8],[9]

1.2.2 Intrinsic bipolar transistor operation

SiGe HBT's operates in the same manner as vertical Si NPN bipolar transistors. The intrinsic transistor is composed of three unique regions: N-type emitter, P-type base, and N-type collector. The current flows through the NPN HBT from the collector to the emitter. The device is typically operated in the forward mode where the base-emitter junction is forward biased. The SiGe intrinsic NPN regions can be electrically interpreted as two PN junctions back to back, connected by a very thin P-type SiGe base region. The forward biased, base-emitter junction charge carriers diffuse across the base region before recombining. The carriers reach the other PN junction and are "collected" by the strong electric field of the reverse biased base-collector interface. The current flow of charge carriers in the bipolar transistor is achieved by controlling the current of one PN junction with the bias of another PN junction. Optimum current gain and frequency response occurs when the base-collector junction is reverse biased. The full output voltage operating range of the device takes the base-collector junction from forward biased to significantly reverse biased. The model development of this dissertation will focus on the base-emitter forward operating mode and include the physical effects of both reverse and forward bias of the base-collector junction.

The transistor has four states of operation [10]. These operating states are based on the intrinsic junction voltages, VBE and VBC, as diagramed in Figure 1.5b. The active, linear operating state described above is when VBE is forward biased and VBC is negatively biased. The intrinsic junction voltages define the transistor behavior. However, data either measured or applied bias represents the terminal voltages. The terminal voltages include the effects of parasitic resistance, self-heating and the junction voltages. The contributions of these effects must also be modeled. The symbol for the SiGe NPN transistor as shown in Figure 1.5a identifies intrinsic junction voltages and terminal voltages.

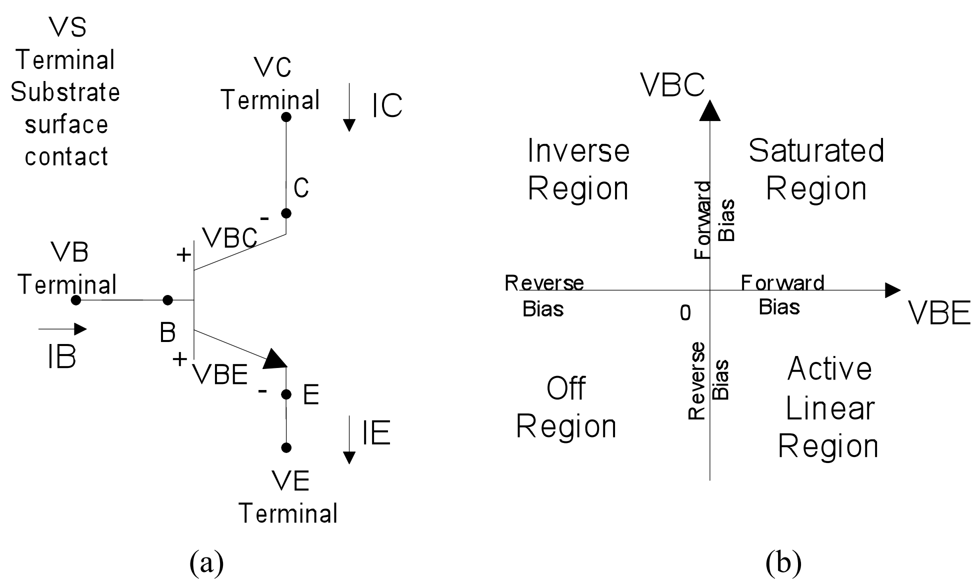

Figure 1.5 (a) Representation of NPN. (b) DC operating regions of the intrinsic HBT[10].

A cross-section of the intrinsic transistor in Figure 1.6 illustrates the regions and junction interfaces under zero bias conditions [11]. PN junction theory provides the basic semiconductor equations and representation of depletion regions at the base-emitter interface and the base-collector interface. The active areas are: the neutral emitter region of thickness, $W_{E,}$ and the zero biased neutral base region of width, W_{B0}. The space charge depletion layers are formed at the emitter-base interface and base-collector interface as indicated. The base-collector depletion layer thickness, W_{CB}, occurs mostly within the lightly doped N^- collector. The active area of the collector is the remaining N^- collector width not overcome by the base-collector depletion region.

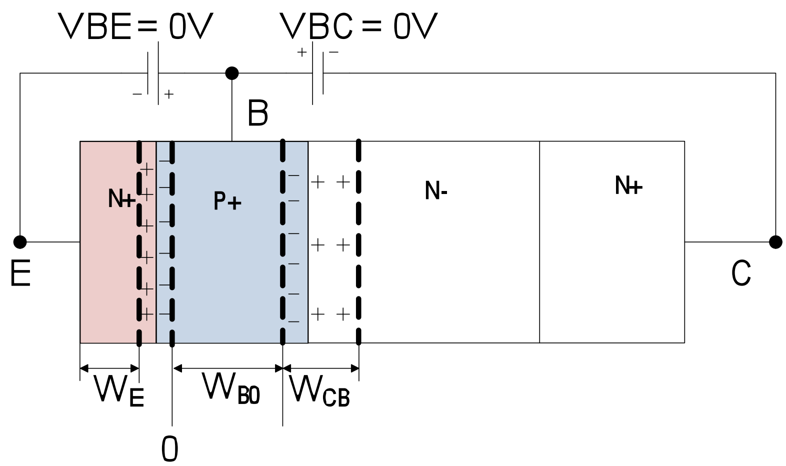

Figure 1.6 Intrinsic cross section, zero biased [11]

The active, linear state of operation occurs when the base-emitter junction is forward biased and the base-collector junction is reverse biased. The effect of bias on the junction interfaces is demonstrated by the cross-section of Figure 1.7. The flow of electrons from emitter to collector generates collector current. A comparison of zero biased and active, linear biased cross-sections in Figures 1.6 and 1.7 indicates that the neutral basewidth, $W_{B,}$ decreases and the base-collector space layer, W_{CB}, increases as voltage is applied.

The resulting decrease in basewidth due to an increase in VBC bias is defined as the forward Early effect [12]. The decrease in the basewidth due to increased VBE bias influences the reverse Early effect. As the reverse bias voltage of the base-collector junction increases the base-collector depletion region expands into the lightly doped N^- epilayer collector.

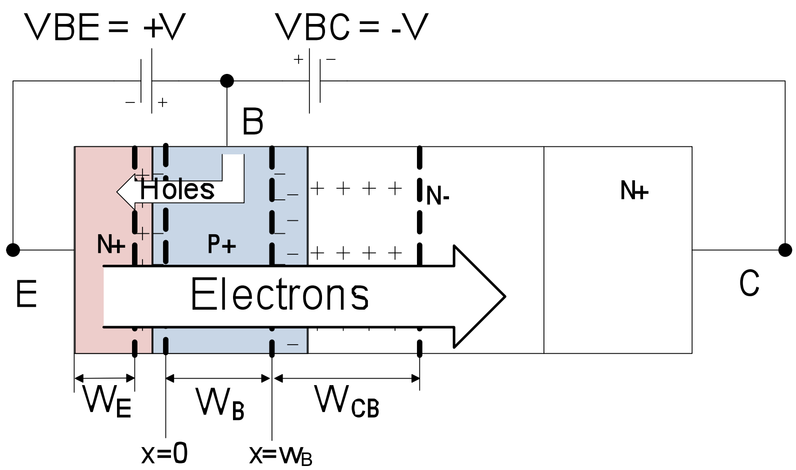

Figure 1.7 Intrinsic cross section operating in the forward active region. The base-emitter junction is forward biased by voltage, VBE. The base-collector junction is reverse biased by voltage, VBC. W_B is the length of the intrinsic base region for the quasi-neutral base definition [11].

Current flow and frequency response are described in terms of the transport of charge carriers from the emitter, through the base region into the collector. The DC and AC performances can be defined in terms of doping concentrations and region thicknesses. These bipolar transistor relationships are summarized in Chapter 2. The basic features of a SiGe base and the SiGe contributions to performance are included in Chapter 2.

1.2.3 Basic bipolar device equations for characterization

The characterization and modeling of SiGe HBT capability is based on measured performance. HBT performance can be defined in terms of large signal and small signal behaviors. The methods of Si transistor characterization also apply to SiGe.

A typical bipolar large signal representation as shown in Figure 1.8 describes basic measurement behavior [10]. However, it will not be complex enough to model the electrical performance of the SiGe HBT advanced device structure.

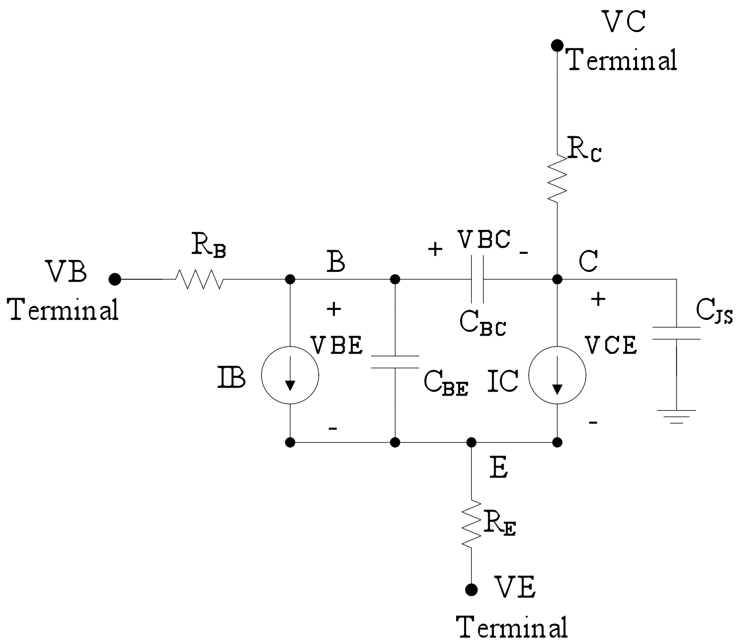

Figure 1.8 Large signal NPN representation [10]

The DC characteristics typically defined for Si can be used in initial characterization of the SiGe HBT. Collector current, IC, in Equation (1.1) is composed of three components [11]. IC has an exponential response to VBE, a direct response to the saturation current, I_S, and exponential response to emitter bandgap narrowing, ΔE_{gb}. The standard characteristics are collector current, IC, defined as:

$$IC = I_S \cdot e^{\left(\frac{qV_{BE}}{kT}\right)} e^{\left(\frac{\Delta E_{gb}}{kT}\right)} \tag{1.1}$$

The DC current gain, β_{DC}, and transconductance, g_m, are defined as:

$$\beta_{DC} = \frac{IC}{IB} \qquad\qquad g_m = \frac{q \cdot IC}{kT} \tag{1.2}$$

The characterization of the transistor has a representation for each resistive and capacitive parasitic component. The biased or measured voltages occur at the outer nodes The inner nodes include the transistor current generation and parasitic effects. The parasitic resistances are accounted for in the emitter region by R_E, in the base region by R_B, and in the collector region by R_C. There is a maximum frequency at which the transistor is able to switch on and off. This frequency corresponds to the time that it takes to move the minority charge carriers through the transistor. The total delay time for the minority charge to travel across a forward biased transistor is the forward transit time, τ_F. The total delay time for the minority charge to travel across a reverse biased transistor is the reverse transit time, τ_R. The diffusion capacitance of each region represents the region's charge transfer capability by the relationship, $C_{diffusion} = g_m\tau$. The depletion capacitance of the base-emitter junction is C_{JE}. The depletion capacitance of the base-collector junction is C_{JC}. The large signal representation for charge is defined by the sum of depletion and diffusion contributions as:

$$C_{BE} = C_{diffusion}\big|_{BE} + C_{depletion}\big|_{BE} \qquad C_{BC} = C_{diffusion}\big|_{BC} + C_{depletion}\big|_{BC} \tag{1.3}$$

The small signal behavior [10] is typically characterized by the linearized hybrid-π model shown in Figure 1.9. This translates well with the large signal representation above.

The dominant small signal frequency characteristic is the small-signal current gain, β_{AC}, and its corresponding cutoff frequency, f_T. This is defined as the frequency at which $\beta_{AC}=1$. The cutoff frequency is defined in terms of transistor components as:

$$f_T = \frac{1}{2\pi\left(\tau_F + R_C C_{JC} + \frac{kT}{q \cdot IC}\left(C_{JE} + C_{JC}\right)\right)} \tag{1.4}$$

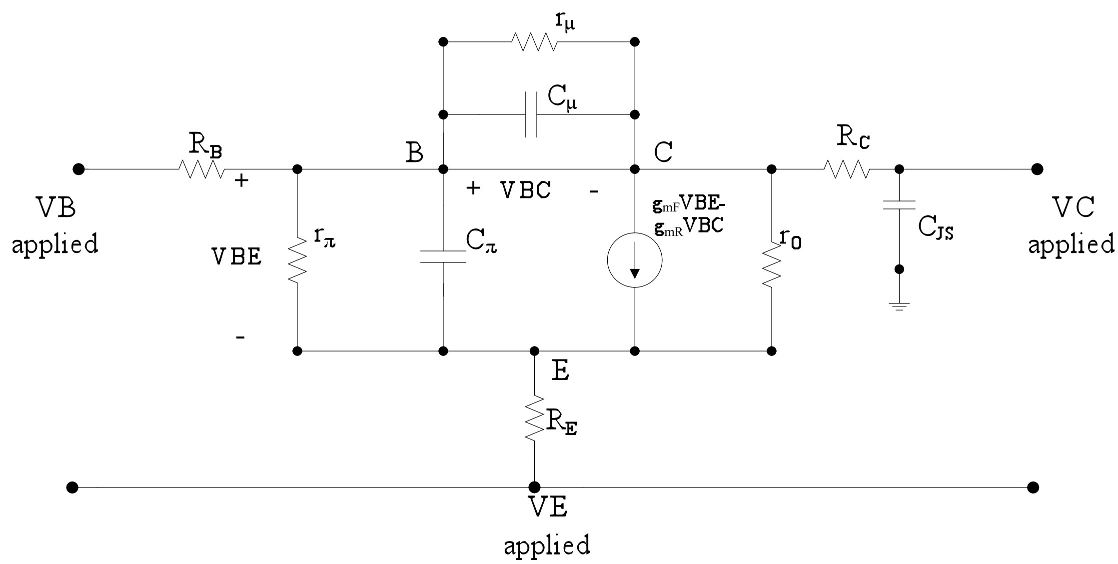

$$r_\pi = \frac{\beta_F}{g_{mF}} \qquad C_\pi = g_{mF}\tau_F + C_{JE} \qquad r_\mu = \frac{\beta_R}{g_{mR}} \qquad C_\mu = g_{mR}\tau_R + C_{JC}$$

Figure 1.9 Linearized hybrid-π model [10]

1.2.4 DC output characteristics across expansive temperature range

DC behavior of the SiGe HBT in the forward operating region is revealed by output characteristic measurements. The collector output voltage of this DC measurement is swept, thereby taking the transistor through each forward operating region: saturation and active linear, as defined in Figure 1.5b. The DC output characteristics measure the collector current as collector-emitter voltage is swept across the forward operating voltage range. The base-emitter junction is forward biased by a constant stimulus. The base-emitter constant bias may be either voltage or current. The output measurement is composed of a family of curves. Each curve of an output voltage sweep is a particular base-emitter bias value.

The transistor is in saturation at low values of collector-emitter voltage, the base-collector is forward biased, and the collector current is limited by the collector region resistance. As the collector-emitter voltage increases the base-collector becomes reverse biased, the collector current increases, and the HBT is in the linear active region of operation. Ideally, the transistor sweep starts with a linear increase in collector current and that becomes constant as the collector-emitter is swept across the output voltage range. However, physical effects due to the device structure and fabrication technology have a large influence on the shape and performance of the collector current curves. The primary physical effects that can strongly influence performance of small, SiGe HBT advanced structures are: quasi-saturation, variable collector resistance, forward and reverse Early effects, self-heating, and non-linearity at upper output voltage. The large-signal and small signal characterizations of the previous section are not intended to represent these physical effects. An advanced compact model which includes physical effects is needed to represent full performance behavior [13].

A compact model and corresponding parameter values must fit the entire forward output operating range. In this work, the objective is to develop a single expansive temperature, SET, model and the corresponding model parameter set which represents the measured output characteristics over an ambient temperature range from 93K to 300K for an applied voltage, VCE, of 0V to 3.3V. An initial, visual assessment of the output characteristics of the measured SiGe HBT, will help identify what influential physical effects are present. Output measurements at two ambient temperatures: 300K and 162K, shown in Figures 1.10 and 1.11, can be compared to get an indication of how the physical effects influence the DC behavior as the ambient temperature decreases into the cryogenic temperature region. The output characteristics at each ambient temperature are measured with a constant base-emitter voltage and a constant base current stimulus. A comparison at each ambient temperature shows dramatic differences between the two types of base biased stimulus: constant base voltage and constant base current. Visually one can clearly see significant difference in the behavior of collector current (IC). This difference is attributed to self-heating effects of the HBT. The pronounced slope of the IC

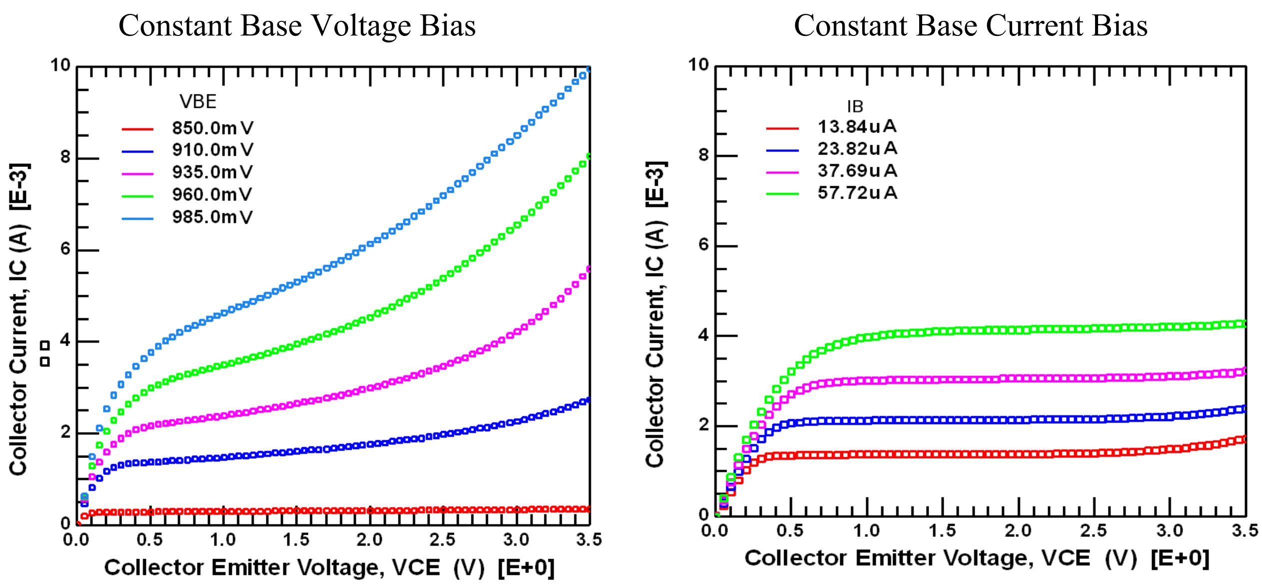

(a) (b)

Figure 1.10 Measured output characteristics at ambient temperature 300K. (a)Base biased with constant voltage source. (b)Base biased with constant current source.

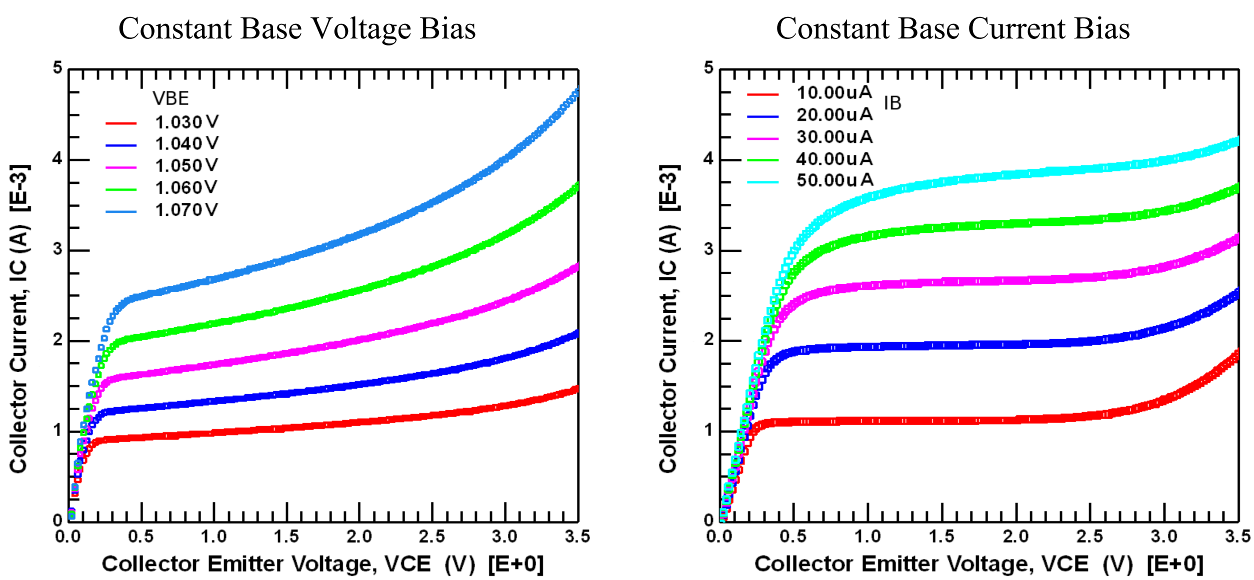

(a) (b)

Figure 1.11 Measured output characteristics at ambient temperature 162K. (a)Base biased with constant voltage source. (b)Base biased with constant current source.

saturated operating region indicates the saturation region collector resistance is large. The IC curves have a weak knee at increased base bias levels indicating that quasi-saturation is present in the normal bias operating range. The upper level of the output operating range becomes non-linear indicating that avalanche breakdown is influential in the transistor's operating range. The significant slope of IC in the linear region of the constant base bias output measurements indicate that basewidth modulation, Early effects, are of significant influence.

Self-heating. The SiGe HBT modeled has shallow trench oxide and deep trench isolation as seen in the device cross-section of Figure 1.4. These technology features are known to increase the self-heating effects. The influence of self-heating is clearly indicated in a comparison of the two base bias source output measurements. At equal values of measured IC the output curve of the constant base voltage bias has a much larger slope and smaller breakdown voltage behavior than that of the constant base current bias. This behavior indicates that self-heating effects are very significant and must be included in all parameter extractions and optimizations. Initial thermal impedance is extracted at each ambient temperature in Chapter 5 and the influence of thermal impedance is added to Chapter 7, ambient temperature models and the Chapter 8, SET model by parameter optimization.

Saturation and quasi-saturation. The saturated region collector resistance is extracted from the inverse slope of IC before the knee of the output curve. The quasi-saturation region resistance is the varying resistance within the knee of the IC curves. The collector resistance within the quasi-saturation region is clearly a function of bias, and therefore, not easily extracted. These collector resistance effects are also known to have a tremendous influence on the behavior of frequency response at higher collector currents. At larger base bias stimulus the collector current in and near saturation significantly alters the collector resistance. The voltage drop due to the current passing through the higher resistance of this lightly N^- collector region collector resistance debiases the intrinsic base-collector junction. This results in increased intrinsic base width; which was identified by Kirk and became known as the Kirk effect [14]. The physical effects of quasi-saturation were first modeled by Kull [15]. The Kull model has become a basic description for quasi-saturation in compact bipolar modeling. The original Kull model is described in Chapter 2 [15] and the Mextram implementation is described in Chapter 3.

Breakdown – avalanche. Non-linearity in the upper voltage range is consistently present at all ambient temperatures. As the ambient temperature decreases, the region of non-linear appears to expand further into the linear region. This effect is some form of breakdown. The existing weak avalanche breakdown effects will be used to model this effect [13].

Early voltage. Basewidth modulation, Early effect, is clearly evident from the slope of the IC curve in the linear region. The effect is very significant to the output characteristics. The measured Early effects are extracted in Chapter 5 at each temperature. In Chapter 7 the extracted parameters influencing Early effects are optimized to produce ambient temperature models. In Chapter 8 the ambient temperature models are used to define temperature equations. These equations are placed in a temperature modified Mextram model, SET model, which can produce the output characteristics over a very wide temperature range.

1.2.5 DC linear characteristics – Gummel across expansive temperature range

Operation of the HBT in the linear active bias region is characterized with a Gummel common-base configuration measurement. The focus is on the behavior of IC and IB as VBE is forward biased. The resulting behavior of β_F as function of IC defines the β_F regions. The lower IC region of decreasing β_F is due to low level injection. The upper IC region of decreasing β_F is due to high level injection. The influence of reverse Early voltage is present in the IB behavior in the constant β_F region.

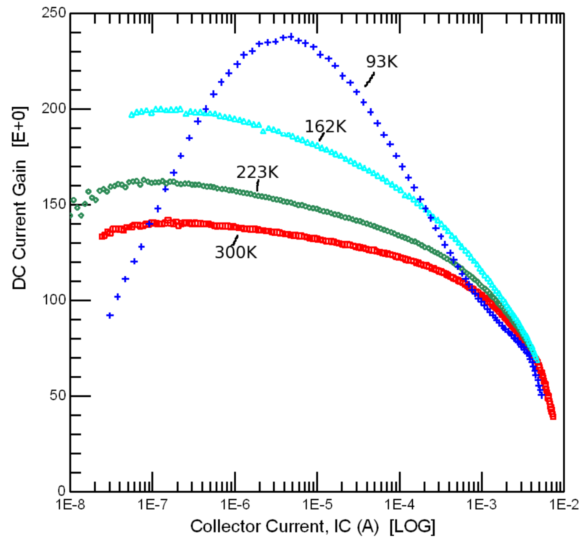

Figure 1.12 Measured DC Current Gain vs. Log(Collector Current) at ambient temperatures: 300K, 223K, 162K, 93K

All three parasitic resistances: R_C, R_B, and R_E can influence both the IC and IB curves. The quantity and behavior of β_F as a function of measured IC is critical to identifying first and second order effects that have a significant influence in the device performance. Figure 1.12 is a summary of measured β_F vs. Log(IC) at all four ambient temperatures at an applied VBC bias of -1V.

Maximum β_F continues to increase as the ambient temperature decreases. β_F more than doubles at 93K compared to 300K. The decrease of β_F at lower IC values as a function of temperature is an indication that high level injection changes as temperature decreases. High level injection becomes more significant at 162K and tremendous at -93K. This creates some difficult challenges to modeling. The region of IC values where high level injection is influential overlap with where IC needed to be biased for optimum frequency response as we will see in the next section. Therefore modeling of the high level injection and resistance effects must be included in the expansive temperature range modeling.

1.2.6 AC - Small signal representation and cutoff frequency across expansive temperature range

The AC data was obtained from S-parameter measurements. The device was biased in the linear operating region. For model development, the AC measurements were biased at the same values as the linear DC Gummel measurements above. The S-parameters measurements were converted to H-parameters.

The measurement f_T is calculated from the h21 measurements [16] at each ambient temperature and is plotted in Figure 1.13. The f_T response is very high and increases as temperature decreases. The collector current, IC, at which f_T is maximum is defined as IC_{max}. As temperature decreases IC_{max} increases slightly. However, there is very little increase in f_T below 162K.

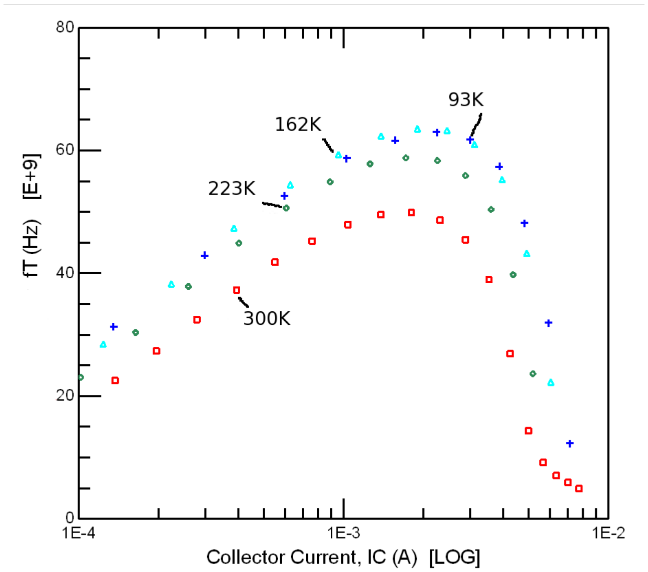

Figure 1.13 Cutoff frequency, f_T vs. Log(Collector Current) measured at: 300K, 223K, 162K, 93K

The high current region has a steep drop in f_T which indicates that collector resistance, base-collector junction voltages and high level injection will all be significant contributors to modeling the f_T region at IC_{max} and beyond.

1.3 Challenging modeling effects of SiGe HBT DC and AC performance

The SET model, the Cryo-adjusted ambient temperature models and each corresponding model parameter set must accurately simulate the SiGe HBT modeling measurements over the temperature range, 300K to 93K. The SiGe HBT measured performance has spectacular frequency response and DC capability, but it also has many nonideal behaviors. These nonideal behaviors are typically second-order effects in classic ion-implanted type vertical NPN processes and usually occurred beyond the designed operating regions. However, as the overview of electrical characteristics showed many of the nonideal behaviors are influential in the normal HBT's operating regions.

So in summary there will be many challenging model effects that must be included in the expansive temperature range of the SiGe HBT. Self heating must be included in the model due to the tremendous shifts in VBE that it produces. This small device was expected to have significant parasitic resistances and the electrical characteristics confirm their large values. Each of the three parasitic resistances will have to be accurately modeled over temperature or the intrinsic transistor behavior will not be correct. Quasi-saturation is present in the output measurements and will have to be correctly modeled for both the DC measurements and in the high current rolloff region of f_T. High level injection effects also influence AC performance and must be modeled concurrently with the DC current gain performance at colder temperatures. All of the above influences and exceptional performance occurs over a small operating voltage range, the VCE upper limit is 3.3V.

1.4 Breakout of dissertation

Chapter 2 includes the background of the SiGe HBT and bipolar modeling. The distinctions and contributions of the advanced bipolar process features are summarized and the physics of a SiGe base is reviewed.

The Mextram 504.7 model release is reviewed in Chapter 3. An overview of the software tools and implementation for model extraction and optimizations are presented in Chapter 4.

The measured device data at four ambient temperatures is summarized in Chapter 5. Initial parameter extractions from data and the definition of bias operating regions are included.

An overview of the modeling process is presented in Chapter 6. The unique behavior that was included in the Cryo Mextram 504.7 model code is presented. The extraction and optimization methodology common to developing each ambient temperature is summarized in Chapter 7. The optimized model parameter set for each ambient temperature and the corresponding simulated fits to measured data are included in Chapter 7.

The parameter temperature equations for the single expansive temperature model are presented in Chapter 8. The summary of the SET Mextram 504.7 model, the model parameter set and fitted results are completed as well.

In Chapter 9, the development of temperature equations that support a Mextram modified model will be concluded. The success of optimizing model parameters which predict DC and AC behaviors over a very wide temperature range, far down in the cryogenic temperature region, will be presented. Also, the limits reached in this work and the direction of further research will be discussed.

2 Background – SiGe HBT and bipolar models

The SiGe HBT's exceptional performance is due to a combination of technologies. These technologies can be divided into two groups: the first is the advanced Si fabrication techniques that yield submicron features, and the second technology is using a SiGe alloy as the intrinsic base region. The electrical contributions of each technology feature must be correctly weighted in the model to successfully fit the DC and AC performance over a very expansive temperature range. Chapter 2 will review the physical capabilities of advanced vertical NPN Silicon bipolar fabrication technologies used for SiGe HBT fabrication and the contributions of SiGe bandgap engineering. Some of the physical relationships are also used to calculate initial model parameter values. The last part of the chapter discusses the background of bipolar modeling. Bipolar modeling has been built upon the Ebers-Moll model [17] and integrated charge control relationship, ICCR, of Gummel and Poon [18]. These theories are the backbone of advanced bipolar models. The Mextram model used in the single expansive temperature model developed in this work is built upon these concepts.

2.1 Advanced silicon bipolar fabrication technology features

There are several types of commercial vertical NPN SiGe HBT device structures. SiGe processes use advanced fabrication technologies to optimize performance characteristics. These process technologies were developed to maximize gain and frequency response of Si bipolar devices. The fabrication technologies focus on two independent areas of improvement: the intrinsic transistor performance and the reduction of parasitics inherent to a device structure.

The intrinsic transistor performance is optimized by the transistor's doping profile and layer thicknesses. The development of in-situ doped epitaxial layers allows extremely accurate control of doping concentration and layer growth rate. This technology greatly improves the ability to tailor doping profiles and minimize region thicknesses [19].

The second area of focus that fabrication techniques address is the minimization of parasitic resistance and capacitance within the intrinsic and extrinsic regions of the transistor. Doped polysilicon fabrication techniques allow self-alignment, thereby reducing contact spacing and area, as well as minimizing extrinsic contact resistances [11]. Shallow trench oxide isolation and deep trench poly filled isolation also reduce spacing rules and minimize area. The parasitic resistance and capacitance of each region is process specific and dependent upon the physical structure. High frequency analog and digital circuit designs require bipolar device structures to have minimum parasitic resistances and capacitances.

The intrinsic Si bipolar device has fundamental performance limits due to the relationship between doping concentrations and region thicknesses. Changes of either will improve the performance of one electrical characteristic, but unfortunately will begin to degrade another. The intrinsic transistor cross section of Figure 2.1 indicates the charge carrier concentration and layer thickness of each region, which relate to the electrical characteristics defined by the Si process design equations below.

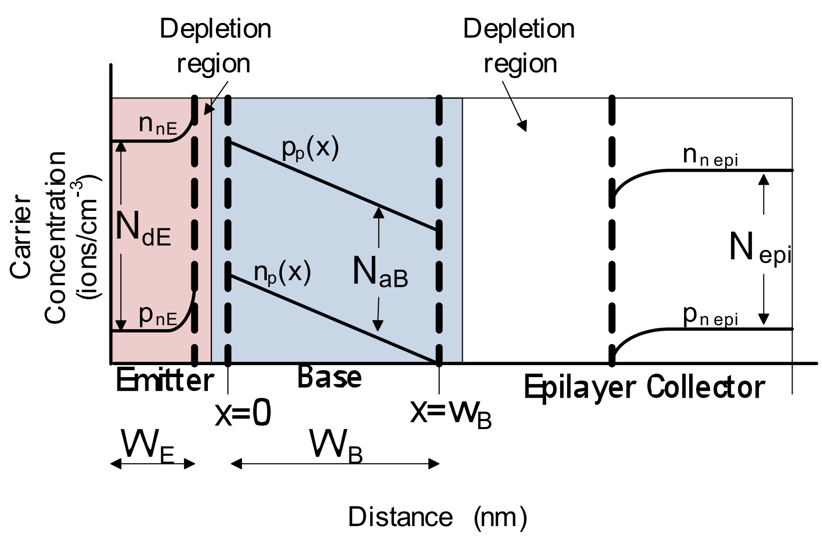

Figure 2.1 Charge carrier concentration across an intrinsic cross section. Uniform doping was used and not drawn to scale [20].

The relationship between electrical performance and process technology features of doping concentrations, diffusivity, and region thickness are summarized in Equations (2.1) thru (2.8) [11].

The Si NPN bipolar process Equations (2.1), (2.2) and (2.3) define DC currents and current gain of a heavily doped base with base bandgap narrowing included:

$$IC = \frac{qA_E D_{nB} n_{io}^2}{W_B N_{aB}} e^{\frac{qV_{BE}}{kT}} e^{\frac{q\Delta E_{gb}}{kT}} \quad \text{and} \quad IS = \frac{qA_E D_{nB} n_{io}^2}{W_B N_{aB}} \tag{2.1}$$

$$IB = \frac{qA_E D_{pE} n_{io}^2}{W_E N_{dE}} e^{\frac{qV_{BE}}{kT}} \tag{2.2}$$

$$\beta = \frac{IC}{IB} = \frac{D_{nB} W_E N_{dE} e^{\frac{q\Delta E_{gb}}{kT}}}{D_{pE} W_B N_{aB}} \tag{2.3}$$

q	Magnitude of electron charge, (C)
k	Boltzmann constant (eV/K)
T	Device temperature (K)
W_B	Intrinsic base width (nm)
W_E	Neutral emitter width (nm)
A_E	Active emitter area (um^2)
n_{i0}	Intrinsic concentration of undoped Si (cm^{-3})
N_{dE}	Electron donor concentration in the emitter (cm^{-3})
D_{pE}	Diffusion coefficient of holes in the emitter (cm^2/s)
N_{aB}	Hole acceptor concentration in the neutral base (cm^{-3})
D_{nB}	Diffusion coefficient of electrons in the base (cm^2/s)
ΔE_{gb}	Bandgap narrowing due to heavy doping in the base (cm^{-3})

The frequency response of the device is defined by cutoff frequency, $f_{T,}$ and is dependent upon the collector current, IC. For bipolar devices, f_T is typically defined as:

$$f_T = \frac{1}{2\pi\left(\tau_F + \frac{kT}{q \cdot IC}\left(C_{JE} + C_{JC}\right) + R_C C_{JC}\right)} \tag{2.4}$$

The depletion junction capacitances are defined by C_{JE} and C_{JC}. The forward transit time, τ_F, is the sum of the times required to travel through each region of the intrinsic transistor. The travel time needed for excess charge to pass through each region is defined as: τ_E, emitter transit time for the emitter region, τ_B, base transit time of the neutral base region, and τ_C , collector transit time for the collector space charge regions. The total transit time for a Si bipolar device is therefore described by the following equations:

$$\tau_F = \tau_E + \tau_B + \tau_C \tag{2.5}$$

$$\tau_E = \frac{Q_E}{IC} = \frac{W_E W_B N_{aB}}{2 N_{dE} D_{nB}} \tag{2.6}$$

$$\tau_B = \frac{Q_B}{IC} = \frac{W_B^2}{4 D_{nB}} \tag{2.7}$$

$$\tau_C = \frac{Q_C}{IC} = \frac{W_C}{2 \nu_{sat}} \tag{2.8}$$

Q_B	Charge of the intrinsic base region
Q_E	Charge of the emitter region
Q_C	Charge of the base-collector depletion region
ν_{sat}	Base-collector saturation drift velocity due high electric field (cm/s)
W_C	Base-collector depletion region width (nm)

For a Si device the typical forward charge transit times of each region, are defined in the Equations (2.6), (2.7) and (2.8). In advanced Si devices the base transit time is assumed to have a non-uniform base doping from emitter to collector interfaces in order to maximize the accelerating built-in field. The tailoring of the base doping profile allows the denominator factor of τ_B to range from 2.5 to 4. The denominator factor of 4 reflects precision in-situ doping of a non-uniform base profile to minimize base transit time [11].

Advanced Si devices have a thin intrinsic basewidth and are heavily doped. This combination yields the highest cutoff frequency and maximum operating voltage range without decreasing DC current gain, β_{DC}. Reducing the basewidth will decrease the base transit time, thereby increasing cutoff frequency. However, punchthrough of the collector to emitter regions occurs if the base region is too thin. Heavily doping the intrinsic base region prevents punchthrough. The drawback to a very high base doping concentration is that β_{DC} decreases. Therefore, Si processing technologies have taken Si intrinsic doping and region thickness to the basic limits of Si material. The f_T and β_{DC} relationships discussed above are summarized in Table 2.1. [11]

Performance Enhancement	Process Technique	Advantage	Disadvantage
f_T increases	decrease basewidth	τ_B decrease	breakdown voltage decreases due to punchthrough
punchthrough voltage increases	increase base doping	depletion regions decrease	β_{DC} decreases
R_B(total) decreases	increase base doping	R_B(intrinsic) decreases	β_{DC} decreases
f_T increases	increase collector doping	τ_C decreases	breakdown voltage decreases

Table 2.1 Performance enhancements of intrinsic Si transistors

Polysilicon fabrication enables the use of self-aligned fabrication techniques that reduce layout spacing dimensions. A double polysilicon process of poly emitter and polysilicon extrinsic base minimizes the spacing rules between emitter and extrinsic base regions [11]. The overall size of the regions can be reduced, thereby reducing junction areas and peripheries which reduce components, C_{JE} and C_{JC} [21]. Polysilicon emitters can be very heavily doped to reduce emitter resistance, R_E. Extrinsic polysilicon base regions are also heavily doped to minimize extrinsic base resistance. The extrinsic polysilicon base regions are grown over shallow trench isolation to reduce parasitic base-collector capacitance.

In-situ doped epitaxially grown layers allow optimum control of doping and layer thickness. Very thin intrinsic base layers of less than 100 nm are possible and can be heavily doped with precise control. A lightly doped N^- collector region is fabricated by epitaxially growing an N^- Si layer of a few hundred nm in thickness on top of the heavily doped N^+ buried collector layer [19].

The following table summarizes the benefits of Si and SiGe advanced process technologies discussed above.

Process Feature	**Enhancement**	**Frequency Response Component Improved**
polysilicon-emitter	minimizes peripheral base-emitter capacitance	C_{JE} decreased
polysilicon extrinsic base	reduces base-collector capacitance	C_{JC} decreased
thin, in situ P^+ epitaxial grown base	minimizes basewidth, increases intrinsic base doping	τ_F decreased R_B decreased
epitaxial grown collector region	lightly-doped N^- region reduces capacitance at B-C interface	C_{JC} decreased
buried N^+ collector	N^+ with surface collector contact thru deep N+ plug	R_C decreased
shallow trench oxide	reduces extrinsic base-collector capacitance	C_{JC} decreased
deep trench	lateral isolation between devices	C_{JS} decreased
substrate surface contact by deep P^+ plug to the P^- substrate	device isolation	$R_{Substrate}$ decreased

Table 2.2 Process features of advanced bipolar transistors

Shallow trench oxide is used for lateral isolation. It greatly reduces the parasitic base-collector capacitance by removing the P-N junction between the extrinsic base and active collector region. Deep trench isolation greatly reduces layout dimensions over junction isolation methods thereby reducing area and periphery capacitances.

2.2 Saturation, quasi-saturation and Kull's theory

Saturation. Optimum bipolar performance, as described in the previous section, requires the transistor be biased in the linear, forward active operating state, so that the base-emitter junction is forward biased and the base-collector junction is reverse-biased. When the transistor is biased in the saturated operating state the DC and AC performance becomes greatly diminished. A cross-section of the intrinsic transistor biased in saturation is shown in Figure 2.2.

In saturation the output voltage is small; the base-emitter junction is forward biased by a constant stimulus, which results in the base-collector junction being forward biased. The bipolar terminal voltages interact by the relationship of:

$$VCE = VBE - VBC \tag{2.9}$$

The DC output measurement of Figure 2.3 shows the dependence of IC on the output voltage in the saturation operating state. For small values of VCE, the collector current is small and slowly increasing as the output voltage increases. In the saturated region the linear relationship of IC to VCE is dominated by a constant collector resistance. The saturated collector resistance, R_{Csat}, is composed of a constant resistance contribution from each resistive collector region.

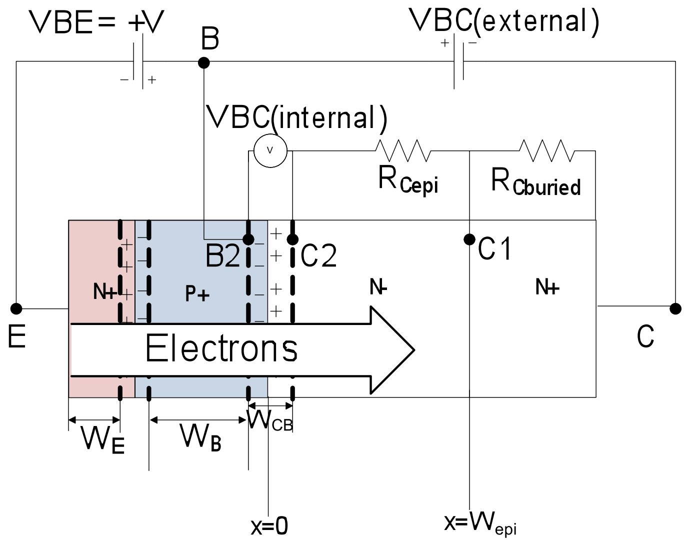

VBC(external)	External base-collector voltage, VBC, defined as nodes B and C. Total voltage is the sum of the base-collector junction voltage and the voltage drops across the various collector regions
VBC(internal)	Internal base-collector junction voltage, V_{B2C2}, between metallurgical interface of base and N- collector epilayer, defined at nodes B2 and C2
R_{epi}	N^- collector epilayer variable resistance. Voltage drop, V_{C1C2}, is due to R_{epi}.
R_{buried}	N^+ buried collector constant resistance. Voltage drop $V_{C1C}$is due to R_{buried}.
W_{epi}	Total thickness of the N^- collector epilayer
x=0	Base-collector epilayer interface, the epilayer edge is referenced to 0
$x=W_{epi}$	Interface of the N- epilayer collector layer and N+ buried collector layer, the end of the epilayer and defined as W_{epi}

Figure 2.2 Intrinsic cross section of quasi-saturation region. The base-emitter junction is forward biased, by voltage, VBE. The external base-collector voltage is reverse biased. However the internal base-collector junction interface is forward biased [11].

Quasi-Saturation. The collector region of an advanced bipolar device is typically composed of two uniquely doped N^-type regions. A lightly doped collector epilayer adjacent to the base decreases the base-collector junction deletion capacitance but is resistive. The large collector epilayer resistance is dependent on the current flow through the region. The collector current dependence causes collector bias and resistance variations. As the output voltage increases, the collector current increases moving the transistor junctions out of the saturation operating state. However the increased collector current through the epilayer can increase the voltage drop across the epilayer until quasi-saturation occurs. The weak knee behavior of IC in Figure 2.3 illustrates the effect of quasi-saturation.

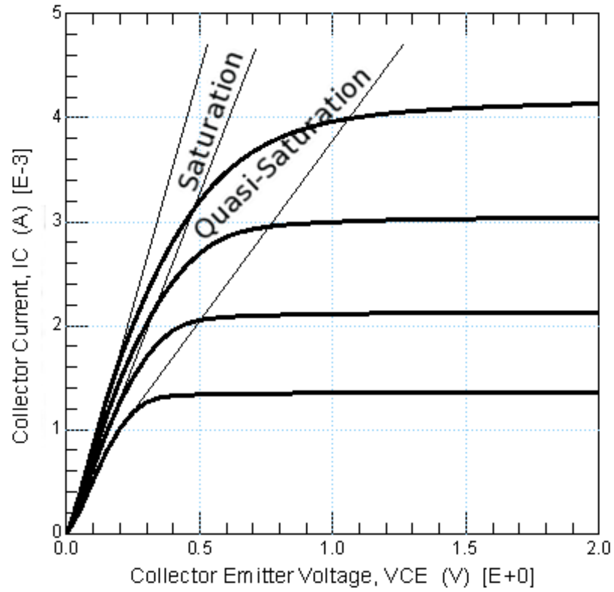

Figure 2.3 Output measurement indicating the saturation and quasi-saturation regions.

The voltage contributions of the primary effects happening between the base and collector terminals are defined in the following equations:

$$\underset{\text{Base-Collector voltage}}{\text{VBC(external)}} = \underset{\text{Junction interface voltage}}{\text{VBC(internal)}} + \underset{\substack{\text{epi region}\\ N^{-}\text{epi variable resistance voltage}}}{IC \cdot R_C(\text{variable})} + \underset{\substack{\text{buried region}\\ N^{+}\text{buried constant resistance voltage}}}{IC \cdot R_C(\text{constant})} \qquad (2.10)$$

The device is in quasi-saturation when the base-collector internal junction voltage becomes forward biased even though the base-emitter junction is forward biased and the external base-collector is reverse biased [11]. The reason for this nonideal bipolar behavior is that the forward current through the N^- epilayer causes a voltage drop across the N^- collector epilayer region which is large enough to cause the internal base-collector junction to be forward biased.

The voltage drop in the collector epilayer is due to one, or two simultaneous causes. The singular cause is an ohmic voltage drop across the epilayer. The dual cause is due to base widening, Kirk effect, and simultaneously ohmic resistance.

Base-widening, Kirk effect. The Kirk effect [14] occurs when forward bias of the base-collector interface junction injects holes into the N^- epilayer. High level injection occurs in the epilayer when the internal base-collector junction voltage, $V_{B2C2,}$ is approximately equal to the junction diffusion voltage, VDC. The diffusion voltage of the P^+ base-N^- epilayer collector interface as defined in Equation (2.11).

$$VDC = V_T \cdot \ln\left[\frac{N_{epi}^2}{n_i^2}\right] \tag{2.11}$$

N_{epi}	Effective collector epilayer doping concentration
n_i	Collector intrinsic concentration

When the high level injection bias condition of V_{B2C2}=VDC occur, the charge densities of the base-epilayer are shown in Figure 2.4 [22]. At C2, base-collector epilayer interface the electron and hole densities are equal. High injection of holes into the N^- epilayer occurs between x=0 and $x=x_i$ which causes the electron density to also increase in this region due that charge neutrality be maintained. The base therefore widens and between the epilayer interface, x=0, and x_i the electron density is greater than the epilayer doping concentration, N_{epi}. Between $x=x_i$ and the epilayer interface to the buried layer at C1, collector behaves in an ohmic conduction.

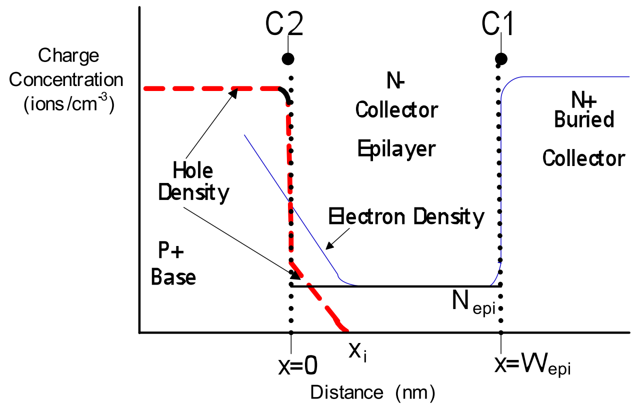

N_{epi}	Doping concentration of the N^- collector epilayer
$x=x_i$	Injection layer thickness measured from the base-collector interface into the N^- epilayer
$x=W_{epi}$	Thickness of the entire N^- epilayer collector layer

Figure 2.4 Electron and hole densities versus collector region of an NPN base-collector region. The base-N⁻ collector epilayer interface starts at x=0. The thickness of the epilayer is at x=Wepi. [22]

Kull quasi-saturation theory. The Kull model [15] of quasi-saturation addresses the two effects in terms of an epilayer current and charge. The Kull model implements the quasi-saturation effects with one current equation, I_{epi}, based on the doping concentrations and carrier mobility. The Kull quasi-saturation model was the first to describe the behavior of conductivity modulation and carrier drift velocity saturation. The Kull model assumes quasi-neutrality inside the N^- epilayer collector under all conditions.

In Kull's theory the hole densities are calculated at each edge of the epilayer in terms of the internal and external base-collector voltages. The base-N^- epilayer interface hole density, p_0, and the hole density at the N^-epilayer interface to N^+ buried collector, p_W, are defined as:

$$p_0 = \frac{1}{2}\sqrt{1 + 4\exp\left[\frac{V_{B2C2} - VDC}{V_T}\right]} - \frac{1}{2} \qquad (2.12)$$

$$p_W = \frac{1}{2}\sqrt{1 + 4\exp\left[\frac{V_{B2C1} - VDC}{V_T}\right]} - \frac{1}{2} \tag{2.13}$$

p_0	Hole density at base/collector epilayer interface, normalized with respect to N_{epi}
V_{B2C2}	Voltage across base/collector epilayer junction
p_W	Hole density at epilayer/N^+ buried collector interface, normalized with respect to N_{epi}
V_{B2C1}	Total voltage drop from the base-N^- collector epilayer interface to the N^-epilayer-N^+ buried layer interface. Sum of voltages, V_{B2C2}, the base-collector epilayer junction and V_{C1C2}, the voltage drop across the N^- epilayer.

Kull's theory separately defines the non-ohmic resistance contribution of the hole injection thickness layer, x_i, and the ohmic resistance contribution of the remaining epilayer, (W_{epi}-x_i). The non-ohmic injection layer resistance contribution is based on the critical voltage, V_c, of the injection layer's electric field. Electrons are transported from base to collector epilayer by drifting across the electrical field, $E(x_i)$ of the injection layer at saturation velocity, ν_{sat}. Kull related the critical voltage of the injection layer in terms of the normalized holes densities, p_0 and p_W defined in Equations (2.12) and (2.13) as:

$$V_C = V_T\left(2p_0 - 2p_W - \ln\left[\frac{1 + p_0}{1 + p_W}\right]\right) \tag{2.14}$$

The sum of the critical voltage, $V_{C,}$ and the voltage across the epilayer from the base interface to the N^+ buried layer interface, V_{C1C2}, is divided by the total ohmic epilayer resistance, R_{epi}, to determine the epilayer current, I_{epi}, in Equation (2.15).

$$I_{epi}\left[\text{Kull}\right] = \frac{(V_C + V_{C1C2})}{R_{epi}} \tag{2.15}$$

The Kull model takes into account velocity saturation (Kirk effect). However, the Kull model assumes quasi-neutrality in the high electric field of the injection layer. In Chapter 3 the Mextram quasi-saturation model will modify the Kull model for non-quasi-neutrality conditions that occur during velocity saturation.

2.3 SiGe base physics

SiGe bipolar processes utilize the Si bipolar process technologies described in the preceding section to improve their electrical performance. However, the SiGe bipolar device can maintain current gain at much higher frequencies than the Si bipolar device. The main difference of the two bipolar types is in their base regions. The base of the homojunction Si structure is an epitaxially grown silicon layer. Si performance is limited by doping concentration and thickness of the Si base layer. The base region of the heterojunction structure is a very thin layer of epitaxially grown SiGe alloy. The base heterojunctions and the tailoring of the Ge profile provide the ability to increase frequency response and decrease base resistance, while maintaining breakdown voltages and current gain. This section will focus on the contributions of the SiGe base.

The growth of an in-situ doped SiGe alloy layer of intrinsic base is engineered for a particular Ge concentration profile type. The contributions of SiGe bandgap engineering can be appreciated by reviewing two types of Ge concentration profiles; constant and graded [21].

2.3.1 Constant Ge concentration analysis

A SiGe HBT designed with a constant Ge concentration across the base provides the opportunity to consider the differences between Si and SiGe. The pseudomorphic SiGe material is grown with a constant Ge concentration between two unstrained Si epitaxial layers to form the base. SiGe has a smaller energy bandgap, $E_{g,SiGe}$ than Si energy bandgap, $E_{g,Si}$. The percentage amount of Ge concentration determines $E_{g,SiGe}$. The difference in bandgap, $\Delta E_{g,Ge}$, due to Ge concentration is typically 75 meV per 10% Ge concentration[21]. Energy bandgap diagrams are very helpful in understanding the contributions of the SiGe base layer. The energy bandgap comparison of a Si base transistor to a SiGe HBT with a constant Ge profile type [11] is shown in Figure 2.5. The bandgaps demonstrates the barriers to electron flow from emitter to collector.

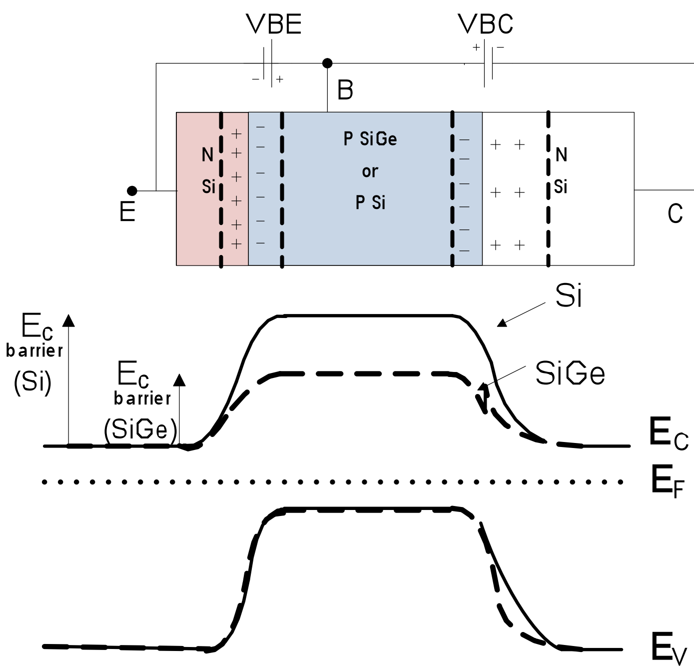

Figure 2.5 Bandgap diagrams comparison of Si (solid line) and constant Ge in SiGe base (dashed line) equivalent NPN transistors at zero-bias.[23]

For SiGe, the reduction of bandgap energy occurs in the conduction band. The valence band of SiGe is equal to that of Si. Electrons transporting from emitter to base see a lower conduction band barrier height, $E_{Cbarrier}$ for SiGe as compared to Si. The barrier height for holes is the same for both SiGe and Si. Therefore, the collector current of SiGe is greater than that of Si for the same base current. Most importantly, the current gain increases for the SiGe base. The heterojunction provides the opportunity to replace the current gain lost when basewidth is decreased and base doping is increased. The SiGe basewidth is therefore designed to be very thin and heavily doped to reduce the base transit time, $\tau_{B,}$ and reduce base resistance.

2.3.2 Graded base Ge concentration analysis

The constant profile bandgap diagram of Figure 2.5 clearly indicates the current gain benefits of SiGe over Si. The graded profiles vary from triangular to trapezoidal [21]. The trapezoidal Ge concentration profile provides a combination of current gain and additional frequency response improvement over a constant Ge concentration profile.

The HBT modeled has a graded Ge concentration with a trapezoidal profile. This grading creates a heterojunction interface at the emitter-base junction, with the emitter being Si and the base being SiGe. Likewise, the base epi-collector interface is a heterojunction. The SiGe HBT is more accurately defined as a double heterojunction bipolar transistor. The trapezoidal profile of Ge concentration across the base and the corresponding bandgap diagram [21] is shown in Figure 2.6. The graded Ge concentration profile is linearly reduced across the base starting at the B-C interface during the epi-base layer growth. The lower Ge concentration at the B-E interface produces the largest base bandgap energy. As the graded Ge concentration increases in the direction of emitter to collector, it produces a continually reducing bandgap. The reduction in bandgap, $\Delta E_{g,Ge}$, across the base from emitter to collector produces a quasi-drift field that enhances the electrons transfer, thereby decreasing the base transit time, τ_B.

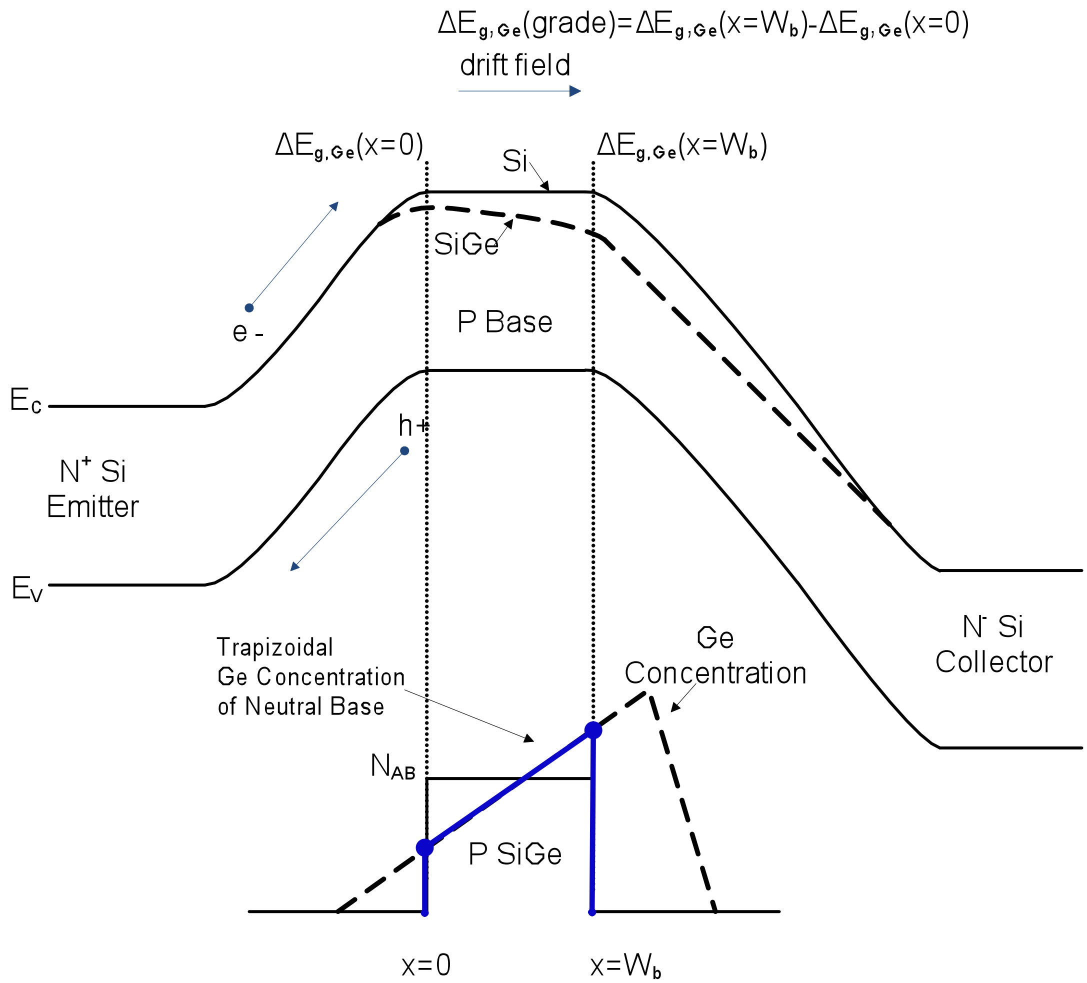

Figure 2.6 Comparison of Si(solid line) and SiGe(dash line) bandgap energy diagrams. A corresponding Ge trapezoidal profile is drawn in a base of constant doping concentration, N_{AB}. x=0 represents the edge of the E-B depletion region in a quasi-neutral base biased at VBE. x=w_B represents the length of the quasi-neutral base, located at the edge of the B-C depletion region [21].

$\Delta E_{g,Ge}$(grade) is the total germanium influenced bandgap narrowing across neutral base region:

$$\Delta E_{g,Ge(grade)} = \Delta E_{g,Ge(x=W_B)} - \Delta E_{g,Ge(x=0)} \tag{2.16}$$

$\Delta E_{g,Ge}(x=0)$ is the germanium influenced bandgap narrowing at the emitter- neutral base interface. $\Delta E_{g,Ge}(x=W_b)$ is the germanium influenced bandgap narrowing at the neutral base-collector interface.

The heterojunction interfaces and grading of Ge concentration across the base creates three very beneficial effects. The emitter-base interface heterojunction increases the electron flow by a factor $\exp(\Delta E_{g,Ge(grade)}/kT)$.

- The first benefit is that the larger electron flow increases the collector current, IC_{SiGe} without increasing the base current of the emitter base interface. So the IC_{SiGe} is greater than the IC_{Si} of an equivalent Si transistor.
- The second effect follows that an increased IC_{SiGe} for the same base current therefore increases the SiGe DC current gain, $\beta_{SiGe,}$ compared to the β_{Si} of the silicon transistor.
- The third benefit is a drift field is created across the neutral base that increases the electron injection from emitter to collector from the linear grading of Ge concentration. This increased drift field decreases the electron transit time across the base. The SiGe base transit time, $\tau_{B\ SiGe}$, is much less the silicon bipolar, $\tau_{B\ Si}$.

Another method of evaluating the differences between a graded base SiGe and Si transistor is by the design equations of: IC_{SiGe}, β_{SiGe}, $\tau_{B,SiGe}$, and $\tau_{E,SiGe}$ derived by Harame [21]. The derivations are based the Moll-Ross relation of Equation (2.22). Harame's equations and comparisons to Si equivalent equations are based on the conditions of low-level injection, Boltzman's statistics, and constant base doping. The Si collector current, IC_{Si}, defined in Equation (2.1) is repeated in Equation (2.17) for a comparison with Harame's derivation of SiGe collector current, IC_{SiGe}, in Equation (2.18).

$$IC_{Si} = \frac{qA\bar{D}_{nB} n_{io}^2}{W_B N_{aB}} e^{\frac{qV_{BE}}{kT}} e^{\frac{\Delta E_{gb}}{kT}} \tag{2.17}$$

$$IC_{SiGe} = \frac{qAD_{nB} n_{io}^2}{W_B N_{aB}} e^{\frac{qV_{BE}}{kT}} e^{\frac{\Delta E_{gb}}{kT}} \times \left(\frac{(\bar{N}_C \bar{N}_V \bar{D}_{nB})_{SiGe}}{(N_C N_V D_{nB})_{Si}} \right) \left(\frac{\Delta E_{g,Ge(grade)}}{kT} \right) \left(\frac{e^{\frac{\Delta E_{g,Ge(x=0)}}{kT}}}{1 - e^{\frac{\Delta E_{g,Ge(grade)}}{kT}}} \right) \tag{2.18}$$

q	Unit charge, (C)
k	Boltzmann constant (eV/K)
T	Device temperature, (K)
W_B	Intrinsic base width of quasi-neutral base at bias (nm)
A_E	Emitter Area (um^2)
n_{i0}	Intrinsic concentration of undoped Si (cm^{-3})
N_C	Constant density of states in the conduction band of Si (cm^{-3})
N_V	Constant density of states in the valence band of Si (cm^{-3})
D_{nB}	Constant diffusion coefficient of electrons in the base of Si (cm^2/s)
$\bar{N}_C$	Average density of states in the conduction band of SiGe (cm^{-3})
$\bar{N}_V$	Average density of states in the valence band of SiGe (cm^{-3})
$\bar{D}_{nB}$	Average diffusion coefficient of electrons in the base of SiGe (cm^2/s)
N_{aB}	Hole concentration in the neutral base, constant base doping assumed(cm^{-3})
ΔE_{gb}	Bandgap narrowing due to heavy doping in the emitter (eV)

A comparison of the two IC equations clearly shows the opportunity for SiGe to be greater. The strain enhancement of SiGe [24] produces a $\frac{(\bar{D}_{nB})_{SiGe}}{(D_{nB})_{Si}} > 1$. Strain enhancement increase collector current but the majority of increase in IC_{SiGe} as compared to IC_{Si} is from the contribution of the bandgap differences.

Since the base currents of Si and SiGe are equal for equivalent transistors the increase in IC_{SiGe} is immediately translated to an increase in β. A comparison of SiGe DC current gain, β_{SiGe}, to Si DC current gain, β_{Si}, is defined in the design equation by Harame [21] in Equation (2.19).

$$\frac{\beta_{SiGe}}{\beta_{Si}} \approx \left.\frac{IC_{SiGe}}{IC_{Si}}\right|_{VBE} = \frac{\left(\frac{\left(\bar{N}_C \bar{N}_V \bar{D}_{nB}\right)_{SiGe}}{\left(N_C N_V D_{nB}\right)_{Si}}\right)\left(\frac{\Delta E_{g,Ge(grade)}}{kT}\right) e^{\frac{\Delta E_{g,Ge(x=0)}}{kT}}}{1 - e^{\frac{\Delta E_{g,Ge(grade)}}{kT}}} \tag{2.19}$$

The reduced base transit time, τ_B, of SiGe as compared to Si is defined by Harame [21] in the Equation (2.20). This is a basic process design equation for linear graded SiGe transistors.

$$\frac{\tau_{B,SiGe}}{\tau_{B,Si}} = \frac{2kT}{\Delta E_{g,Ge(grade)}} \frac{\left(D_{nB}\right)_{Si}}{\left(\bar{D}_{nB}\right)_{SiGe}} \left(1 - \frac{kT}{\Delta E_{g,Ge(grade)}} e^{\frac{-\Delta E_{g,Ge(grade)}}{kT}}\right) \tag{2.20}$$

The reduction of SiGe emitter transit time as compared to Si is defined by Harame [21] in Equation (2.21) and also used in process design calculations.

$$\frac{\tau_{E,SiGe}}{\tau_{E,Si}} = \frac{1 - e^{\frac{-\Delta E_{g,Ge(grade)}}{kT}}}{\left(\frac{\left(\bar{N}_C \bar{N}_V \bar{D}_{nB}\right)_{SiGe}}{\left(N_C N_V D_{nB}\right)_{Si}}\right)\left(\frac{\Delta E_{g,Ge(grade)}}{kT}\right) e^{\frac{\Delta E_{g,Ge(x=0)}}{kT}}} \tag{2.21}$$

2.4 SiGe BiCMOS process and applications

Bipolar processing technology developed during the 1990's made the SiGe HBT viable [19]. The ability to grow in situ doped silicon films with precise control is by the processing method of LTE, Low Temperature Epitaxy, also called UHV/CVD, Ultra High Vacuum/Chemical Vapor Deposition [21, 25]. The Si and Ge lattice structures have a mismatch of 4.2%. Therefore the SiGe layer is grown under strain to fit the initial Si lattice by LTE method. Boron is included as the very thin SiGe alloy layer is grown. The LTE method thus produces a very thin, intrinsic basewidth of precise controlled ion concentration. The silicon-germanium heterojunction bipolar device is capable of high frequency response with a reasonable breakdown voltage for high speed and low-voltage applications. IBM qualified the IBM5AM process to customers in 1998 [19]. Most foundries today have a SiGe HBT as a key component in their high performance BiCMOS processes. Advancement of unique processing techniques has been continuing to present day.

SiGe HBT BiCMOS processes have been tailored to meet the high performance requirements of the mixed-signal, analog and RF blocks in next generation advanced communication and system integration applications [4], [26], [27]. The majority of commercial circuit designs are manufactured in CMOS only processes. Fabrication costs of CMOS are often less than a bipolar only or BiCMOS process [28]. Generally, CMOS performance is equivalent to bipolar at lower voltages and currents. However, a CMOS only solution cannot meet the specifications for many communications applications or system integration designs on the scale of a system on a chip, SOC. The main commercial application for HBT BiCMOS is in the areas of wireless communications and fiber optic, where bipolar device behavior is needed [4, 27]. The analog and RF sections of these advanced circuits require the HBT to be incorporated into a CMOS only process. Therefore, the baseline of the SiGe BiCMOS processes use standard RF/Digital CMOS-only processing flows of a specific lithographic dimension. Minimum additional processing steps are needed to build the HBT. The HBT modeled in this study was fabricated from a SiGe BiCMOS process using the fabrication techniques of a 0.5µm minimum feature size [7].

2.5 Bipolar modeling background

The complexity of integrated circuit design requires a computer aided design software approach. The mainstay program for circuit simulation is SPICE based [29]. The input is a circuit level description composed of device elements represented by models. The output of SPICE is in the form of voltages and currents as a function of time, frequency, and temperature. Two types of bipolar models are used to represent bipolar device electrical performance in circuit simulations. One type is the table model; the second type is the compact model.

The table model is composed of tables of data used directly or in conjunction with interpolation formulas. Creating a model is as simple as taking a measurement to obtain the data tables. However, simulations using table models require large amounts of memory and are therefore infrequently used in simulations. This type of model is typically used when a compact model approach is not possible.

Compact models have been the preferred approach for circuit simulation, for over 50 years. A compact model is composed of simplified physical equations representing equivalent circuits of lumped elements. The parameters in the equations have a physical identity if possible. The model equations are defined in relation to one-dimensional cross-sectional theory. The model must define the terminal characteristics of the transistor and accurately represent the electrical performance, voltage and current as a function of time and temperature.

All bipolar compact models developed have been a combination of physics and empirical expressions. The primary transistor behavior is physics based. The first order effect of electron transfer from emitter to collector in a NPN device is defined by the dependence of current to exponential voltages, VBE and VBC. The second order effects are usually described by empirical expressions. A chronological list of the significant compact bipolar models and contributing theories are listed in Table 2.3. The models share some common traits.

1954	Ebers-Moll Injection Model – theory published[17, 18]
1955	Moll-Ross Theory Base Charge Control – theory published [30]
1957	Ebers-Moll Transport Model - simulation implementation [10]
1970	Gummel-Poon Model – Integrated Charge Control Model [18]
1985	Kull Theory - Quasi-Saturation Theory [15]
1985	MEXTRAM [31]
1995	HICUM [32]
1995	VBIC95 [33]

Table 2.3 Bipolar model development throughout time.

All of the above compact bipolar models have utilized the common emitter transport form of the Ebers-Moll model illustrated in Figure 2.11. Ebers-Moll is based on current. Models after Ebers-Moll were based on the relationship of minority charge. A charge description was first discussed by Moll and Ross [30]. Gummel and Poon later developed a complete base charge representation that was used in the classic Gummel Poon model [18]. All advanced models developed since use some form of charge control relationship. In the remainder of the chapter we will review the operation of the Ebers-Moll model, the charge control relationship and the main features of the advanced models. The following chapter will focus on the details of the standard Mextram model.

2.5.1 Ebers-Moll models

Ebers and Moll presented a simple, nonlinear DC bipolar transistor model [17] in 1954. This model was adapted for computer simulation and was the most used bipolar model until the Gummel-Poon bipolar model. The model was based on physics and was intended to represent the ideal DC bipolar behavior of all four operating states indicated in Figure 1.5b. The Ebers-Moll model is based on current and current gain.

We will review the three forms of the Ebers-Moll model summarized by Getreu [10]. The injection model, a common-base configuration, provides an intuitive understanding of the model's operation. The transport model, also a common-base configuration, is mathematical equivalent to the injection version. The original Ebers-Moll theory described the reference currents as the currents "injected" in the base. The simulation friendly transport version described the reference currents as the currents flowing through, "transporting" across the base and being collected.

Finally the common-emitter transport version of the Ebers-Moll is defined. This form has been used in all bipolar models since. It is computationally friendly and is directly compatible to the hybrid-π small signal model.

2.5.1.1 Injection and transport models in common-base configuration

The Ebers-Moll injection model is a common-base configuration of back-to-back diodes and two current dependent current sources as shown in Figure 2.7. The back-to-back diodes represent the emitter-base diode and base-collector diode. The model's reference currents are the diodes. The two ideal diodes represent the exponential behavior between currents, I_F and I_R, and junction voltages, VBE and VBC. Their equations are defined in Table 2.4. The two current dependent sources represent the transistor action.

When the model is operating in the forward active state the base-collector is reverse biased so the diode current, I_R, is basically open circuited. The path of current is the forward diode, I_F, and the current across the dependent current generator, $\alpha_F I_F$. The forward diode current has a saturation current, I_{ES}. The common-base forward current gain is α_F. When the model is operating in the reverse state, the base emitter diode is basically open circuited and the path of current is the reverse diode, I_R, and the current across the dependent current generator, $\alpha_R I_R$. The reverse diode current has a saturation current, I_{CS}. The common-base reverse current gain is α_R.

Injection	**Transport**
Reference Currents: $I_F = I_{ES}\left(e^{\frac{V_{BE}}{V_T}} - 1\right)$ $I_R = I_{CS}\left(e^{\frac{V_{BC}}{V_T}} - 1\right)$	Reference Currents: $I_{CC} = \alpha_F I_F = I_S\left(e^{\frac{VBE}{V_T}} - 1\right)$ $I_{EC} = \alpha_R I_R = I_S\left(e^{\frac{VBC}{V_T}} - 1\right)$
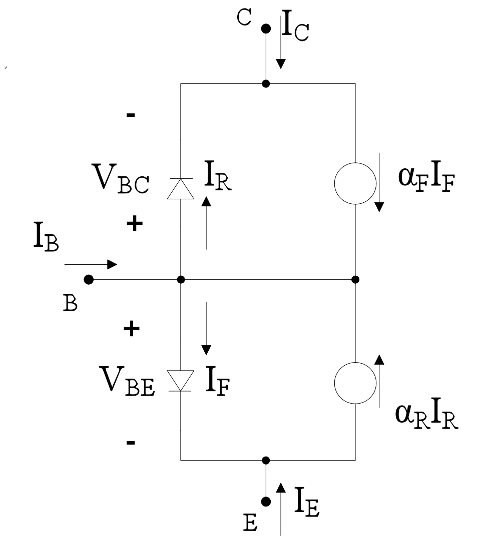 **Figure 2.7 Injection version of Ebers-Moll in common-base configuration**	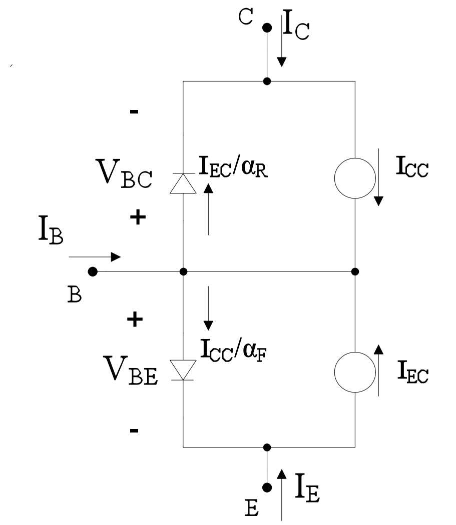 **Figure 2.8 Transport version of Ebers-Moll in common-base configuration**
Node Currents: $I_B = (1-\alpha_F)I_F + (1-\alpha_R)I_R$ $I_C = \alpha_F I_F - I_R$ $I_E = -I_F + \alpha_F I_R$	Node Currents: $I_B = \left(1-\frac{1}{\alpha_F}\right)I_{CC} + \left(1-\frac{1}{\alpha_R}\right)I_{EC}$ $I_C = I_{CC} - \frac{I_{EC}}{\alpha_R}$ $I_E = I_{EC} - \frac{I_{CC}}{\alpha_F}$

Table 2.4 Injection and transport versions of Ebers-Moll model in common-base configurations [10]

Ebers and Moll use the reciprocity relation, $\alpha_F I_{ES} = \alpha_R I_{CS} = I_S$ to reduce the diode saturation current to a single value I_S.

The injection version is very intuitive to understand. However, the transport version of Figure 2.8 is the preferred form for simulation. The transport version use dependent current sources to provide a simpler reference current than the injection model. The reference current sources require only one constant parameter I_S that is steady over decades of current. The injection version has an α factor that decreases at low currents thereby causing I_S to vary. The two versions are mathematically equal. In the transport version the reference currents are the dependent current sources, I_{CC} and I_{EC} shown in Table 2.4.

<table>
<tr>
<td>
Current gain configuration relationships:

$$\alpha_F = \frac{\beta_F}{1+\beta_F} \qquad \beta_F = \frac{\alpha_F}{1-\alpha_F}$$

$$\alpha_R = \frac{\beta_R}{1+\beta_R} \qquad \beta_R = \frac{\alpha_R}{1-\alpha_R}$$
</td>
<td>
Reference Currents:

$$I_{CC} = I_S\left(e^{\frac{VBE}{V_T}} - 1\right)$$

$$I_{EC} = I_S\left(e^{\frac{VBC}{V_T}} - 1\right)$$
</td>
</tr>
<tr>
<td>
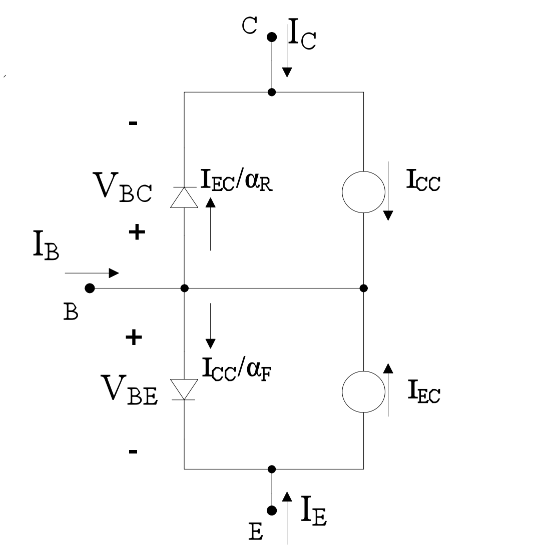

Figure 2.9 Common-base configuration of Ebers-Moll transport version.
</td>
<td>
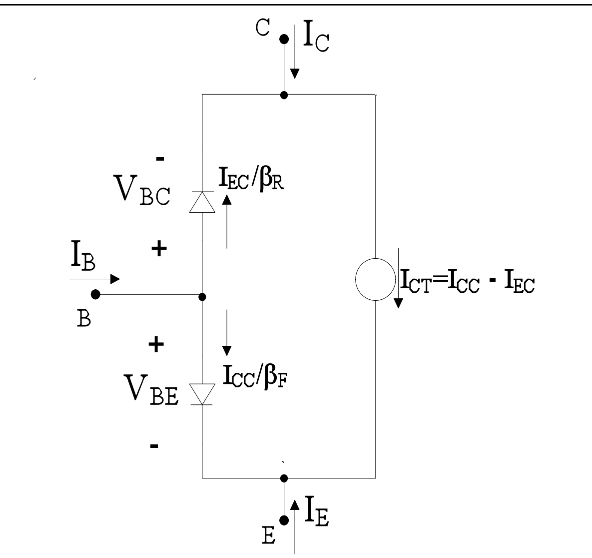

Figure 2.10 Common-emitter configuration of Ebers-Moll transport version.
</td>
</tr>
</table>

Table 2.5 Conversion from common-base to common-emitter configurations of the transport version of the Ebers-Moll model [10].

2.5.1.2 Transport version model of common-emitter configuration

The common-emitter configuration of the Ebers-Moll transport model is the form most useful and upon which all further bipolar model developments are based. Conversion from common-base of Figure 2.9 to common-emitter of Figure 2.10 is achieved by applying the relationship between α and β defined in the following equations of Table 2.5 and summing the nodes of the common base configuration in terms of β. The resulting node configuration is common-emitter as shown in Figure 2.10.

The common-emitter current gain, β, is the standard characteristic defining bipolar current behavior. The total collector current, I_{CT}, defines the current from collector to emitter. The common-emitter configuration of the Ebers-Moll transport model as shown in Figure 2.11 can be directly related to the hybrid-π model of Figure 2.12.

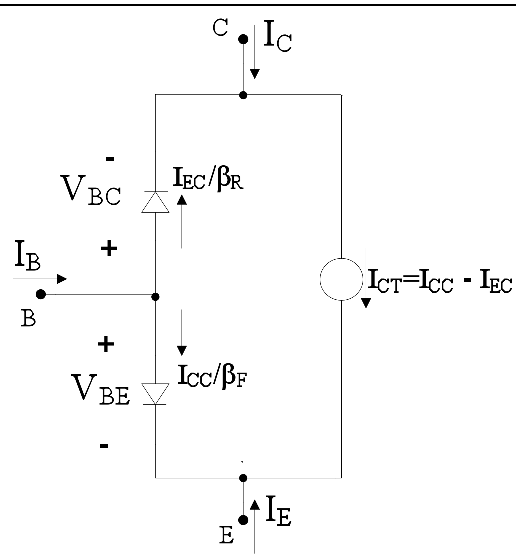

Figure 2.11 Transport version of Ebers-Moll in common-emitter configuration

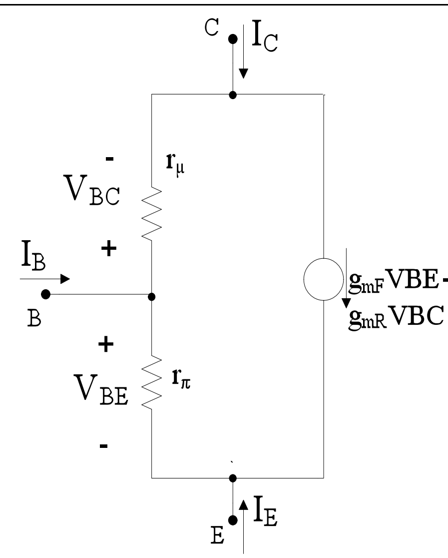

Figure 2.12 Ebers-Moll linearized hybrid π model

Table 2.6 Transport version of Ebers-Moll Model in common-emitter configuration [10]

2.5.2 Moll-Ross relation and Integrated Charge Control Relation, ICCR

In 1955, Moll and Ross presented the theory that basic characteristics could be related to diffusion of minority charge transport across the base. This theory led to ICCR, Integrated Charge Control Relationship, developed by Gummel and Poon.

The bipolar transistor characteristics could be modeled by accounting for the minority carrier charge transport in the base region. The following equation is a generalized version of Moll-Ross [30] and is also the Gummel-Poon charge control equation [21] for low-level injection conditions. The flow of electrons passing from the emitter to collector is then described by this charge control equation defines the current, I_N, as the current from collector to emitter:

$$I_N = \frac{qA_E n_{i0}^2\left(e^{\frac{qV_{BE}}{kT}}-1\right)}{\int_0^{W_B}\frac{N_{AB}(x)n_{i0}^2}{D_{nB}(x)\,n_{iB}^2(x)}dx} = \frac{qA_E n_{i0}^2\left(e^{\frac{qV_{BE}}{kT}}-1\right)}{G_B} \tag{2.22}$$

x	Position in the base, the emitter side is 0 and W_B is the collector side (nm)
W_B	Intrinsic base width (nm)
$N_{AB}(x)$	Doping concentration as a function of distance, x, within the base (cm^{-3})
q	Elemental charge (C)
A_E	Area of active emitter (um^2)
$D_{nB}(x)$	Diffusion coefficient as function of distance, x, within the base (cm^2/s)
$n_{iB}(x)$	Intrinsic carrier concentration as a function of distance, x, within the base (cm^{-3})
n_{i0}	Intrinsic carrier concentration of the undoped Si base (cm^{-3})

The Gummel number, G_B, is defined as:

$$G_B = \int_0^{W_B}\frac{N_{AB}(x)}{D_{nB}(x)}\frac{n_{i0}^2}{n_{iB}^2(x)}dx \tag{2.23}$$

The generalized form of ICCR takes into consideration that the components of the Gummel number may vary as a function of position, x, within the neutral base. The ICCR equation for Si transistors can be simplified by the assumptions $n_{iB}(x)$ and $D_{nB}(x)$ are constant resulting in n_{iB} and D_{nB} throughout the base.

$$G_B = \frac{1}{D_{nB}} \int_0^{W_B} N_{AB}(x)dx \tag{2.24}$$

The Gummel number is now proportional to the total base charge, Q_B. Si transistor model applications of ICCR theory therefore replace G_B with the total base charge, Q_B:

$$I_N = \frac{qD_{nB}n_{i0}^2 A_E}{\int_0^{W_B} N_{AB}(x)dx}\left(e^{\frac{V_{BE}}{V_T}} - e^{\frac{V_{BC}}{V_T}}\right) = \frac{qD_{nB}n_{i0}^2 A_E}{Q_B}\left(e^{\frac{V_{BE}}{V_T}} - e^{\frac{V_{BC}}{V_T}}\right) \tag{2.25}$$

Base charge is defined as:

$$Q_B = qA\int_0^{W_B} N_{AB}(x)dx \tag{2.26}$$

2.6 Advanced bipolar models

The models developed after Gummel-Poon versions were intended to represent advanced bipolar processes. There were three separate advanced bipolar model approaches resulting in three different models: VBIC, HiCUM and Mextram. VBIC was developed by an industry driven team from AT&T and TI [33]. HiCUM was developed by Michael Schroder [32]. Mextram was developed by Phillips Semiconductor [31].

Two of these advanced bipolar models, the Mextram model and HICUM model, have been adopted as industry standardized models. Since their initial introductions, developers of both models have continually updated the models to more accurately represent the advanced Si bipolar structures. Numerical smoothness and the results of first and higher order derivatives are critical to acceptance of a bipolar model. Convergence and distortion are essential features. Both models have produced excellent representations of advanced Si bipolar processes. The choice of Mextram for development of an expansive temperature model and model parameters was based on the availability of existing documented extraction techniques, the mathematical soundness of the model equations and its support of SiGe current charge equations.

2.7 Mextram major features

The Mextram 504 level model released in the late 1990's was tailored for advanced bipolar processes. Process features accounted for by Mextram are double polysilicon, SiGe devices, high voltage capability and RF structures. Mextram has significant support in accurately modeling the low doped N^- collector region. The collector epilayer is the area controlling quasi-saturation and high-level injection effects.

The Mextram is based on an implementation of ICCR with an inclusion of charge in the emitter and collector regions. The standard self-heating model is included in Mextram. The parasitic PNP effects are included in an extrinsic section. Quasi-saturation has a physical modeling approach that is based on the Kull quasi-saturation theory. However, Mextram has included additional effects in the quasi-saturation equations: base widening, Kirk effect and hot-carrier effects in the collector epilayer. Chapter 3 is a detailed review of Mextram 504.

3 Mextram 504.7 model

An advanced vertical NPN bipolar compact model is required for reduced geometry, advanced bipolar/BiCMOS processes. The higher frequency response, lower breakdown voltages and quasi-saturation effects of these advanced bipolar structures could no longer be accurately modeled by the classic Gummel-Poon bipolar model [18]. Therefore, Mextram was developed by the semiconductor industry and eventually released into the public domain.

The core of Mextram is based on the Gummel-Poon base charge model. The uniqueness of Mextram [34] resides in the physical effects incorporated into the model:

- Contributions of a graded SiGe base profile to current are included in the quasi-neutral base calculation
- Early effects are bias dependent
- Extensive temperature scaling
- Self-heating model
- Accurate modeling of the lightly doped N^- collector epilayer
- Low-level nonideal base currents
- High-level injection effects
- Weak avalanche
- Charge storage effects
- Depletion capacitances are split between intrinsic and extrinsic regions
- Base resistance include current crowding and conductivity modulation effects
- Distributed high-frequency effects
- Parasitic PNP and substrate effects
- Mathematical smoothing and numerical limiting

The Mextram model was created by Koninklijke Philips Electronics N.V [13]. Mextram is an acronym for "most exquisite transistor model". Philips placed the Mextram level 503 in the public domain [35] in 1994. Several enhancements followed throughout the years culminating in the Mextram level 504 release. After this significant work by Phillips, Delft University became responsible in 2007 for the organization, development and release of Mextram [2]. The Philips semiconductor group that created Mextram has become NXP Semiconductors. Subsequent Mextram releases have been reviewed and approved by the semiconductor industry Compact Modeling Council, CMC [36]. Model equations are released in Verilog-A language format by Delft University under their version control [2].

The Mextram model is intended to be physically based, both in its equations and model parameters. The standard parameter extraction method for a model parameter set [35] relies on direct extraction and the physical description of the structure, with minimum or no parameter optimization. The intent of Mextram level 504 was for the parameters to have a physical meaning. The expectation was that parameters could be extracted directly from measured data and process information. Parameters and physical relationships have been added to later releases to minimize the interdependence of different effects and parameters.

The work of this dissertation utilized the Mextram 504.7 release in Verilog-A code [2]. All cryogenic and single expansive temperature model development in this work is an add-on to Mextram 504.7 code. The objective was to utilize this industry standard model implementation over the full temperature range of the project with minimum math modifications.

3.1 Components of Mextram

The Mextram compact model is based on the physics of the bipolar transistor. Mextram relies on the Ebers-Moll [17] and Gummel-Poon [18] bipolar models. Mextram utilizes the Ebers-Moll transport theory of Figure 2.10 to describe current flow from emitter to collector. Gummel-Poon is based on the integrated charge control relation, ICCR, of Equation (2.22) to sum the total minority base charge transport [18]. Mextram takes a similar base charge transport approach, but also includes the impact of the Early effects on the junction depletion voltages.

Mextram has an extensive equivalent circuit of resistances and capacitances to physically represent the advanced bipolar devices. The equivalent circuit is defined by the different regions and doping concentrations of each region. This physics based relationship can be seen by overlaying an advanced bipolar device cross-section on to the full Mextram equivalent circuit [13],[34] as shown in Figure 3.1. The cross-section gives way to intrinsic and extrinsic regions of the transistor represented in the model. The Mextram model is composed of branch currents, charges and resistances. Each branch represents a physical area of the vertical bipolar structure. The inclusion of more components is intended to permit the parameters to have physical meaning.

The model consists of external and internal nodes. The external nodes represent the contact point on the device surface: base node, B, the collector node, C, and the emitter node, E. The substrate external node is the substrate node, S, which represents the substrate directly beneath the device. The region directly beneath the active device is the last common point of the substrate that can be associated with a layout. There are seven internal nodes: B1, B2, E1, C2, C1, C4 and C3. These nodes provide the internal voltage biases needed for each current and charge. The elements of the equivalent model circuit consist of constant value components as well as non-linear components.

The Mextram model can be divided into three sections: intrinsic, extrinsic, and extended. The Mextram equations of each section will be reviewed in detail in the following sections.

Current	Branch Description	Nodes:
I_N	Transfer current, from emitter to collector	C2-E1
I_{C1C2}	Collector epi-layer resistance	C2-C1
I_{B1B2}	Variable base resistance	B1-B2
I_{B1}	Ideal base-emitter diode	B2-E1
I^S_{B1}	Sidewall ideal base-emitter diode	B2-E1
I_{B2}	Non-ideal base-emitter diode	B2-E1
I_{B3}	Non-ideal base-collector	B1-C4
I_{avl}	Avalanche	C2-B2
I_{ex}	Extrinsic base-collector	B1-C4
XI_{ex}	Split of extrinsic base-collector	B-C3
I_{sub}	Substrate	B1-S
XI_{sub}	Factor split of substrate	B-S
I_{Sf}	Substrate failure	C1-S

Resistor	Branch Description	Nodes:
RE	Emitter resistance	E-E1
RBC	Base contact resistance	B-B1
RCC	Collector contact resistance	C-C3
RCBLX	Extrinsic buried collector resistance	B2-E1
RCBLI	Intrinsic buried collector resistance	B2-E1

Charge	Branch Description	Nodes:
Q_{BEO}	Base-emitter surface overlap	B-E
Q_{BCO}	Base-collector surface overlap	B-C
Q_E	Emitter	B2-E1
Q_{tE}	Base-emitter depletion	B2-E1
Q^S_{tE}	Sidewall base-emitter depletion	B1-E1
Q_{BE}	Base-emitter diffusion	B2-E1
Q_{BC}	Base-collector diffusion	B2-C2
Q_{tC}	Base-collector depletion	B2-C2
Q_{epi}	Collector epilayer diffusion	B2-C2
Q_{B1B2}	AC current crowding charge	B1-B2
Q_{tex}	Extrinsic base-collector depletion	B1-C4
XQ_{tex}	Extrinsic base-collector depletion	B-C3
Q_{ex}	Extrinsic base-collector depletion	B1-C4
XQ_{ex}	Extrinsic base-collector depletion	B-C3
Q_{tS}	Collector-substrate depletion	C2-S

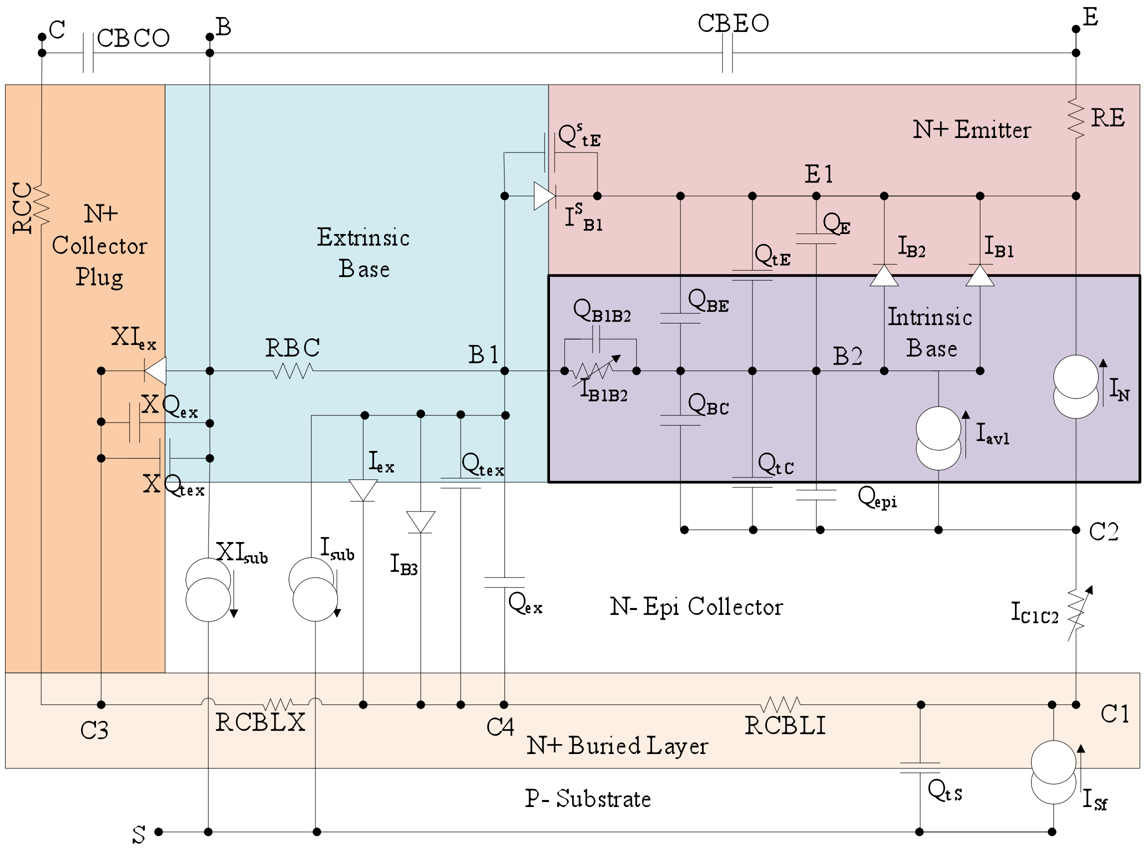

Figure 3.1 Equivalent circuit of full Mextram 504.7 [34]

The intrinsic transistor is composed of the elements generating the transfer current, I_N, within the internal nodes: E1, B1, and C2. The parasitic resistors reside between these internal nodes and the external nodes. The intrinsic transistor and resistor elements are identified in Figure 3.3 and described in Section 3.2.

The extrinsic components represent the parasitic PNP and substrate effects. The extrinsic components are indicated in Figure 3.4 and described in Section 3.3. Extrinsic components are connected between the intrinsic base at nodes B1 and the extrinsic buried collector resistor at node C4. The extrinsic section also includes a base-emitter sidewall contribution between internal nodes, B1 and E1. The substrate effects are included in the extrinsic section by elements between nodes, B1 and S and nodes, C1 and S.

The Mextram model has extended modeling capability that can be activated through the use of flag model parameters. An extension to the model equations can be activated to include: the distributed high frequency effects in the intrinsic base region, avalanche currents modified for high current conditions and activation of additional components in the extrinsic section. The additional elements are placed between the external base contact node, B and the edge of the buried collector node, C3, seen in Figure 3.1. The extended components available are described in Section 3.4.

3.1.1 Mextram 504.7 model parameters

The model parameters are grouped by functionality and model sections. Some model parameters are adjusted by temperature and some are independent of temperature. The following is a summary of all model parameters in the Mextram 504.7 model [34].

Flag parameters turn on extra sections of the model.

Parameter	Value	Model Features:
EXMOD	1	Activates extending modeling – all branches with an ending of ex: XI_{ex} - External Base-Collector diode current split factor, XI_{sub} - Base-Substrate diode current XQ_{ex} - External Base-Collector diffusion charge split factor
	0	Deactivates extending modeling branches
EXPHI	1	Activates AC current-crowding of pinched base underneath the emitter.
	0	Deactivates AC current crowding
EXAVL	1	Activates an empirical equation for avalanche current if I_{AVL} > IHC
	0	No modification of base avalanche current equations

Table 3.1 Flag model parameters

Splitting parameters are used to distribute a fraction of the junction capacitances and currents to their sidewalls or external areas. These parameters should be used based on process knowledge and measured data. The branch splitting parameters are defined below:

Parameter	Value	Model Features:
XEXT	Range of 0 to 1	Extrinsic Base-Collector depletion charges split factor, XQ_{tex} Q_{tex}
XIBI	Range of 0 to 1	Sidewall fraction of Base-Emitter diode current, I^S_{B1}, split by a factor, XIBI
XCJE	Range of 0 to 1	Sidewall fraction of depletion capacitance in the base-emitter junction that is split by XCJE
XCJC	Range of 0 to 1	Fraction of base-collector depletion capacitance directly beneath the active emitter that is split by XCJC

Table 3.2 Branch splitting model parameters

The intrinsic and extrinsic sections of the model often interact with the same parameters. However, each parameter has a primary operating section and is indicated below. Certain parameters are influenced by temperature shifts. The temperature dependency of each parameter is identified.

Parameter	Description	Section	Temperature	Unit
IS	Saturation current	Intrinsic	Dependent	A
IK	High-level injection knee current	Intrinsic	Dependent	A
ISS	Saturation current of parasitic PNP transistor	Extrinsic	Dependent	A
IKS	High-level injection knee current of parasitic PNP transistor	Extrinsic	Dependent	A
VEF	Forward Early voltage at zero bias	Intrinsic	Dependent	V
VER	Reverse Early voltage at zero bias	Intrinsic	Dependent	V
BF	Current gain of ideal forward base current, I_{B1} branch	Intrinsic	Dependent	
BRI	Current gain of ideal reverse base current, I_{ex} branch	Extrinsic	Dependent	
IBF	Saturation current of nonideal forward base current, I_{B2} branch	Intrinsic	Dependent	A
MLF	Non-ideality factor of nonideal forward base current, I_{B2} branch	Intrinsic	Independent	
IBR	Saturation current of nonideal reverse base current, I_{B3} branch	Extrinsic	Dependent	A
VLR	Crossover voltage of nonideal reverse base current, I_{B3} branch	Extrinsic	Independent	V
WAVL	Effective width of the collector epilayer for avalanche current, I_{avl} branch	Intrinsic	Independent	m
VAVL	Voltage describing the curvature of the avalanche current, I_{avl} branch	Intrinsic	Independent	V
SFH	Spreading factor of the avalanche current	Intrinsic	Independent	

Table 3.3 Intrinsic and extrinsic model parameters

When the following SiGe model parameters are other than zero a different formulation of Early effect contribution to the normalized base charge, q_B, is implemented. The use of DEG invokes a calculation of base charge that includes the effects of a graded SiGe base profile as described in Section 3.2.2.2.

Parameter	Description	Section	Temperature	Unit
DEG	SiGe graded base bandgap difference	Intrinsic	Dependent	V
XREC	Factor of base recombination by SiGe base	Intrinsic	Independent	

Table 3.4 SiGe model parameters

The parasitic resistances can be divided into two groups. The group below consists of constant and variable resistances associated with all parasitic resistances except the collector epilayer.

Parameter	Description	Section	Temperature	Unit
RE	Constant resistance of emitter	Resistance	Dependent	Ω
RBC	Constant resistance of external base	Resistance	Dependent	Ω
RBV	Low current resistance of intrinsic base, I_{B1B2} branch	Resistance	Dependent	Ω
RCC	Constant resistance of external collector	Resistance	Dependent	Ω
RCBLI	Constant resistance of intrinsic N^+ buried layer of collector beneath active transistor	Resistance	Dependent	Ω
RCBLX	Constant resistance of extrinsic N^+ buried layer of collector beneath extrinsic regions	Resistance	Dependent	Ω

Table 3.5 Parasitic resistance model parameters

The second group of parameters associated with resistance describes the N^- epilayer collector resistance and bias behavior.

Parameter	Description	Section	Temperature	Unit
RCV	Low current resistance of epilayer, I_{C1C2} branch	Intrinsic	Dependent	Ω
SCRCV	Space charge resistance of epilayer, I_{C1C2} branch	Intrinsic	Independent	Ω
IHC	Critical current due hot carriers in the epilayer, I_{C1C2} branch	Intrinsic	Independent	A
AXI	Smoothing parameter in the epilayer model, I_{C1C2} branch	Intrinsic	Independent	

Table 3.6 N^- epilayer collector resistance and bias model parameters

The transit time of charge in each region is defined by unique equations. Parameters used exclusively in the charge equations are grouped below.

Parameter	Description	Section	Temperature	Unit
TAUE	Minimum transit time of emitter charge	Intrinsic	Dependent	sec
MTAU	Non-ideality factor of emitter charge	Intrinsic	Independent	sec
TAUB	Transit time of the base	Intrinsic	Dependent	sec
TEPI	Transit time of the epilayer collector	Intrinsic	Dependent	sec
TAUR	Reverse transit time	Intrinsic	Dependent	sec

Table 3.7 Charge model parameters

The model parameters for junction depletion voltage and capacitance equations are grouped below.

Parameter	Description	Section	Temperature	Unit
CJE	Depletion capacitance of the base-emitter junction at zero bias	Intrinsic	Dependent	C
AJE	Diffusion voltage constant capacitance factor for forward bias of base-emitter junction	Intrinsic	Independent	
PE	Grading coefficient of base-emitter depletion capacitance	Intrinsic	Independent	
VDE	Built-in diffusion voltage of the base-emitter junction	Intrinsic	Dependent	V
CJC	Depletion capacitance of base-collector junction at zero bias	Intrinsic	Dependent	C
AJC	Diffusion voltage constant capacitance factor for forward bias of base-collector junction	Intrinsic	Independent	
PC	Grading coefficient of base-collector depletion capacitance	Intrinsic	Independent	
VDC	Built-in diffusion voltage of the base-collector junction	Intrinsic	Dependent	V
XP	Fraction of the base-collector depletion capacitance that is constant. Ratio of depletion layer thickness at zero bias to epilayer thickness	Intrinsic	Dependent	
MC	Collector current modulation factor for base-collector depletion capacitance	Intrinsic	Dependent	
CJS	Depletion capacitance of collector-substrate junction at zero bias	Intrinsic	Dependent	C
PS	Grading coefficient of collector-substrate depletion capacitance	Intrinsic	Independent	
VDS	Built-in diffusion voltage of the collector-substrate junction	Intrinsic	Dependent	V

Table 3.8 Depletion junction model parameters

Temperature definition model parameters are entered in degrees Celsius. Conversion to degrees Kelvin is done within the model. All model equation operations are performed with Kelvin units. The model can be shifted by temperature for multiple reasons. The ambient or simulation temperature differs from the model reference temperature or the device experiences self-heating. The self-heating model circuit within Mextram 504.7 is discussed in Section 3.5.

The following model parameters support the temperature associated with the set of model parameters and the self-heating equations.

Parameter	Description	Unit
TREF	Model reference temperature	C
DTA	Location specific temperature charge from TREF	C
RTH	Thermal resistance of self-heating effects	Ω
CTH	Thermal capacitance of self-heating effects	F

Table 3.9 Temperature reference model parameters

The following group of model parameters is temperature coefficients in relation to mobility of each region of the transistor that are used in the temperature equations of Section 3.5. The following table indicates what model parameters are influenced by each temperature coefficient model parameter.

Parameter	Description from Process	Parameter Influenced
AQBO	Zero bias base charge temperature coefficient	RBV BF IS VER VEF TAUB DEG
DAIS	IS equation temperature coefficient	IS
AE	Emitter doping temperature coefficient	RE BF
AB	Base doping temperature coefficient	RBV BF IS IK TAUE TAUB
AEX	Extrinsic base doping temperature coefficient	RBC
AEPI	Epilayer collector doping temperature coefficient	RCV TEPI
AC	Extrinsic contact collector doping temperature coefficient	RCC
ACBL	Buried layer collector doping temperature coefficient	RCBLX RCBLI
AS	Substrate doping temperature coefficient	ISS IKS
ATH	Self heating temperature coefficient	RTH

Table 3.10 Temperature coefficient model parameters

The second group of temperature model parameters is the various bandgap voltages used in the model parameter temperature equations of Section 3.6. For each bandgap voltage model parameter all model parameters influenced are indicated.

Parameter	Description from Process	Parameter Influenced
DVGBF	Bandgap delta of forward current gain	BF
DVGBR	Bandgap delta of reverse current gain	BR
VGB	Base bandgap voltage	VDE IS
VGC	Collector bandgap voltage	VDC IBR
VGJ	Base-emitter recombination bandgap voltage	IBF
DVGTE	Emitter charge difference bandgap voltage	TAUE
VGS	Substrate bandgap voltage	VDS ISS

Table 3.11 Bandgap voltage temperature model parameters

The noise model for Mextram supports flicker noise with three model parameters and one parameter for white noise in the avalanche model equations. Noise analysis was not included in this work. The reader is referred to the Mextram physics manual for further information on the noise equations of the model.

Parameter	Description	Section	Temperature
KF	Flicker noise coefficient for the ideal base current	Extended	Independent
KFN	Flicker noise coefficient for the nonideal base current	Extended	Independent
AF	Flicker noise exponent	Extended	Independent
KAVL	Flag switch to activate white noise due to avalanche	Extended	Independent

Table 3.12 Noise model parameters

3.1.2 Nomenclature

A specific notation style will be used in the following chapters. Model parameters are capitalized, as an example, IS, the parameter for saturation current. Model parameters adjusted by a temperature equation are in bold font ending with an underscore T, such as **IS_T**. Internal calculated components are of normal font and utilize subscripts to distinguish uniqueness, for example: I_N, is the internally calculated transfer current. The nodal differential voltages determined by the circuit simulator are capitalized italic font, for example ***VB1E1***, the simulated voltage between nodes B1 and E1.

All work in the following Mextram equations and definitions are exclusively in terms of a vertical NPN transistor. However, Mextram can be defined as a vertical PNP as well, with the appropriate bias and sign conversions.

The model equations associated with the intrinsic base to epilayer collector interface are complex. The model uses the following distinctions between the base-collector depletion voltage, V_{tc}, the simulated base-epilayer collector voltage, ***VB2C2***, and equation calculation of the base epilayer collector voltage, V^*_{B2C2}. The following definitions are used:

V_{tc} - Depletion voltage of the base-collector epilayer between B2-C1 calculated by Equation (3.37)

VB2C2 – Simulator calculated voltages between nodes B2-C2.

V^*_{B2C2} - Voltage calculated between B2-C2 from Equation (3.51)

3.1.3 Temperature definitions

The effects of temperature are included in all simulations. The temperature of the device during a simulation is defined at each bias step. Defined in Equation (3.1), the device temperature, Tk, is composed of the simulation temperature, TEMP, the effects of device self-heating, and specific location temperature shifts.

$$Tk = TEMP + \Delta T + DTA + 273.15 \tag{3.1}$$

Device Temperature at each bias pt.	=	Simulation Temperature	+	Self Heating Temperature Shift	+	Location Specific Temp. Shift	+	Conversion to units, Kelvin

The model parameters identified in Section 3.1.3 are developed for a given reference temperature. The reference temperature model parameter, TREF, is defined in degrees Celsius and converted to Kelvin.

$$Tmodel = TREF + 273.13 \tag{3.2}$$

Model Temperature	=	Model Temperature Parameter	+	Conversion to units, Kelvin

The model parameters that are temperature dependent are adjusted by their corresponding temperature equation. The temperature equations are calculated by using a temperature ratio, t_N, which represents the device temperature shift from the model reference temperature. The temperature ratio between the device temperature, Tk, and the model reference temperature, Tmodel, is defined by t_N as:

$$t_N = \left(\frac{Tk}{Tmodel}\right) \tag{3.3}$$

Each model parameter with temperature dependence was identified in the parameter tables of Section 3.1.1. The individual model parameter temperature equations are described in the parameter shifted by temperature, Section 3.6.

Current and charge equations are derived from electron and hole densities relationships with the help of the thermal voltage, V_T. The Mextram formulations therefore include the thermal voltage calculations below using the device temperature, Tk, at each bias point [13].

$$V_T = \frac{k \cdot Tk}{q} \qquad \frac{1}{V_{\Delta T}} = \frac{q}{k}\left(\frac{1}{Tk} - \frac{1}{Tmodel}\right) \tag{3.4}$$

q	Unit charge, Coulombs
k	Boltzmann constant

The difference in thermal voltage between the temperature of the device and that of the model temperature is defined as $\frac{1}{V_{\Delta T}}$. The difference in thermal voltages is used in the model temperature equations of Section 3.5.

3.1.4 Depletion voltage and charge

Depletion voltages and charges of the base-emitter interface and base-collector interface have significant influence in the Mextram formulations. The depletion voltage is used in a way that is unique to Mextram. The bias influences of the depletion voltages are included in the Early effects.

Therefore, the PN junction relationship of depletion capacitance, depletion voltage and charge will be reviewed in terms of the physical characteristics and the model form. The depletion voltage techniques described in the compact model implementation are utilized for each of the three junctions. The compact model implementation to the base-emitter junction and intrinsic base-collector junction is detailed in depletion charge Section 3.2.3. The model implementation of the collector-substrate junction is part of the extrinsic transistor portion of the Chapter 3. The collector-substrate depletion charge is described in Section 3.3.4.

3.1.4.1 Physical form of PN junction depletion capacitance

Classical representation of PN junction depletion capacitance [13] as a function of voltage is defined in Equation (3.5). Using the relationship of capacitance to voltage, $C = Q/V$, the corresponding charge is defined as a function of applied voltage in Equation (3.6).

$$C(V) = C_0\left(1 - \frac{V}{V_D}\right)^{-p} \tag{3.5}$$

C_0	Depletion capacitance at zero bias
V_D	Diffusion voltage
p	Grading coefficient
V	Applied (branch) voltage

$$Q(V) = \int_0^V C(V)dV = \frac{C_0 V_D}{(1-p)}\left(1 - \left(1 - \frac{V}{V_D}\right)^{(1-p)}\right) \tag{3.6}$$

However, the physical form does not represent the modeled C-V behavior well under strong forward bias conditions. When $V = V_D$ a singularity occurs and for $V > V_D$ the physical form of capacitance experiences continuity and inaccuracy problems as can be seen in Figure 3.2.

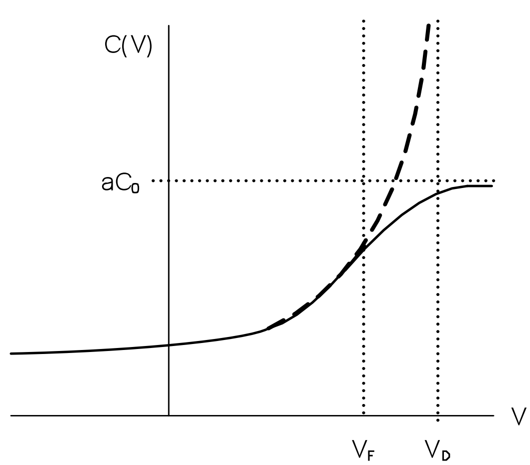

Figure 3.2 Junction depletion capacitance versus voltage. The ideal, physical C-V Equation (3.5) is the dashed line. The Mextram model implementation of Equation (3.7) is the solid line [13].

3.1.4.2 Compact model form of junction depletion capacitance, diffusion voltage and depletion charge

The model implementation of depletion capacitance and charge removes the singularity that occurs in the physical form of Equation (3.5) and provides for smoothness, i.e. continuous first and higher order derivatives. The compact model form of depletion capacitance responds as an ideal PN junction until the node voltage is approximately equal to the diffusion voltage, V_D. Then the model holds the capacitance to a constant value for $V \geq V_D$. The Mextram model implementation illustrates this behavior in Figure 3.2. All advanced bipolar models use the following derivation of Equation (3.7) for the depletion C(V) effect [13]. The variables: V_j and V_F are utilized in Equation (3.7) and defined by Equations (3.8) and (3.9).

$$C(V) = \frac{C_0}{\left(1 - \frac{V_j}{V_D}\right)^p}\left(\frac{dV_j}{dV}\right) + \frac{C_0}{\left(1 - \frac{V_F}{V_D}\right)^p}\left(1 - \frac{dV_j}{dV}\right) \tag{3.7}$$

V	Branch voltage
V_j	Junction voltage which is an(adjusted) branch voltage
C_0	Depletion capacitance at zero bias
V_D	Diffusion voltage
p	Grading coefficient
V_F	Switching voltage to engage constant C

The implementation of V_j and V_F has differed through the years between the three advanced bipolar compact models. The Mextram 504.7 uses the HICUM model formulation [37],[13] for V_j. The term V_{ch} has been found to have strong influence on the value of C(V=0) at higher temperatures [13]. Mextram uses the definition, $V_{ch} = 0.1 \cdot V_D$, for the base-emitter interface. The Mextram equation for V_j is:

$$V_j = V - V_{ch} \cdot \ln\left[1 + \exp\left[\frac{(V - V_F)}{V_{ch}}\right]\right] \tag{3.8}$$

V_{ch}	Numerical voltage to avoid singularity capability
a	Constant capacitance factor

Switching voltage, V_F, relates to V_D and capacitance constant factor, a, in the following:

$$V_F = V_D\left(1 - a^{\frac{-1}{p}}\right) \tag{3.9}$$

Control of the depletion capacitance is achieved by redefining the forward simulated branch voltage, V, to an adjusted junction voltage, V_j. A switch voltage, V_F, controls the influence of diffusion voltage, V_D [13].

Junction depletion capacitances measurements are the physical method of characterizing bipolar transistor junction interfaces. However, the model is implemented in terms of charge. Therefore, in Mextram the depletion capacitance behavior must be translated to charge and depletion voltage. The corresponding Mextram model form of Equation (3.10) is the depletion charge [13].

$$\begin{aligned} Q_t(V) &= \int_0^V C(V)dV \\ &= \frac{C_0 V_D}{1-p}\left(\left(1 - \frac{V_{j0}}{V_D}\right)^{1-p} - \left(1 - \frac{V_j}{V_D}\right)^{1-p}\right) + \frac{C_0}{\left(1 - \frac{V_F}{V_D}\right)^p}\left(V - V_j + V_{j0}\right) \end{aligned} \tag{3.10}$$

V_{j0}	Adjusted junction voltage at V=0, V_j(V=0)

The Mextram form of depletion charge, Q_t, is implemented for each junction interface branch charge. Each junction depletion charge has a zero-biased capacitance, C_0, and a branch specific depletion voltage, V_t, of the form:

$$Q_t = C_0 V_t \tag{3.11}$$

The depletion voltage, V_t, of Equation (3.12) responds to the simulated node voltage, V, model parameters and the adjusted junction voltage, V_j. The model parameters: V_D, p and a are unique to each junction interface.

$$V_t = \left(\frac{V_D}{1-p}\right)\left(1-\left(1-\frac{V_j}{V_D}\right)^{1-p}\right) + a\left(V - V_j\right) \tag{3.12}$$

3.2 Intrinsic transistor and resistances

The intrinsic transistor of the full Mextram model [34] is formed within the internal nodes: E1, B1 and C1 as shown in Figure 3.3. Mextram, like all other bipolar compact models utilized the Ebers-Moll transport model of Figure 2.5 to define current flow and bias dependence. The intrinsic structure is similar to the Gummel-Poon model. Mextram uses a quasi-neutral base, QNB, to calculate the emitter to collector transfer current, I_N. The quasi-neutral base defines the intrinsic base region under zero-bias conditions.

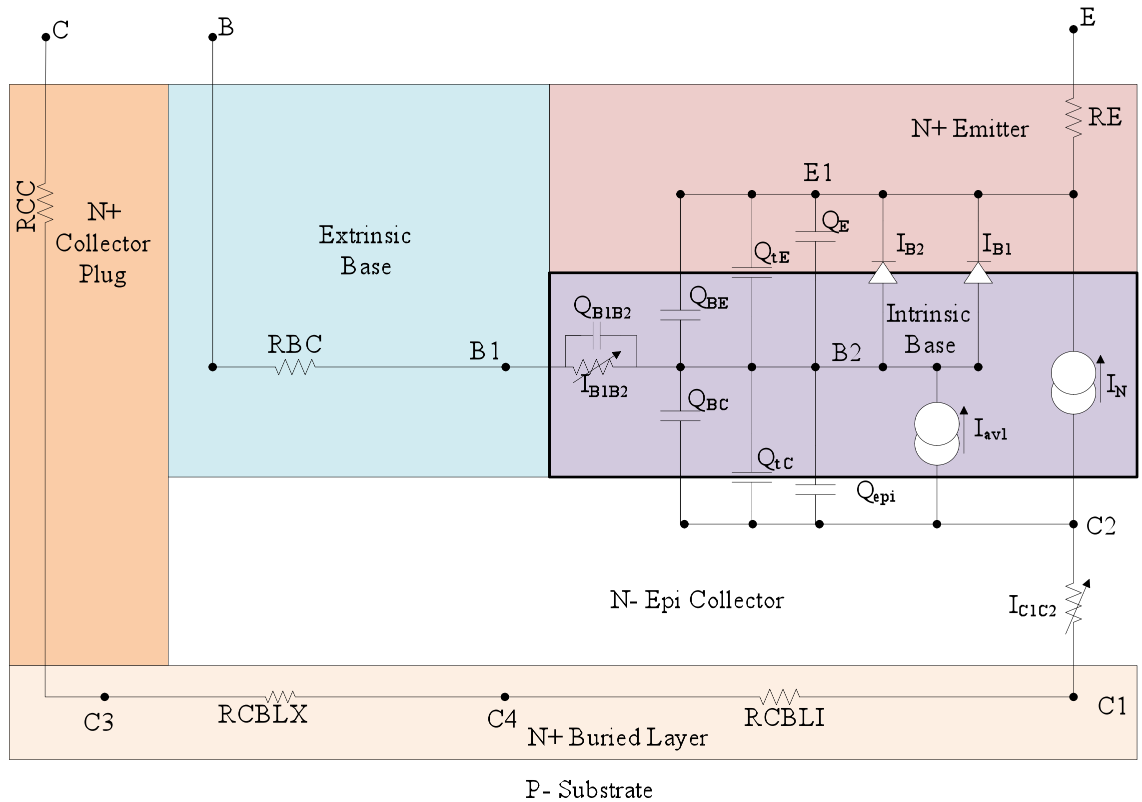

Figure 3.3 Intrinsic section of Mextram 504.7 equivalent circuit schematic [34]

The parasitic resistances are in series with the intrinsic transistor. These resistances represent the different regions: The resistance of the emitter region is represented by RE. The base resistance is composed of two contributors, a constant extrinsic resistance and a variable intrinsic resistance. The extrinsic base region is represented with RBC. The intrinsic base region resistance is actually a variable current source, I_{B1B2}. The collector resistance is the sum of multiple collector regions: The lightly doped N^- collector epilayer is represented by a variable current source, I_{C1C2}. The heavily doped N^+ buried collector region is divided in intrinsic resistance, RCBLI, and extrinsic resistance, RCBLX [34]. The collector resistance component attributed to the heavily doped N^+ plug that provides a low resistance connection from the N^+ buried layer to the metal collector contact on the Si top surface is defined by RCC [34].

3.2.1 I_N, transfer current

Mextram uses a quasi-neutral base approach in the interpretation of transfer current, I_N, from the Gummel integrated charge control relationship [18], ICCR, of Equation (2.22). The transfer current, I_N, is defined as the current flow from collector to emitter [13].

$$I_N = \frac{q^2 A_E^2 D_n n_{i0}^2}{Q_B}\left(e^{\frac{VB2E1}{V_T}} - e^{\frac{V_{B2C2}^*}{V_T}}\right) \tag{3.13}$$

The conventional Si BJT approach described in Section 2.4 is defined with the Gummel number, G_B, of Equation (2.23) being equated to total base charge, Q_B:

$$G_B = \int_{x_{E1}}^{x_{C2}} \frac{N_{AB}(x)}{D_{nB}(x)} \frac{n_{i0}^2}{n_{iB}^2(x)} dx \quad \rightarrow \quad Q_B = qA_E \int_{x_{E1}}^{x_{C2}} N_{AB}(x) dx \tag{3.14}$$

The graded Ge concentration profile type SiGe transistor has a varying intrinsic concentration, $n_{iB}(x)$, across the base region thereby preventing G_B from being equated to Q_B. Mextram has a SiGe formulation [13] for Q_B derived from a G_B calculation which is described in Section 3.2.2.2.

The integration of the base ion concentration, $N_{AB}(x)$, in Equation (3.14) is from x_{E1} to x_{C2}. x_{E1} is the emitter edge of the emitter base depletion region and corresponds to Mextram node, E1. x_{C2} is the collector edge of the of the base-N^-epi collector depletion region and corresponds to the Mextram node, C2. The Mextram approach includes the influence of applied voltage bias on the depletion junction models.

The Mextram formulation of transfer current, I_N, is Equation (3.15). I_N, is composed of three terms: I_f, the forward current, I_r, the reverse current, and the normalized base charge, q_B, explained in the following Section 3.2.2. The forward current and reverse current are defined below. The normalized base charge is defined in the following section.

$$I_N = \frac{I_f - I_r}{q_B} \tag{3.15}$$

Forward current, I_f, is exponentially dependent on the simulator node voltage, ***VB2E1***, and thermal voltage, V_T, in Equation (3.16). The reverse current, I_r, is exponentially dependent on the equation voltage V^*_{B2C2}, between internal nodes, B2-C2 as defined in Equation (3.17). In the equations presented normal fonts applied to calculated components and variables of the model. Bold, italicized fonts represent simulated node and branch voltages. Model parameter values are capitalized and temperature adjusted model parameters are capitalized, bold and end with a _T. The nomenclature used in the following equations

$$I_f = \mathbf{IS\_T} \cdot \exp\left[\frac{\boldsymbol{VB2E1}}{V_T}\right] \tag{3.16}$$

$$I_r = \mathbf{IS\_T} \cdot \exp\left[\frac{V^*_{B2C2}}{V_T}\right] \tag{3.17}$$

Adjusted	Description	Model	Unit
IS_T	Saturation Current	IS	A

Table 3.13 Temperature adjusted parameter of branch current, I_N

The temperature adjusted model parameter, **IS_T,** of the saturation current parameter, IS, includes the effects of temperature shifting from the ambient temperature model. Section 3.5.5 describes the temperature behavior of IS. **IS_T** is defined in Equation (3.105). An initial value for IS can be calculated from the physics definition of IC in Equation (2.1).

IS typically is extracted from DC data at each ambient temperature from the linear operating region. The applied VBE must be biased low enough that IC is not influenced by resistances and high level injection effects. The Gummel measurements of Section 5.2.3 provide the needed DC linear operating region to extract an IS for each of the four ambient temperature measurement of the device modeled.

3.2.2 q_B, normalized base charge

The normalized base charge, q_B, is defined as the total base charge, Q_B, divided by the base charge at zero bias, Q_{B0},

$$q_B = \frac{Q_B}{Q_{B0}} = \frac{\text{Total Base Charge}}{\text{Base Charge at Zero Bias}} \tag{3.18}$$

The total base charge, Q_B, is the sum of all charge in the regions from the emitter-base interface to the base-collector interface [13].

$$\underset{\substack{\text{Total}\\\text{Base}\\\text{Charge}}}{Q_B} = \underset{\substack{\text{Neutral}\\\text{Base}\\\text{Charge}}}{Q_{B0}} + \underset{\substack{\text{Depletion}\\\text{Charges}}}{Q_{tE} + Q_{tC}} + \underset{\substack{\text{Diffusion}\\\text{Charges}}}{Q_{BE} + Q_{BC}} \tag{3.19}$$

Q_{B0}	Total base charge at zero bias
Q_{tE}	Base-emitter depletion charge
Q_{tC}	Base-collector depletion charge
Q_{BE}	Base-emitter diffusion charge
Q_{BC}	Base-collector diffusion charge

The physical meaning of the normalized base charge, q_B, can be defined by two effects as shown in Equation (3.20). The first effect is base width modulation, Early effect, described by the depletion region charges and a zero-biased intrinsic base region charge. The second effect is high-level injection occurring at higher currents. High level injection is described by the sum of base-emitter and base-collector diffusion charges in relation to the zero-biased intrinsic base charge. The Mextram formulation of these two effects is defined in Equation (3.21).

$$q_B = \frac{Q_{B0} + Q_{tE} + Q_{tC}}{Q_{B0}} + \frac{Q_{BE} + Q_{BC}}{Q_{B0}} \tag{3.20}$$

Normalized Base Charge	=	Early Effects	+	High Level Injection Effects

$$q_B = q_1 + q_1\left(\frac{1}{2}n_0 + \frac{1}{2}n_B\right) \tag{3.21}$$

q_1	Normalized base charge due to Early effect, from Equation (3.22)
n_0	Normalized electron density at emitter edge of the neutral base region, defined in Equation (3.44)
n_B	Normalized electron density at collector edge of the neutral base region, defined in Equation (3.44)

The next sections define the Mextram formulation for the Early effect and high level injection effects of Equation (3.22). However, before going to the Early effect sections some overall conditions about the Early effect implementation should be noted.

The final form of Early effect, q_1, in Equation (3.22) includes a mathematical limit to prevent the Mextram equation of Early effect, q_0, from having a zero value during simulation. The denominator q_B of the transfer current, I_N, in Equation (3.15) cannot be allowed to be zero in a model simulation. Therefore, q_1 is mathematically prevented from equaling zero by applying Equation (3.22) to the Mextram definition of Early effect, q_0.

$$q_1 = \frac{1}{2}\left(q_0 + \sqrt{q_0^2 + 0.01}\right) \tag{3.22}$$

Physically, q_0=0 could occur during punch-through conditions. Very large reverse bias applied to the junctions of the base-emitter and base-collector would allow the depletion regions to touch each other. The mathematical limiting of the Early effect above prevents the model from diverging during a simulation.

In Mextram [34], the Early effect, q_0, can be calculated for two different situations; Si base or grade SiGe base type transistor. The Si base transistor is the standard calculation and defined by Early effect charge, q_0^Q, as detailed in Section 3.2.2.1. The second situation is for a graded Ge profile SiGe base transistor. In the case of a SiGe transistor the transfer current, I_N, is calculated in terms of Gummel number, $G_{B,}$ and a current version Early effect charge, q_0^I, is used for all current equations. The charge version, q_0^Q, is used in all other areas of the Mextram model for both Si and SiGe. Superscript notation of Q for charge and I for current will be maintained in the following sections to distinguish the version of Early effect charge [13].

3.2.2.1 q_0^Q, Early effect for Si transistors

The Early effect defines the modulation of the transfer current, $I_{N,}$ due to changes in the effective base width caused by bias. The depletion region widths varied as a function of bias at the intrinsic base-collector interface and intrinsic base-emitter interface.

The normalized base charge, $q_{B,}$ of Equation (3.21) reduces to $q_B = q_0^Q$, if diffusion charge is neglected and only Early effects remain. The Early effect charge, q_0^Q, as can be seen in the following equation:

$$q_0^Q = \frac{Q_B}{Q_{B0}} = 1 + \frac{Q_{tE}}{Q_{B0}} + \frac{Q_{tC}}{Q_{B0}} \tag{3.23}$$

The Mextram formulation for q_0 is determined by the two depletion charges and the zero-bias base charge. The depletion charges are defined in Section 3.2.3. Simplified relationships between depletion charge and depletion voltage for the base emitter interface and base-collector interface are formed:

$$V_{tE} = \frac{Q_{tE}}{(1-XCJE)\cdot \mathbf{CJE\_T}} \qquad V_{tC} = \frac{Q_{tC}}{XCJC\cdot \mathbf{CJC\_T}} \tag{3.24}$$

The zero bias base charge, Q_{B0}, is defined as:

$$\begin{aligned} Q_{B0} &= \mathbf{VER\_T}\cdot\left((1-XCJE)\cdot \mathbf{CJE\_T}\right) \\ &= \mathbf{VEF\_T}\cdot\left(XCJC\cdot \mathbf{CJC\_T}\right) \end{aligned} \tag{3.25}$$

Adjusted	Description	Model	Unit
VER_T	Reverse Early voltage of intrinsic transistor at zero bias on emitter-base and base-collector	VER	V
VEF_T	Forward Early voltage of intrinsic transistor at zero bias on emitter-base and base-collector	VEF	V

Table 3.14 Temperature adjusted parameters in Si version of basewidth modulation, q_1 contribution to normalized base charge, q_B

The combination of the Equations (3.24) and (3.25) provides the relationship between depletion charge and zero-bias base charge needed:

$$\frac{Q_{tE}}{Q_{B0}} = \frac{V_{tE}}{\mathbf{VER\_T}} \qquad \frac{Q_{tC}}{Q_{B0}} = \frac{V_{tC}}{\mathbf{VEF\_T}} \tag{3.26}$$

The Early effect, q_0^Q, is simplified with the above equations to yield a definition in terms of the Mextram calculated depletion voltages and Early model parameters [34].

$$q_0^Q = \frac{Q_B}{Q_{B0}} = 1 + \frac{V_{tE}}{\mathbf{VER\_T}} + \frac{V_{tC}}{\mathbf{VEF\_T}} \tag{3.27}$$

The Early voltage model parameters, VEF and VER, are not the measured Early voltage of the output characteristics. The parameters are the effective values when no voltage is applied to either interface junction. This method is designed to yield a measured Early voltage that responds to applied bias [34, 35].

3.2.2.2 q_0^I, Early effect of a graded SiGe base

The q_0^Q derivation for Si transistors in Section 3.2.2.1 is sometimes adequate for modeling SiGe transistor behavior. However, accurate modeling of SiGe processes requires the inclusion of the graded Ge profile contributions. The SiGe physics of Section 2.3 described the bandgap narrowing of the base due to Germanium, $\Delta E_{G(grade)}$. The Mextram 504 model includes the SiGe current contributions by readdressing the Gummel charge control relationship of I_N in Equation (2.15) in terms of the Mextram neutral quasi-base [13]. [34], [38]. The Ge bandgap narrowing requires a thorough assessment of the Gummel number, G_B, component within the Gummel Poon ICCR relationship of Equation (2.15).

$$G_B = \int_{xE1}^{xC2} \frac{N_{AB}(x)}{D_{nB}(x)} \frac{n_{i0}^2}{n_{iB}^2(x)} dx \tag{3.28}$$

x	Location in the base region measured as distance starting at the emitter, x_E, and ending at the collector interface, x_C
$N_{AB}(x)$	Doping concentration as a function of distance, x
$D_{nB}(x)$	Diffusion coefficient as function of distance, x
$n_{iB}(x)$	Intrinsic carrier concentration of base region as a function of distance, x
n_{i0}	Intrinsic carrier concentration of undoped Si

In Si transistors $n_{iB}(x)$ is assumed to remain constant during the integration from emitter to collector edge. In SiGe the value of $n_{iB}(x)$ can vary significantly across the base due to the SiGe bandgap changing as the Ge% concentration changes [21]. The intrinsic concentration has an exponential relationship with the SiGe bandgap difference of:

$$n_{iB}^2(x) \propto \exp\left[\frac{x}{W_{b0}} \frac{\Delta E_{G(grade)}}{kT}\right] \tag{3.29}$$

$\Delta E_{G(grade)}$	Difference in bandgap at the edges of the neutral base due to SiGe base, at zero-bias
W_{b0}	Zero-biased neutral base width

Mextram added the model parameter **DEG_T** to represent $\Delta E_{G(grade)}$. The SiGe current contribution, q_0^I, of Equation (3.30) is calculated using the SiGe intrinsic carrier concentration in terms of the Gummel numbers instead of base charge. The derivation is the base Gummel number, G_B, divided by the zero-biased base Gummel number, G_{B0}. The Mextram formulation [13], [38] of q_0^I is Equation (3.30).

$$q_0^I = \frac{G_B}{G_{B0}} = \frac{\exp\left[\left(1 + \frac{V_{tE}}{\mathbf{VER\_T}}\right)\cdot\left(\frac{\mathbf{DEG\_T}}{V_T}\right)\right] - \exp\left[\frac{-V_{tC}}{\mathbf{VEF\_T}}\cdot\frac{\mathbf{DEG\_T}}{V_T}\right]}{\exp\left[\frac{\mathbf{DEG\_T}}{V_T}\right] - 1} \tag{3.30}$$

Adjusted	Description	Model	Unit
DEG_T	Bandgap difference across graded SiGe base	DEG	V
VER_T	Reverse Early voltage of intrinsic transistor	VER	V
VEF_T	Forward Early voltage of intrinsic transistor	VEF	V

Table 3.15 Temperature adjusted parameters in SiGe version of basewidth modulation, q_0^I contribution to normalized base charge, q_B

The SiGe version, q_0^I, reduces to the Si version, q_0^Q, of Equation (3.27) when DEG=0.

3.2.3 Depletion charges

Within the intrinsic transistor there are two junction interfaces; base-emitter and base-collector. PN junction depletion theory applies to both junctions. The Mextram model represents each junction at its corresponding internal nodes with a depletion charge branch. The depletion charge and its associated depletion voltage are calculated using the Mextram method defined in Section 3.1.4. The following sections introduce the two intrinsic interfaces, models and corresponding model parameters:

Q_{tE} - base-emitter depletion charge
Q_{tC} - base-collector depletion charge

The influence of temperature on these interfaces is significant. A model parameter that is temperature dependent is written in bold font and ends with underscore T. The temperature influence of the model parameters is defined in Section 3.6.

3.2.3.1 Q_{tE}, base-emitter depletion charge

The base-emitter depletion charge of the intrinsic transistor, Q_{tE}, is between nodes B2-E1. Q_{tE} corresponds to the intrinsic portion of the physical base-emitter depletion capacitance. This intrinsic depletion charge is implemented in Mextram by the method described in Section 3.1.4 and uses the relationship of charge to capacitance defined in Equation (3.10).

The base-emitter depletion capacitance, C_{tE}, of the transistor is split between the bottom and sidewall of the emitter-base. The bottom component is the capacitance of the intrinsic base-emitter junction. The sidewall component is a parasitic effect between the emitter and extrinsic base region. The parameter, XCJE, defines the fraction of base-emitter depletion capacitance which is attributed to the sidewall. The fraction (1-XCJE) of emitter depletion capacitance is the contribution of the emitter-intrinsic base interface. The emitter depletion charge, Q_{tE}, and parasitic sidewall depletion charge, Q_{tE}^{S}, follow the splitting of C_{tE}.

The intrinsic emitter depletion charge, Q_{tE}, corresponds to the fraction (1-XCJE) of C_{tE}, base-emitter depletion capacitance. The remainder of the C_{te} split corresponds to Q_{tE}^{S}. Q_{tE} and Q_{tE}^{S} are defined utilizing the Mextram implementation [34] of Equation (3.11) in the following:

Intrinsic Bottom:
$$Q_{tE} = (1 - \text{XCJE}) \cdot \mathbf{CJE\_T} \cdot V_{tE} \tag{3.31}$$

Extrinsic Sidewall:
$$Q_{tE}^{S} = \text{XCJE} \cdot \mathbf{CJE\_T} \cdot V_{tE} \tag{3.32}$$

Adjusted	Description	Model	Unit
CJE_T	Base-emitter depletion capacitance at zero bias	CJE	F
VDE_T	Base-emitter diffusion voltage	VDE	V

Table 3.16 Temperature adjusted parameters in base-emitter depletion charge, Q_{te}

The emitter junction depletion voltage, V_{tE}, is implemented using the Mextram depletion voltage method of Section 3.1.4 and Equation (3.12) defining V_t. The base emitter depletion model parameters: **VDE_T**, PE, and AJE correspond directly to the V_t variables: V_D, p, a of Equation (3.12). The emitter voltage, ***VB2E1,*** corresponds to the branch voltage, V. The correlation of the base-emitter depletion junction model to the Mextram depletion charge model [34]is summarized in Table 3.17.

$$V_{tE} = \frac{\mathbf{VDE\_T}}{(1-\mathrm{PE})} \cdot \left(1 - \left(\frac{1 - V_{jE}}{\mathbf{VDE\_T}}\right)^{(1-\mathrm{PE})}\right) + \mathrm{AJE} \cdot \left(\boldsymbol{VB2E1} - V_{jE}\right) \tag{3.33}$$

Base-Emitter Depletion Voltage Variable	Base-Emitter Depletion Junction Description	Depletion Junction Compact Model Voltage Variables
V_{tE}	Base-emitter depletion voltage	V_t
V_{jE}	Adjusted base-emitter junction branch voltage	V_j
VDE_T	Base-emitter diffusion voltage model parameter adjusted for temperature	V_D
V_{FE}	Base-emitter switching voltage	V_F
AJE	Base-emitter constant capacitance factor	a
VB2E1	Base-emitter constant capacitance factor	V

Table 3.17 Mapping of base-emitter depletion voltage and charge to compact model implementation of depletion behavior in Section 3.1.4.2

The emitter adjusted junction voltage, V_{jE}, and switch voltage, V_{FE}, follow the same method as defined in Equations (3.8) and (3.9). The adjusted junction voltage, V_j, defined in Equation (3.8) is implemented for this interface with V_{ch}=0.1V_D as shown in the equations below.

$$V_{jE} = \boldsymbol{VB2E1} - 0.1 \cdot \mathbf{VDE\_T} \cdot \ln\left[1 + \exp\left[\frac{(\boldsymbol{VB2E1} - V_{FE})}{0.1 \cdot \mathbf{VDE\_T}}\right]\right] \tag{3.34}$$

$$V_{FE} = \mathbf{VDE\_T} \cdot \left(1 - \mathrm{AJE}^{\frac{-1}{\mathrm{PE}}}\right) \tag{3.35}$$

3.2.3.2 Q_{tC}, base-collector depletion charge

Q_{tC} is the base-collector depletion charge between nodes B2-C2 of the intrinsic transistor schematic in Figure 3.3. Q_{tC}, and the depletion voltage, V_{tC}, physically represent the depletion effects of the intrinsic base and N^- collector epilayer. Therefore, Q_{tC} corresponds to the intrinsic portion of the total base-collector depletion capacitance measured. The contributors to the total base-collector depletion capacitance are the intrinsic base-collector junction and all extrinsic base-collector junction interfaces. The Mextram model [34] uses the parameter XCJC to define the fraction of total base-collector capacitance that is directly beneath the emitter. Therefore the depletion charge, Q_{tC}, in Equation (3.36) includes the model parameter, XCJC, as a factor of the total base-collector capacitance, **CJC_T**, and depletion voltage, V_{tC}. The intrinsic depletion charge Q_{tC} utilizes the Mextram depletion charge method described in Section 3.1.4 and the relationship of charge to capacitance defined in Equation (3.11).

$$Q_{tC} = \mathbf{XCJC} \cdot \mathbf{CJC\_T} \cdot V_{tC} \tag{3.36}$$

Adjusted	Description	Model	Unit
CJC_T	Base-collector depletion capacitance at zero bias	CJC	F
VDC_T	Base-collector diffusion voltage	VDC	V

Table 3.18 Temperature adjusted parameters in base-collector depletion charge, Q_{tC}

The base-collector junction goes from forward to reverse bias as the transistor is biased across the full output operating range. Therefore, the depletion voltage, V_{tC}, needs to respond accordingly as the transistor is biased through the various operating regions. The Mextram formulation of $V_{tC,}$ defined in Equation (3.37) reacts to all transistor operating bias states by including the effects of quasi-saturation and high current injection [34], [13].

The depletion voltage, V_{tC}, consists of two components:

- Voltage of the depleted charge region of the intrinsic base and N^- collector
- Voltage across the collector epi-layer due to modulation effects

The depletion voltage, V_{tC}, includes the modulation of the epilayer that is not consumed into the depletion region by splitting voltages of each section. The ratio model parameter, **XP_T,** splits the two voltages. **XP_T** represents the fraction of the total N^- collector epilayer that is depleted.

$$V_{tC} = (1 - \mathbf{XP\_T}) \cdot V_{cv} + \mathbf{XP\_T} \cdot \boldsymbol{VB2C1} \tag{3.37}$$

Adjusted	Description	Model	Unit
XP_T	Ratio of depletion layer thickness at zero bias to epilayer thickness	XP	

Table 3.19 Temperature adjust parameter in the intrinsic base-collector depletion charge

The effects of the epilayer thickness and current modulation are defined in the voltage contribution, V_{cv} of Equation (3.38).

$$V_{cv} = \frac{\mathbf{VDC\_T}}{(1 - \mathrm{PC})}\left(1 - f_I\left(1 - \frac{V_{jC}}{\mathbf{VDC\_T}}\right)^{1-\mathrm{PC}}\right) + f_I \cdot b_{jC}\left(V_{junc} - V_{jC}\right) \tag{3.38}$$

The first component of V_{cv} is based on the Mextram depletion voltage implementation of Section 3.1.4. The second component of V_{cv} is the contribution of current modulation, Kirk effect, described in Section 2.2. The term f_I defined in Equation (3.41) is the current modulation contribution.

Base-Collector Depletion Voltage Variable	Description	Depletion Junction Compact Model Voltage Variables
V_{tC}	Base-collector depletion voltage	V_t
V_{jC}	Adjusted base-collector junction branch voltage	V_j
V_{junc}	Base-collector modified junction voltage which includes epilayer voltage drop	None
VDC_T	Base-collector diffusion voltage model parameter adjusted for temperature	V_D
b_{jc}	Constant capacitance factor calculated using model parameter AJC and temperature adjusted model parameter **XP_T**	a
f_I	Current modulation of Kirk effect	none
MC	Collector current modulation factor for base-collector depletion capacitance	none

Table 3.20 Mapping of base-collector depletion voltage and charge to the compact model implementation of depletion behavior in Section 3.1.4.2

This standard Mextram depletion approach defines the adjusted junction voltage, V_{jC}, the switching voltage, V_{FC}, and constant capacitance factor, b_{jC}.

$$V_{jC} = V_{junc} - V_{ch} \cdot \ln\left[1 + \exp\left[\frac{\left(V_{junc} - V_{FC}\right)}{V_{ch}}\right]\right] \tag{3.39}$$

$$V_{FC} = \mathbf{VDC\_T}\left(1 - b_{jC}^{\frac{-1}{PC}}\right) \qquad b_{jC} = \frac{\mathbf{AJC - XP\_T}}{1 - \mathbf{XP\_T}} \tag{3.40}$$

These calculations provide the quasi-saturation contribution in the collector depletion voltage. f_I produces the behavior of what occurs when the depletion width responds to the charge of electrons travel through the collector epilayer at saturated velocity. Equation (3.41) consists of the epilayer current, I_{C1C2}, defined in Equation (3.60), and the model parameter for the hot-carrier current, IHC. Both are described in the epilayer current of Section 3.2.5.

$$f_I = \left(1 - I_{C1C2}\frac{I_{C1C2}}{I_{C1C2} + IHC}\right)^{MC} \quad (3.41)$$

3.2.4 Diffusion charges

The diffusion charge is associated with the flow of carriers through the transistor. In Mextram 504.7 the charge density of the each region is defined individually:

Q_E- emitter diffusion charge
Q_{BE}- base diffusion charge
Q_{BC}- collector diffusion charge
Q_{epi}-epilayer diffusion charge

Each region has an individual transit time and the influences specific to that region are taken in account in the following diffusion charge definitions.

3.2.4.1 Q_E, emitter diffusion charge

The emitter diffusion charge, Q_E, is the hole charge on the emitter side of the neutral base. The intrinsic transistor cross-section of Figure 1.7 indicates the emitter side is within W_E and the neutral base region is within W_B. Q_E defines the diffusion charge between nodes B2 and E1 in the equivalent circuit schematic of Figure 3.3. This diffusion charge is dependent on the hole density through the emitter. The hole density is proportional to the electron density of the emitter-base depletion region. Therefore, the relationship for Q_E defined in Equation (3.42) is dependent on: an exponential behavior of ***VB2E1***, base-emitter voltage, a minimum emitter transit time and the influence of high-level injection. The temperature adjusted model parameter for minimum emitter transit time, **TAUE_T**, is typically defined at the collector current, IC_{max}, when the maximum cutoff frequency, f_{Tmax}, is measured. The model parameter non-ideality factor, MTAU provides a degree of independence from **TAUE_T** in determining the behavior of emitter diffusion charge [13].

$$Q_E = \mathbf{TAUE\_T} \cdot \mathbf{IK\_T} \left(\frac{\mathbf{IS\_T}}{\mathbf{IK\_T}} \right)^{\frac{1}{\mathrm{MTAU}}} \left(\exp\left[\frac{\boldsymbol{VB2E1}}{\mathrm{MTAU} \cdot V_T} \right] - 1 \right) \tag{3.42}$$

Adjusted	Description	Model	Unit
TAUE_T	Minimum emitter layer transit time	TAUE	s
IK_T	High injection knee current	IK	A
IS_T	Saturation current	IS	A

Table 3.21 Temperature adjusted parameters in emitter diffusion charge, Q_E

3.2.4.2 Q_{BE}, base diffusion charge and Q_{BC}, collector diffusion charge

The base diffusion charge is calculated from the electron density in the base. The base-emitter diffusion charge, $Q_{BE,}$ is between nodes B2 and E1 in Figure 3.3. The base-collector diffusion charge, $Q_{BC,}$ is between nodes B2 and C2 in Figure 3.3. The diffusion charges for the model are based on the simple theory of linear electron density in the base [13]:

$$n(x) = n(0)\left(1 - \frac{x}{W_B}\right) + n(W_B)\frac{x}{W_B} \tag{3.43}$$

The normalized base charge densities at the edges of the neutral base region are n_0 and n_B. The normalized base charge densities are solved using the theory of linear electron density in Equation (3.43), the ICCR relationship of Equation (3.13), and the conditions of high level injection as [13]:

$$n_0 = \frac{4\frac{\mathbf{IS\_T}}{\mathbf{IK\_T}}\exp\left[\frac{\boldsymbol{VB2E1}}{V_T}\right]}{1+\sqrt{1+4\frac{\mathbf{IS\_T}}{\mathbf{IK\_T}}\exp\left[\frac{\boldsymbol{VB2E1}}{V_T}\right]}} \qquad n_B = \frac{4\frac{\mathbf{IS\_T}}{\mathbf{IK\_T}}\exp\left[\frac{V^*_{B2C2}}{V_T}\right]}{1+\sqrt{1+4\frac{\mathbf{IS\_T}}{\mathbf{IK\_T}}\exp\left[\frac{V^*_{B2C2}}{V_T}\right]}} \tag{3.44}$$

The resulting base diffusion charges, Q_{BE} and Q_{BC} are then dependent on the base transit time, **TAUB_T**, the base charge component, q_1 of Equations (3.20) and (3.21), the neutral base charge at the emitter edge of the base, n_0, or the collector edge of the base, n_B, and defined as:

$$Q_{BE} = \frac{1}{2} q_1 Q_{B0} n_0 = \frac{1}{2} q_1 \cdot \left(\mathbf{TAUB\_T} \cdot \mathbf{IK\_T}\right) \cdot n_0 \tag{3.45}$$

$$Q_{BC} = \frac{1}{2} q_1 Q_{B0} n_B = \frac{1}{2} q_1 \cdot \left(\mathbf{TAUB\_T} \cdot \mathbf{IK\_T}\right) \cdot n_B \tag{3.46}$$

Adjusted	Description	Model	Unit
TAUB_T	Minimum base transit time	TAUB	s
IK_T	Collector-emitter high injection knee current	IK	A

Table 3.22 Temperature adjusted parameters of charges: base diffusion, Q_{BE} and collector diffusion, Q_{BC}

3.2.4.3 Q_{epi}, epilayer diffusion charge

The diffusion charge in the epilayer collector region, Q_{epi}, defined in Equation (3.47) is derived from the temperature adjusted model parameter for epilayer transit time, **TEPI_T**, and the charge within the epilayer. Q_{epi} represents the diffusion charge between nodes B2 and C2 in the intrinsic NPN model equivalent circuit schematic of Figure 3.3. The charge within the epilayer is defined in terms of the quasi-saturation adjusted epilayer current branch, I_{C1C2}, components: $\frac{x_i}{W_{epi}}$, p_0^*, p_W. These components are discussed the following Section 3.2.5, I_{C1C2}, epilayer current [13].

$$Q_{epi} = \mathbf{TEPI\_T}\frac{2V_T}{\mathbf{RCV\_T}}\left(\frac{x_i}{W_{epi}}\right)\left(p_0^* + p_W + 2\right) \tag{3.47}$$

$\frac{x_i}{W_{epi}}$	Ratio of the thickness of the injection layer, x_i, to the width of the total collector epilayer, W_{epi}
p_0^*	Hole density at base/collector epilayer interface, normalized with respect to N_{epi}
p_W	Hole density at epilayer/N^+ buried collector interface, normalized with respect to N_{epi}

Adjusted	Description	Model	Unit
TEPI_T	Transit time of collector epilayer	TEPI	s
RCV_T	Ohmic resistance of collector epilayer	RCV	Ω

Table 3.23 Temperature adjusted parameters of the epilayer collector diffusion charge, Q_{epi}

3.2.5 I_{C1C2}, epilayer current

The Mextram 504.7 model includes quasi-saturation behavior. The quasi-saturation equations represent the physical effects of the variable voltage drop of the N^- collector epilayer in advanced NPN bipolar device structures. The epilayer collector is voltage and current dependent. The Mextram model represents the modulation of current in the epilayer by branch current, I_{C1C2}, between nodes C1 and C2 in [34] Figure 3.3. I_{C1C2} describes the bias and resistive behavior of the N^- collector epilayer region. The equations include: ohmic resistance, base widening due to the Kirk effect and the hot carrier behavior of velocity saturation in the epilayer. The collector epilayer is difficult to model since these effects often operate simultaneously.

Quasi-saturation starts when $V_{B2C2}^* = VDC$. The voltage drop across the epilayer, ***VC1C2***, when quasi-saturation starts is V_{qs} and is defined by the electric field Equation (3.48)

$$V_{qs} = VDC - \boldsymbol{VB2C1} = -\int_0^{W_{epi}} E(x)dx \tag{3.48}$$

The low doped N^- epitaxially grown collector makes an interface with the intrinsic P^+ base layer. For low collector currents this epilayer has a constant ohmic resistance, RCV, and is defined by the temperature adjusted model parameter **RCV_T**. At higher collector currents the electric field is not constant and a space charge resistance, SCRCV, is defined for the effective resistance. At higher currents several effects are taking place and the resistance of the epilayer is dependent on the current flow. The effects are summarized in the following table:

Three Operating Regions of Epilayer Collector			
Description	Depletion	Ohmic	High Current
Electric Field, E	E high, $\upsilon=\upsilon_{sat}$	E low, $\upsilon<\upsilon_{sat}$	E high
Onset of quasi-saturation, I_{qs}		$\frac{V_{qs}}{RCV}$	$\frac{V_{qs}}{SCRCV}$
Effective resistance		RCV	SCRCV

Table 3.24 Conditions of the operating regions of the epilayer collector

The epilayer current, I_{epi}, (Kull version), and the voltage of the critical field, V_{CRIT}, are described earlier within Chapter 2 in the Kull model [15] of Section 2.2 and repeated here.

$$I_{epi}\left[\text{Kull}\right]=\frac{(V_{CRIT}+\boldsymbol{VC1C2})}{\mathbf{RCV\_T}} \tag{3.49}$$

$$V_{CRIT}=V_T\left(2p_0-2p_W-\ln\left[\frac{1+p_0}{1+p_W}\right]\right) \tag{3.50}$$

p_0	Hole density at base/collector epilayer interface, normalized with respect to N_{epi}
p_W	Hole density at epilayer/N^+ buried collector interface, normalized with respect to N_{epi}

Calculated intrinsic-base-epilayer collector voltage, V^*_{B2C2}. The use of a calculated voltage instead of a simulator voltage was found to improve the smoothness of current transitions between the base-epilayer depletion interface and the injection layer in the N^- epilayer collector [13]. Mextram uses a recalculated intrinsic base-collector interface voltage, V^*_{B2C2}, which takes into account the quasi-saturation effects on the hole density at the interface, p_0, defined in Equation (2.12) of Kull's model [34]. The Mextram, quasi-saturation modified interface hole density, p^*_0, is calculated to include the current and thickness of the injection layer. The intrinsic base-collector voltage for the interface of B2-C2 nodes, V^*_{B2C2} is calculated from:

$$V^*_{B2C2} = \mathbf{VDC\_T} + V_T \cdot \ln\left[p^*_0(p^*_0 + 1)\right] \tag{3.51}$$

p^*_0	Hole density at base/collector epilayer interface, normalized with respect to $N_{epi,}$

V^*_{B2C2} is used in the calculation of:

- I_r, reverse current, in Equation (3.17)
- $Q_{BC,}$ base-collector intrinsic charge, Equation (3.46)
- Q_{epi}, epi-layer collector charge, Equation (3.47)

Mextram has modified the Kull model of Section 2.2 in several ways [13]. The Mextram derivation of epilayer current originates with Kull's theory but has a different approach to velocity saturation effects. Mextram does not assume the epilayer is quasi-neutral and includes the higher velocity saturation effects. The resulting Mextram derivation is very mathematical, but well defined in the Mextram documentation [13]. The discussion here will focus on the epilayer current contribution at the parameter and bias simulation level. The electric field at high currents is no longer constant. The definitions of electric field are:

$$\frac{dE}{dx} = \frac{qN_{epi}}{\varepsilon}\left(1 - \frac{I_{epi}}{IHC}\right) \qquad \int_0^{Wepi} E(x)dx = \boldsymbol{VB2C2} - VDC \tag{3.52}$$

Here, IHC is the hot carrier current defined by saturation velocity of the critical electric field boundary condition of [35]:

$$E(x_i) = -\frac{\nu_{sat}}{\mu_{nO}} = -IHC \cdot \frac{RCV}{W_{epi}} \tag{3.53}$$

The mobility of the epilayer, μ_{epi}, is calculated from Klaassen's mobility model [39] using an coefficient, α of 0.68.

$$\mu_{epi} = \mu_{min} + \frac{\mu_{max} - \mu_{min}}{1 - \left(\frac{N_{epi}}{N_{ref}}\right)^{\alpha}} \tag{3.54}$$

N_{epi}	Effective collector epilayer doping concentration (cm^{-3})
N_{ref}	NPN reference concentration of epilayer(9.7E16 cm^{-3})
μ_{min}	Maximum mobility of collector epilayer (52 cm^2/Vs)
μ_{max}	Maximum mobility of collector epilayer (1417 cm^2/Vs)

And with initial values for model parameters: VDC, IHC, RCV, SCRCV, and XP determined by process based calculations:

$$IHC = q \cdot N_{epi} \cdot A \cdot \nu_{sat} \tag{3.55}$$

$$VDC = V_T \cdot \ln\left[\frac{N_{epi}^2}{n_i^2}\right] \tag{3.56}$$

$$RCV = \frac{W_{epi}}{q\mu_{epi} N_{epi} A} \tag{3.57}$$

$$SCRCV = \frac{W_{epi}^2}{2\varepsilon \nu_{sat} A} \tag{3.58}$$

$$XP = \frac{\sqrt{2\varepsilon VDC}}{qN_{epi}} \tag{3.59}$$

N_{epi}	Effective collector epilayer doping concentration (cm^{-3})
W_{epi}	Thickness of collector epilayer layer (nm)
q	Elemental charge (1.609E-19 C)
ε	Dielectric constant of collector epilayer (1.036E-10 C/Vm)
n_i	Collector intrinsic concentration (cm^{-3})
ν_{sat}	Saturation velocity of collector epilayer (8.0E4 m/s)
A	Area of active emitter, represents area of intrinsic transistor (m^{-2})

The final definitions [34] of quasi-saturation voltage, V_{qs}, quasi-saturation current, I_{qs}, and I_{C1C2} are therefore:

$$V_{qs} = \mathbf{VDC\_T} + 2V_T \cdot \ln\left[\frac{I_{epi}\mathbf{RCV\_T}}{2V_T} + 1\right] - \boldsymbol{VB2C1} \tag{3.60}$$

$$I_{qs} = \frac{V_{qs}}{SCRCV}\left(\frac{V_{qs} + IHC \cdot SCRCV}{V_{qs} + IHC \cdot \mathbf{RCV\_T}}\right) \tag{3.61}$$

$$I_{C1C2} = \frac{V_{qs}}{SCRCV\left(1 - \frac{x_i}{W_{epi}}\right)^2}\left(\frac{V_{qs} + IHC \cdot SCRCV\left(1 - \frac{x_i}{W_{epi}}\right)}{V_{qs} + IHC \cdot \mathbf{RCV\_T}}\right) \tag{3.62}$$

$\frac{x_i}{W_{epi}}$	Ratio of the thickness of the injection layer, x_i, to the width of the total collector epilayer, W_{epi}

Adjusted	Description	Model	Unit
RCV_T	Ohmic resistance of collector epilayer	RCV	Ω
VDC_T	Base-collector diffusion voltage	VDC	V

Table 3.25 Temperature adjusted parameters of the epilayer

3.2.6 Base current contributors

There are multiple elements contributing to base current, IB, at the external node B of the Mextram 504.7 model. We will group the contributors into three groups:

- Intrinsic base current contributors of the intrinsic transistor
  - I_{B1}– forward ideal intrinsic base-emitter current, nodes B2-E1
  - I_{B2} – forward nonideal ideal intrinsic base-emitter current, nodes B2-E1
  - I_{avl} – avalanche current, nodes B2-C
- Extrinsic base current contributors, mainly due to parasitic PNP
  - I^S_{B1} – forward sidewall ideal ideal sidewall base-emitter current, nodes B1-E1
  - I_{B3} – reverse nonideal base-collector current, nodes B1-C1
  - I_{ex} – reverse ideal base-collector current, nodes B1-C1
- Extended base current contributors
  - XI_{ex} – external base-collector current splitting current from I_{ex}, nodes B-C
  - XI_{sub} – base-substrate current splitting current from I_{sub}, nodes B-S

The sum of these currents is equal to the total value of simulated base current, IB. In the following subsection the intrinsic base currents will be discussed. The extrinsic base current contributors will be defined in Section 3.3. The extended base current contributors are discussed in Section 3.4.

3.2.6.1 $\mathbf{I_{B1}}$, $\mathbf{I^S_{B1}}$, ideal forward base current, bottom and sidewall

The ideal forward base current is the base current between the intrinsic nodes B2-E1 and the extrinsic base nodes B1-E1. The bottom is the intrinsic base current, I_{B1}. The total base-emitter current [13] can be split into bottom and sidewall components by the parameter XIB1.

Intrinsic Bottom:

$$I_{B1} = (1 - \mathrm{XIB1})\frac{\mathbf{IS\_T}}{\mathbf{BF\_T}}\left(\exp\left[\frac{\boldsymbol{VB2E1}}{V_T}\right] - 1\right) \tag{3.63}$$

Extrinsic Sidewall: $$I_{B1}^{S} = XIB1\frac{\mathbf{IS\_T}}{\mathbf{BF\_T}}\left(\exp\left[\frac{\boldsymbol{VB1E1}}{V_T}\right]-1\right) \tag{3.64}$$

Adjusted	Description	Model	Unit
IS_T	Saturation current	IS	A
BF_T	Forward current gain	BF	

Table 3.26 Temperature adjusted parameter for current I_{B1} and I_{B1}^{S}

3.2.6.2 I_{B2}, nonideal forward base current

The nonideal forward current, I_{B2}, is typically due to recombination in the base-emitter space charge layer and at the surface [13]. The current is part of the intrinsic transistor and is across the nodes B2-E1. The model parameter MLF is a non-ideality factor that allows independence to the base current in the low base-emitter bias region where I_{B2} will be dominant [13].

$$I_{B2} = \mathbf{IBF\_T}\left(\exp\left[\frac{\boldsymbol{VB2E1}}{MLF \cdot V_T}\right]-1\right) \tag{3.65}$$

Adjusted	Description	Model	Unit
IBF_T	Saturation current of the nonideal forward base current	IBF	A

Table 3.27 Temperature adjusted parameters for current I_{B2}

3.2.6.3 I_{avl}, weak avalanche base current

Avalanche current is generated in the collector, primarily in the collector epilayer, when impact ionization occurs within high electric fields. In the Mextram model [13], the avalanche current branch, I_{avl}, is located between nodes B2 and C2. The current model is based on Chynoweth's empirical law of ionization coefficients [40].

$$\alpha_n\left[E(x)\right] = A_n \exp\left(\frac{-B_n}{\left|E(x)\right|}\right) \tag{3.66}$$

A_n	Avalanche coefficient, NPN value =7.05E07 m^{-1}
B_n	Critical electric field, NPN value =1.23E08 m^{-1}

E(x) is the electric field as a function of distance x from the base-collector interface. The avalanche current is calculated to be the epilayer current, I_{C1C2}, times the ionization coefficient across the entire epilayer as defined in Equation (3.65).

$$I_{avl} = I_{C1C2} \cdot \int_0^{Weff} \alpha_n\left[E(x)\right] dx \tag{3.67}$$

This impact ionization contribution is then defined as a generation factor, G_m in the I_{avl} Equation (3.68).

$$G_m = \int_0^{Weff} \alpha_n\left[E(x)\right] dx \tag{3.68}$$

The integral of the electric field of the epilayer is determined in quasi-saturation and determined by the maximum critical field, E_m and location of the injection layer x/λ_D [13].

$$\left|E(x)\right| = E_m\left(1 - \frac{x}{\lambda_D}\right) \approx \frac{E_m}{1 + x/\lambda_D} \tag{3.69}$$

E_m	Maximum electric field
x_d	Depletion layer thickness base-collector epilayer interface
λ_D	Interception point in the collector where the extrapolated electric field is zero

E_m and λ_D are further defined as:

$$E_m = \frac{(\mathbf{VDC\_T} + \boldsymbol{VB2C1}) + 2 \cdot \mathrm{VAVL}}{\mathrm{WAVL}} \sqrt{\frac{(\mathbf{VDC\_T} + \boldsymbol{VB2C1})}{(\mathbf{VDC\_T} + \boldsymbol{VB2C1}) + \mathrm{VAVL}}} \quad (3.70)$$

$$\lambda = \frac{\mathrm{WAVL}^2 \cdot E_m}{2 \cdot \mathrm{VAVL}} \quad (3.71)$$

V_{AVL}	Voltage describing the derivative of the electric field at low currents
W_{AVL}	Effective thickness of collector epilayer layer for avalanche

Therefore G_m is the combination Equations (3.65) through (3.70) to be:

$$G_m = \frac{A_n}{B_n} \cdot E_m \cdot \lambda \left(\exp\left[\frac{-B_n Tk}{E_m}\right] - \exp\left[\frac{-B_n Tk}{E_m}\left(1 + \frac{W_{eff}}{\lambda}\right)\right]\right) \quad (3.72)$$

So that the avalanche branch current, I_{avl} is epilayer current, I_{C1C2}, of Equation (3.60) and the generation factor of Equation (3.71) in the following:

$$I_{avl} = I_{C1C2} \cdot G_m \quad (3.73)$$

3.2.7 I_{B1B2}, variable base current

The variable intrinsic base resistance is due to two effects and represented by the variable intrinsic base current, I_{B1B2} in Equation (3.56). One effect is conductivity modulation, modeled by the base charge, q_B^Q, of Equation (3.27). The second physical effect modeled is current crowding through the use of **RBV_T**. The resistance is modeled based on the applied voltage in the intrinsic region between nodes, B1-B2. The DC and small-signal effects are both taken into account by this method [13].

$$I_{B1B2} = \frac{2V_T\left(\exp\left[\frac{\boldsymbol{VB1B2}}{V_T}\right]-1\right)+\boldsymbol{VB1B2}}{\frac{3\mathbf{RBV\_T}}{q_B^Q}} \tag{3.74}$$

Adjusted	Description	Model	Unit
RBV_T	Low current resistance of intrinsic base, I_{B1B2} branch	RBV	Ω

Table 3.28 Temperature adjusted parameters for I_{B1B2}

Note that for the variable base resistance of SiGe q_0^I of Equation (3.30) is not used in derivation of base charge, q_B^Q .

3.2.8 RE, RBC, RCC, RCBLX, and RCBLI resistances

RE, the emitter resistance is between nodes E-E1. The value of RE is the amount of parasitic resistance in the poly-emitter and intrinsic emitter regions. The emitter resistance model parameter, **RE_T**, includes the effects of temperature on the model's emitter resistance [13].

RBC, the base contact resistance between B-B1 represents the parasitic resistance of the extrinsic base regions. This area is typically heavily doped and low resistance. The extrinsic base resistance parameter, **RBC_T**, includes the effects of temperature, thereby adjusting RBC.

RCC, the collector contact resistance is between nodes C-C3. RCC represents the parasitic resistance of the heavily doped N^+ plug region from the surface contact to the N^+ buried collector layer. The collector contact resistance parameter, **RCC_T**, includes the effects of temperature on the model's collector resistance [13].

RCBLX, the extrinsic collector N^+ buried layer resistance is between internal nodes C3-C4. In the 504.7 model release the buried layer resistances, extrinsic and intrinsic were added. The extrinsic collector N^+ buried layer resistance parameter, **RCCex_T**, includes the effects of temperature on the extrinsic buried layer resistance [34].

RCBLIX, The intrinsic collector N^+ buried layer resistance is between the internal nodes, C4-C2. This parasitic resistance represents the intrinsic N^+ buried layer of the collector beneath the active transistor region. The intrinsic collector N^+ buried layer resistance parameter, **RCCin_T**, includes the effects of temperature in collector intrinsic buried layer [34].

The temperature adjusted model parameters of each resistance is listed in Table 3.29.

Adjusted	Description	Model	Unit
RE_T	Constant resistance of emitter	RE	Ω
RBC_T	Constant resistance of external base	RBC	Ω
RCC_T	Constant resistance of external collector	RCC	Ω
RCCin_T	Constant resistance of intrinsic N^+buried layer of collector beneath active transistor	RCBLI	Ω
RCCex_T	Constant resistance of extrinsic N^+buried layer of collector beneath extrinsic regions	RCBLX	Ω

Table 3.29 Temperature adjusted parameters for resistances

3.3 Extrinsic transistor

The extrinsic areas of the Mextram model represent the reverse and parasitic effects due to the PNP formed in the base-collector-substrate regions. The extrinsic components have been added to the intrinsic transistor of Figure 3.2 with the extrinsic areas of advanced bipolar structures circled in red below in Figure 3.4.

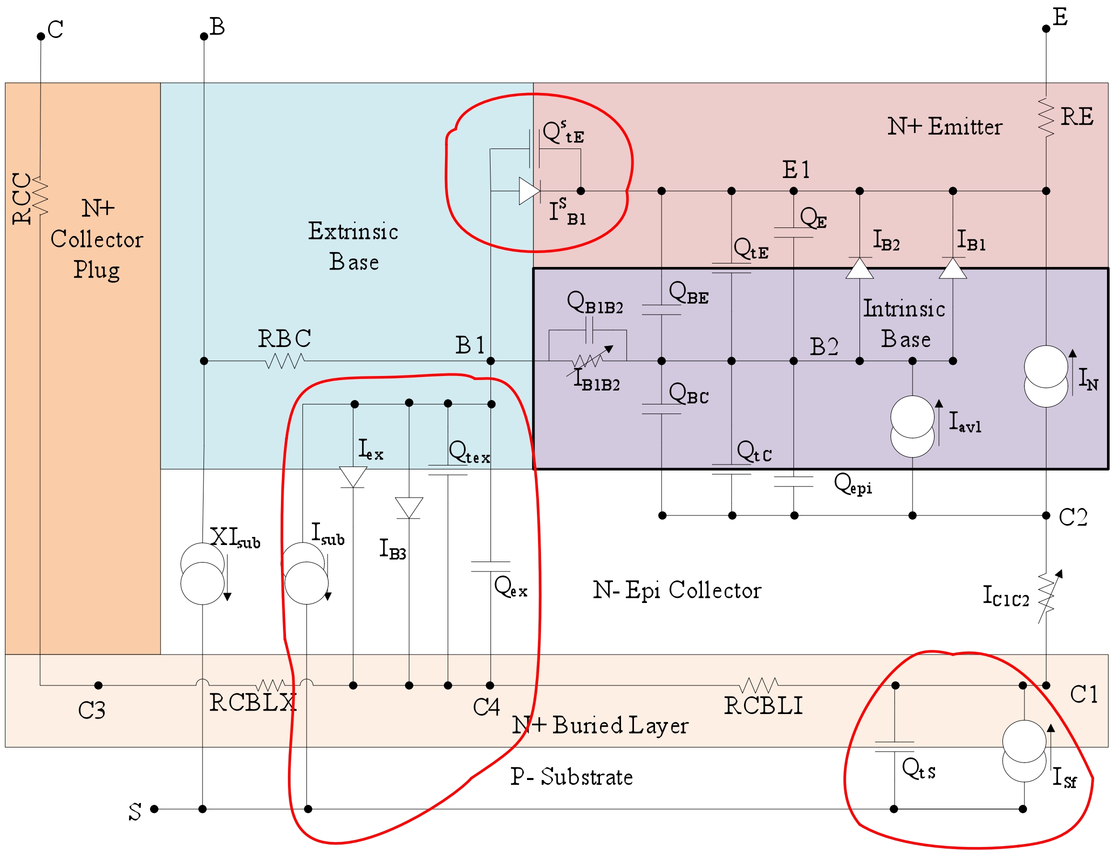

Figure 3.4 Mextram 504.7 extrinsic regions circled in red [34]

3.3.1 I_{ex}, extrinsic base current

The extrinsic base current, I_{ex}, between nodes B1-C4 represents the ideal reverse current of the parasitic PNP. The ideal current component is exponentially dependent on the simulator voltage, ***VB1C1,*** and inversely proportionally to the reverse current gain, BRI. The definition of I_{ex} in Equation (3.73) does not include PNP Early effects, but it does include the transition between low-level injection and high-level injection. I_{ex} is then defined to include the interpolation between the two injection levels in a manner similar to the diffusion charge of the main transfer current, I_n [34].

$$I_{ex} = \frac{1}{\mathbf{BRI\_T}}\left(\frac{1}{2}\mathbf{IK\_T}\cdot n_{Bex} - \mathbf{IS\_T}\right) \tag{3.75}$$

An electron density, n_{Bex}, is defined representing the extrinsic base-collector interface just like n_B of Equation (3.44) was defined for calculation of diffusion charge in Equation (3.46).

$$n_{Bex} = \frac{\frac{4\mathbf{IS\_T}}{\mathbf{IK\_T}}\exp\left[\frac{\boldsymbol{VB1C1}}{V_T}\right]}{\left(1+\sqrt{1+\frac{4\mathbf{IS\_T}}{\mathbf{IK\_T}}\exp\left[\frac{\boldsymbol{VB1C1}}{V_T}\right]}\right)} \tag{3.76}$$

Adjusted	Description	Model	Unit
IS_T	Saturation current	IS	A
IK_T	Forward knee current	IK	A
BRI_T	Reverse current gain	BRI	

Table 3.30 Temperature adjusted parameters for extrinsic current I_{ex}

3.3.2 I_{B3}, nonideal reverse base current

An approximation of Shockley-Read-Hall recombination theory [13], [11] is used to model the current from recombination in the depletion layers. The current is exponentially dependent on ($\boldsymbol{VB1C1}/V_T$) at small junction voltages, but at a certain voltage the current crosses over to having a dependence of ($\boldsymbol{VB1C1}/2V_T$).

$$I_{B3} = \mathbf{IBR\_T}\frac{\exp\left[\frac{\boldsymbol{VB1C1}}{V_T}\right]-1}{\exp\left[\frac{\boldsymbol{VB1C1}}{2V_T}\right]+\exp\left[\frac{VLR}{2V_T}\right]} \tag{3.77}$$

Adjusted	Description	Model	Unit
IBR_T	Saturation current of nonideal reverse base current	IBR	A

Table 3.31 Temperature adjusted parameter for current I_{B3}

3.3.3 I_{sub}, substrate current

The substrate current represents the parasitic PNP behavior when the NPN device is biased in the saturated and reverse operating regions. I_{sub} takes the form of the transfer current for the parasitic PNP behavior [13]. High-level injection behavior is represented by the reverse knee current, **IKS_TM**.

$$I_{sub} = \frac{2\mathbf{ISS\_T}\left(\exp\left[\frac{\boldsymbol{VB1C1}}{V_T}\right]-1\right)}{1+\sqrt{1+4\frac{\mathbf{IS\_T}}{\mathbf{IKS\_TM}}\exp\left[\frac{\boldsymbol{VB1C1}}{V_T}\right]}} \quad (3.78)$$

Adjusted	Description	Model	Unit
ISS_T	Saturation current of NPN	ISS	A
IS_T	Reverse parasitic PNP saturation current	IS	A
IKS_TM	Knee current of parasitic PNP behavior from base-collector substrate regions	IKS	A

Table 3.32 Temperature adjusted parameters for current I_{sub}

3.3.4 Q_{tS}, collector-substrate depletion charge

The complete depletion charge of collector to substrate is Q_{tS} and defined as [13]:

$$Q_{tS} = \mathbf{CJS\_TM}\left(\frac{\mathbf{VDS\_T}}{(1-PS)}\left(1-\left(1-\frac{V_{jS}}{\mathbf{VDS\_T}}\right)^{1-PS}\right)+AJS(\boldsymbol{VSC1}-V_{jS})\right) \quad (3.79)$$

Adjusted	Description	Model	Unit
CJS_TM	Collector-substrate depletion capacitance at zero bias	CJS	F
VDS_T	Collector-substrate built-in voltage	VDS	V

Table 3.33Temperature adjusted parameters for Q_{ts}

3.4 Extending model features

Additional diode and capacitance features are available in the external area of the transistor by activating flag model parameters. These branches are only present if activated. The extended branches are circled in red in the full Mextram 504.7 equivalent circuit schematic [34] of Figure 3.5 and consist of:

- XI_{ex} - External base-collector diode current splitting I_{ex}, nodes B-C3
- XQ_{tex} – External base-collector depletion charge splitting Q_{tex},nodes B-C3
- XQ_{ex} - External Base-collector diffusion charge splitting Q_{ex}, nodes B-C3
- XI_{sub} - Base-Substrate diode current splitting I_{sub}, nodes B-C

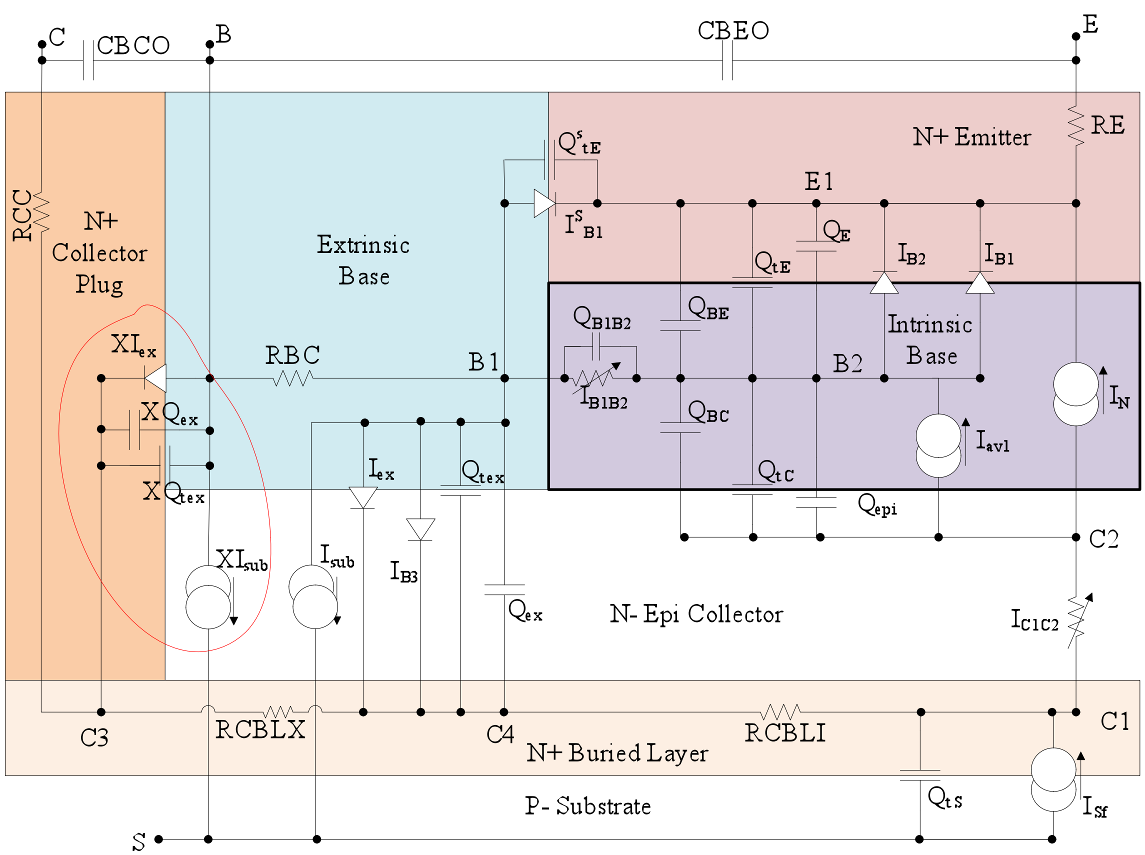

Figure 3.5 Mextram 504.7 extended model regions circled in red on the full model equivalent circuit schematic [34]

The flag model parameter, EXMOD, determined the activation of the above branches. If EXMOD=1 the above branches are present. The model parameter XEXT is applied to define the value of each branch. The value of above branch is determined to be the value of the corresponding extrinsic branch times the factor XEXT. The corresponding extrinsic branch is revalued to be (1-XEXT) of its original value.

External Branches Activated	Extrinsic Branch Modifications
XI_{ex}=XEXT· I_{ex}	I_{ex}=(1-XEXT)· I_{ex}
XQ_{tex}=XEXT· Q_{tex}	Q_{tex}=(1-XEXT)· Q_{tex}
XQ_{ex}=XEXT·Q_{ex}	Q_{ex}=(1-XEXT)· Q_{ex}
XI_{sub} =XEXT· I_{sub}	I_{sub}=(1-XEXT)· I_{sub}

Table 3.34 Branch modifications if extended modeling is activated

Extending modeling of the base diffusion charges includes distributed high frequency effects in the intrinsic base. This would be activated by the setting the flag parameter EXPHI=1. Then the above Equation (3.45) for Q_{BE} and Equation (3.46) for Q_{BC} would be modified to:

$$Q_{BE} \rightarrow \frac{2}{3} Q_{BE} \qquad\qquad Q_{BC} \rightarrow \frac{1}{3} Q_{BE} + Q_{BC} \tag{3.80}$$

Avalanche current generation under high current conditions, I_{C1C2} > IHC, is modeled in Mextram as an optional feature. The model flag parameter EXAVL=1 activates an empirical formula for the branch current, I_{AVL}, when epilayer current is greater than the critical current, IHC.

3.5 Self-heating

With current flow, power is generated, as is heat. The device temperature increases from its ambient temperature due to power dissipation. This device behavior is termed self-heating. The device temperature rise can be related for DC conditions to the power dissipation by a linear relationship of:

$$\Delta T = RTH \cdot P_{diss} \tag{3.81}$$

The thermal resistance model parameter, RTH, has units of K/W. RTH is extracted from an output measurement biased with a constant base current. In oxide isolated bipolar processes the thermal resistance is large and significant device temperature increases can occur as the DC bias is increased.

Power dissipation, $P_{diss,}$ is composed of a DC bias component and a thermal storage charge component [13].

$$P_{diss} = \frac{\Delta T}{RTH} + CTH \frac{d\Delta T}{dt} \tag{3.82}$$

For Mextram the simple, commonly used self-heating circuit [13], [34] of Figure 3.6 represents the above linear relationship. The temperature rise, ΔT, is the voltage V(dT) of the temperature node, dT. The power dissipation is represented as a current source.

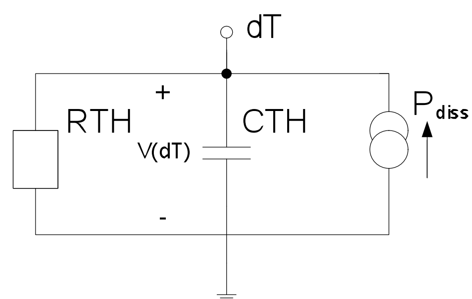

Figure 3.6 Self-heating model configuration

In general the DC biased bipolar power dissipation is:

$$P = (IC \cdot VCE)_{applied} + (IB \cdot VBE)_{applied} \tag{3.83}$$

For the Mextram model [34], the DC component of P_{diss} is calculated by summing all branch currents and their corresponding voltage nodes:

$$\begin{aligned} P_{diss} &= I_N(\boldsymbol{VB2E1} - V^*_{B2C2}) + I_{C1C2}\left(V^*_{B2C2} - \boldsymbol{VB2C1}\right) \\ &- I_{AVL} \cdot V^*_{B2C2} + \frac{\boldsymbol{VEE1}^2}{RE} + \frac{\boldsymbol{VCC1}^2}{RCC} + \frac{\boldsymbol{VBB1}^2}{RBC} \\ &+ I_{B1B2} \cdot \boldsymbol{VB1B2} + (I_{B1} + I_{B2})\boldsymbol{VB2E1} + I_{B1S} \cdot \boldsymbol{VB1E1} + \\ &(I_{ex} + I_{B3} + I_{sub})\boldsymbol{VB1C1} + (XI_{ex} + XI_{sub})\boldsymbol{VBC1} + \\ &(XI_{sub} + I_{sub} - I_{Sf})\boldsymbol{VC1S} \end{aligned} \tag{3.84}$$

The charge component of P_{diss} is dependent on the thermal mass or thermal capacitance, CTH, and the small signal change of the thermal node, d(ΔT)/dt:

$$P_{diss} = CTH \cdot \frac{d\Delta T}{dt} \tag{3.85}$$

CTH cannot be set to zero. That would imply that self-heating is infinitely fast. Typically, the self-heating effect is much slower than the circuit application being simulated. A common estimate is CTH=1μs/RTH [41], [35]. If more device structure information is known, CTH can be calculated.

Therefore, with each bias point a device temperature, Tk, is calculated. Tk at each bias includes the ambient temperature and the self-heating temperature increase. Each temperature is used at its corresponding bias point to adjust the model parameter temperature shifting equations and define the simulation temperature.

3.6 Parameters shifted by temperature

Several Mextram model parameters are closely related to the physical transistor. Temperature significantly influences the transistor's physical characteristics. Therefore, model parameters are adjusted by individual temperature equations in order for the model parameters to track with temperature.

The relationship between model parameters and temperature is defined by the intrinsic carrier concentration and the carrier's mobility using the following relationship:

$$
\begin{aligned}
n_i^2 &= N_C N_V \exp\left[-\frac{V_g}{V_T}\right] \\
&= n_{iREF}^2 t_N^3 \exp\left[-\frac{V_g}{V_{\Delta T}}\right]
\end{aligned}
\qquad (3.86)
$$

N_C	Density of states in the conduction band
N_V	Density of states in the valence band
V_g	Bandgap voltage
t_N	Ratio of device temperature, Tk, to model temperature, Tmodel as defined in Equation (3.3)
n_{iREF}	Intrinsic concentration at the reference temperature

Mobility has an inverse relationship with temperature. The temperature coefficient is material dependent.

$$\mu \propto \frac{1}{T^A} \qquad (3.87)$$

Klaussen mobility model [39], [42] is used by Mextram to establish the temperature coefficient, A, for each region based on the doping. The results of Klaussen's model in terms of temperature coefficients and dopant concentrations [35] are used for defining coefficient values.

The basics of conductivity, $\sigma = q(\mu_N n + \mu_P p)$, and Einstein's relationship, $\frac{D}{\mu} = \frac{kT}{q}$ are used in establishing the model parameter temperature equations[13].

Parameter	Description from Process	Parameter Influenced	Equation Coefficient Component
AQBO	Zero bias base charge temperature coefficient	RBV BF IS VER VEF TAUB DEG	AB-AQBO AE-AB-AQBO 4-AB-AQBO+DAIS AQBO AQBO AQBO+AB-1 AQBO
DAIS	IS equation temperature coefficient	IS	4-AB-AQBO+DAIS
AE	Emitter doping temperature coefficient	RE BF	AE AE-AB-AQBO
AB	Base doping temperature coefficient	RBV BF IS IK TAUE TAUB	AB-AQBO AE-AB-AQBO 4-AB-AQBO+DAIS 1-AB AB-2 AQBO+AB-1
AEX	Extrinsic base doping temperature coefficient	RBC	AEX
AEPI	Epilayer collector doping temperature coefficient	RCV TEPI	AEPI AEPI-1
AC	Extrinsic contact collector doping temperature coefficient	RCC	AC
ACBL	Buried layer collector doping temperature coefficient	RCBLX RCBLI	ACBL ACBL
AS	Substrate doping temperature coefficient	ISS IKS	AS AS
ATH	Self heating temperature coefficient	RTH	ATH

Table 3.35 Temperature parameters and parameters influenced

The bandgap influences due to temperature are described with temperature parameters are included for each region and for forward and reverse current gain. All of the bandgap temperature parameters and the other model parameters they influence are listed in Table 3.36.

Parameter	Description from Process	Parameter Influenced
DVGBF	Bandgap delta of forward current gain	BF
DVGBR	Bandgap delta of reverse current gain	BR
VGB	Base bandgap voltage	VDE IS
VGC	Collector bandgap voltage	VDC IBR
VGJ	Base-emitter recombination bandgap voltage	IBF
DVGTE	Emitter charge difference bandgap voltage	TAUE
VGS	Substrate bandgap voltage	VDS ISS

Table 3.36 Bandgap temperature parameters and the model parameters they effect

3.6.1 Depletion voltage temperature equations

The relationship between depletion voltage and temperature utilizes the definition of intrinsic concentration in Equation (3.86). The basic definition of junction depletion voltage, $V_{D,}$ is defined by doping concentrations and intrinsic concentration in Equation (3.88). By replacing n_i with the temperature based Equation (3.84), a well defined relationship between depletion voltage, VD_T, and temperature is established in Equation (3.86) which is applicable to all three junction interfaces [13].

$$\begin{aligned} VD\_T &= V_T \ln\left[\frac{N_A N_D}{n_i^2}\right] = \frac{kT}{q}\ln\left[\frac{N_A N_D}{n_{iREF}^2 t_N^3 \exp\left[\frac{-V_g}{V_{\Delta T}}\right]}\right] \\ &= -3V_T \cdot \ln\left[t_N\right] + V_d t_N + (1-t_N)V_g \end{aligned} \quad (3.88)$$

The corresponding temperature equation of each junction depletion voltage is defined below.

$$\mathbf{VDE\_T} = -3V_T \cdot \ln\left[t_N\right] + VDE \cdot t_N + (1-t_N)\cdot VGB \quad (3.89)$$

$$\mathbf{VDC\_T} = -3V_T \cdot \ln\left[t_N\right] + VDC \cdot t_N + (1 - t_N) \cdot VGC \tag{3.90}$$

$$\mathbf{VDS\_T} = -3V_T \cdot \ln\left[t_N\right] + VDS \cdot t_N + (1 - t_N) \cdot VGS \tag{3.91}$$

3.6.2 Depletion capacitance temperature equations

Junction depletion capacitance at zero bias also varies with temperature. Mextram's equations for capacitance versus temperature are based on the depletion voltage parameters change with temperature [34]. Using the basic definition of depletion capacitance in Equation (3.92), with permittivity, ε, and junction area, A, the depletion depth can be seem to have a direct dependence on depletion voltage, V_D.

$$C_j = \frac{\varepsilon A}{x_D} \qquad \text{and} \qquad x_D \propto V_D^p \tag{3.92}$$

The temperature equations for zero biased capacitance of base-emitter, CJE and collector-substrate, CJS, are defined by applying the corresponding temperature adjusted depletion voltage parameters of **VDE_T** and **VDS_T**.

$$\mathbf{CJE\_T} = CJE \cdot \left(\frac{VDE}{\mathbf{VDE\_T}}\right)^{PE} \tag{3.93}$$

$$\mathbf{CJS\_T} = CJS \cdot \left(\frac{VDS}{\mathbf{VDS\_T}}\right)^{PS} \tag{3.94}$$

The base collector capacitance is composed of a voltage dependence term and a constant value term which is controlled by the model parameter XP. Therefore temperature influence on the zero-biased base-collector capacitance parameter, CJC, maintains the separate contributions by the following derivation for **CJC_T** and **XP_T**:

$$\mathbf{CJC\_T} = \mathrm{CJC} \cdot \left((1 - \mathrm{XP}) \cdot \left(\frac{\mathrm{VDC}}{\mathbf{VDC\_T}} \right)^{\mathrm{PC}} + \mathrm{XP} \right) \tag{3.95}$$

$$\mathbf{XP\_T} = \frac{\mathrm{XP}}{\left((1 - \mathrm{XP}) \cdot \left(\frac{\mathrm{VDC}}{\mathbf{VDC\_T}} \right)^{\mathrm{PC}} + \mathrm{XP} \right)} \tag{3.96}$$

3.6.3 Resistance temperature equations

Resistance changes as a function of temperature. When the device temperature differs from the reference temperature the resistance parameter value must be adjusted correctly. All resistances in Mextram [34] vary with temperature using a power law dependency. This relationship is based on resistance being inversely proportional to conductivity. The conductivity of a region is based on the total mobility of majority and minor carriers and their respective concentrations. The simplified mobility vs. temperature relationship of Equation (3.87) provides a temperature coefficient for each physical region of the transistor. The unique parasitic resistance parameter for each region uses a power law relationship of temperature change ratio, t_N, to doping coefficient model parameter, A(region). The temperature coefficient model parameters are defined for each region in Table 3.35.

The emitter and extrinsic base resistances have doping coefficient parameters, AE and AEX respectively.

$$\mathbf{RE\_T} = \mathrm{RE} \cdot t_N^{\mathrm{AE}} \tag{3.97}$$

$$\mathbf{RBC\_T} = \mathrm{RBC} \cdot t_N^{\mathrm{AEX}} \tag{3.98}$$

The intrinsic base resistance uses a combination of coefficient parameters. AB represents the intrinsic base doping under bias. AQBO represents the intrinsic base charge at zero bias.

$$\mathbf{RBV\_T} = \mathrm{RBV} \cdot t_N^{(\mathrm{AB}-\mathrm{AQBO})} \tag{3.99}$$

The resistance of the collector regions is defined by separate model parameters and each also has its unique doping temperature coefficient model parameter as defined below [34].

$$\mathbf{RCC\_T} = \mathrm{RCC} \cdot t_N^{\mathrm{AC}} \tag{3.100}$$

$$\mathbf{RCCex\_T} = \mathrm{RCBLX} \cdot t_N^{\mathrm{ACBL}} \tag{3.101}$$

$$\mathbf{RCCin\_T} = \mathrm{RCBLI} \cdot t_N^{\mathrm{ACBL}} \tag{3.102}$$

$$\mathbf{RCV\_T} = \mathrm{RCV} \cdot t_N^{\mathrm{AEPI}} \tag{3.103}$$

3.6.4 SiGe base charge and Early voltage temperature equations

The base charge calculation that includes the graded SiGe contribution relies on the model parameter DEG to represent the bandgap difference across the base due to the changing Ge% concentration for collector edge to emitter edge. The bandgap difference changes as a function of temperature. Mextram 504.7 uses a power law relationship between temperature change, t_N and the zero-bias base charge coefficient, AQBO, as shown in the following to represent **DEG_T**, the model value at a specific device temperature [34].

$$\mathbf{DEG\_T} = \mathrm{DEG} \cdot t_N^{\mathrm{AQBO}} \tag{3.104}$$

Base width modulation is affected by temperature. The forward and reverse Early parameters, VEF and VER, have temperature equations which represent the temperature effects on base width. The temperature equations below rely on the relationship of Equation (3.25) which defines the interaction between Q_{B0}, Early parameters and capacitance parameters. The temperature equation for **VEF_T** is therefore defined by including the temperature effects of Q_{B0} and **CJC_T**.

$$\mathbf{VEF\_T} = \mathrm{VEF} \cdot t_N^{AQBO} \left((1 - \mathrm{XP}) \left(\frac{\mathrm{VDC}}{\mathbf{VDC\_T}} \right)^{PC} + \mathrm{XP} \right)^{-1} \tag{3.105}$$

The temperature equation of **VER_T** is defined by including the temperature effects of Q_{B0} and **CJE_T** as shown in the following equation.

$$\mathbf{VER\_T} = \mathrm{VER} \cdot t_N^{AQBO} \left(\frac{\mathrm{VDE}}{\mathbf{VDE\_T}} \right)^{-PE} \tag{3.106}$$

3.6.5 Current and gain temperature equations

The physical definition of IC in Equation (2.1) defines the initial value of IS. This initial value of IS included in Table 3.35 is the starting point for the IS temperature equation, **IS_T**. The temperature relationships of the diffusion coefficient, mobility, intrinsic carrier concentration and independent parameter, DAIS form the power law coefficient. The intrinsic concentration's exponential bandgap relationship to temperature is the basis for an exponential temperature term [34].

$$\mathbf{IS\_T} = \mathrm{IS} \cdot t_N^{(4-AB-AQBO+DAIS)} \exp\left[\frac{-\mathrm{VGB}}{V_{\Delta T}} \right] \tag{3.107}$$

The knee current parameter, IK, also shifts as function of temperature. The temperature equation is defined by the dependence on temperature of the diffusion coefficient, base width and zero-biased base charge and approximated to the following equation of **IK_T**.

$$\mathbf{IK\_T} = \mathrm{IK} \cdot t_N^{(1-AB)} \tag{3.108}$$

The temperature equation for the forward gain parameter, BF, is derived from the physic's definition of β_{Si} in Equation (2.3) for silicon transistors. The temperature relationship of the individual components in Equation (2.3) are summed and translated to form an intertwined temperature coefficient relationship. There is an exponential dependence on the difference of bandgap voltage between the base and emitter which requires a model parameter, DVGBF.

$$\mathbf{BF\_T} = \mathrm{BF} \cdot t_N^{(AE-AB-AQBO)} \exp\left[\frac{-\mathrm{DVGBF}}{V_{\Delta T}}\right] \tag{3.109}$$

The temperature equation of the reverse gain parameter, **BRI_T**, has an exponential dependence on the difference of bandgap voltage between base and collector, DVGBR.

$$\mathbf{BRI\_T} = \mathrm{BRI} \cdot \exp\left[\frac{-\mathrm{DVGBR}}{V_{\Delta T}}\right] \tag{3.110}$$

The temperature Equations (3.110) and (3.111) for the nonideal forward and reverse currents are a combination of physics and empirical methods [13].

$$\mathbf{IBF\_T} = \mathrm{IBF} \cdot t_N^{(6-2\cdot MLF)} \exp\left[\frac{-\mathrm{VGJ}}{V_{\Delta T} \cdot \mathrm{MLF}}\right] \tag{3.111}$$

$$\mathbf{IBR\_T} = \mathrm{IBR} \cdot t_N^2 \exp\left[\frac{-\mathrm{VGC}}{2V_{\Delta T}}\right] \tag{3.112}$$

The temperature Equations (3.112) and (3.113) adjust the substrate currents. These are also a combination of physics and empirical fitting [13].

$$\mathbf{ISS\_T} = \mathrm{ISS} \cdot t_N^{(4-AS)} \cdot \exp\left[\frac{-VGS}{V_{\Delta T}}\right] \tag{3.113}$$

$$\mathbf{IKS\_T} = \mathrm{IKS} \cdot t_N^{(1-AS)} \left(\frac{\mathbf{IS\_T}}{\mathrm{IS}}\right)\left(\frac{\mathrm{ISS}}{\mathbf{ISS\_T}}\right) \tag{3.114}$$

3.6.6 Transit time temperature equations

The background description of parameter TAUE's temperature dependence is not straightforward. The Mextram physics manual [13] has a history of past work and thoughts on TAUE's temperature relationship that is available to the reader. The temperature equation has an exponential dependence on the model parameter DVGTE. The physical definition of this parameter is $\mathrm{DVGTE} = (V_{GE} - V_{GB}) / \mathrm{MTAU} \cdot V_T$. The term $(V_{GE} - V_{GB})$ is the difference in bandgap between the emitter and base.

$$\mathbf{TAUE\_T} = \mathrm{TAUE} \cdot t_N^{(AB-2)} \cdot \exp\left[\frac{-\mathrm{DVGTE}}{\Delta V_T}\right] \tag{3.115}$$

The base transit time parameter, TAUB, is physically defined in Equation (2.7). The temperature equation, **TAUB_T**, is a power law relationship of temperature. The coefficients relationship is based on the temperature dependence of base width, diffusion constant and mobility.

$$\mathbf{TAUB\_T} = \mathrm{TAUB} \cdot t_N^{(AQBO+AB-1)} \tag{3.116}$$

The temperature equation for the epilayer transit time, **TEPI_T**, is based on a physical description that is identical to the base transit time. The values differ with the width being that of the epilayer, and the diffusion constant being of epilayer material instead of base.

$$\mathbf{TEPI\_T} = \mathrm{TEPI} \cdot t_N^{(\mathrm{AEPI}-1)} \tag{3.117}$$

The temperature equation for reverse transit time, **TAUR_T**, is defined as ratio of the total of temperature adjusted base and epilayer transit times compared to the total transit time of base and epilayer at the model reference temperature.

$$\mathbf{TAUR\_T} = \mathrm{TAUR}\frac{(\mathbf{TAUB\_T} + \mathbf{TEPI\_T})}{(\mathrm{TAUB} + \mathrm{TEPI})} \tag{3.118}$$

3.6.7 Self-heating impedance equations

The self-heating circuit in the Mextram 504.7 model was described in Section 3.5. In the self-heating model two parameters, RTH and CTH, are needed. The model parameter representing thermal impedance, RTH, is the value of thermal resistance at the model's reference temperature, TREF. The ambient temperature, $T_{Ambient}$, is also the simulation temperature, TEMP. When $T_{Ambient}$ changes from the reference temperature the value of RTH must be corrected. The model parameter temperature equation, **RTH_T**, is defined to adjust RTH as the ambient temperature changes in Equation (3.119).

$$\mathbf{RTH\_T} = \mathrm{RTH} \cdot \left(\frac{T_{Ambient}}{\mathrm{TREF}}\right)^{\mathrm{ATH}} \tag{3.119}$$

The thermal capacitance, CTH, is not defined to change with temperature in the Mextram 504.7 model.

4 Mextram model structure and modeling tools

The Mextram model equations for release 504.7 were reviewed Chapter 3. The compact model equations were implemented in the Verilog-A language [2]. This programming language is portable and supported by most analog simulators. Verilog-A capabilities and ease of use have made it the compact model language requested by the semiconductor industry. The industry's designated standardizing body, Compact Modeling Council, CMC, requires that all standardized compact models be released in Verilog-A language [36].

The structure of the Verilog-A code version of the Mextram 504.7 model is described in the following section. The 504.7 release was modified in a minimal way in order to generate the four ambient temperature model parameter sets. More extensive modifications of the parameter temperature equations were required in order to produce the single expansive temperature, SET, model of Mextram 504.7.

The model parameter fitting method and software tools used in model and parameter set development are described in Section 4.2. The modeling method utilized a commercial modeling software approach by Agilent Technologies, Inc.

4.1 Mextram 504.7 model release

Mextram 504.7 bipolar model [2] was released in the standardized language of Verilog-A. A high-level language, Verilog-A provides the capability to describe analog behavior of conservative systems and is a subset of the Verilog-AMS language developed in the 1990's. The implementation of V2.2 standards has quickly made Verilog-A the language preference in compact model development [43]. Verilog-A utilizes through and across variables, with electrical relationships defined by Kirchhoff current and voltage laws. The language is intuitive but is procedural in form, similar to the C language. Verilog-A is very attractive to model developers since derivatives are handled by the compiler. Previous model development in C languages required hand calculated derivatives which were often a source of error and limited model development.

Mextram model development and Verilog-A code release is coordinated by Delft University of Technology. Model version releases, reference documentation, and recommended parameter extractions techniques are available from the web site of Delft [2]. Mextram was created by the semiconductor division of Phillips Electronics, Inc [13], which split. The group is now the semiconductor company, NXP, Inc. Phillips placed Mextram into public domain in 1994. The modeling community has greatly benefited from the Phillips/NXP creation and Delft University's skilled continuation of model development.

The 504.7 release has several options available. The full release supports, with and without substrate terminals. It also provides each terminal version with or without the self-heating model included. Each version has a specific model card name. The SiGe HBT modeled utilizes the model card name of bjt504t, which calls the Verilog-A code for a bipolar transistor with a substrate terminal included and with the self-heating model implemented [2].

Verilog-A module, bjt504t, consists of the files [2] shown in Table 4.1. A cryogenic version for the ambient temperature models was created from the Mextram 504.7 code by modifying the existing code and recompiling it as the model, bjt504t. A single expansion temperature, SET, model was created from the cryogenic ambient temperature Mextram code by modifying the parameter temperature equations. This model is defined as bjt504tcryo. A detailed summary of the modifications and file structure used in the cryogenic ambient temperature Mextram code and the SET Mextram code are listed in the Appendix.

Filename	Contribution	Description
bjt504t.va	Module	Purpose: Full definition of Mextram model Action: Define module and ports then loads the following files that define the parameters and analog block section (module for Mextram model)
frontdefine.inc	Model constants	Purpose: Limiting Functions Action: Assigns values to model constants in Mextram equations (part of analog block)
parameters.inc	Model parameters	Purpose: Value passed into the model equations from the circuit Action: Declaration of data type and range defined (requirement of module)
variables.inc	Internal variables	Purpose: Define variables for internal equations of model Action: Declaration of data type, (part of analog block)
tscaling.inc	Parameter temperature equations	Purpose: Model parameter values shifted by changes in temperature Action: Equations to be calculated, (part of analog block)
evaluate.inc	Mextram model equations	Purpose: Defines all components of Mextram model Action: Equations defining all parts Mextram (analog block)

Table 4.1 Verilog-A model file summary for Mextram 504.7 [2]

4.2 Modeling software environment

The modeling environment is the software tools and methods which the modeler uses to produce model parameter values that best represent the device electrical behavior. The final value of each parameter in the model set is obtained when the modeler has a “good fit”, which means there is minimum error between the simulated model data and the measured device data.

The software environment chosen for this work was IC-CAP, a commercial software system by Agilent Technologies, Inc. [44]. IC-CAP, Integrated Circuit Characterization and Analysis

Program, has the complete set of capabilities needed for modeling: data acquisition, database control, analysis, optimizers, model extraction modules, commercial simulator interfaces, and internal custom programming. For this work, the data acquisition was done outside of IC-CAP and manually loaded into IC-CAP custom defined setups. All analysis and optimization was done within IC-CAP. The standard modeling approach of a released standardized model in the IC-CAP environment is shown in Figure 4.1.

Model simulated data, both DC and AC, are generated by Agilent's commercial analog/RF simulator ADS, Advanced Design System [45]. ADS interfaces directly with IC-CAP. The standard Mextram 504.7 release model is already compiled and available to ADS.

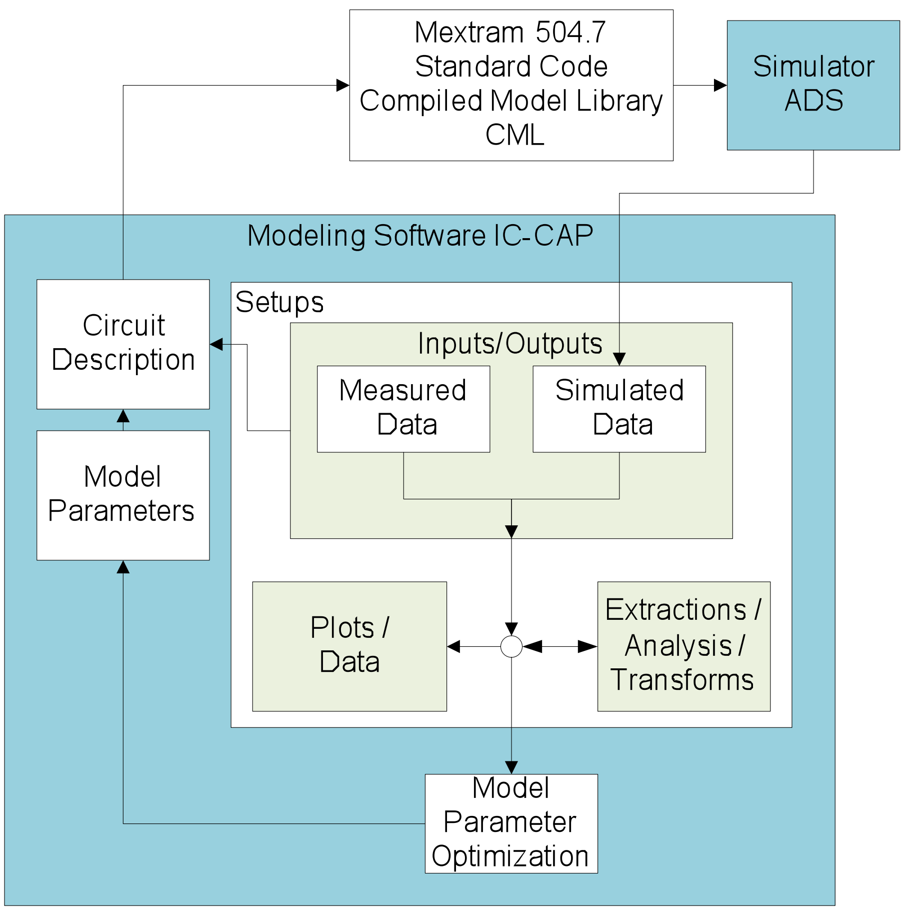

Figure 4.1 Standard IC-CAP software modeling environment

IC-CAP has a Mextram extraction module that closely follows the parameter extraction procedures of the Phillips [35] and Delft extraction manual [2]. This parameter extraction approach relies on process information and unique parameters dominating specific operating regions. The process information is used to calculate parameter value using design equations such as those discussed in Chapter 2. The remaining parameters are extracted with simple equations and numerical techniques in the operating regions where those parameters are known to dominate the model equations. This approach of minimal parameter optimization is often thought to create a more realistic, physically base model parameter set.

However, several conditions were not typical. The cryogenic modeling process information was limited. In a particular operating region, standard extractions are easily solved by a single dominant parameter. Unfortunately, the operating regions in cryogenic data environment do not allow single parameters to dominate. Instead, multiple parameters must be optimized. The inclusion of SiGe effects alters the typical silicon extraction relationships of parameters. These unique conditions required a custom approach that relied on optimization and not the packaged extraction module. The cryogenic modeling approach is shown in Figure 4.2. This approach required manual control of most steps in the process shown in Figure 4.2.

Essential to this cryogenic approach was the ability to quickly modify the Mextram Verilog-A code to output internal model equation calculations or branch component simulated data. This internal model data was automatically loaded with all other simulation data into IC-CAP. The parameter influence on internal currents, voltages and model calculations could then be determined. This influence assisted in defining the grouping of parameters in optimizations as well as defining parameter influence in different operating regions. Then parameters could be optimized to internal component data as well as output terminal current and voltages.

Additionally, the Mextram Verilog-A code was modified for both the ambient modeling and the SET model development. The Verilog-A code was compiled by the Tiburon compiler that is part of the IC-CAP and ADS software environment [44]. The circuit section of IC-CAP will automatically direct the model Verilog-A code to the compiler if a compiled version is not present in the compiled model library, CML, cache directory. The ADS simulator looks in the CML directories and executes the compiled model file.

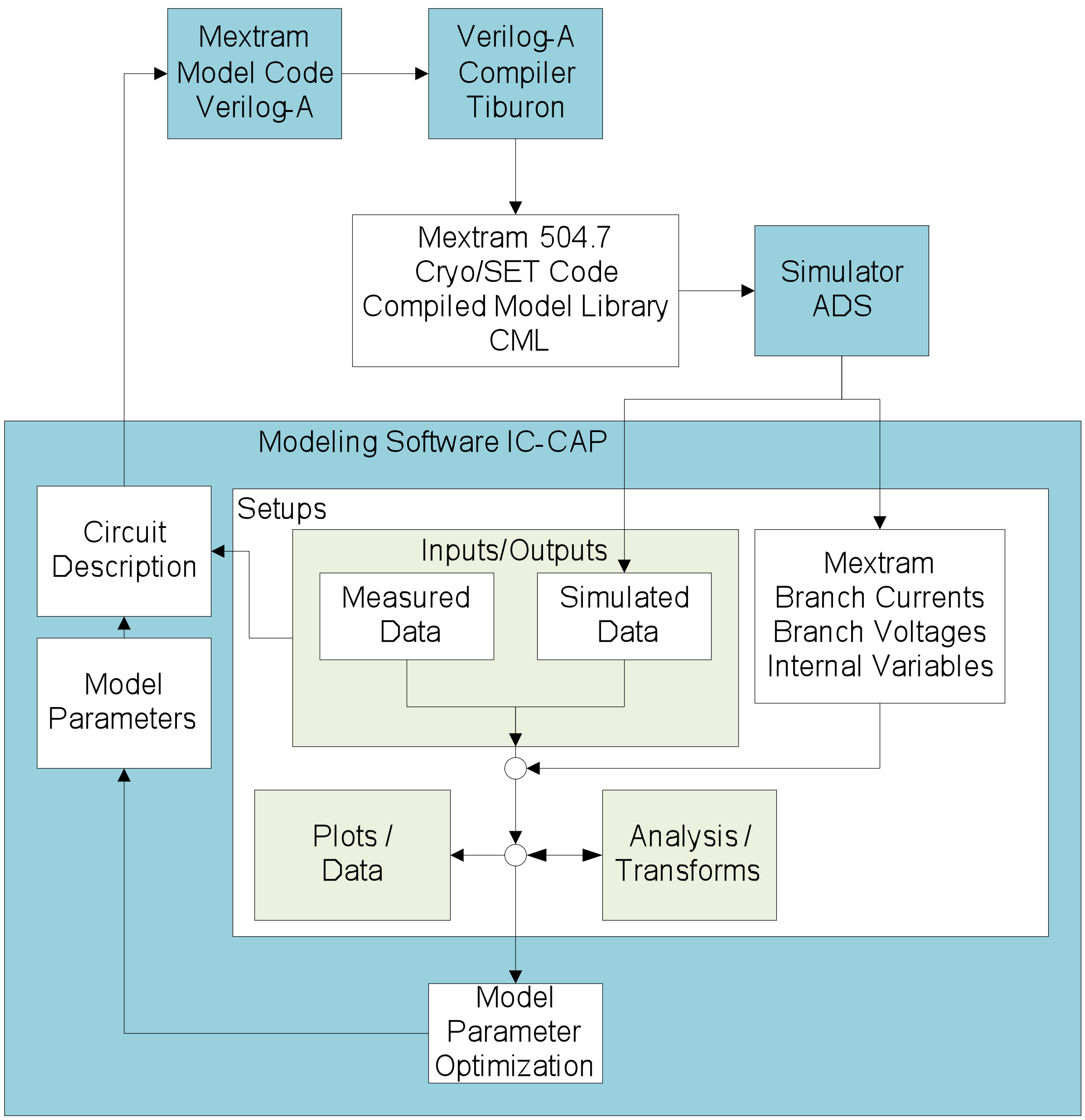

Figure 4.2 Custom cryogenic modeling software environment

5 Device structure and measurement data

This chapter presents the regions of the device structure, the process information and the measured performance of the SiGe HBT modeled. Process information is utilized to define model parameter values. Model parameters are also directly extracted from measured data. A preliminary set of model parameters can be formed from the combination of device information and initial parameter extractions.

Industry standardized bipolar transistor compact models requires an understanding of device structure and process capability. The models are a combination of device physics and empirical fitting. Sections of the model can be activated or weighted to represent parasitic or extrinsic regions of a device. Therefore, identification of the electrical regions and the amount of contribution is critical to creating a model and evaluating parameters. Proper region identification was found to be critical to model development in an extremely low temperature environment and across a wide temperature range.

Both the device characteristics and measured performance are used to extract model parameters. However, for this work it was found that basic extractions were inadequate and parameter optimization, by fitting the measured data to simulated SPICE data, was required. Various configurations of DC measurements and S-parameter measurements were needed for extraction and fitting. Each type of measurement was taken at a specific ambient temperature. The measurements are summarized by measurement type and ambient temperature in the following chapter.

5.1 Device structure

Advanced high frequency bipolar devices fabricated in BiCMOS technology are built by adding a minimum number of compatible process steps to a standard RF CMOS process flow.

The classic silicon bipolar fabrication approach of ion-implantation and annealing is not compatible with RF CMOS processing flows due to the high temperatures required during anneal. Also, implant/anneal techniques cannot provide the control needed for extremely thin, highly doped intrinsic base layers. Higher frequency bipolar devices require epitaxial growth and in-situ doping methods. Epitaxy growth and doping techniques by low temperature methods, at around 500 ^{o}C, make it possible for SiGe HBT's and CMOS to be compatible in a single technology [21],[19]. The full process cross-section of the SiGe HBT modeled includes: first level aluminum metallization, tungsten (W) interconnect plugs and P^{+} substrate access is shown in Figure 5.1.

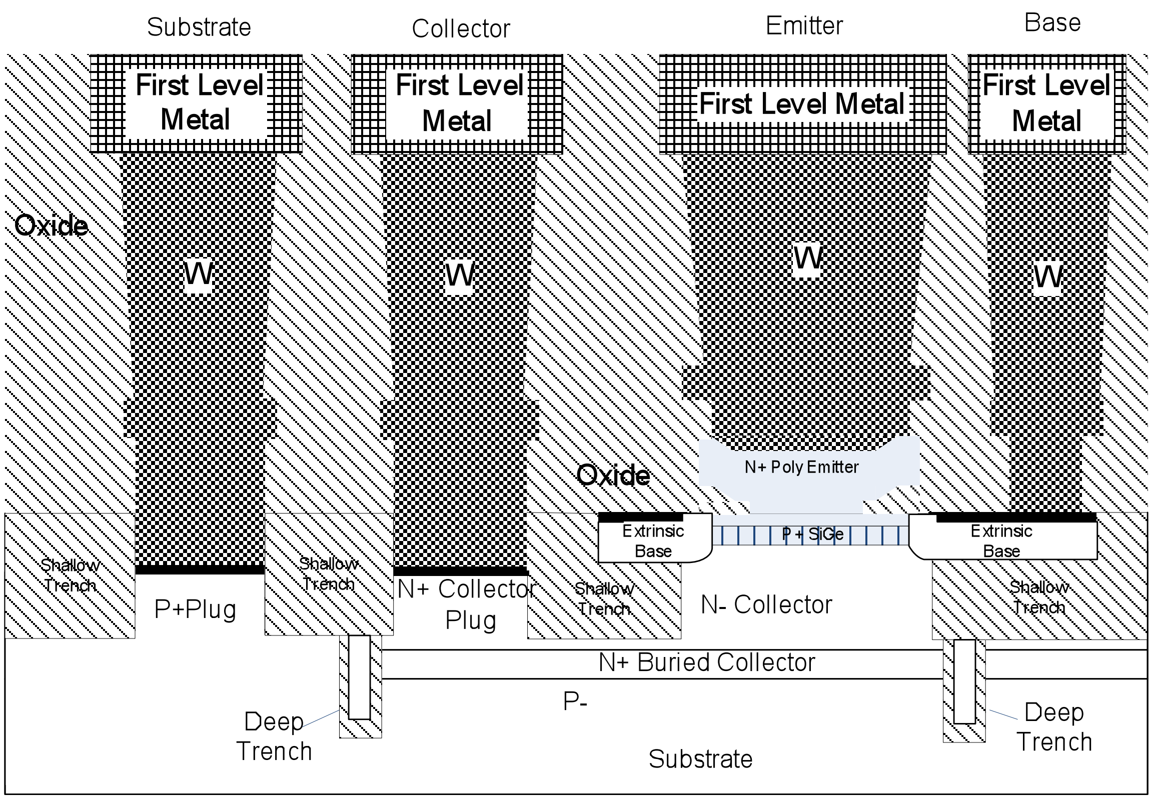

Figure 5.1 Cross-section indicating P^{-} substrate surface contact and deep trench device isolation[25],[9].

Device-to-device isolation is obtained by a deep trench surrounding the transistor. The poly filled deep trench go beyond the depth of the N^{+} buried collector and terminates well into the P^{-}

substrate. Thus the device is sidewalled isolated and junction isolated on the bottom. Surface contact to the P^- substrate is made by a deep P^+ plug implant, as shown in the full transistor cross-section of Figure 5.1. The high temperature P^+ implant and annealing process steps occur prior to the lower temperature process steps in the fabrication flow [28]. The P^+ access to the substrate layer is not included in the standard layout of the transistor. The designer has complete freedom to place a P^- substrate contact any distance from the device structure [7]. Therefore, the model development of the SiGe HBT for the P^- substrate stops at the P^- layer within the material.

The SiGe HBT has a minimum feature size, polysilicon doped emitter of 0.5µm x 2.5µm [7]. The electrical regions are overlaid onto a cross-section of the intrinsic transistor in Figure 5.2. The heavy doping ability of polysilicon type emitters reduces emitter resistance. Surface contact to the intrinsic base is through the extrinsic P^+ polysilicon base region extending from the intrinsic base on all four sides, thereby reducing the base resistance. The 4-sided P^+ polysilicon extrinsic base region has a complete silicided contact that is accessed by metallization on one side of the emitter. The extrinsic base region sets above shallow trench isolation thereby, reducing base-collector capacitance.

In general, high frequency response bipolar devices must have a heavily doped, thin, intrinsic base width and a lightly doped collector width. Epitaxial growth techniques provide precise control of layer thickness and heavy doping ability.

The active areas of the SiGe HBT are formed by in situ doped epitaxial growth methods. The doping profile [21] of the modeled SiGe HBT in Figure 5.3 indicates the intrinsic layer thicknesses and charge concentrations of the device structure. The process information of the modeled SiGe HBT cross-section drawn above has been summarized in Table 5.1.

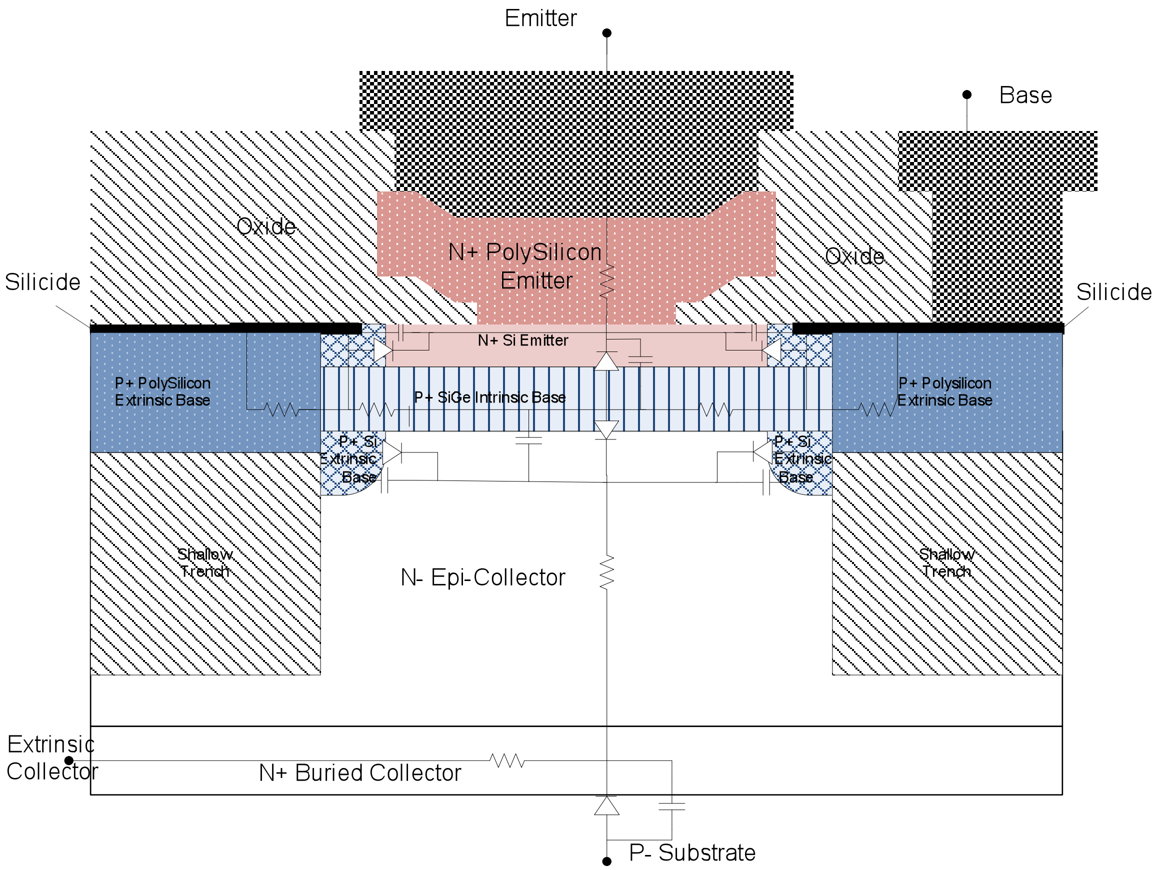

Figure 5.2 SiGe HBT intrinsic transistor cross-section. Electrical regions indicated. 0.5µm x 2.5µm emitter SiGe HBT

Active Region	Width (nm)	Dopant, Concentration (cm^{-3})	Bandgap Difference
Emitter Epi-layer	W_E = 40	As N_{dE} = $5 \cdot 10^{20}$ to $1.5 \cdot 10^{19}$	
Intrinsic Base Epi-layer	W_B = 80	B^+ N_{aB} = $5 \cdot 10^{18}$	$\Delta E_{g,Ge(grade)}$=37.5meV Trapezoidal Ge% profile 8% to 3%
Epi-Layer Collector	W_{epi} =380	P^- N_{epi} = $4 \cdot 10^{16}$ to $2 \cdot 10^{17}$	
Buried Layer Collector	W_{buried} =150	As N_{buried} = 10^{18} to $2 \cdot 10^{19}$	

Table 5.1 Intrinsic region widths and dopant concentrations of modeled SiGe HBT [21]

The difference between the SiGe HBT and silicon high frequency bipolar structure occurs in the very thin epitaxial base region. The SiGe HBT is a SiGe alloy and not silicon. The SiGe HBT's epi-base layer is grown on top of the thicker Si lightly doped collector epitaxial layer of approximately 400nm.

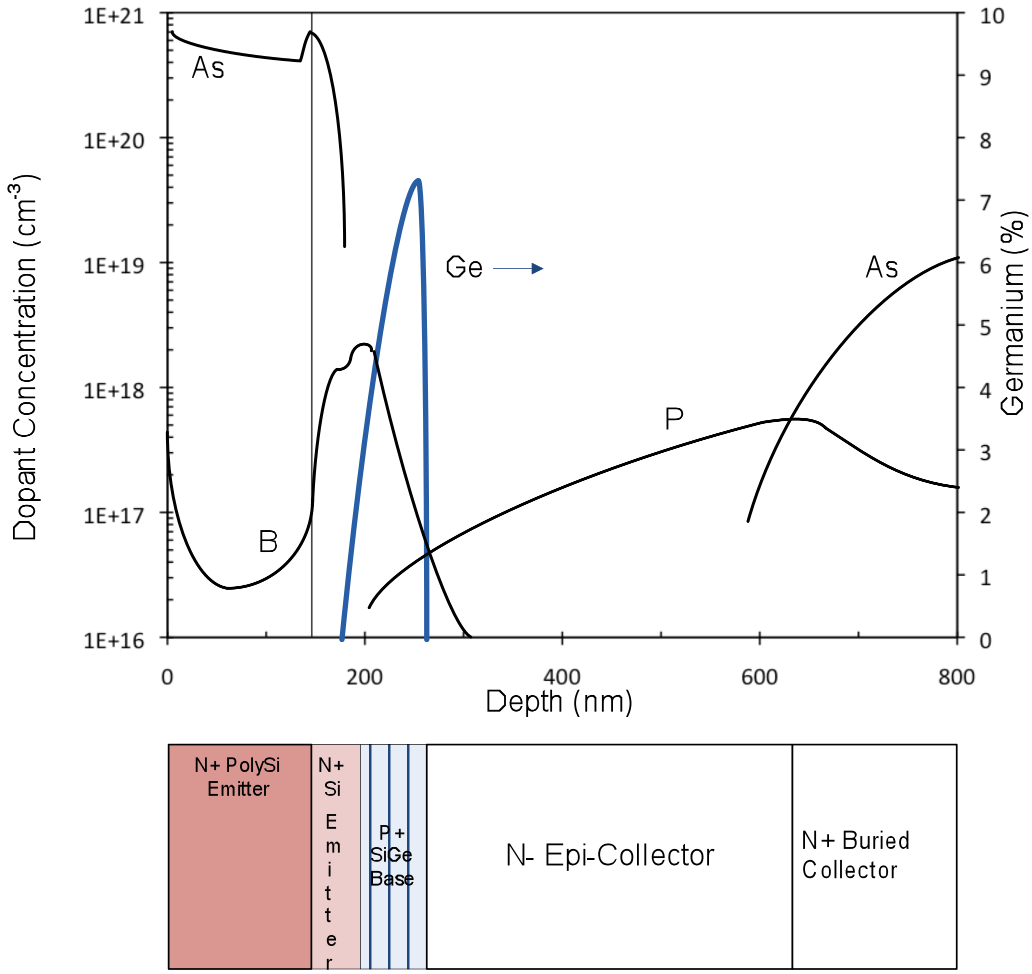

Figure 5.3 Intrinsic HBT impurity profile vs. depth with the Ge% trapezoid profile within the base region indicated [21]. Note: Ge% is defined on a linear scale by the right-side vertical axis. The dotted line indicates the interface between the polysilicon emitter and Si epitaxial emitter region.

At the interface of the N^- epi-layer collector and P^+ base epi-layer, a high concentration of germanium (Ge%) is introduced. The Ge% is then linearly reduced as the base epi-layer is grown with a high P^+ doping concentration. The inclusion of a Ge% concentration is abruptly stopped at the P^+ base interface to the N^+ emitter epilayer, thereby forming a trapezoidal Ge% profile in the intrinsic base. The trapezoidal Ge% profile of the modeled SiGe HBT is included in the doping profile [21] of Figure 5.3. This profile is from the classic Meyerson & Harame paper [21] which describes the Ge% profile gradient ranging from 8% to 3% across the base. A bandgap difference, $\Delta E_{g,Ge(grade)}$, of approximately 37.5 meV would be expected by applying the graded Ge% concentration base analysis of section 2.3 and the design figure of merit that 10% Ge concentration produces a bandgap difference of 75 meV [21]. The SiGe base epi-layer is grown to a precise depth for two reasons. First, an exact trapezoidal shaped Ge% profile is required across the intrinsic base layer. Second, the stress increases as the SiGe layer thickness increases. The SiGe epitaxial base is being compressed as it is grown onto the Si epitaxial collector layer. However, very thin epilayers are able to maintain the stress stability of the pseudomorphic growth of a SiGe alloy layer. The modeled process has a SiGe alloy layer of approximately 80nm in depth.

The SiGe alloy layer requires a very thin Si buffer layer be grown on top. The buffer layer maintains the strained lattice structure of the alloy. This thin epilayer also becomes the emitter region. A polysilicon emitter is formed on the thin Si emitter buffer layer. The Si buffer emitter layer receives a high N^+ doping concentration during the poly-emitter implant. The Si emitter layer is approximately 40nm thick.

The Mextram model makes use of the device regions and processing information for model topology and initial parameter values. Doping concentrations correspond to mobility which is used to determine temperature coefficient parameters. The epilayer parameters are initially calculated from the N^- epi-collector doping and thickness.

5.2 Measurements

The ambient, “at temperature,” models and the single expansive temperature, SET, model were obtained from the DC and AC measurements. The following sections present this data and the initial characterization information relevant to each measurement The modeling measurements were taken at four ambient temperatures: 300K, 223K, 162K and 93K.

All measurements were taken in support of the SiGe project for NASA, Exploration Technology Development Program (ETDP) [46], through grant NNL06AA29C. The principal investigator was Dr. John D. Cressler of Georgia Institute Technology, and the project was titled, "Silicon-Germanium Integrated Electronics for Extreme Environments," [47]. All measurements were taken at the Georgia Tech research lab. Dr. Cressler's research group took all measurements using a cryostat and a cryogenic temperature on-wafer probe station.

5.2.1 Measurement environment

Measurements in the cryogenic temperature range are extremely difficult. DC and low frequency measurements have been possible for some time by using cryogenic temperature chambers, cryostats. However, on-wafer high frequency S-parameter measurements at cryogenic temperatures are a very recent development.

Any minor differences between the DC and AC measurements were due to variations in the IBM5AM process. It was not possible for the DC measurements and AC measurements to be taken from the same chip material or modeling test structure layout. The DC measurements of the HBT were taken in a cryostat by Georgia Tech. A chip was mounted and bonded in a ceramic package for all DC measurements taken in the cryostat. A DC specific layout of the SiGe device on the testchip was used for all DC measurements. In the layout, the base, emitter, and collector terminals of the device were brought out to separate bondpads and the substrate terminal was shared with other bipolar devices in the DC module. The AC measurements were taken on a different chip using an on-wafer custom probe station at Georgia Tech. The probe station is designed with cryogenic temperature capability. The on-wafer measurements were taken by probe contact to the device on a chip. High frequency, RF, 50 Ω ground-signal-ground, G-S-G, probes contacted the bondpads of the S-parameter device modeling structure layout. The

S-parameter layout was a standard two-port RF probe G-S-G pad configuration connecting the base and collector to signal pads and the emitter connected to ground pads, thereby establishing a common-emitter configuration. The emitter and substrate surface contact are connected by metallization to reduce substrate noise.

5.2.2 DC output measurements

The output characteristics measurement captures an HBT's DC behavior in the forward operating regions. The output voltage is swept from 0V to the model's upper voltage limit while applying a constant stimulus to the base terminal. The collector current, IC, is measured as a function of the collector-emitter voltage, VCE. A family of IC versus VCE curves is measured by repeating the VCE sweep for several base stimulus values. The output sweep takes the HBT from the saturation region to the forward linear operating region. The base stimulus keeps the base-emitter junction forward biased, while the output sweep takes the base-collector junction from forward biased to reverse biased.

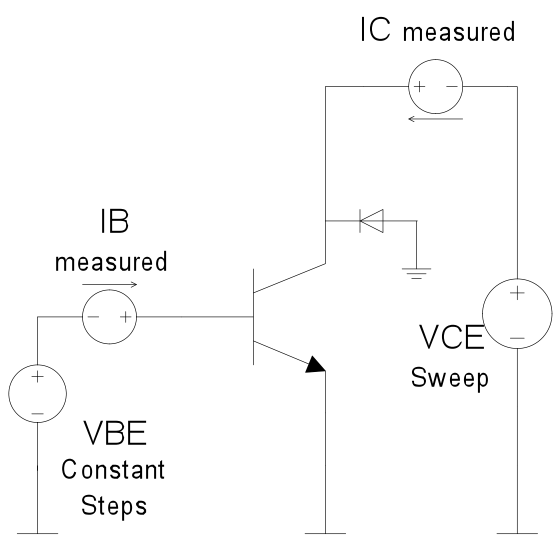

Figure 5.4 Output measurement setup, constant base-emitter voltage bias steps

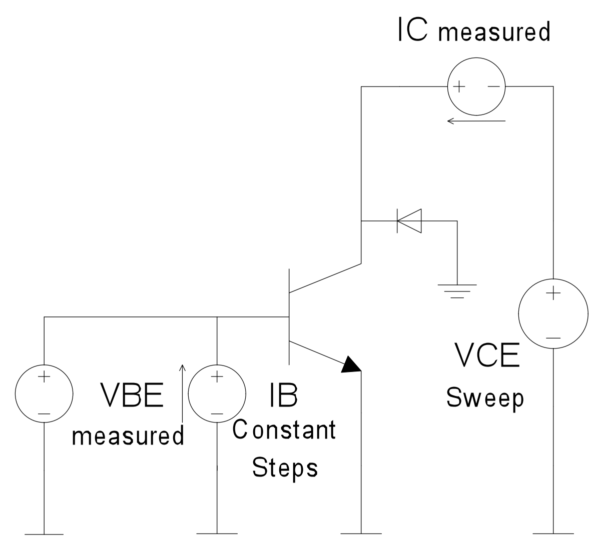

Figure 5.5 Output measurement setup, constant base current steps

The output characteristics were measured by two different constant base stimulus setups at each ambient temperature. The base bias values for each measurement were selected to produce equivalent output curves of IC versus VCE across the temperature range. One output measurement in Figure 5.4 was biased with a constant base-emitter voltage setup. The second output measurement setup in Figure 5.5 was biased with a constant base current.

When the two base bias setups have very similar output IC curves, self-heating is not present. Comparison of the two base bias stimulus types finds significant self-heating at each of the four ambient temperatures in Sections 5.2.2.1 through 5.2.2.4. The base voltage bias stimulus measurements clearly indicate device heating as collector current flow increases. Therefore, modeling the self-heating contribution is an essential step that must be accurate before transistor model parameter values are defined.

The output characteristics of primary influence: forward Early voltage, saturation region collector resistance and self-heating are summarized in each of the following ambient temperature data sections of output data. The constant base current biased output measurements were used for Mextram model parameter optimization at each ambient temperature as described in Chapters 6 and 7.

Forward Early Voltage. The output characteristic of forward Early voltage, VA, describes the change in basewidth as a function of changing base-collector voltage. Measured Early voltage was calculated from output conductance, g_0, or linear region slope of IC versus VCE[10].

$$g_0 = \frac{d\,IC}{d\,VCE}\bigg|_{VBE=constant} = \frac{IC}{VA} \tag{5.1}$$

The measured Early voltage is included for both base bias setups. However, the constant base voltage bias is extremely influenced by self-heating effects and of limited use in defining model parameters. The constant base current biased output measurements were used in developing model parameter values. The measured forward Early voltage decreased significantly as the base bias increased. Therefore the model parameter VEF, effective forward Early voltage, is not the singularly dominate parameter in the linear region of the output characteristics. The optimization approach and results are discussed in Chapters 6, 7..

Collector resistance in saturation region. The collector resistance in the saturated region, R_{Csat}, was described in Section 2.2. The resistance is equal to the inverse of the slope of an IC curve in saturation [10] . An average R_{Csat} was extracted from the IC versus VCE curves for each ambient temperature.

Self-heating. Self heating was a dominating behavior in the modeled device at an ambient temperature of 300K. The amount self-heating influence decreased as the ambient temperature decreased but remained a non-negligible effect. The actual device temperature is the sum of the ambient temperature and the self-heating contribution. The VBE versus VCE measurements of the constant base current bias configuration are included for each ambient temperature. By measuring ΔVBE, the change in base-emitter voltage, as VCE is swept through the linear operating range the self-heating model parameters can be extracted [35]. Since the self-heating effects are overwhelming for a large percent of the operating bias range, they must be extracted before the mid-current and high-current parameters are extracted and optimized. The self-heating model in Section 3.5 was used [13]. The impact and modeling approach of self-heating is presented in the following chapter.

5.2.2.1 Output characteristics measurements, 300K ambient temperature

For an ambient temperature environment of 300K, the output measurements of IC versus VCE biased with a constant base emitter voltage and a constant base current are shown in Figure 5.6 and 5.7, respectively. The dramatic differences in IC behavior between the two types of base bias are due to self-heating effects. For each measurement there is a corresponding table summarizing: measured Early voltage, the defined linear operating region and collector current, IC, at VCE=1.8V. The average value of saturated collector

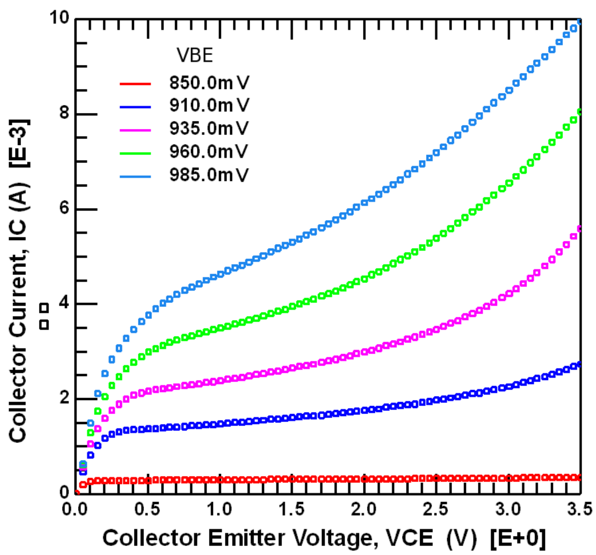

Figure 5.6 Output measurement IC vs. VCE Constant base voltage bias, VBE steps. Ambient temperature, 300K

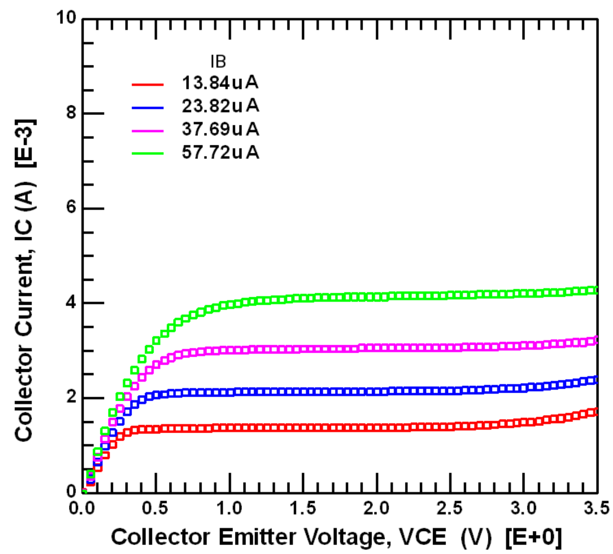

Figure 5.7 Output measurement IC vs. VCE Constant base current bias, IB steps. Ambient temperature, 300K

Base Bias	Voltage Range of Linear Region			VCE 1.8V
VBE V	Lower V	Upper V	Early Voltage	IC mA
0.850	0.15	3.50	16.5V	0.29
0.910	0.35	3.00	5.4V	1.72
0.935	0.45	2.80	4.1V	2.87
0.960	0.70	2.40	1.8V	4.27
0.985	1.10	2.10	1.8V	5.70

Table 5.2 Ambient temperature, 300K. VBE, base bias output characteristics

Base Bias	Voltage Range of Linear Region			VCE 1.8V
IB µA	Lower V	Upper V	Early Voltage	IC mA
13.8	0.35	2.80	135V	1.36
23.8	0.50	2.90	126V	2.13
37.7	0.70	3.00	120V	3.04
57.7	1.10	3.10	86V	4.12

Table 5.3 Ambient temperature, 300K. IB base bias output characteristics

Saturated Collector Resistance

At 300K:	Constant VBE	Constant IB
R_{Csat}	93.5 ohms	146 ohms

Table 5.4 R_{Csat} of output measurements for each bias configuration. Ambient temperature, 300K

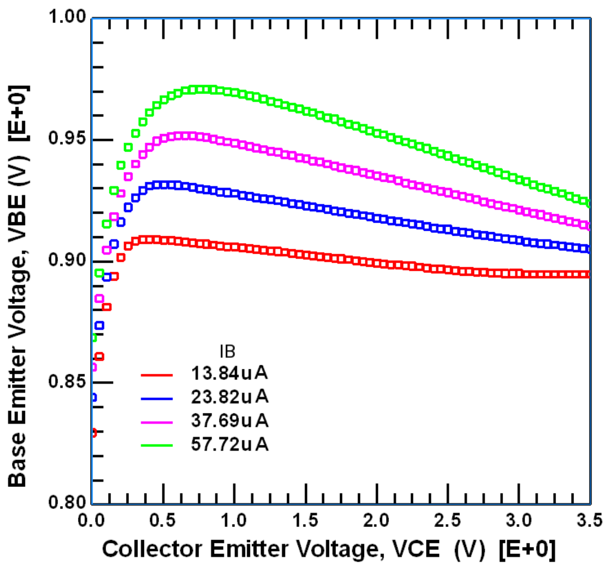

Base Bias	Voltage Range of Linear Region		
IB µA	Lower V	Upper V	ΔVBE
13.8	0.35	2.80	13.8mV
23.8	0.50	2.90	22.2mV
37.7	0.70	3.00	30.5mV
57.7	1.10	3.10	36.4mV

Figure 5.8 Output measurement of VBE vs. VCE for constant IB bias of Figure 5.7. Ambient temperature, 300K. ΔVBE, base-emitter voltage change, due to device self-heating indicated.

resistance for each measurement type is included in an additional table. Measurement of VBE versus VCE, shown in Figure 5.8, indicates how the external base-emitter voltage responds to self-heating when biased with a constant base current.

At the ambient temperature, 300K, the device's operating bias range produces a change in VBE, ΔVBE, of greater than 30mV. The self-heating effects are so significant that their effect must be accounted for before extracting model parameters. The measured Early voltage decreases by approximately 50V in the bias range to be modeled. This indicates that the linear region of the output characteristics is influenced by more than basewidth modulation of the base-collector junction voltage. The knee of the IC curve is soft requiring quasi-saturation modeling.

5.2.2.2 Output characteristics measurements, 223K ambient temperature

The output measurements, IC versus VCE in an environment of 223K, ambient temperature are summarized in the following section. Measurement with a constant base voltage bias configuation is shown in Figure 5.9. Measurement with a constant base current bias configuration is shown in Figure 5.10. Each measurement has a corresponding summary table of output characteristics. The average value of saturated collector resistance, for each. base bias configuration is listed in Table 5.7. Measurement of VBE versus VCE in the

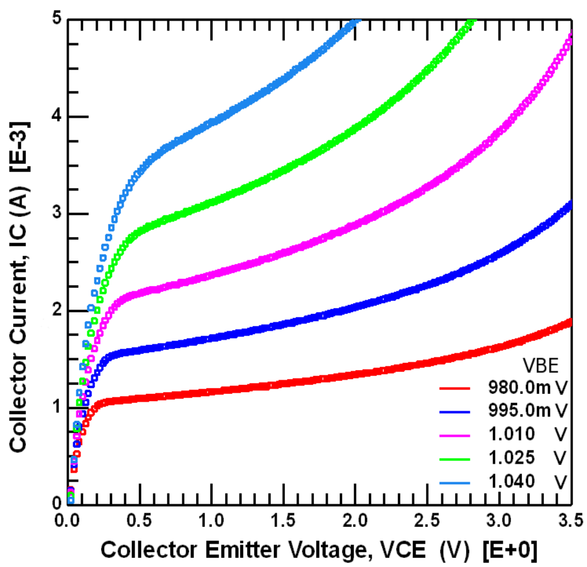

Figure 5.9 Output Measurement IC vs. VCE Base bias of constant VBE steps. Ambient temperature, 223K

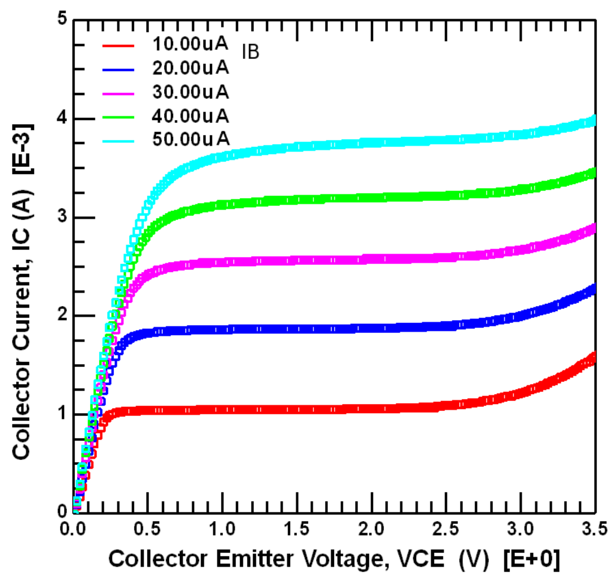

Figure 5.10 Output Measurement IC vs. VCE. Base bias of constant IB steps. Ambient temperature, 223K

Base Bias	Voltage Range of Linear Region			VCE 1.8V
VBE V	Lower V	Upper V	Early Voltage	IC mA
0.980	0.40	2.0	6.4V	1.29
0.995	0.40	1.8	5.4V	1.96
1.010	0.40	1.6	5.0V	2.76
1.025	0.50	1.6	4.0V	3.69
1.040	0.60	1.5	3.6V	4.73

Table 5.5 Ambient temperature, 223K. IB base bias output characteristics

Base Bias	Voltage Range of Linear Region			VCE 1.8V
IB µA	Lower V	Upper V	Early Voltage	IC mA
10	0.50	2.0	150V	1.04
20	0.74	2.2	133V	1.86
30	1.20	2.4	146V	2.57
40	1.40	2.6	86V	3.19
50	1.70	2.7	54V	3.74

Table 5.6 Ambient temperature, 223K VBE base bias output characteristics

Saturated Collector Resistance

At 223K:	Constant VBE	Constant IB
R_{Csat}	76 ohms	140 ohms

Table 5.7 R_{Csat} of output measurements for each base bias configuration. Ambient temperature, 223K

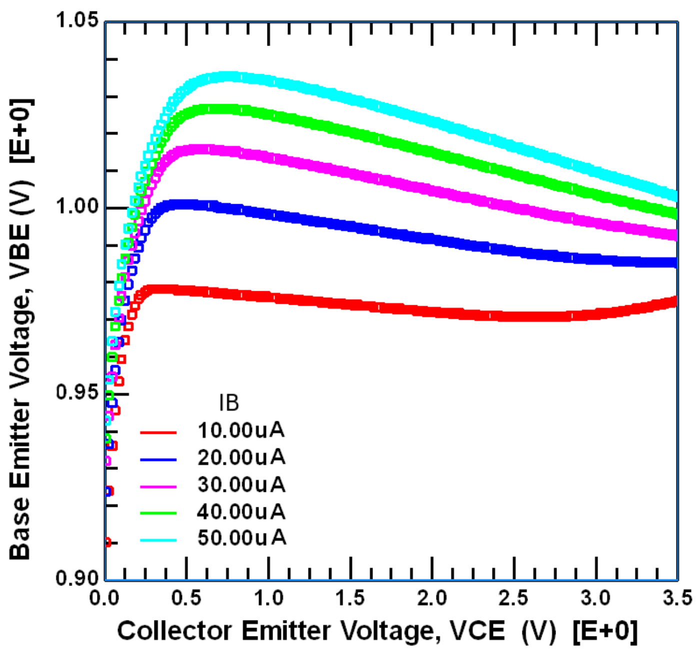

Base Bias	Voltage Range of Linear Region		
IB µA	Lower V	Upper V	ΔVBE
10	0.50	2.0	5.7mV
20	0.74	2.2	9.7mV
30	1.20	2.4	11.0mV
40	1.40	2.6	13.0mV
50	1.70	2.7	13.0mV

Figure 5.11 Output Measurement of VBE vs. VCE for constant IB bias of Figure 5.10. Ambient temperature, 223K. ΔVBE, base-emitter voltage change, due to device self-heating indicated.

constant base current bias configuration is shown in Figure 5.11. The change in external base-emitter voltage, ΔVBE, across the linear active region is shown in Figure 5.11

At the ambient temperature, 223K, the amount of change in VBE, ΔVBE, that occurred across the bias operating range decreased when compared to the 300K ambient temperature. At 223K, ΔVBE ranged less than 10mV compared to 300K ambient temperature change of more than 30mV. This indicates that the self-heating effects decrease as temperature decreases. All modeling will need to include the change in self-heating as a function of temperature. The measured Early voltage decreases by approximately 100V over the operating range, indicating additional influences that were not present at 300K. The saturated collector resistance is not changing drastically as temperature decreases.

5.2.2.3 Output characteristic measurements, 162K ambient temperature

Output measurements in a 162K ambient temperature environment are summarized in the following section. Measurement of IC versus VCE for a constant base voltage bias configuration is in Figure 5.12 and the corresponding output characteristics are summarized in

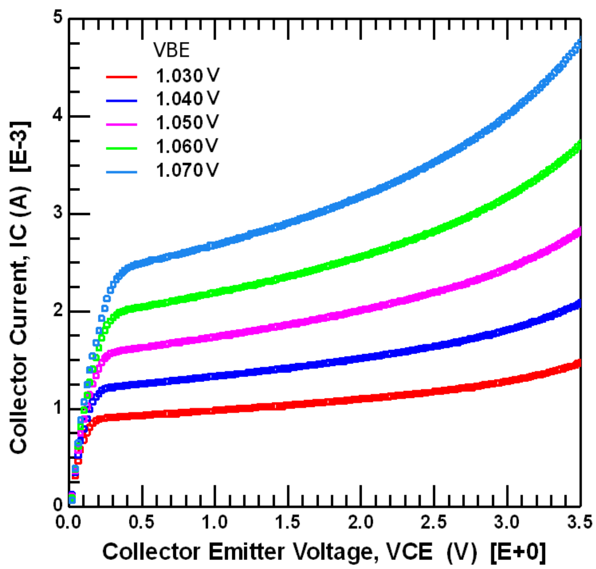

Figure 5.12 Output Measurement IC vs. VCE Base bias of constant VBE steps. Ambient temperature, 162K

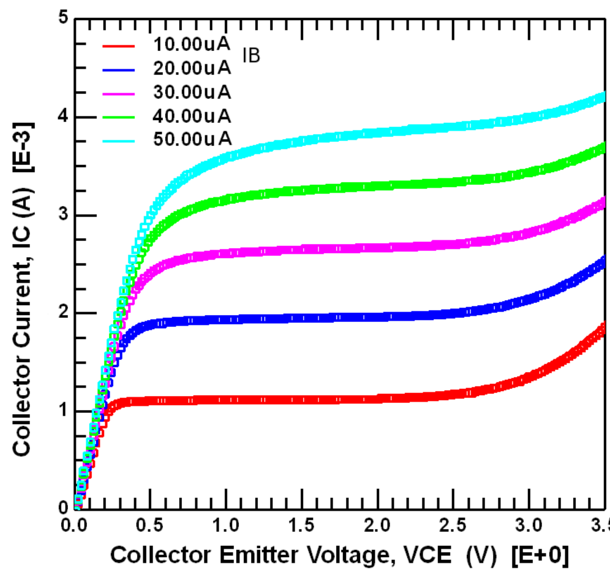

Figure 5.13 Output Measurement IC vs. VCE Base bias of constant IB steps. Ambient temperature, 162K

Base Bias	Voltage Range of Linear Region			VCE 1.8V
VBE V	Lower V	Upper V	Early Voltage	IC mA
1.030	0.20	2.2	8.3V	1.07
1.040	0.30	2.0	7.1V	1.47
1.050	0.30	1.9	6.3V	1.94
1.060	0.40	1.8	5.6V	2.49
1.070	0.50	1.8	5.5V	3.06

Table 5.8 Ambient temperature, 162K. VBE base bias output characteristics

Base Bias	Voltage Range of Linear Region			VCE 1.8V
IB µA	Lower V	Upper V	Early Voltage	IC mA
10	0.60	2.0	106V	1.11
20	0.90	2.2	88V	1.95
30	1.30	2.6	60V	2.66
40	1.50	2.6	46V	3.28
50	1.80	2.8	31V	3.81

Table 5.9 Ambient temperature, 162K. IB base bias output characteristics

Table 5.8. Measurement of IC versus VCE for the constant base current bias configuration is in Figure 5.13 and the characteristics are summarized in Table 5.9. The average value of saturated collector resistance, for each base bias configuration is listed in Table 5.10. VBE versus VCE measured during the constant base current stimulus is shown in Figure 5.14, as is a summary of the change in VBE, ΔVBE, across the linear active region.

Saturated Collector Resistance

At 162K:	Constant VBE	Constant IB
R_{Csat}	87 ohms	150 ohms

Table 5.10 R_{Csat} of output measurements for each base bias configuration. Ambient temperature 162K

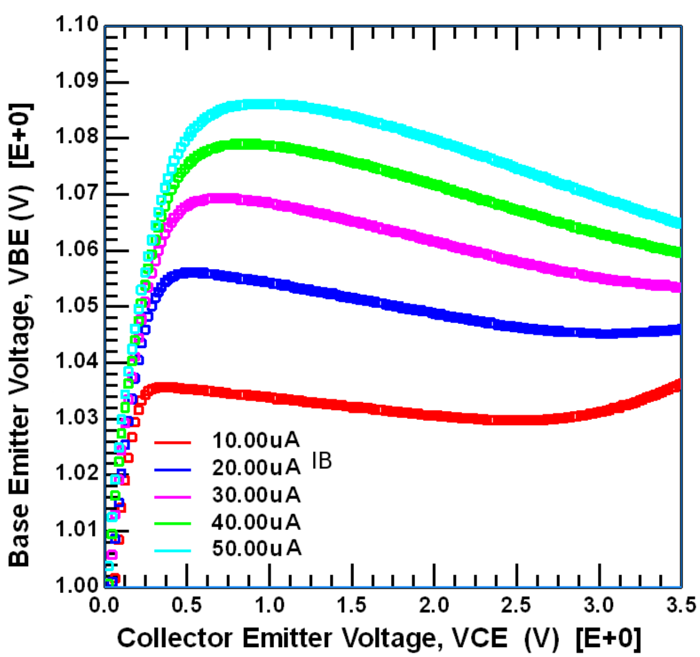

Base Bias	Voltage Range of Linear Region		
IB µA	Lower V	Upper V	ΔVBE
10	0.60	2.0	5mV
20	0.90	2.2	7mV
30	1.30	2.6	10mV
40	1.50	2.6	10mV
50	1.80	2.8	11mV

Figure 5.14 Output Measurement VBE vs. VCE. Base biased with constant IB steps. Ambient temperature, 162K. ΔVBE, base-emitter voltage change, due to device self-heating indicated.

The change in VBE, ΔVBE, across the device operating bias range is slightly less than the ambient temperature of 223K. The measured Early voltage values are decreasing as the temperature decreases. The change in Early voltage as a function of base bias is approximately

70V. The VCE voltage range of the linear operating region is decreasing as temperature decreases. The VCE range of the quasi-saturation operating region is increasing as the ambient temperature decreases. The saturated collector resistance was approximately the same value in an ambient temperature of 162K as the R_{Csat} value measured at 300K ambient.

5.2.2.4 Output characteristic measurements, 93K ambient temperature

93K ambient temperature environment, output measurements are summarized in the following section for the two base bias configurations. Measurement of IC versus VCE for a constant base voltage bias configuration is shown in Figure 5.15. The constant base-emitter voltage measurement was not used in analysis or modeling due to abnormal behavior in the quasi-saturation and the beginning of the linear region. The IC behavior was probably due to DC oscillation at VBE step range. Oscillation behavior is common in DC measurements of high f_T, bipolar devices due to the measurement impedance mismatch between the input voltage source and the input of the base-emitter junction of the device [48]. The IC versus VCE measurement for the constant base current bias configuration is shown in Figure 5.16. The constant base current bias stimulus measurements were typical and showed no signs of oscillations.

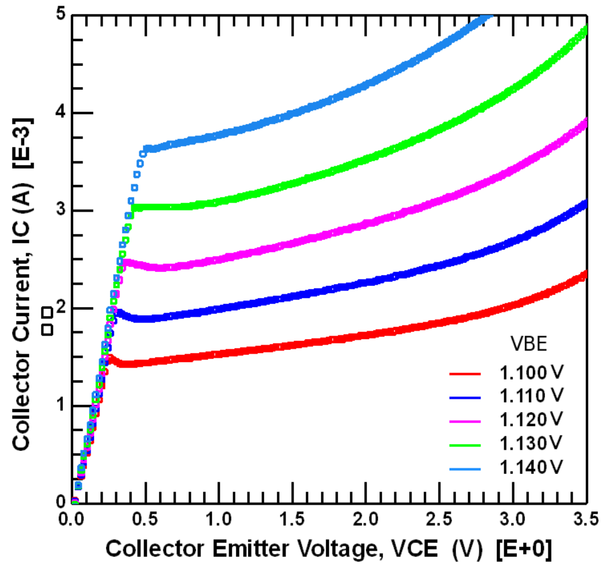

Figure 5.15 Output Measurement IC vs. VCE. Base bias of constant VBE steps. Ambient temperature 93K

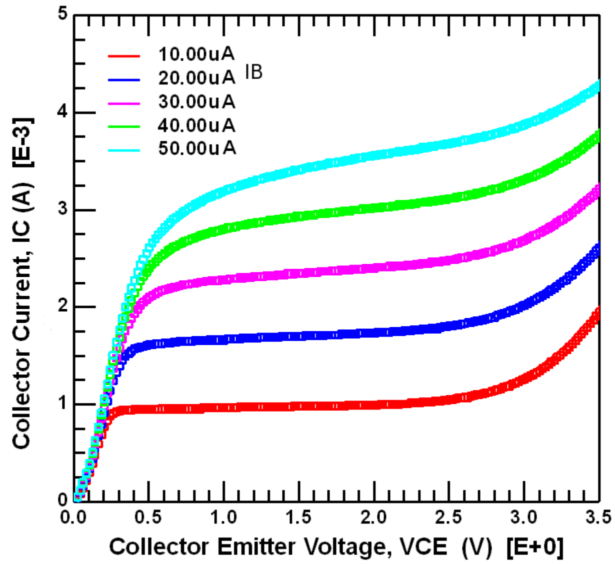

Figure 5.16 Output Measurement IC vs. VCE. Base bias of constant IB steps. Ambient temperature 93K

Base Bias	Voltage Range of Linear Region			VCE 1.8V
IB µA	Lower V	Upper V	Early Voltage	IC mA
10	0.40	2.1	38V	0.98
20	0.70	2.5	21V	1.71
30	0.90	2.5	20V	2.38
40	1.20	2.6	16V	2.98
50	1.50	2.7	12V	3.50

Table 5.11 Ambient temperature, 93K. IB base bias output characteristics

Saturated Collector Resistance

At 93K:	Constant VBE	Constant IB
R_{Csat}	Not available	140 ohms

Table 5.12 R_{Csat} of output measurement for the constant base current configuration only. Ambient temperature, 93K.

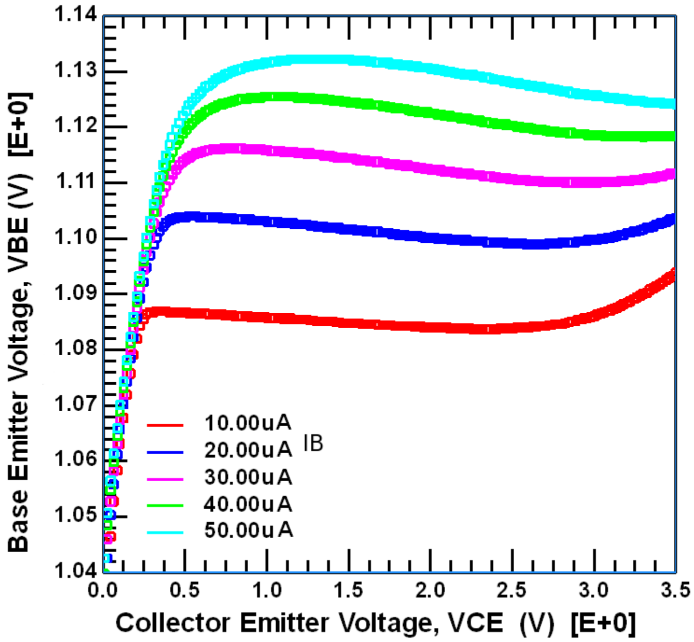

Base Bias	Voltage Range of Linear Region		
IB µA	Lower V	Upper V	ΔVBE
10	0.40	2.1	3mV
20	0.70	2.5	5mV
30	0.90	2.5	5mV
40	1.20	2.6	5mV
50	1.50	2.7	5mV

Figure 5.17 Output Measurement VBE vs. VCE. Base biased with constant IB steps. Ambient temperature, 93K. ΔVBE, base-emitter voltage change, due to device self-heating indicated.

The output characteristics for the constant base current bias are summarized in Table 5.11 and the measurement of VBE versus VCE during constant base current bias is shown in Figure 5.17. The saturated collector resistance of the constant base current is listed in Table 5.12.

In the ambient temperature environment of 93K the range of change in base-emitter voltage, ΔVBE, was approximately 2mV. The magnitude of ΔVBE was 5mV for several bias. The small values of ΔVBE indicate small self-heating effect contributions. Therefore, the self-heating modeling effects need to reflect the measured effects. The approach to determining the model parameters must change as the self-heating diminishes with temperature. These changes in effects required a manual, custom approach to extracting and optimizing the parameters as the temperature decreased. The measured Early voltage drastically decreased at the ambient temperature of 93K. Small Early voltages indicate the presence of large basewidth modulation effects. The saturated collector resistance has the same approximate value at 93K as was measured at 300K. The quasi-saturation voltage range approximately doubled in size from room temperature, 300K to the cryogenic temperature, 93K. The voltage range of the linear region is further decreased at the higher end of VCE voltage. Non-linearity in IC due to breakdown effects begin to occur in the lower IB bias curves at VCE values of 2.1V.

5.2.3 DC Gummel measurements

The linear region of device operation is captured by a DC Gummel measurement. The purpose of this measurement is to obtain the model parameters that have a major influence on the device in the linear region. The base-emitter junction is forward biased and the base-collector junction is reverse biased. The sweep of the base-emitter voltage clearly defines the regions of low, mid, and high-level electron injection behavior [10]. This measurement allows the model parameters and equations describing each region to be extracted or optimized in their region of influence.

5.2.3.1 Gummel measurement configuration

A common-base measurement configuration [10] is used for the Gummel measurement as shown in Figure 5.18. The base is grounded and a constant positive DC bias is applied to the collector terminal, thereby reverse biasing the applied base-collector junction. The device's collector-substrate interface is reverse biased by a constant negative voltage applied to the substrate surface contact connection. The emitter voltage is swept through a range of negative DC bias steps, thereby forward biasing the B-E junction and placing the bipolar device in the forward linear region of operation. The currents of the terminals are measured at each VBE bias step.

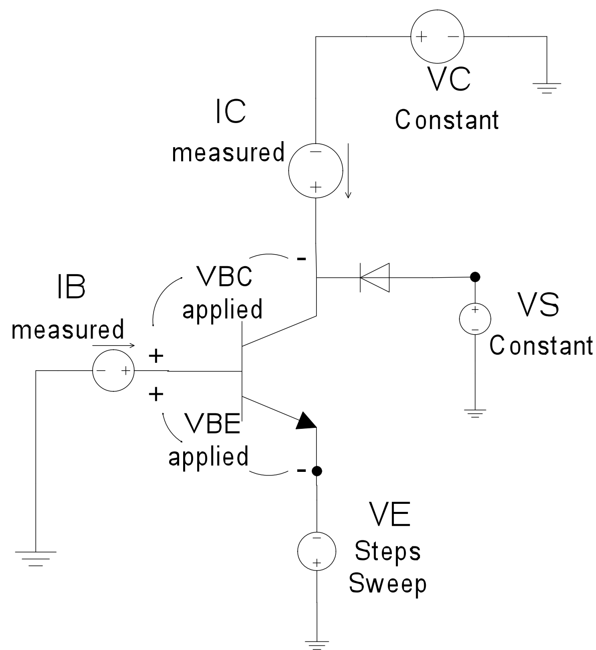

Figure 5.18 Gummel Measurement Setup, VC=1V

5.2.3.2 Gummel linear operating region verification

In this work, DC modeling used Gummel measurements of an applied VC=1 V. One volt bias insured that the internal B-C junction remained reverse biased. A voltage drop across the epi-collector region is present as collector current, IC, flows and acts to de-bias the internal B-C junction. De-biasing the base-collector interface will move the Gummel data from the linear region of operation into the quasi-saturation region. The quasi-saturation region is clearly present in this device technology, as can be seen by the soft knee area of the output measurements. Therefore, an awareness of the operating region as a function of bias must be continually maintained at each temperature in the next few chapters.

A comparison of several different VBC biased Gummel measurements with an output characteristic measurement biased by a constant base-emitter voltage stimulus assisted in verifying if the Gummel measurement remained in the linear region. The Gummel measurement can be overlaid onto an output characteristic measurement by converting the VBE sweep to VCE through summing the terminals: VCE=VBE-VBC. The Gummel measurements of VBC=0V, VBC= -1V, and VBC= -2V were converted. The three Gummel 300K measurements were overlaid onto the 300K output characteristic measurement in Figure 5.19.

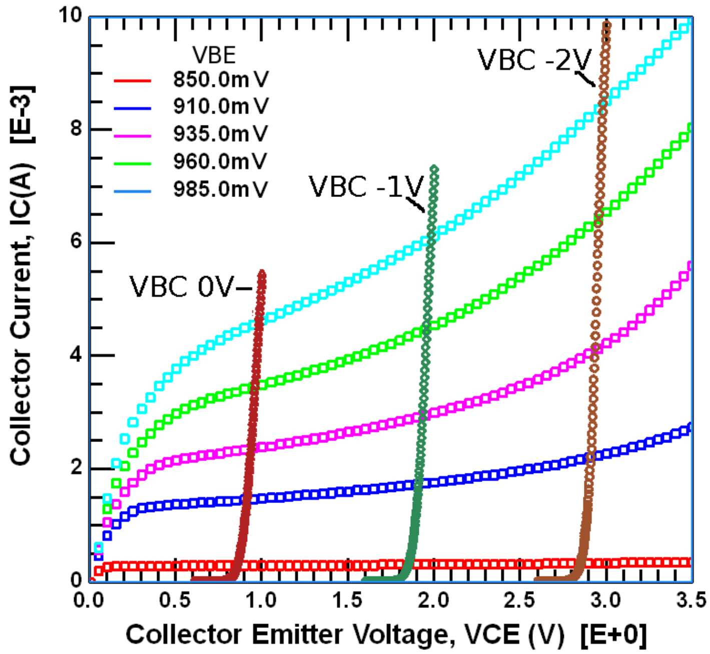

Figure 5.19 Overlay of multiple biases of Gummel measurements onto an output characteristics measurement of constant VBE bias steps in 300K ambient temperature. The Gummel biases were VBC of 0V, -1V and -2V.

From this plot the operating regions can be seen. The Gummel measurement of VBC=0V resides in quasi-saturation. The VBC= -2V Gummel measurement is in the non-linear region before breakdown. The Gummel measurement of VBC= -1V is the only bias that remains within the linear region to a limit of IC=4mA.

5.2.3.3 Extracted characteristics from Gummel measurements

The classic Gummel measurement is a measure of currents, IB and IC, as a function of applied base-emitter voltage, VBE. Several device characteristics and initial parameters can be directly extracted from the Gummel plots. The Gummel measurements are plotted in two forms:

Gummel Current - Collector current, IC, and base current, IB, are plotted on a logarithmic scale, y-axis against a linear scale, x-axis of applied base-emitter voltage, VBE.

Gummel Current Gain - DC current gain, β_F, is plotted on a linear y-axis against a logarithmic scale x-axis of collector current, IC.

For the Gummel current plot, there are three VBE bias regions present: low, mid, and high-level injection. Each region exhibits an exponential relationship between the linear x-axis of VBE and the logarithmic y-axis of currents, IC and IB such as:

$$I = I(0)\left(\exp\left[\frac{VBE}{n \cdot V_T}\right] - 1\right) \tag{5.2}$$

The initial model parameters of each region can be extracted by extrapolating the straight-line of the current curve in that region [10]. The model parameter representing I(0) is the y-intercept of the extrapolated line in that region. The model parameter for the non-ideality factor, n, is determined by the slope of curve in that region. For Gummel plots with a y-axis of $\log_{10}$ scale the slope must include a 2.3 factor in the denominator to translate the exponential term. For these initial extractions the thermal voltage, V_T, is assumed to at the ambient temperature.

The low-level injection region is at small applied VBE bias. Typically IB has some type of recombination current present causing a non-ideality factor to be greater than one. Therefore the current gain is less than the mid-region gain. The mid-level region is the next VBE bias range, defined where the current gain, β_F, is maximum and constant. High-level injection is the upper region when the slope of the IC curve begins to rolloff, thereby causing β_F to decrease. The model parameters representing the non-ideality factor and current intercept for each region are:

Exponential relationship	Low-level injection	Mid-level injection	High-level injection
Current, I	IB	IC	IC
Non-ideality factor, n	MLF	NF	Value of 2
Intercept, I(0)	IBF	IS	IK

Table 5.13 Parmeter extractions from Gummel measurement, Log(IB,IC) vs. VBE

The non-ideality model parameter, NF, is not a Mextram 504.7 model release parameter. NF is a new model parameter, added to support the cryogenic temperature version of Mextram 504.7 [34].

5.2.3.4 Gummel measurement at ambient temperature 300K

The Gummel measurement in an ambient temperature of 300K was biased at a constant VBC= -1V using the setup configuration of Figure 5.18. The two Gummel plots of this linear active region measurement are shown in Figure 5.20 and Figure 5.21.

Table 5.14 summarizes the extracted model parameters at 300K. The parameters extracted as described above are inexact and parameter optimization is required. There is almost no

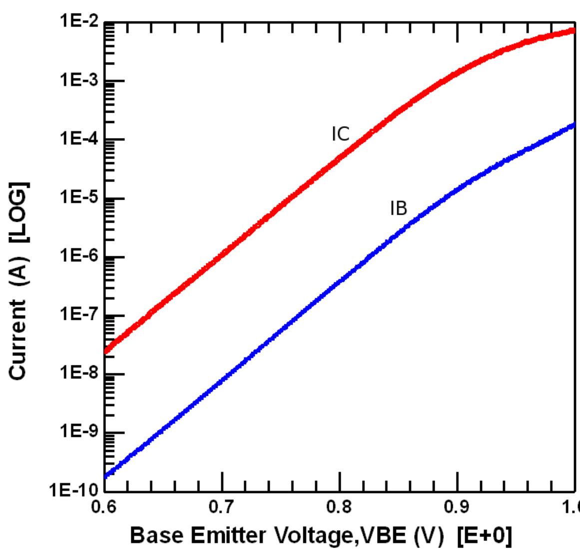

Figure 5.20 Gummel Measurement Log(IC, IB) vs. VBE at VBC= -1V Ambient Temperature, 300K

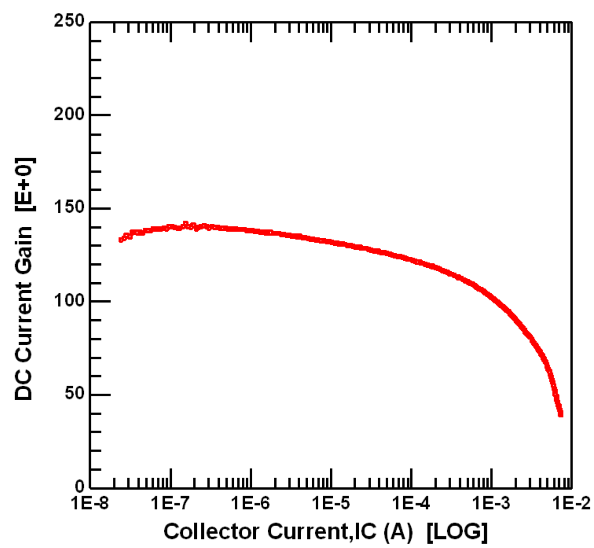

Figure 5.21 Gummel Measurement Current Gain, β_f vs. Log(IC) at VBC= -1V Ambient Temperature, 300K

Initial Parameter	Extracted Value
IS	2.4E-18 A
IK	1.2 mA
NF	1.0
IBF	3.9E-20 A
MLF	1.06

Table 5.14 Extracted model parameter from Gummel measurement in ambient temperature 300K

Limits of Mid Range		
Characteristic:	Lower	Upper
β_F	141	128
IC	0.2 μA	30.0 μA
VBE	0.654 V	0.788 V

Table 5.15 Gummel characteristics in ambient temperature, 300K

low-level injection region. The lower limit of measurement accuracy is 20pA in the IB measurement. The onset of the low-level electron injection region corresponds to an IC of 40nA based on the β_F behavior. The high-level injection region forms an extremely soft knee in the current gain plot. The value of IK should not be determined from measurement extraction only. The three regions are defined for later parameter optimization using the small mid-range of approximately two decades of current dynamic range. In the mid-level injection region, β_F is sloping downward, which indicates that the reverse Early parameter, VER, is influencing the IB curve.

5.2.3.5 Gummel measurement at ambient temperature 223K

In an ambient temperature of 223K the DC Gummel measurement was biased at a constant VBC= -1V. Two Gummel plots of this linear active region measurement are used in modeling and defining the device performance. The full DC dynamic range of IC and IB as function of the base-emitter voltage bias is shown in the Gummel current plot of Figure 5.22. The response of DC current gain, β_F, to collector current, IC, is in the Gummel current gain plot of Figure 5.23.

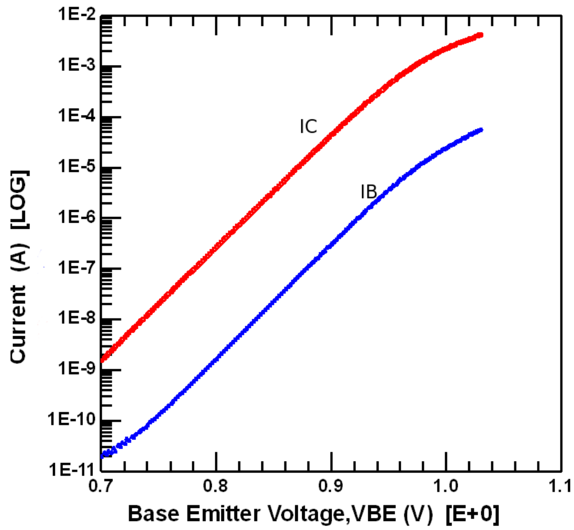

Figure 5.22 Gummel Measurement Log(IC,IB) vs. VBE at VBC= -1V Ambient Temperature, 223K

Initial Parameter	Extracted Value
IS	3.7E-25 A
IK	0.9 mA
NF	1.0
IBF	2.6-25 A
MLF	1.16

Table 5.16 Extracted model parameter from Gummel measurement in ambient temperature 223K

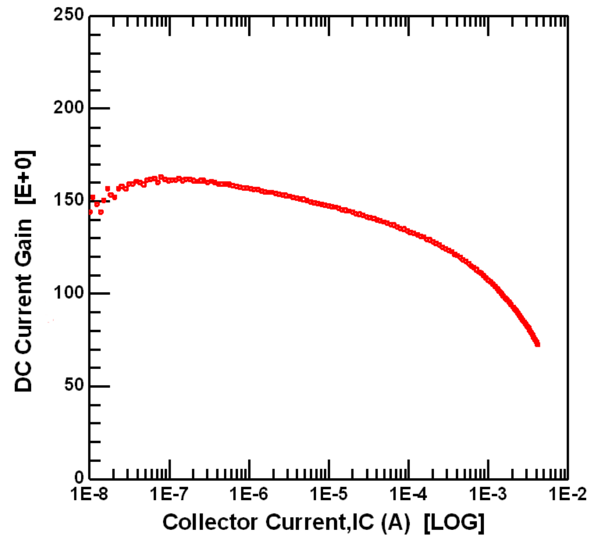

Figure 5.23 Gummel Measurement Current Gain, β_f vs. Log(IC) at VBC= -1V Ambient Temperature, 223K

Limits of Mid Range		
Characteristic:	Lower	Upper
β_F	167	145
IC	0.2 µA	16 µA
VBE	0.792V	0.880V

Table 5.17 Gummel characteristics in ambient temperature, 223K

The Gummel data in an ambient temperature of 223K is similar in behavior to the 300K data. The rolloff of the low-level region is minor; making the low level parameters small. The rolloff of the high-level region is very soft. The extracted value of forward knee current model parameter, IK, is therefore vague. The maximum value of β_F has increased as temperature decreased. However, the dynamic current range of the mid-level β_F region is decreasing as result of the soft high-level injection effects. Optimization of the model parameters is required.

5.2.3.6 Gummel measurement at ambient temperature 162K

The Gummel measurement in an ambient temperature of 162K was biased with a constant VBC= -1V. The two Gummel plots are shown in Figure 5.24 and Figure 5.25 and the extracted model parameters are summarized in Table 5.18. The mid-level injection characteristics are defined in Table 5.19.

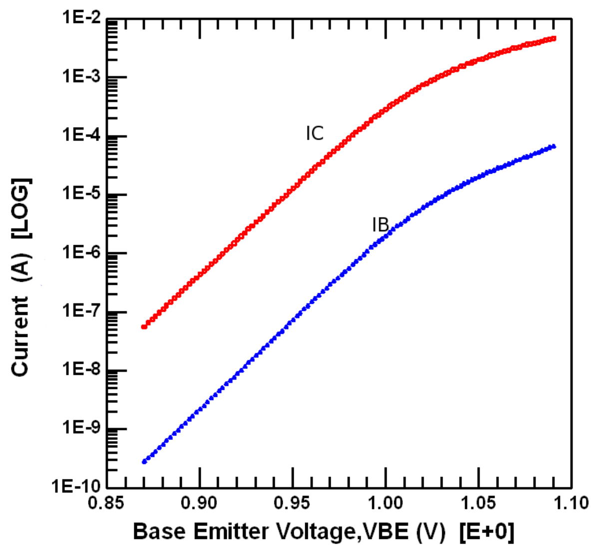

Figure 5.24 Gummel Measurement Log(IC,IB) vs. VBE, at VBC= -1V Ambient Temperature, 162K

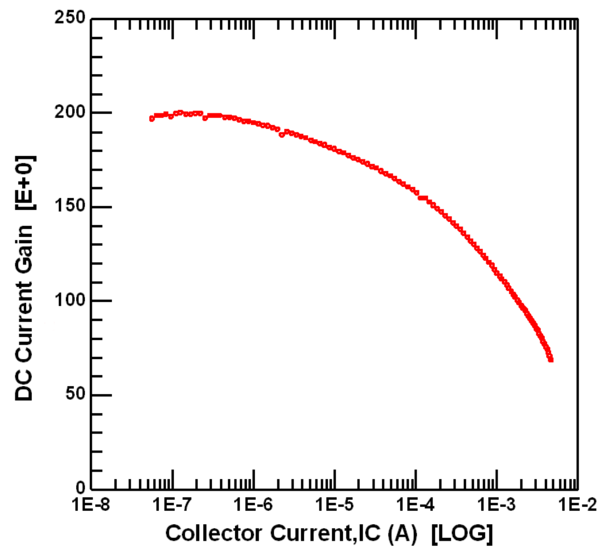

Figure 5.25 Gummel Measurement Current Gain, β_f vs. Log(IC) at VBC= -1VAmbient Temperature, 162K

Initial Parameters	Extracted Value
IS	9.6E-34 A
IK	0.5 mA
NF	1.04
IBF	4.4E-36 A
MLF	1.1

Table 5.18 Extracted model parameter from Gummel measurement in ambient temperature 162K

Limits of Mid Range		
Characteristic:	Lower	Upper
β_F	200	188
IC	0.2 μA	3 μA
VBE	0.890V	0.930V

Table 5.19 Gummel characteristics in ambient temperature, 162K

The Gummel data at 162K shows the same trends as the higher temperature measurements. However, at this temperature there is only a slight indication of low-level injection behavior in the measureable range. Measured current below 20 pA is noisy and displays too much randomness for extraction or optimization. Also, the high level injection knee occurs at lower current levels than at higher temperatures and is becoming even softer and less defined. The extracted parameters in these regions cannot be used. The dynamic current range of the constant β_F region continues to decrease at the lower temperature. The value of β_F increased at 162K.

The significant difference in the Gummel data at this cryogenic temperature is the mid-level injection non-ideality factor, NF, is increasing from the ideal value of 1. The value of NF is 1.04 and is a unique SiGe HBT behavior in the cryogenic temperature range. Inclusion of an ideality factor in the exponential relationship of voltage to current must be added to the Mextram model equations.

5.2.3.7 Gummel measurement at ambient temperature 93K

The Gummel measurement in an ambient temperature of 93K was biased at a constant VBC= -1V. The two Gummel plots of this linear active region measurement are shown in Figure 5.26 and Figure 5.27. The extracted model parameters are summarized in Table 5.20. The characteristics of the mid-level injection region are summarized in Table 5.21.

The Gummel data at 93K is distinctly different in behavior as compared to the higher cryogenic temperature data. There is a clear presence of recombination base current at lower VBE bias points. The resulting low-level injection region has a large rolloff in β_F from the mid-level injection region. The dynamic IC range is less than a decade in the mid-level injection region. The ultra shallow mid-level region creates a severe β_F peaking effect. The current gain

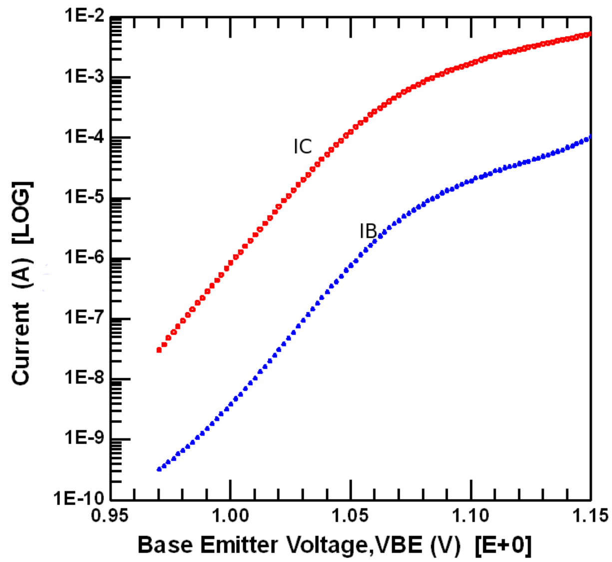

Figure 5.26 Gummel Measurement Log(IC,IB) vs. VBE, at VBC= -1V Ambient Temperature, 93K

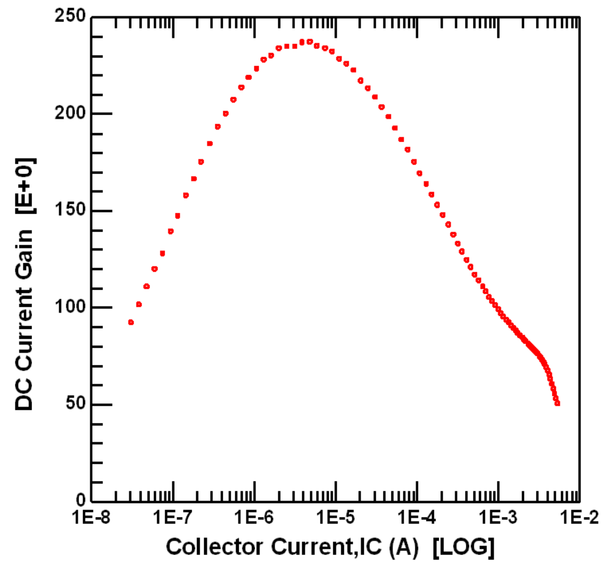

Figure 5.27 Gummel Measurement Current Gain, β_f vs. Log(IC) at VBC= -1V. Ambient Temperature, 93K

Initial Parameter	Extracted Value
IS	4.1E-55 A
IK	0.1 mA
NF	1.10
IBF	2.2E-39 A
MLF	1.7

Table 5.20 Extracted model parameter from Gummel measurement in ambient temperature 93K

Limits of Mid Range		
Characteristic:	Lower	Upper
β_F	234	229
IC	2.0 μA	11 μA
VBE	1.008V	1.024V

Table 5.21 Gummel characteristics in ambient temperature, 93K

increases to a maximum of 234 but begins to decrease at approximately IC=15 μA. High level injection rolloff begins at IC less than 100 μA. Rolloff in the high-level injection region is severe. Therefore DC current gain, $\beta_{F,}$ is continually decreasing in the most common current operating region. The model parameters, IS and NF are extracted from a very narrow mid-level region with a limited number of data points. However, it is clear that the non-ideality factor, NF, has continued to increase, going from 1.04 at 162K to 1.10 at 93K as the temperature decreased.

The exponential relationship of NF with current makes the accuracy of the parameter value critical to the success of developing the model.

5.2.4 AC data

AC data is necessary for small signal characterization and parameter extractions. Standard AC measurements of high-frequency bipolar devices are 2-port network, Vector Network Analyzer, VNA, measurements of scattering, S-parameters. The S-parameter 2-port VNA network translates well to the linearized, hybrid-π model of Figure 1.9 for characterization of small-signal bipolar behavior.

S-parameter measurements of high frequency bipolar devices are typically taken by probing a RF configured test structure of the bipolar device at wafer/chip level on a precise RF probe station. A 50 Ω impedance environment is maintained throughout an RF probed measurement setup. 50 Ω impedance termination, at the device, is obtained by making RF probe contact to the ground-signal-ground, G-S-G, metal bondpads on the chip surface. The two-port measurement reference plane is set to the bondpad surface by a probe-tip calibration method. For RF measurements of less than 20 GHz, probe-tip calibration is done using a standard short, open, load (50Ω), thru (SOLT) calibration technique and calibration chip of standards [49]. Calibration and measurement accuracy is further enhanced by measuring an open "dummy" RF test structure and subtracting its parasitic effects from the device measurements. By using on-wafer open calibration test structures, the 2-port measurement reference plane is moved to the surface metallization above the device terminals [49]. Modeling and characterization accuracy is greatly improved since the AC measurement is now starting very close to the indicated B, E, and C terminals indicated on the model overlay of the device cross-section in Figure 6.2.

The research lab of Georgia Tech has the specialized cryogenic temperature equipment to take RF measurements at "on-wafer/chip" level, in a cryogenic temperature environment. Dr. John Cressler's research group developed this capability. Their group took all the SiGe RF measurements at Georgia Tech as part of the NASA, EDTP project [46], "SiGe Integrated Electronics for Extreme Environments." The RF measurements were taken by probing an RF configured SiGe HBT test structure layout on the SiGe chip, in a custom probe station manufactured by Lakeshore. The RF probe station is equipped with a cryogenic temperature chamber which houses the chip level chuck pedestal and RF probes.

RF measurements were taken at the same four ambient temperatures: 300K, 223K, 162K and 93K, at which the DC measurements were taken. The 2-port S-parameter SiGe HBT measurement setup [50] is diagramed in Figure 5.28. The HBT is connected and biased in a common-emitter configuration for all RF measurements. The base terminal of the HBT receives both DC bias and Port 1 RF signal through RF probe contact to the base signal bondpad. The collector terminal receives DC bias and Port 2 RF signal through the RF probe contact to the collector signal bondpad. The emitter terminal is connected to DC/RF ground through both RF probes. Each RF probe makes contact to the two ground/emitter bondpads when it makes contact to the signal pad. The ground/emitter pads sandwich the signal pads. The G-S-G pad layout configuration provides a 50 Ω RF termination to both the base terminal and the collector terminal of the transistor. The emitter is shorted to the substrate at the chip level in the RF test structure circuit. On chip metallization connects the emitter bondpad to the entire backside of the chip and thereby the HBT substrate. Surface access of the backside is through a deep P^+ plug implant as shown in the device cross-section of Figure 5.1.

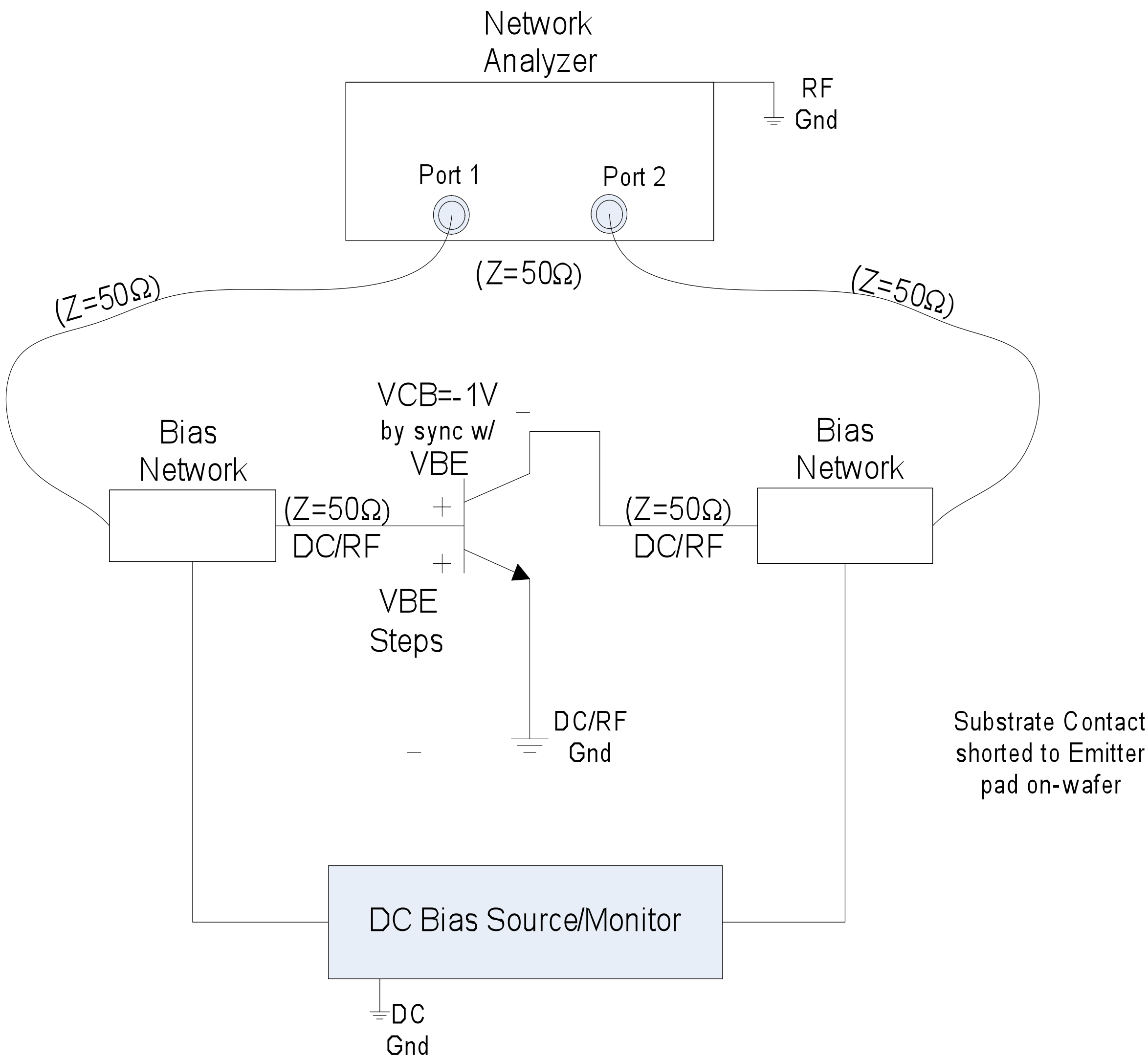

Figure 5.28 AC data configuration for S-Parameter measurements

AC measurements were taken by DC biasing the HBT in the linear active operating region. The S-parameter measurements over wide frequency range at each DC operating point. The operating points were over a range of VBE bias values with a constant VBC bias applied and were selected to correspond with Gummel measurements. The collector voltage bias, VC, was synchronized by a 1V offset to the applied base voltage, VB. This voltage offset provided a constant applied base-collector terminal voltage, VBC, of -1V. At each DC bias point the four S-parameters: S11, S21, S12, and S22 were measured over a frequency range of 1 GHz to 30 GHz in 1 GHz steps. The VBE bias range was adjusted for each ambient temperature. The applied VBE needed to generate an IC of approximately 100μA on the low end and less than 4 or 5 mA on the high end. The applied VBE increased as temperature decreased to keep the device biased in the modeling range.

Interpretation of modeling information from direct S-parameter measurements is limited. Small-signal characterization and the parameter influences on AC behavior are better adapted to 2-port h-parameter (hybrid) and 2 port y-parameter networks [51]. Fortunately, 2-port S-parameter VNA measurements can be well represented as h-parameter and y-parameter networks. The y-parameters are used to de-embed the parasitics of the bondpads and metal connections from the device measurements. By converting the S-parameters of both measurements to y-parameters the open structure's y-parameters can be subtracted from the y-parameters of the measured device. This results in y-parameters of the device behavior only, without pad parasitics. The y-parameters are then converted back to S-parameters, yielding de-embedded S-parameter device data [50]. All AC modeling and characterization work was done with de-embedded S-parameters measurements.

The S-parameter measurements in an ambient temperature of 162K are shown in Figure 5.29.

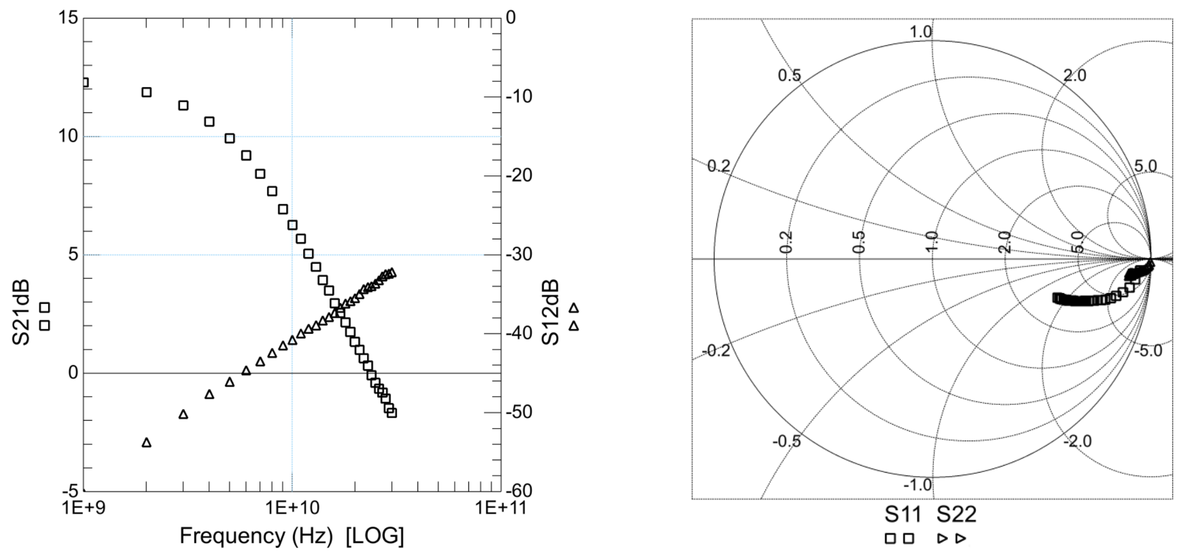

Figure 5.29 S21dB and S12dB on the left. S11 and S22 on the right in the Smith chart. De-embedded S-parameters measured at ambient temperature, 162K.
HBT DC biased in linear region at VBE= 1.03V and VBC= -1V.

The 2-port h-parameter network of Figure 5.30 has a direct relationship to the small-signal hybrid-π bipolar model of Figure 1.9 [10]. The frequency response of the small-signal current gain, β_{AC}, is relatable to h_{21}. The cutoff frequency, f_T, is defined as the frequency at which β_{AC}=1.

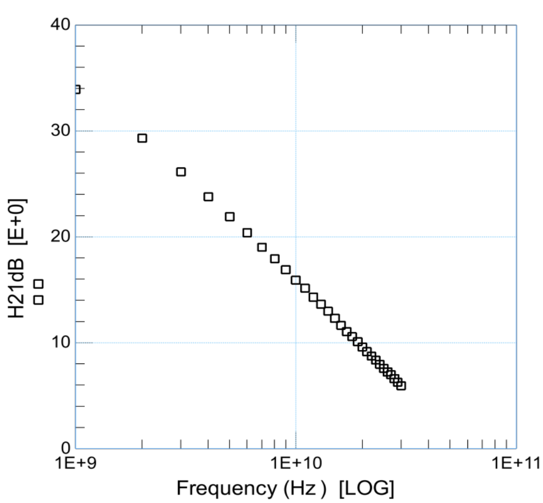

Figure 5.30 H21dB vs. Log(Frequency). Ambient temperature, 162K

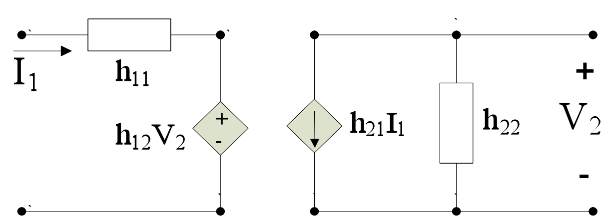

h_{11}=input impedance
h_{21}=forward current gain
h_{12}=reverse voltage gain
h_{22}=output admittance

$I_1=h_{11}I_1 + h_{12}V_2$
$V_2=h_{21}I_1 + h_{22}V_2$

Figure 5.31 h-parameter 2-port network [50]

The cutoff frequency, f_T, can be found by extrapolating the straight line curve of h21dB to the x-axis. The β_{AC}=1 occurs at this interception frequency. The h21dB values form a straight line with a slope of 20dB/decade. For consistency with the modeling and characterization however, f_T was determined by selecting a single frequency, 10 GHz, and using the relationship of $f_T = f_0 \times h_{21}$. Therefore in an ambient temperature of 162K the modeled HBT has a f_T of 62.2GHz when biased at VBE=1.03V. f_T was extracted for each VBE bias point from the S-parameter measurements at the four ambient temperatures. f_T was plotted as a function of VBE for all temperature as shown in Figure 5.32.

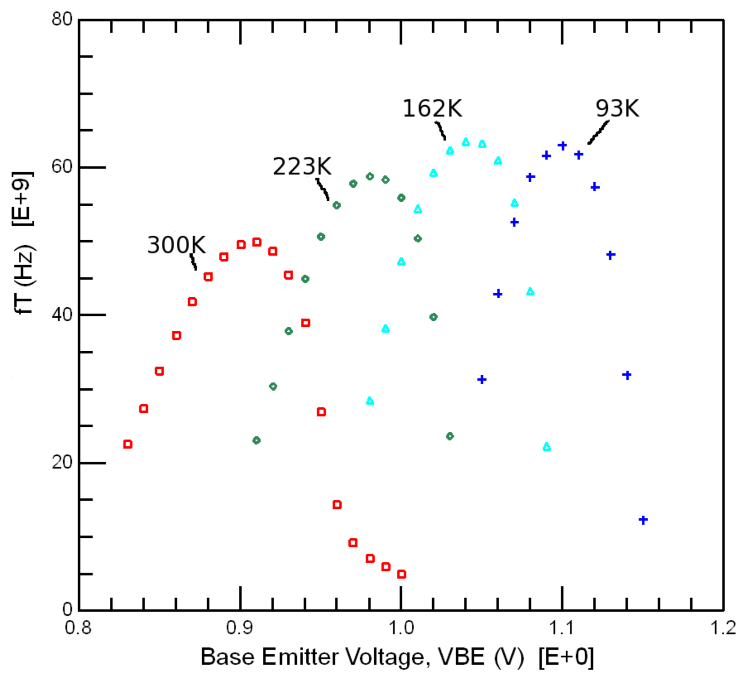

Figure 5.32 f_T vs. Base-Emitter Voltage for ambient temperatures: 300K, 223K, 162K, 93K. Each temperature is indicated and defined by color.

There is an increase of approximately 200mV in VBE operating voltage as temperature decreases as shown in Figure 5.32 when comparing peak f_T bias points.

A more common and useful form for modeling is to define f_T in terms of the collector current as is shown in Figure 5.33. f_T versus Log(IC) is plotted for each of the four ambient temperatures.

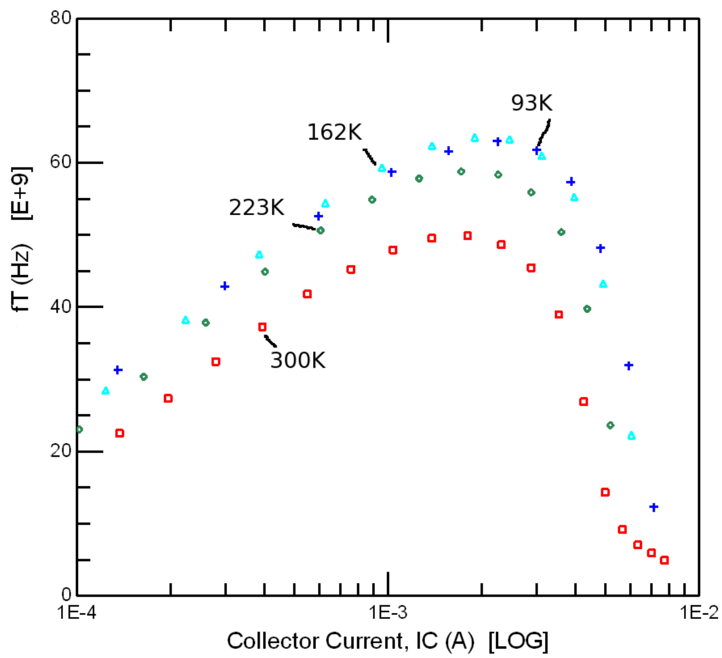

Figure 5.33 f_T vs. Log(Collector Current). Data for ambient temperatures: 300K, 223K, 162, 93K are indicated and defined by color.

The increase of f_T as temperature decreases is attributed to the contribution of the Germanium bandgap effects. The base transit time, τ_B, and emitter transit time, τ_E, decrease with temperature due to the exponential relationship of $\frac{\Delta E_{g,Ge(grade)}}{kT}$, as defined in Equations (2.20) and (2.21)[21]. The measured AC data indicates that the maximum f_T is occurring at slightly higher IC values as the temperature decreases. This slight increase is attributed to the Kirk effect beginning at slight higher IC values due to the saturation velocity decreasing with temperature[52]. At 93K, both β_F in Figure (5.27) and f_T in Figure (5.33) exhibit a steep rolloff at high collector currents. This behavior is attributed to high-level injection heterojunction barrier effects at the base-collector heterojunction interface [52]. The impact to HBT performance is controlled by the process design of the amount of bandgap offset energy at the base-collector heterojunction interface, $\Delta E_{g,Ge}(x = W_b)$, defined in Figure 2.6 [21]. The epilayer collector doping at this interface is also critical to the rolloff and beginning of the Kirk effect [52].

6 Factors influencing the ambient temperature model parameter extractions

The primary objective of this cryogenic temperature SiGe model development process was to develop one model that represented DC and AC measured behavior from 300K to 93K. The single expansive temperature, SET, model was developed to represent the DC quasi-saturation and linear regions of operation as well as the AC small signal behavior, over this wide temperature range, as explained in Section 1.1 and illustrated in Figure 1.3.

In order to reach our primary objective, four ambient "at temperature" models were optimized and fitted to the data of the previous chapter. The primary factors found to influence the ambient temperature model parameter extraction approach are summarized in this chapter. The four ambient temperature models/parameters and the fitted model results are presented in Chapter 7. Each ambient temperature model has a unique model parameter set, but uses the same modified Mextram model equations. The code modifications needed to support the ambient temperature region were minimal. The ambient temperature model developed in this work differs from the standard Mextram 504.7 model. The standard model was modified with the addition of non-ideality factor parameters and the expansion of certain numerical ranges in the 504.7 code.

The four ambient temperature model parameter sets provided the temperature behavior of the model parameters over the expansive temperature range. The development of the SET model in Chapter 8 was based on the ambient models' parameter behavior. The SET model/parameter extraction approach required two development steps:

> 1st Step - Develop four, ambient temperature, "at temperature", SiGe model/parameter sets. Each model/parameter set was developed by fitting the same model equations to the DC and AC device data measured at that ambient temperature. Therefore, any

changes in the model equations for one temperature would have to be applicable to the other three temperatures. The primary factors which influenced the development of the four ambient temperature models will be discussed in this chapter. The fitting of model parameters for each ambient temperature model are discussed in Chapter 7.

2nd Step - Develop temperature equations and corresponding parameter values which represent the parameters' behavior throughout the four ambient temperature parameter sets. Create one SET model parameter set by combining: 300K ambient model parameter set, the modified Mextram model equations, and the temperature shifting model equations/parameters that represent the expansive temperature range. The results of creating the SET model are presented in Chapter 8.

Development of the four ambient temperature models required a common parameter extraction approach. Each model was fitted to the same modified Mextram model equation code. The device electrical performance at the four ambient temperatures had some common characteristics and trends. However, at colder ambient temperatures the performance exhibited some unique behaviors, as discussed in Chapter 5. Several primary factors were found to describe this unique performance. A common parameter extraction approach was used to include these primary factors. The SiGe HBT's electrical performance over a wide temperature range influenced the modification of the Mextram model equations and model parameter extractions. The primary factors influencing the four ambient temperature model/parameters sets reviewed in this chapter are:

- Identification of the Mextram configuration features needed to represent the SiGe device structure and definition of the corresponding model parameters.

  (Section 6.2)

- Definition of model parameters associated with physical device characteristics. (Section 6.3)
- Determination of the 504.7 temperature parameter values from process. (Section 6.4)
- Utilization of SiGe model equations instead of Si model version. (Section 6.5)
- Determination of the model operating conditions to be fitted for each ambient temperature. (Section 6.6)
  - Model parameters defined by physical device characteristics
  - Bias and frequency range
  - Self-heating effects
  - Addition of model parameters representing non-ideality factors, NF and NR
- Modifications of the standard Mextram 504.7 code for ambient models. (Section 6.7)
  - Expansion of the 504.7 numerical control for low temperature ambient modeling
  - Addition of parameters, NF and NR
  - Expansion of parameter ranges, and changing variables to parameters

6.1 Overview of ambient temperature model parameter extraction methods

The Mextram model was based in physics. The strategy taken for the Mextram standard parameter extraction methodologies was that they also be physically based [35]. In the standard extraction approach shown in Figure 6.1, the parameters are either derived from physical characteristics of the device structure or are extracted directly from measured data. Parameters are extracted from measured data by first order derivations using graphical techniques [35]. The data is arranged in workable graphical forms of either a linear, exponential or logarithmic format. Simple physical formulas are applied to a measurement operating region which corresponds to model equations and parameters that are dominate in the region. This method of extraction provides a direct connection to the physical model definitions and works well when the operating regions are clearly distinct.

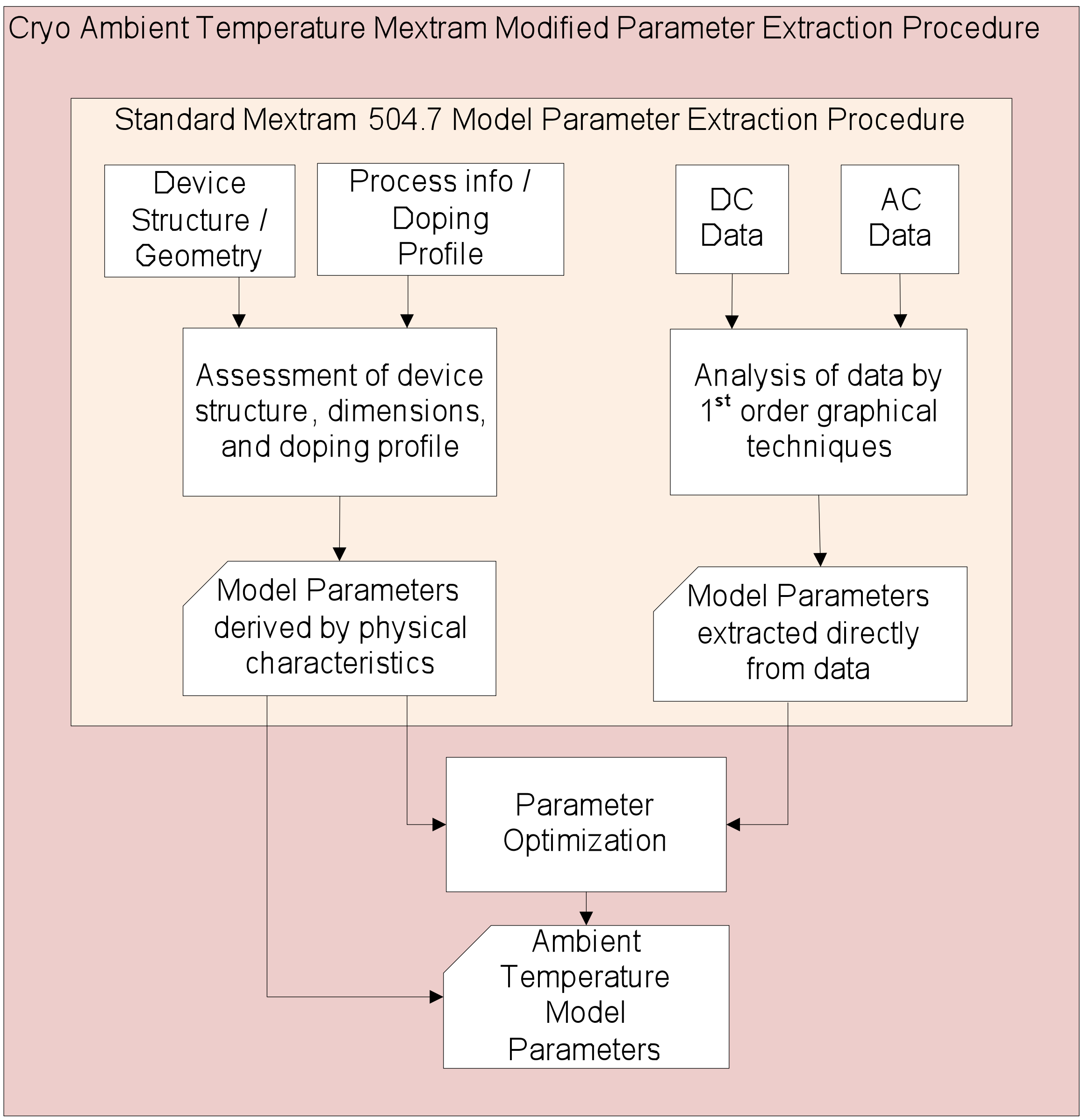

Figure 6.1 Ambient temperature model parameter extraction method

However, when operating regions do not have clearly defined numerical transitions, the overlapping physical effects require parameter optimization techniques to correctly balance the effects. The parameter extractions of the four ambient temperature models required optimization of the initial physically generated parameter values. The optimization focused approach of cryogenic modeling encompasses the standard parameter extraction methodology as shown in Figure 6.1. This parameter optimization extraction methodology was needed to get accurate fits of ambient temperature models over the wide temperature range.

The parameters derived from physical characteristics utilized process information of Section 5.1 and the physical design relationships of Chapters 2 and 3. In the standard extraction methodology these results would be the final parameter values. For the cryogenic work that approach did not produce accurate models. Therefore, the physically derived parameters were individually reviewed to determine which parameters should be optimized. It was determined that the branch switch model parameters and the temperature parameters worked well when derived strictly from process information, as illustrated in Figure 6.2. The approaches for these two groups of model parameters are summarized in Sections 6.2 and 6.4.

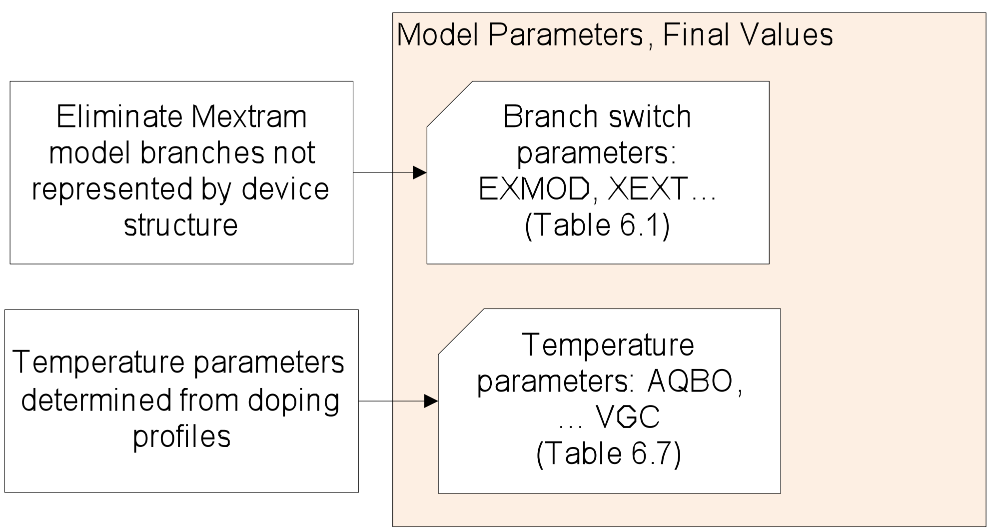

Figure 6.2 Model parameters derived from physical characteristics

Model parameters that were initially derived from physical characteristics but then found to require optimization are grouped in Figure 6.3. It was determined that the junction capacitances and their respective splitting parameters, the SiGe bandgap parameter, and the quasi-saturation parameters all needed further optimization. The extraction approaches for these groups of model parameters are summarized in Sections 6.3 and 6.5.

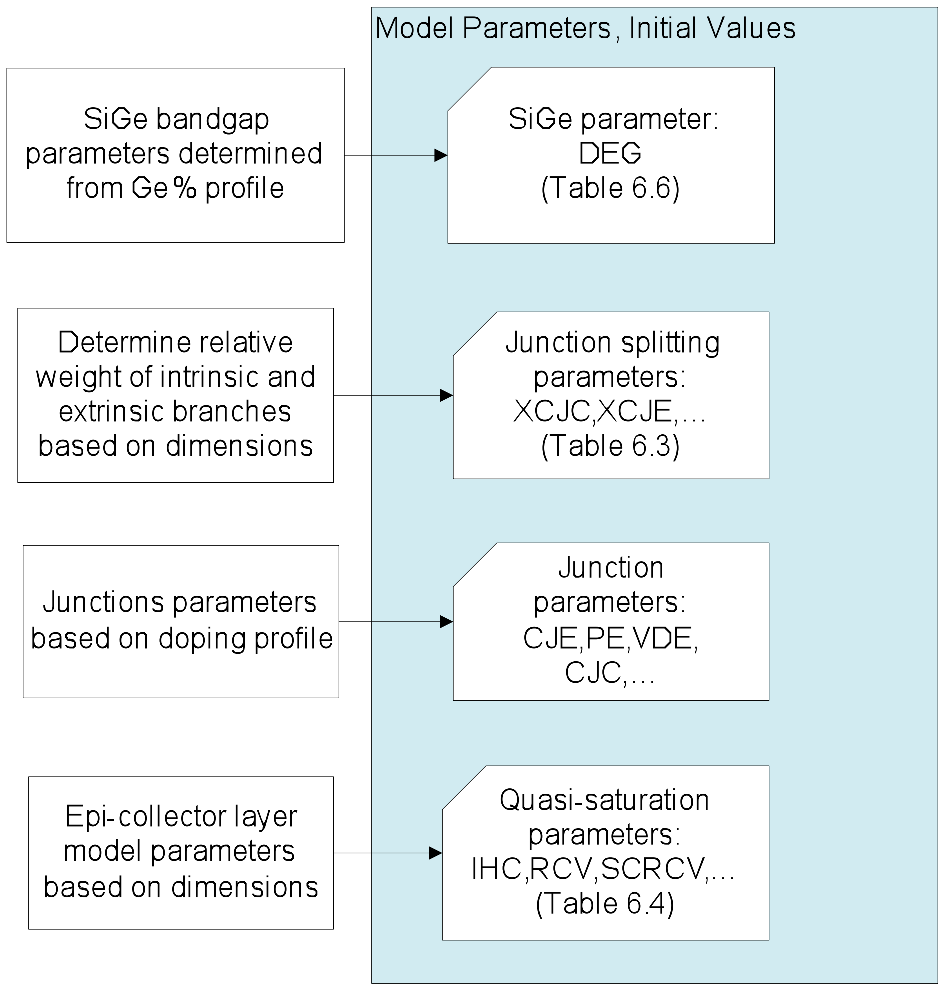

Figure 6.3 Model parameters requiring optimization from initially physical based values

In the standard extraction methodology of Figure 6.1, the second part of extracting model parameters is to determine the values directly from measurements. For this cryogenic modeling project, the standard approach of extracting parameters from measurements only provide an initial starting value for the parameters. The model could not be fitted accurately without parameter optimization. The cryogenic ambient temperature extraction methodology used to determine initial parameters values is summarized in Figure 6.4.

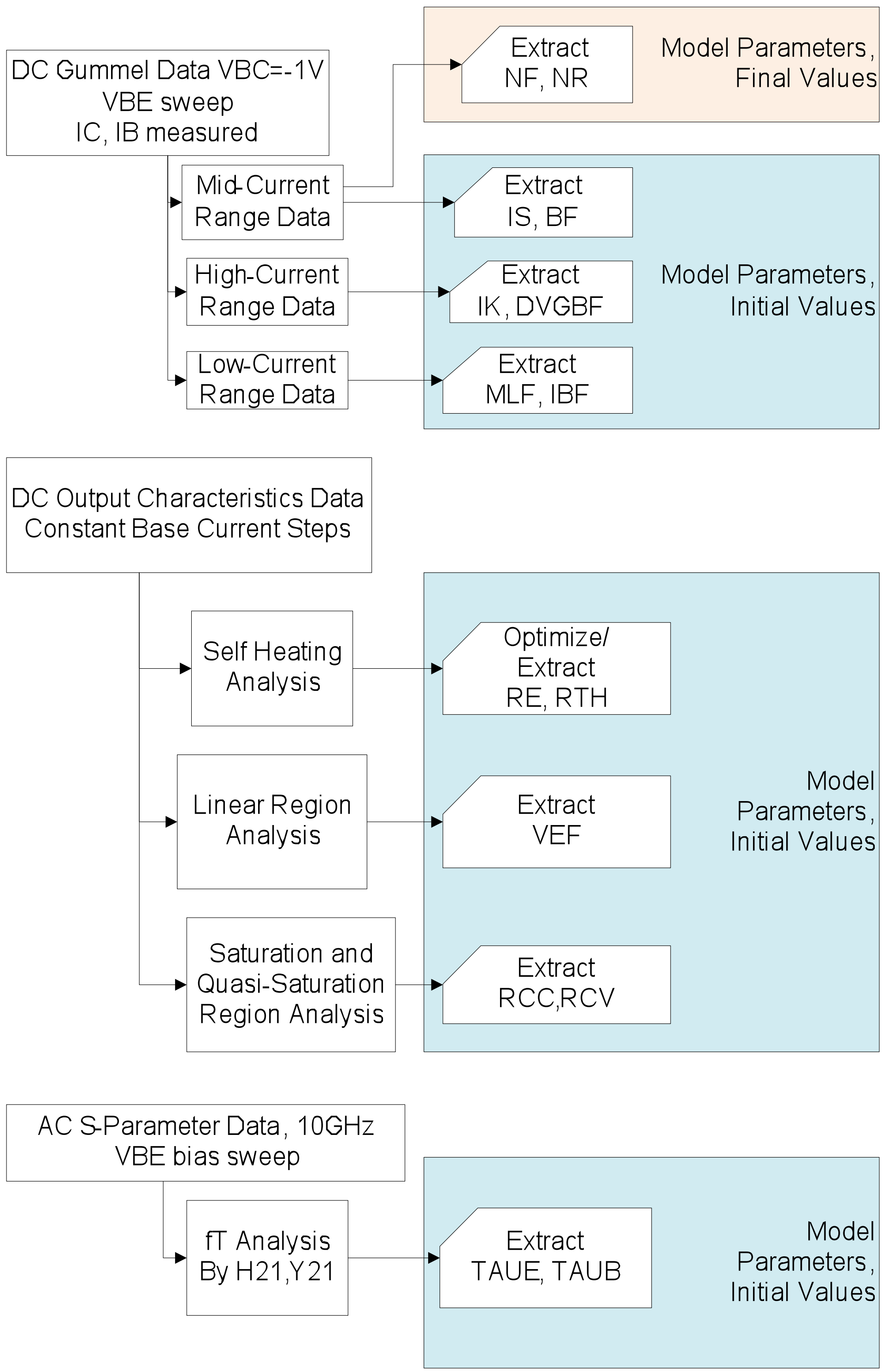

Figure 6.4 Model parameters initially extracted from data

6.2 Parameters defining the Mextram feature configuration representing SiGe device structure

The features and model equations of Mextram were discussed in Chapter 3. For the development of the four ambient temperature models, a single configuration of Mextram 504.7 features was used at all temperatures. The SiGe HBT device cross-section of Figure 5.2 can be compared to the full featured Mextram 504.7 circuit schematic [34] of Figure 3.1 which is restructured in Figures 6.5 and 6.6 respectively. The electrical components that represent the cross-section regions can be related to the internal nodes of the Mextram in Figure 6.5. A translation of these components to the branches of the Mextram model allows the SiGe HBT device cross-section to be completely defined in terms of a Mextram circuit schematic and represented in Figure 6.6.

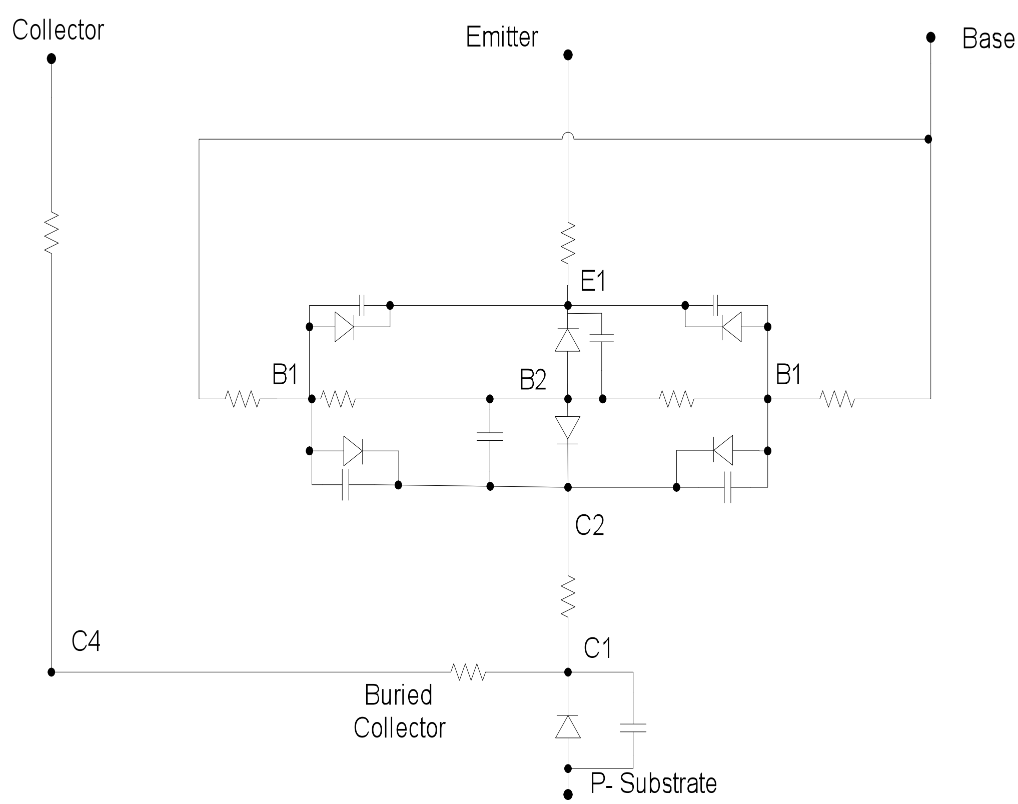

Figure 6.5 Components of the modeled device from cross-section

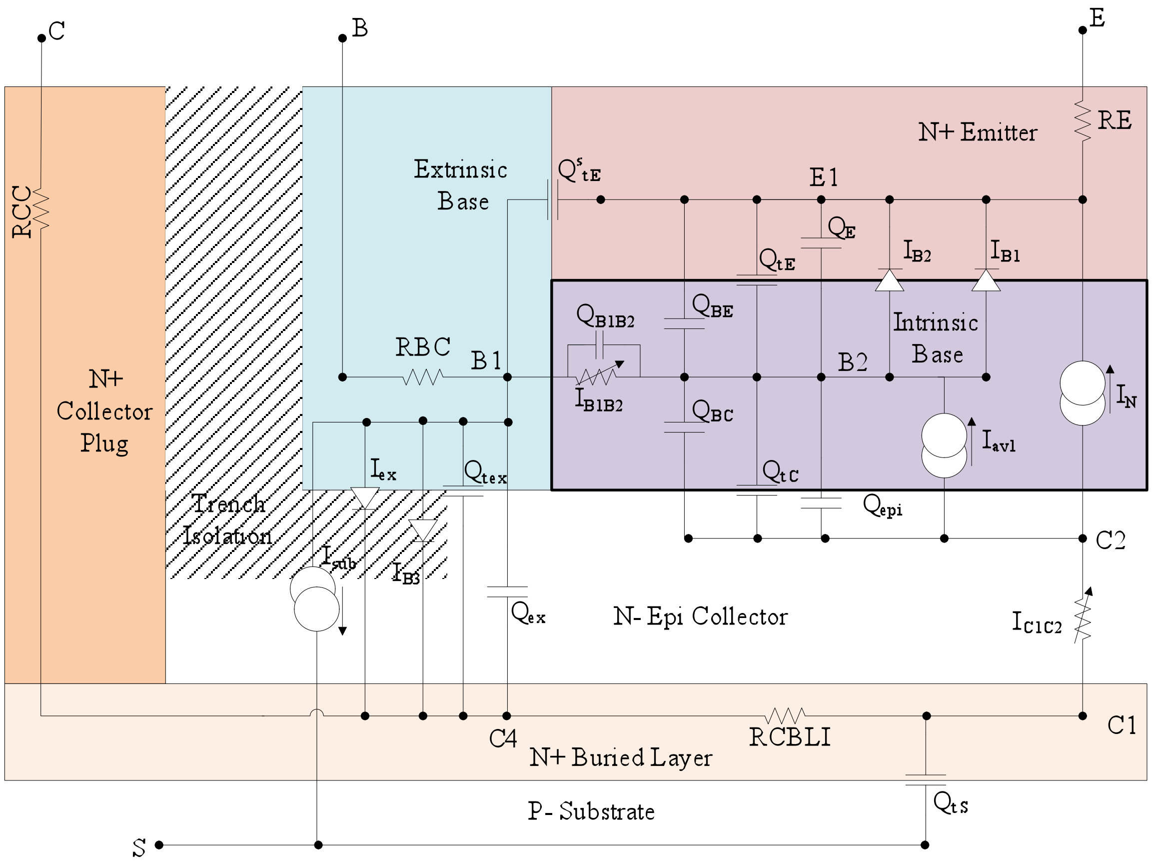

Figure 6.6 Mextram feature configuration for the SiGe HBT modeled, not drawn to scale.

The feature configuration was defined by the settings and values of model parameters. The best practices method is to use the fewest model effects needed to describe measured behavior[13]. Branches were disabled by setting parameter values to zero. Activation of unnecessary features results in incorrect parameter extractions in other model sections. Therefore, the selection of features for the four ambient temperatures depended on the device structure, process capability and the measurements. The individual branches of Mextram 504.7 in Figure 3.1 were reduced to develop the configuration of Figure 6.6 and are described below.

N^+ buried collector region. The buried collector resistance in Mextram 504.7 [53],[34] can be split into an intrinsic buried collector resistance, RCBLI, and an extrinsic buried collector resistance, RCBLX. However, there is not a distinct extrinsic buried collector resistance in our

device structure nor was the split needed for fitting purposes. RCBLX was set to zero. Setting either of the buried collector resistors to zero will collapse the corresponding branch node in simulations, thus node C3 and RCBLX are not present in Figure 6.6.

P^+ extrinsic base region. The extrinsic polysilicon base region resides on top of shallow trench isolation instead of an active N^- type collector region. Therefore, the extended modeling sections of Mextram that represent additional extrinsic base-collector behavior were not activated. Extended modeling deactivation occurs by setting the model flag parameter EXMOD=0. This removes the charge equation branch, XQ_{ex}, the current branches, XI_{ex} and XI_{sub}.

P^+ base interface to N^- collector region. The base-collector depletion charge is split between an intrinsic part and an extrinsic part. The intrinsic base-collector depletion charge represents the capacitance effects directly beneath the active emitter area by the branch charge $Q_{tC.}$ The extrinsic base-collector depletion charge in Mextram 504.7 has two charge branches that can further split the extrinsic base-collector depletion capacitance, Q_{tex} and $XQ_{tex.}$ However, this further splitting was not necessary because of the reduced parasitics of the extrinsic base region. So, the depletion charge branch, XQ_{tex}, was removed by setting parameter XEXT=0. The extrinsic base-collector depletion capacitance was represented with only the extrinsic base-collector depletion charge branch, Q_{tex}.

P^+ base interface to N^+ emitter region. Physically, a sidewall base-emitter junction is present. A capacitive effect was needed to fit the AC behavior using the sidewall base-emitter depletion charge, Q_{tE}^{S}. However, a current effect from the sidewall was not present in the data. Therefore, the sidewall base-emitter diode current branch, I_{B1}^{S}, between nodes B1 and E1 was removed by setting parameter XIBI=0.

Extended modeling features. The overlap capacitance branches from collector-base and base to emitter were removed. These capacitances can only be accurately fitted if custom modeling test structures are measured [13], which were not available. The branches are removed by setting parameters CBEO=0 and CBCO=0.

The avalanche current contribution is between nodes B2 and C2. A snapback effect in the avalanche current effect is an option in this branch. However, it has been found not to be effective [13]. So the avalanche current branch, I_{avl}, uses the standard avalanche behavior described in Chapter 3 by setting parameter EXAVL=0.

The variable intrinsic base resistance represented by current branch, I_{B1B2} has a feature to include equations describing AC crowding of the pinched base beneath the emitter. This effect was found to be slightly effective in fitting the AC data. So the high frequency base resistance effect was included by setting parameter EXPHI=1.

The following table is a summary of the model parameters needed to generate the Mextram model feature configuration of Figure 6.6.

Parameter Value	Simplification of 504.7Model:
EXMOD=0	Removed XI_{ex} branch Removed XI_{sub} branch Removed XQ_{tex} branch
XEXT=0	Removed XQt_{ex} branch and all extrinsic base-collector depletion capacitance is on branch Q_{tex}.
XIBI=0	Removed I_{B1}^{S} branch
EXAVL=0	Removed equations for the avalanche snapback feature
EXPHI=1	Activated equations for AC current crowding the pinched base under emitter.
CBEO=0	Removed external overlap capacitance between base and emitter.
CBCO=0	Removed external overlap capacitance between base and collector.
I_{Sf} branch	Removed the independent current contribution, I_{SF}, between the Substrate-Collector by modifying Verilog-A code

Table 6.1 Mextram model parameters values that generates the Mextram 504.7 configuration features of Figure 6.2 for the SiGe HBT modeled

One modification of the 504.7 code was to remove the non-physical current branch, I_{Sf}, between C1 and S. Its purpose was to alert the circuit designer if the collector-substrate was incorrectly forward biased. However, for model development purposes it was creating false problems during parameter optimizations at the lower temperatures.

The model parameters of Table 6.1 are common to all four ambient temperature models. Utilization of these parameters and the corresponding values allowed the ambient models at the four temperatures to use the same feature configuration.

6.3 Model parameters defined from physical device characteristics

The model parameters derived from the device's physical characteristics are defined in Figure 6.2 and 6.3. In this section, those parameters which can be calculated from the device process information from Section 5.1 are summarized. These were used as the initial values for the device at the ambient temperature of 300K. A comparison of the initial calculated value and the final optimized value at 300K for the model parameters is included to provide insight into how closely the final model related to physical characteristics relationships. Table 6.2 includes some of the frequently used physical characteristics of the SiGe device modeled.

Emitter		Collector Epi-layer	
Width	H_E= 0.5μm		
Length	L_E= 2.5μm		
Area	A_E= 1.25μm^2	Thickness	W_{epi} = 0.4μm
Perimeter	P_E= 6.0μm	Dopant Concentration	N_{epi} = 1E17cm^{-3}

Table 6.2 Physical characteristics of SiGe HBT process modeled [21]

Some of the parameters calculated from physical characteristics are temperature independent parameters and others are dependent on the temperature of the device. Parameters which are temperature dependent are difficult to accurately calculate by physical formulas at temperatures beyond room temperature. The accuracy of the calculated values is dependent on the assumptions of how the process information shifts with temperature.

Temperature Independent Parameters.

The split of junction depletion capacitance between intrinsic and extrinsic regions is defined by model parameters, XCJE and XCJC. The influence of XCJE in the splitting Mextram base-emitter depletion charge, Q_{tE}, branch is described in Section 3.2.3.1. The influence of XCJC in the splitting Mextram base-collector depletion charge, Q_{tC}, branch is described in Section 3.2.3.2. These two parameters are typically considered to be temperature independent and their values are determined from the device structure and layout geometry as defined in Table 6.3.

Model Parameter	Initial Process Calculation		Optimized at 300K ambient temperature
	Method	Value	
XCJE	$\frac{P_E}{P_E + 6A_E / \mu m}$	0.4444	0.3804
XCJC	$\frac{VER \cdot (1 - XCJE) \cdot CJE}{VEF \cdot CJC}$	0.3247	0.2245

Table 6.3 Depletion capacitance branch splitting model parameters values at 300K, calculated and optimized. Values used in all four ambient temperature models and were temperature independent [13].

The avalanche model in the 504.7 release defines the temperature dependence of avalanche parameters, WAVL and VAVL as independent. The parameter values calculated at 300K are compared to the final optimized value in Table 6.4.

Model Parameter	Initial Process Calculation		Optimized at 300K ambient temperature
	Method	Value	
WAVL	W_{epi}	400 nm	245.1 nm
VAVL	$\frac{VDC}{XP^2}$	0.5 V	0.800 V

Table 6.4 Avalanche model parameters at 300K, calculated and optimized [13].

A few of the epi-layer model parameters are temperature independent in the 504.7 standard code. Those quasi-saturation parameters initially derived from physical relationships are listed in Table 6.5.

Model Parameter	Initial Process Calculation		Optimized at 300K ambient temperature
	Method	Value	
IHC	Equation (3.55)	3.51 mA	2.347 mA
SCRCV	Equation (3.58)	2870 Ω	301.4 Ω

Table 6.5 Epi-layer model parameter values at 300K, calculated and optimized [13].

Temperature Dependent Parameters.

Many of the model parameters are temperature dependent in the 504.7 model release as is indicated in the model parameters descriptions at the beginning of Chapter 3. The temperature dependent model parameters that can be derived from physical characteristics are defined below at 300K.

Model Parameter	Initial Process Calculation		Optimized at 300K ambient temperature
	Method	Value	
VDC	Equation (3.56)	0.8238 V	0.8038 V
RCV	Equation (3.57)	113.8 Ω	108 Ω
XP	Equation (3.59)	0.3511	0.3511
MC	$0.5\cdot(1-\mathrm{XP})$	0.3245	0.3245
IK	$\frac{\mathrm{VER}\cdot(1-\mathrm{XCJE})\cdot\mathrm{CJE}}{\mathrm{TAUB}}$	14.17mA	17.69 mA

Table 6.6 Collector epi-layer model parameters at 300K, calculated from process characteristics and optimized [13].

Model Parameter	Initial Process Calculation		Optimized at 300K ambient temperature
	Method	Value	
TAUE	Equation (2.6)	1ps	213.8fs
TAUB	Equation (2.7)	3ps	390.7fs
TEPI	Equation (2.8)	10ps	85.73ps

Table 6.7 Transit time model parameters at 300K, calculated and optimized [13].

6.4 Temperature coefficient and bandgap model parameters

The Mextram 504.7 model responses to temperature change. As the simulation temperature shifts from the model reference temperature the values of particular model parameters change. The model parameters that are temperature dependent and their temperature equations were reviewed in Section 3.6. Fifteen temperature model parameters are used to define the temperature behavior of other model parameters. The temperature effects are inversely proportional to the mobility. The DeGraaf's mobility model [39],[42] is supported by Mextram developers as the means of defining the model temperature coefficient parameters based on the doping concentration. The temperature coefficient model parameters values were determined by applying the doping concentrations of Table 5.1 to the DeGraaf mobility model plots in the Mextram Parameter Extraction manual [35]. The extracted results summarized in Table 6.8.

Parameter	Description from Process	Value
AQBO	Zero bias base charge temperature coefficient	0.363
DAIS	IS equation temperature coefficient	0.0
AE	Emitter doping temperature coefficient	0.2
AB	Base doping temperature coefficient	0.8
AEX	Extrinsic base doping temperature coefficient	0.5
AEPI	Epilayer collector doping temperature coefficient	1.0
AC	Extrinsic contact collector doping temperature coefficient	0.5
ACBL	Buried layer collector doping temperature coefficient	0.5
AS	Substrate doping temperature coefficient	2.0
ATH	Self heating temperature coefficient	1.2

Table 6.8 Temperature coefficient model parameters and values used in ambient temperature models

The value of the zero bias base charge temperature coefficient parameter, AQBO, was initially derived from the DeGraaf mobility plots. However, the final value of 0.363 for AQBO was derived from fitting the SiGe bandgap narrowing parameter DEG over temperature.

The temperature parameters above were used for all four ambient temperature models. The influence of these standard temperature parameters is limited due to the self-heating effects at each ambient temperature. The four ambient temperature model parameter sets were not fitted for any temperatures, other than their respective “at temperature” ambient value. The bandgap voltage model parameters in Table 6.9 were optimized to produce the best fit of all four ambient temperatures.

Parameter	Description from Process	Value
DVGBF	Bandgap delta of forward current gain	10.0mV
DVGBR	Bandgap delta of reverse current gain	-10.0mV
VGB	Base bandgap voltage	1.10V
VGC	Collector bandgap voltage	1.10V
VGJ	Base-emitter recombination bandgap voltage	1.18V
DVGTE	Emitter charge difference bandgap voltage	35.0mV
VGS	Substrate bandgap voltage	1.18V

Table 6.9 Bandgap voltage model parameters used in ambient temperature models

6.5 SiGe model equation approach

The electrical behavior of the SiGe HBT proved difficult to model at lower ambient temperatures. Two critical issues had to be resolved before detailed model fitting of the four “at temperature” ambient temperature data sets could precede.

The first problem encountered, was the Mextram 504.7 released model code did not perform adequately below 223K. The HBT’s unique behavior in a cryogenic temperature environment and numerical handling limitations required modifications for “at temperature”, ambient cryogenic temperature model operations. These issues and the modifications of Mextram 504.7 code are described in Section 6.9.

A second problem was discovered, once code modifications were implemented. Standard extraction routines could not produce a model parameter set which fit both the DC and AC data at all four ambient temperatures in the wide temperature range. The standard parameter extraction routines for the Mextram model release apply to the Mextram Si only equation version. SiGe HBT electrical behavior is often adequately represented by utilizing a standard extraction approach and the Si implementation of base charge defined in Equation (3.27). For those SiGe processes, the model parameter sets are derived by the parameter extraction routines published with the model release. However, it was found that neither the Si only model or standard routines were able to represent the SiGe base HBT behavior over such a wide temperature range.

The output characteristics measurement of collector current, IC, as collector emitter voltage, VCE, is swept across the full operating range while a constant base current is applied could not be fitted to the Si only base charge equation version of Mextram 504.7. Specifically, the Early voltage parameters, VEF and VER, were unable to produce the needed collector current across the linear operating region of the DC output curves. Also, the high current parameters were unable to produce the f_T rolloff beyond ICmax in the AC data. This problem was resolved by including the SiGe bandgap effects in the modeling of the four ambient temperatures.

Development of the SET, single expansion temperature parameter, model and parameter set necessitated the need for a common modeling approach of the output characteristics for each of the four ambient temperature models. The Mextram SiGe bandgap Equations of (3.30) were used and the model parameters were fitted based on the behavior of internal model variables. Optimization of the model parameters was based on internal model variables in addition to the terminal currents and voltages.

The measurement data and simulated model performance of the 300K output characteristics are shown in Figure 6.7. The collector current in the linear operating region is essentially the total transfer current, I_N, defined in Equation (3.15) and repeated below.

$$I_N = \frac{I_f - I_r}{q_B} \tag{6.1}$$

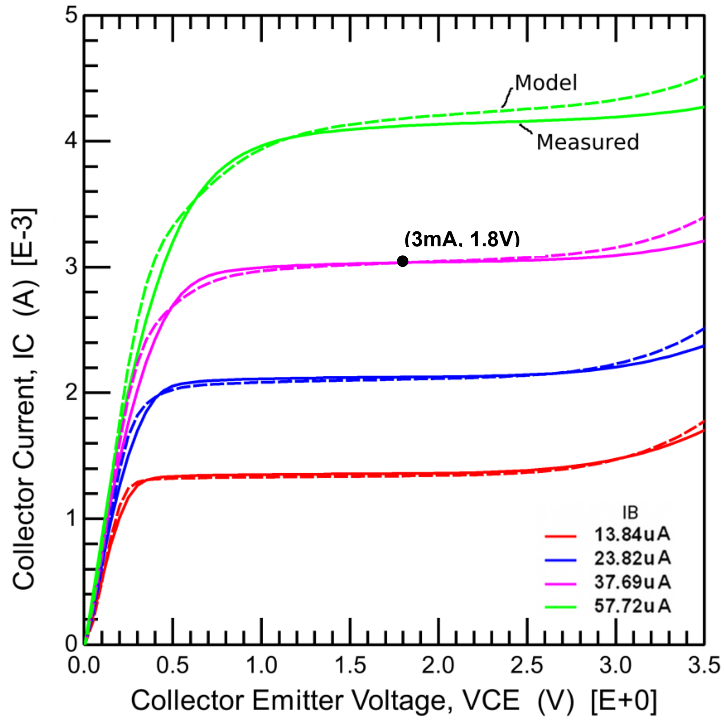

Figure 6.7 Output characteristics at 300K ambient temperature. Measured data is the solid line and model simulation is the dashed line.

By analyzing the internal variable contributions of I_f, I_r and q_B across the simulation of output characteristics at each ambient temperature the model parameters could be optimized. The internal variable of forward current, I_f, was defined in Equation (3.16) and the reverse current, I_r, was defined in Equation (3.17). The internal variables, I_f and I_r, for the 300K ambient model of Figure 6.7 are shown in Figure 6.8. At a bias of VCE=1.8V and base current of 37.7μA, the model collector current is 3mA but I_f=8.73mA and I_r=11.7 μA. Therefore, normalized base charge, q_B, is extremely influential to the fitting of the collector current.

The normalized base charge, q_B, derived from the SiGe base implementation of Equation (3.30) for the 300 K output characteristic simulation above is shown in Figure 6.8 below. The corresponding value of q_B for the constant base current of 37.7 μA varies as function of collector emitter voltage as would be expected due to basewidth modulation effects. At VCE=1.8V the normalized base charge, q_B, is 2.873.

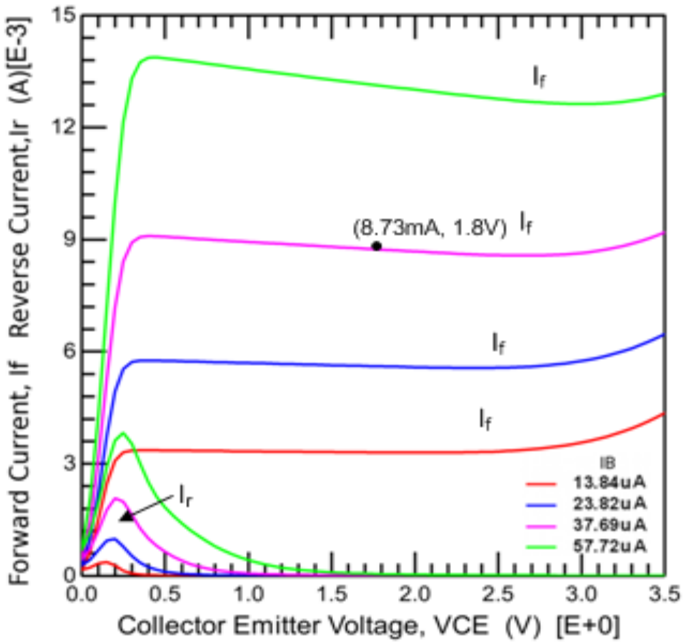

Figure 6.8 Internal model variables, I_f and I_r, as a function of the output characteristics simulation at an ambient temperature of 300K.

The Mextram model provides two options in the definition of current in terms of normalized base charge, q_B [13]. The base charge equation Early effects contribution can be defined in terms of Si only or it can include the effects of a SiGe linear graded bandgap. The Early effects contribution to the normalized base charge can be calculated with: either the Si only definition, q_0^Q, of Equation (3.27), or with a SiGe base definition, q_0^I, in Equation (3.30). The two implementations were described in Sections 3.2.2.1 and 3.2.2.2, respectively. The SiGe base equation is activated by one additional parameter, DEG. The SiGe base bandgap narrowing effects, $\Delta E_{G(grade)}$, are represented by the parameter DEG.

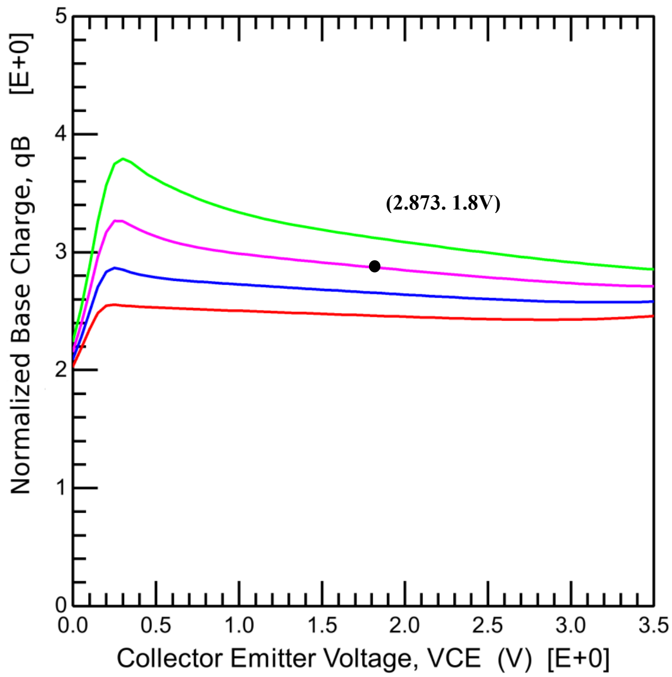

Figure 6.9 Internal model variable of normalized base charge, q_B, as a function of the output characteristics simulation for an ambient temperature of 300K.

The theoretical physics of the SiGe base transistor operation were described in Chapter 2. In Chapter 5, process characteristics of the SiGe HBT modeled were described. The base has a trapezoidal Ge% concentration profile with the Ge% linearly decreasing from the collector side of the base to emitter-base interface [21]. In Section 5.1 the process information of the SiGe HBT indicated that the linear graded Ge% concentration produced a bandgap narrowing in the base due to Germanium, $\Delta E_{G(grade)}$, of approximately 37.5 meV [21]. This was the initial value of DEG used in optimizing the 300K model parameter set.

The final values of DEG for each of the four ambient temperature model parameter sets was determined by multiple optimizations of four primary parameters: DEG, VER, VEF and BF. The parameter optimizations were fitted using constant base current biased output characteristics of the collector current, IC, and normalized base charge, q_B, of Equation (3.21). The response of q_B in the DC output simulations at each temperature assisted in defining each DEG final value.

The internally calculated value of q_B was analyzed in simulations by utilizing the custom modeling method illustrated in Figure 4.2. It was found that the value of q_B, implemented with the SiGe base Early effects, needed to be less than 30 across the VCE bias range of the entire DC output characteristics for a good fit of both DC and AC characteristics. There was a peak value of q_B that was unique to each ambient temperature. The final value of DEG for that ambient temperature was determined when both a low, unique value of q_B and good DC and AC fits were achieved. The resulting values of DEG for the four ambient temperature models are listed in Table 6.10.

Ambient Temperature	DEG
300K	41.0meV
223K	36.8meV
162K	32.8meV
93K	26.8meV

Table 6.10 Final parameter values of DEG for each ambient temperature

Once, the values of DEG were finalized for each temperature all other parameters were determined. The parameters: VEF, VER, and BF were then responsive to optimization when fitting the simulated output characteristics to the measured IC output data. The behavior of q_B in the output characteristics for each ambient temperature model is plotted in Chapter 7.

6.6 Parameter extraction from measurements at the four ambient temperatures

The parameter extraction methodology of the Mextram model release encourages modelers to determine model parameter values by directly extracting parameter values from measurements. Optimization of parameters by fitting the simulated data to the measured data is not encouraged. The standard parameter extraction techniques are dependent on one or only a very few parameters dominating the model equations that represent a measurement region. This approach works well if the device modeled has clearly defined operating regions. However, that was not the case for the advanced SiGe HBT modeled over the expansive temperature range. The DC and AC data of the device modeled was reviewed in Chapter 5. Review of the data at each ambient temperature showed the distinct operating regions shrinking as the temperatures decreased. The reduced operating regions cause the parameter influences to expand beyond the intended region of dominance. Direct extraction from data had to be replaced with custom optimizations of parameters over single and adjacent transistor operating regions. A common approach to parameter extraction at each ambient temperature was taken whenever possible. Parameter extractions directly from measurements as described in Figure 6.4 were used to obtain initial values at the four ambient temperatures. The data trends over temperature and the extraction similarities of each measurement type are summarized in the following subsections. The resulting fitted model at each ambient temperature is presented in Chapter 7.

6.6.1 Output measurements, IC versus VCE

Comparison of the output measurement collector currents at the four ambient temperatures indicates the device's performance varies due to temperature. An output measurement biased at a constant IB=10 μA is used in Figure 6.10 to compare the device performance over temperature. In the linear region, IC is found to increase as the ambient temperature decreases to 162K. IC peaks at 162K decreases at the lower temperature, 93K. Since the same base current was applied at each temperature the variation in collector current resulting from temperature is the result by β_f changing.

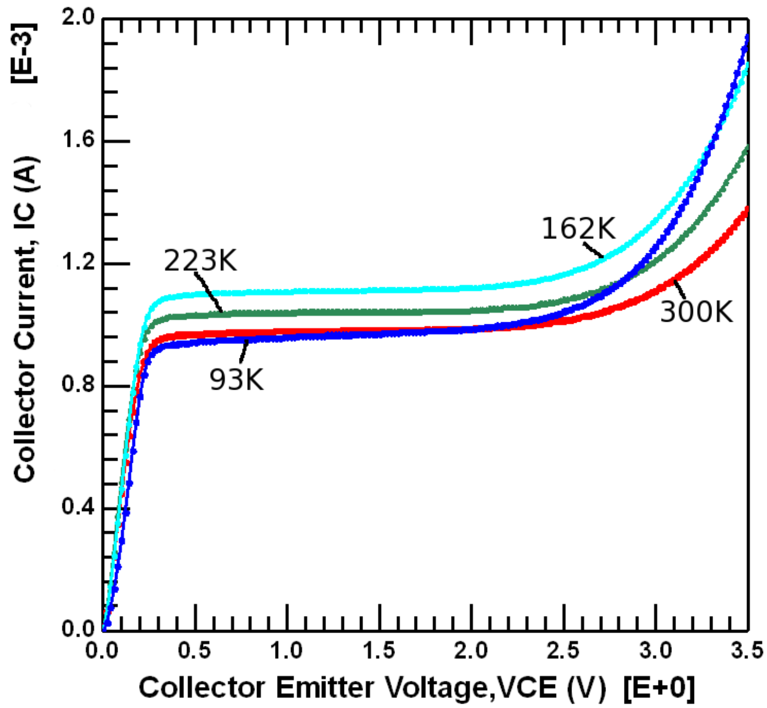

Figure 6.10 Temperature comparison of output measurements, IC vs. VCE. Base-biased with constant IB=10µA at four ambient temperatures.

The measured IC of the constant base bias output characteristics allows the saturation, quasi-saturation, high-level injection and linear regions of operation to be defined. The HBT model equations represent all four operating regions. Each operating region can be associated with a corresponding group of model parameters that have strong influences on the IC equation in each region. Each ambient temperature output measurement operating region can be optimized.

The reverse model parameters and external collector resistance dominate in the saturation region. The collector epi-layer parameters and knee current, IK, are influential to IC in the quasi-saturation and high-level injection region. The Early voltage parameter, VEF, is determined from the linear region. The VCE biases at which the device is no longer linear due to breakdown effects on the high end or quasi-saturation on the low end can be identified. A linear operating region for modeling purposes was defined for each ambient temperature in Chapter 5.

The reverse parameters, epi-layer collector parameters, avalanche parameters and Early effect parameters for each ambient temperature were extracted from the corresponding family of curves for that temperature. The ambient temperature model and fitted results are shown in Chapter 7.

6.6.2 Self-heating parameter extraction from output measurement, VBE versus VCE

Self-heating can be determined from the measured base-emitter voltage of an output-characteristic measurement biased with a constant base current bias applied [13]. The measured base-emitter voltage of the output measurement above which had a constant IB=10μA applied at the four ambient temperatures is shown Figure 6.11. The measured VBE begins to decrease in the linear region as VCE increases for all four ambient temperatures. When self-heating occurs in a device the measured base-emitter voltage will not be constant, but will decrease as the collector-emitter voltage increases.

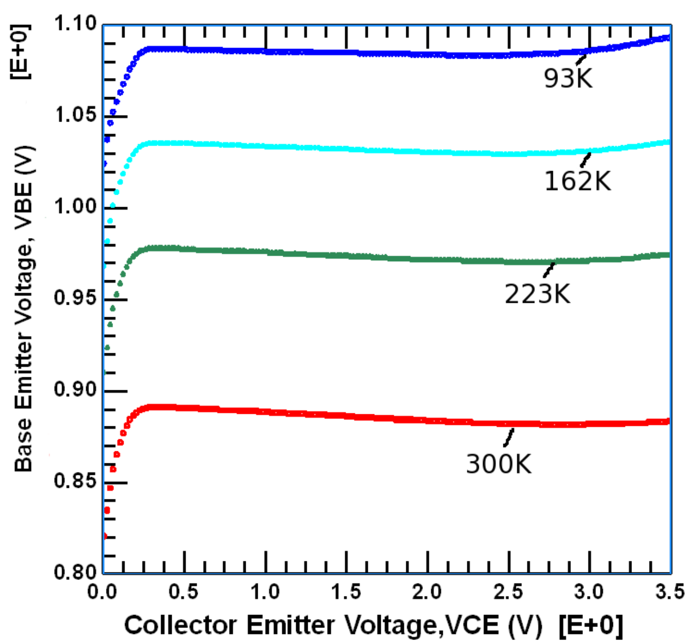

Figure 6.11 Temperature comparison of output measurements, VBE vs. VCE. Base biased with constant IB=10μA at four ambient temperatures.

The standard Mextram 504.7 self-heating model in Section 3.5 has two parameters RTH and CTH and was used for all work. The thermal impedance parameter, RTH, is directly extracted from the VBE curves. The thermal capacitance parameter, CTH was defined to be 241ps based on the physical characteristic of 1μA/RTH [41],[35]. The 300K temperature value for CTH was used for all four ambient temperatures.

Standard extraction techniques place the self-heating analysis before parameter extractions from high current and voltage operating region. Significant self-heating affects the parameter extractions results in the higher biased regions. Quasi-saturation and high level injection are the primary influences at high collector currents and voltages. These measurements could be equally influenced by a rise of the device temperature due to self heating. The high current/voltages operating region parameters affected by self-heating are RCV, SCRCV, IHC, IK, TAUE, TAUB, and TEPI.

The self-heating model of each ambient temperature was finalized by optimizing RTH as the model fits improved for the high current parameters. Optimization of RTH needed to an iterative approach with the high current parameters in order to find a balance of effects between the DC measurements and AC measurements.

6.6.3 Gummel measurements

Forward Gummel measurements provide a complete description of the bipolar device's DC forward linear operating state at a particular VBC bias. A common modeling approach for all ambient temperatures was needed to develop the SET model. Similar extraction and optimization techniques were applied to the three injection operating regions: low-level, mid-level and high-level of the DC Gummel measurements as shown in Figure 6.4.

In Chapter 5, the Gummel measurements at four ambient temperatures were presented and initially characterized. The collector current behavior in the DC linear operating region was compared over the full modeling temperature range. All four ambient temperature Gummel measurements of the measured collector current, IC, versus applied base-emitter voltage, VBE, are plotted in Figure 6.12 and their linear behavior summarized in Table 6.11. The device doesn't exhibit any low level IC leakage at any temperature modeled. However, the IC mid-level region slope is changing at lower temperatures. The non-ideality factor, NF, is clearly not the ideal value of one at lower temperatures. Therefore, the ambient temperature Mextram model was modified to include a forward non-ideality factor, NF, and a reverse non-ideality factor, NR for equivalence. NF was characterized at each temperature in Chapter 5. These

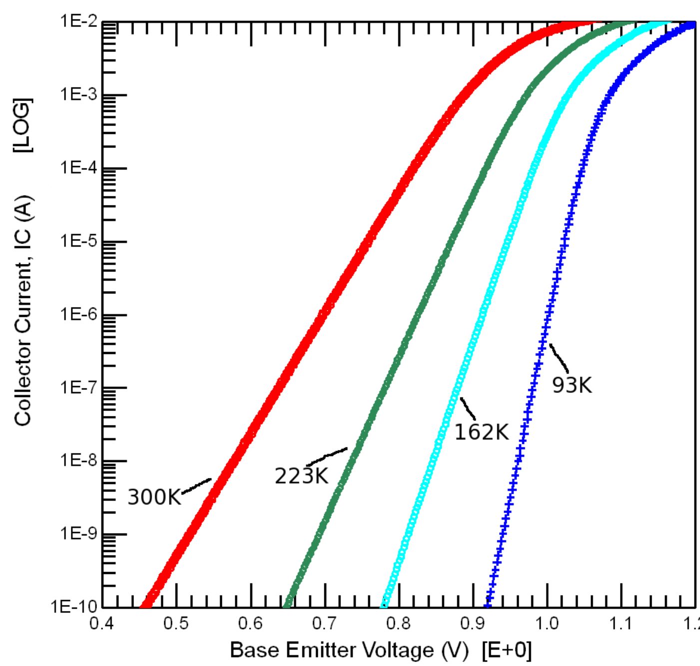

Figure 6.12 Gummel measurements of collector current, IC, vs. base-emitter voltage, VBE, at four ambient temperatures: 300K, 223K, 162K, and 93K. All measurements biased at VBC=-1V.

values were used in the ambient temperature models. The characterization of parameters IS and IK in Chapter 5 provide initial parameters values that were optimized in Chapter 7 to accurately fit all DC and AC measurements. The IC measurements over temperature extend beyond the model range in Figure 6.12. The device model will be fitted to a bias operating range of IC from

50 nA to 4mA. The range is limited by the measurement resolution of IB on the low end and self-heating plus AC current gain degradation on the upper end.

Ambient Temperature	IS A	NF	IK A
300K	2.40E-18	1.00	1.2mA
223K	3.76E-25	1.00	0.9mA
162K	9.56E-34	1.04	0.5mA
93K	4.10E-55	1.10	0.1mA

Table 6.11 Gummel measurement characteristics, IS, NF, and IK were extracted for the four ambient temperatures.

The Gummel measurements' relationship of base current, IB, as a function of temperature is summarized in Figure 6.13. A small amount of low-level injection base current leakage

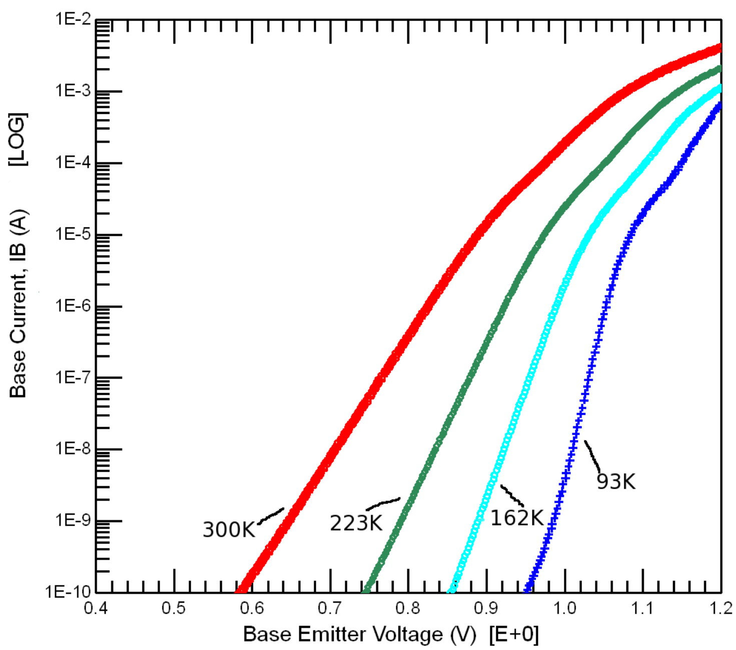

Figure 6.13 Log(IB) vs. VBE of Gummel Measurements at VBC= -1V for ambient temperatures: 300K, 223K, 162K, and 93K

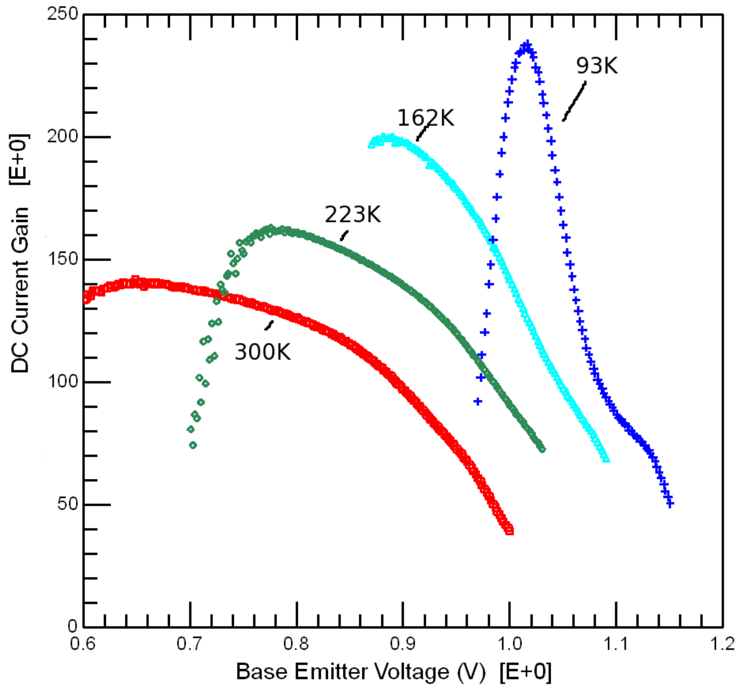

Figure 6.14 β_f vs. Base Emitter Voltage of Gummel measurements at VBC= -1V for ambient temperatures: 300K, 223K, 162K, 93K

begins to occur at the lowest temperature, 93K. The mid-range of IB was found to be very sensitive to reverse early effects.

The behavior of the IB curves changes in the high-level injection region as the temperature decreases in Figure 6.13. At lower temperatures a small kink in the IB knee current begins to occur in the high-level injection region. This behavior is attributed to an increase in quasi-saturation effects at lower temperatures [23].

The Gummel measurements' relationship of DC current gain, β_F, as a function of applied base-emitter voltage, VBE, for all four ambient temperatures is plotted in Figure 6.14. The β_F mid-level range of VBE dramatically decreases as temperature decreases. The results are summarized in Table 6.12. Both IB and IC are contributing to the β_F behavior.

Ambient Temperature	β_F Mid Range	VBE Mid Range	IC Mid Range	ΔIC Mid Range	ΔVBE Mid Range
300K	130	0.654V to 0.788V	0.2μA to 30μA	29.8μA	0.134V
223K	150	0.792V to 0.880V	0.2μA to 16μA	15.9μA	0.088V
162K	192	0.890V to 0.930V	0.2μA to 3μA	2.8μA	0.040V
93K	230	1.008V to 1.024V	2.0μA to 5μA	3.0μA	0.016V

Table 6.12 β_F and mid-range behavior of the Gummel measurement at VBC= -1V for ambient temperatures: 300K, 223K, 162K, 93K

The behavior of β_F as a function of IC at all four ambient temperatures is plotted in Figure 6.15. The current gain is increasing as the ambient temperature decreases. The beginning of high level injection region is similar at 300K and 223K. However, at 162K the high-injection region overlaps the mid current region making it difficult to distinguish the influence of VER and IK in both regions. Optimization in this region required very individual data region definitions.

Several secondary effects had significant influences on both the base and current behavior. The contribution of self-heating modified the internal base-emitter voltage and had a large influence on the parameter fitting in the mid-level current range as well as the high-level current region. The increase in device temperature caused by self-heating also increased the contribution of the forward current gain bandgap parameter, DVBGF. The large parasitic resistances of the device are influencing the base current and collector current behavior in both the mid-level and high-level current regions. These multiple influences in the two regions greatly decrease the ability to directly extract parameters from the specific measurement regions. Parameter optimization was needed to define the balance between operating regions.

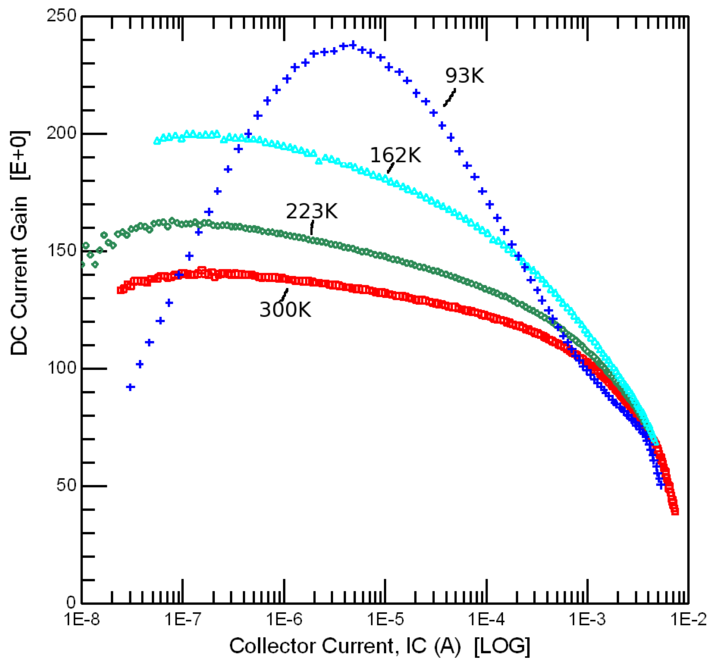

Figure 6.15 Current Gain, β_f vs. Log(Collector Current) of Gummel measurements at VBC= -1V for ambient temperatures: 300K, 223K, 162K, 93K

6.6.4 Summary of AC measurements biased at VC= -1V

The four ambient temperatures S-parameter measurements and their respective translations to cutoff frequency, f_T, as a function of collector current were presented in Chapter 5. The modeling of AC data over the wide temperature range will focus on the format of f_T versus Log(IC) as shown in Figure 6.16. Parameter extraction of AC measurements relied on the optimization of the transit time parameters, high-current parameters and the quasi-saturation parameters [35]. The high-current parameters and quasi-saturation parameters had a large influence on both the DC and AC data to the extent that the output measurement and the f_T curve had to be optimized simultaneously. The peak regions of the f_T curves are modeled through optimization of the base and emitter transit time parameters, TAUB and TAUE. Particularly TAUE, is in control of the peak f_T response through the emitter charge branch, Q_E, of the Mextram model. The emitter charge is derived in Equation (3.42) from the calculation of the hole density of the emitter. The hole density is proportional to the electron density. In Section

6.7.2 we show that the relationship between current and junction voltages requires a non-ideality factor. This modification of current translates to a requirement for the modification of hole density as well. The emitter charge non-ideality factor parameter, MTAU, is already defined in Q_E and will service that purpose. Typically the emitter charge non-ideality factor, MTAU, is set to 1, but at lower cryogenic temperatures MTAU was found to increase beyond 1.

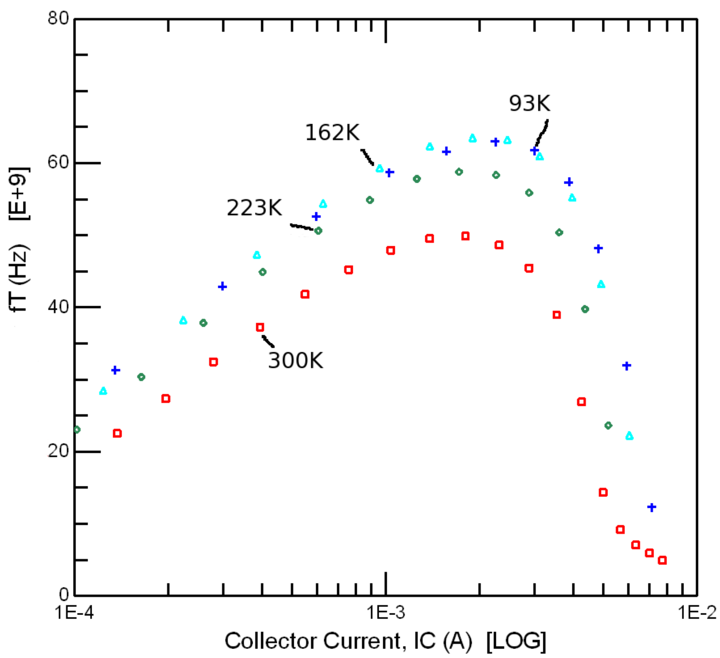

Figure 6.16 f_T vs. Log(Collector Current) for bias of VBC= -1V at ambient temperatures: 300K, 223K, 162K, 93K

6.7 Modifications of Mextram 504.7 code for cryogenic temperatures

The first issue encountered was in simulations below 223K. The Mextram 504.7 released model code would no longer generate current when the HBT was biased in the forward linear operating region. A careful accounting of each branch contribution led to the discovery that the numerical limiting feature of the code was activated and calculations of exponential functions for cryogenic temperatures were not correct.

The second issue was the discovery of a need for a non-ideality factor model parameter in the generation of DC collector current. The Mextram 504.7 code was modified to include this parameter in exponential calculations of the base-emitter voltage. A second parameter was also added to represent the reverse non-ideality factor, NR. This parameter provides a balance between the reverse current and forward current.

6.7.1 504.7 Mextram model is numerical limited below 145K

The standard Mextram 504.7 code was evaluated to determine its ability for cryogenic temperature range operation. Problems were found with the cryogenic temperature performance of the standard 504.7 code. As the TEMP, simulation temperature or TREF, model temperature, was decreased below 145K the standard model equations were unable to produce DC current. Each branch of current in the Mextram Verilog-A code was reviewed. This work found that the cryogenic temperatures were triggering the standard Mextram code's numerical limiting functions and also challenging the quasi-saturation equation limits. The released Mextram code includes numerical limits to assist advanced analog circuits that struggle with non-convergence problems. Non-convergence issues were not encountered during any of the model simulations at cryogenic temperatures with the expanded numerical limits, but it is an issue that could occur with circuit designs in the future.

Mextram has mathematical limiting functions to prevent calculations greater than e^{80}[2]. As temperatures decrease below 145K the standard Mextram begins to limit branch current model equations that have the form of exponential functions, (V/V_t). The base emitter ideal diode branch, I_{b1}, and the forward component of the transfer current, I_f, are severely disrupted. The limiting behavior is demonstrated in the following table:

Temperature K	Thermal Voltage $V_T = \frac{k \cdot T}{q}$	$\frac{1}{V_T}$
300K	0.02584V	$38.695V^{-1}$
162K	0.01396V	$71.658V^{-1}$
148K	0.01275V	$78.437V^{-1}$
143K	0.01232V	$81.179V^{-1}$
133K	0.01146V	$87.283V^{-1}$
123K	0.01060V	$94.379V^{-1}$
93K	0.00801V	$124.824V^{-1}$

Table 6.13 Exponential relationship as a function of temperature which triggers mathematical limiting in Mextram 504.7 model release.

The model has testing and limiting ability for internal calculations that result in extremely small numbers. The numerical limits had to be adjusted for cryogenic temperatures.

6.7.2 Non-ideality factors, NF and NR needed below 223K

The Gummel measurements in Chapter 5 indicated that collector current, IC, needed a non-ideality factor, NF, in the exponential relationship at the colder temperatures. The ideality factor, NF was reintroduced to represent the primary $IC = IS * \exp\left(\frac{VBE}{NF * V_T}\right)$ relationship as the temperature decreases. The standard Mextram does not include NF. The developers of Mextram felt that current day fabrication techniques had improved to the stage that bipolar no longer needed a relationship other than NF=1, and therefore NF was not included in the exponential voltage relationship[54],[13]. The parameter NF is in the classic bipolar models of Ebers-Moll and Gummel-Poon. NF was defined as the ideality factor and it varied from .8 to 2 depending on the material, doping and fabrication techniques of the 1970's – 1990's [10].

The forward non-ideality factor parameter, NF, was introduced in the cryogenic modified Mextram code by modifying the variables to include NF in the exponential calculations of the base-emitter voltage divided by the thermal voltage. In the code the variables modified were eVb1e1 and eVb2e1.

A reverse non-ideality factor parameter, NR, was also introduced in the cryogenic modified Mextram code by modifying the variables that calculated the exponential of the base-collector voltage divided by the thermal voltage. The reverse factor was required to balance the forward factor. The value of NR should be set to the value of NF unless a offset voltage is needed in the output measurements. NR was absolutely essential to the successful use of NF in the parameter extraction and model fitting. NR must be set to the value of NF for the saturation region to correctly be formed in the model simulations.

7 Ambient temperature model results

The complexity of the cryogenic temperature parameter extractions was established in Chapter 6. The modified code described in Section 6.7 was compiled into the CRYO_504.7 Mextram model. This cryogenic Mextram model was used to extract the four ambient temperature model parameter sets. The results of the four ambient temperature model parameter sets are discussed this chapter. The model parameter values of each ambient temperature are presented with the measurement to which they were influential. All four ambient temperature model parameter sets are summarized in Appendix B.

The DC response of each model consists of the output characteristics and the Gummel measurement. The model results of the output characteristics for all four ambient temperature CRYO_504.7 Mextram models are presented in Section 7.1. The gummel measurements and model results at each temperature are found in Section 7.2. AC behavior is represented by the f_T response, which was based on the S-parameter measurements. The model results of the f_T performance are presented in Section 7.3.

7.1 Ambient temperature model results of output measurements

The output characteristic measurement encompasses the full forward operating range of the device. This measurement has a constant base current bias applied and the collector emitter voltage, VCE, is swept across the full forward voltage operation range. At each VCE bias point the collector current, IC, and the external base-emitter voltage, VBE, are measured. A model must accurately simulate the full operating range to be useful. It was very challenging to create a model parameter set for each cryogenic temperature which simulated simultaneously, all output operating regions: saturation, quasi-saturation, linear, and the non-linear high end voltage range.

The model results of each ambient temperature over the full output operating range are presented in Section 7.1.1.

The self-heating effects were significant at all four ambient temperatures in all operating regions except saturation. Therefore, the self-heating behavior had to be accurate before other model parameters could be accurately obtained. The output characteristics with biased constant base current were used to extract the parameter RTH and the model results are plotted at all temperatures in Section 7.1.2.

In order to fit the linear region of the output characteristics, modeling of the four ambient temperature measurements required a unique approach. The Mextram option of including the SiGe bandgap effects in the normalized base charge equations was implemented. The addition of SiGe bandgap effects allowed parameters to respond well while fitting the lower cryogenic temperature output characteristics. The results of all four ambient temperatures are presented in Section 7.1.3.

Modeling of the breakdown region of the output characteristics was done by optimizing the parameters associated with the avalanche current model equations of the Mextram 504.7 model. These parameter results are summarized in Section 7.1.4.

Modeling of the saturation and quasi-saturation effects proved difficult due to the strong interaction of multiple effects. Unique extraction methods were required for both operating regions. The model results and parameters extracted are presented in Section 7.1.5.

7.1.1 Model results of full range output characteristics

The goodness or fit of the CRYO_Mextram504.7 simulated model performance to the output measurement data of the four ambient temperature model parameters sets are shown in Figure 7.1, 7.2, 7.3 and 7.4.

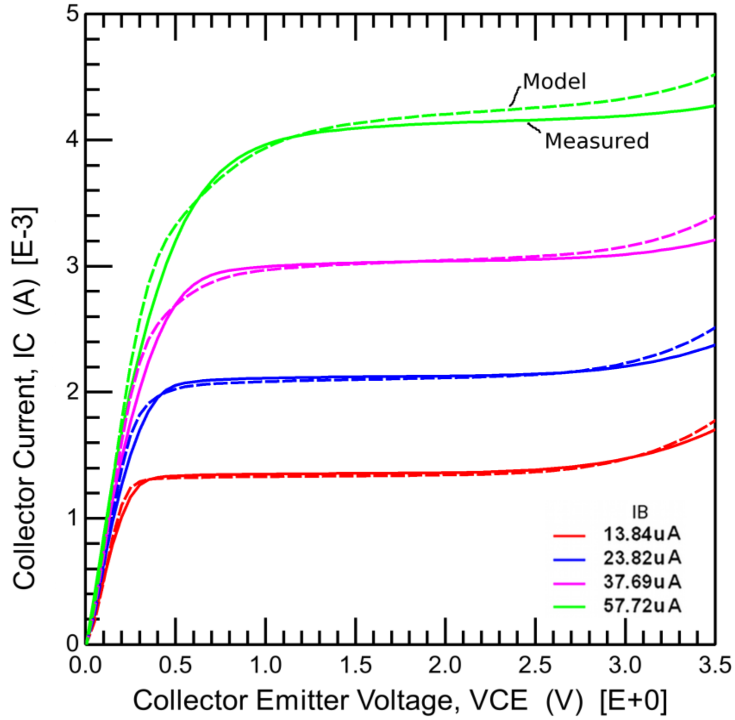

Figure 7.1 Output characteristics at 300K ambient temperature. Measured data is the solid line and model simulation is the dashed line.

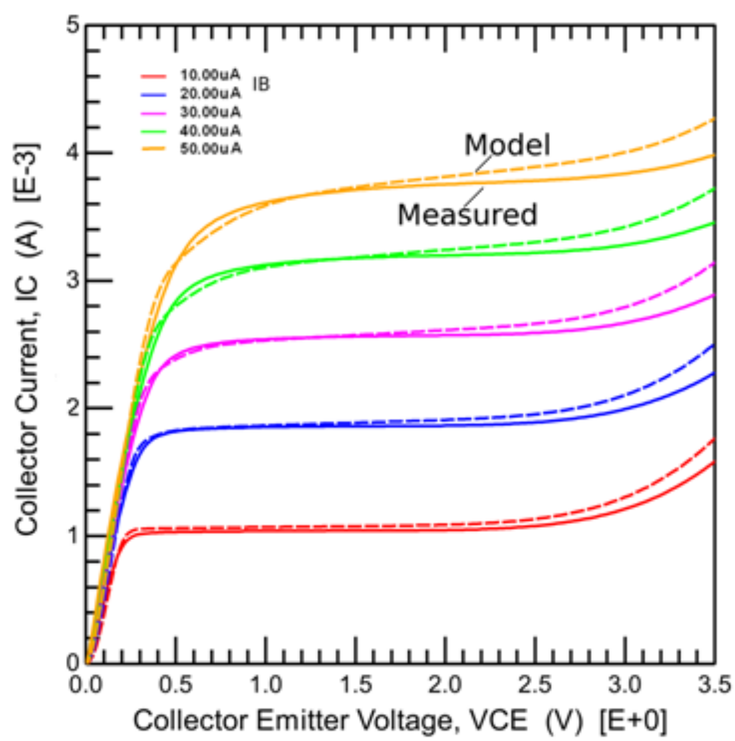

Figure 7.2 Output characteristics at 223K ambient temperature. Measured data is the solid line and model simulation is the dashed line.

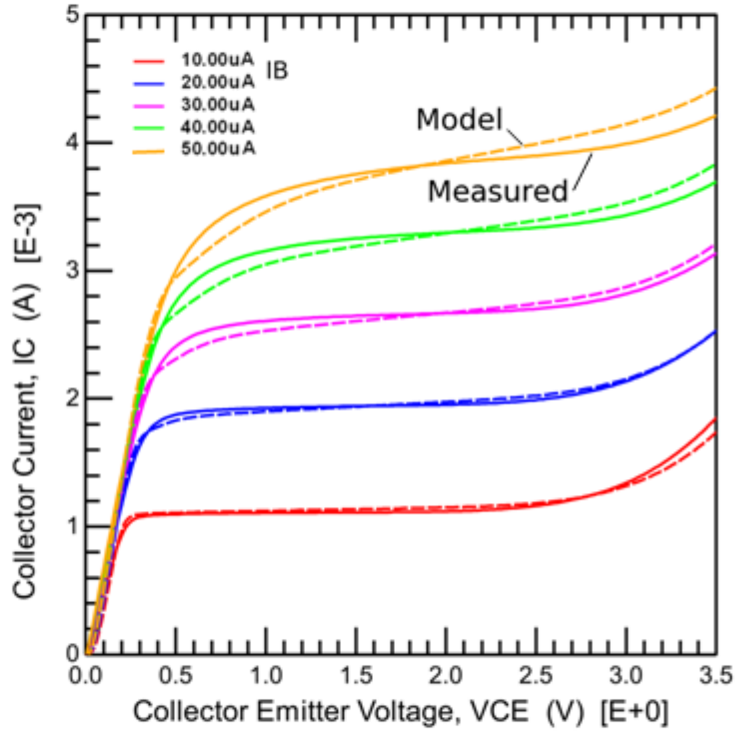

Figure 7.3 Output characteristics at 162K ambient temperature. Measured data is the solid line and model simulation is the dashed line.

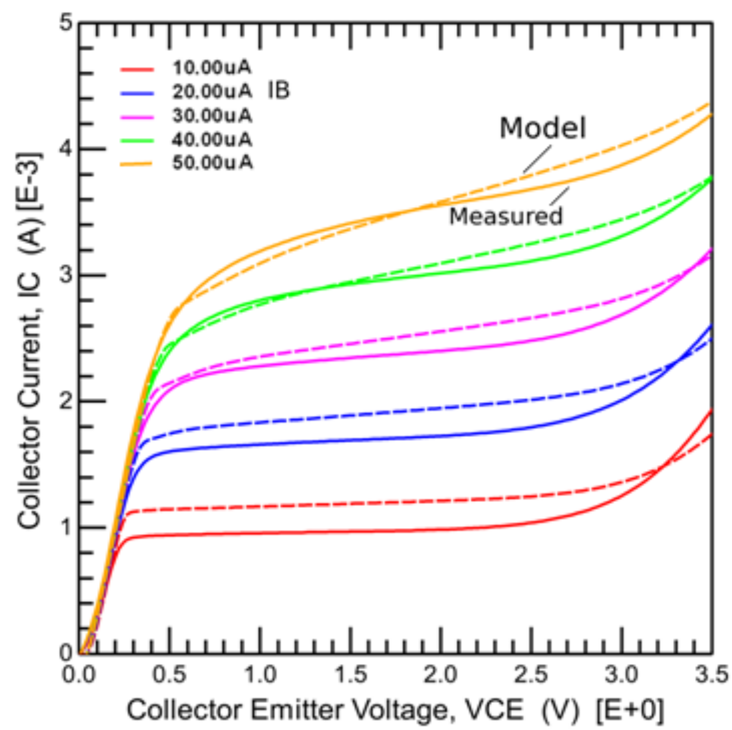

Figure 7.4 Output characteristics at 93K ambient temperature. Measured data is the solid line and model simulation is the dashed line.

7.1.2 Ambient temperature model results of output VBE response measurements for self-heating effects and RE extraction

Parameter RTH. The output characteristic measurements of Chapter 5 revealed the significance of self-heating. There was a large decrease in VBE, ΔVBE, as VCE is sweep and the base current is held constant. The change in VBE is attributed to the device temperature increasing as a function of the applied bias. The basic relationship between temperature change, ΔT, the device thermal impedance model parameter, RTH, and power dissipation, P_{Diss} are used in the self-heating analysis is defined in Equation (3.80), $\Delta T = RTH \cdot P_{Diss}$. The device power dissipation is determined by the standard Mextram 504.7 self-heating model described in Section 3.5. The Mextram model includes a thermal capacitance component as well. The thermal capacitance parameter, CTH was defined to be 241ps for all four ambient temperature models. This value was based on the physical characteristic of 1μA/RTH [41],[35]. The value of RTH for each ambient temperature model was determined by optimization in the linear region of the VBE response. The resulting values of RTH for the four ambient temperatures are listed in Tables 7.1. An RTH value of 5000Ω has large impact on the VBE applied bias at 300K. As the ambient temperature decreased, RTH decreased to 1500Ω at 93K. This high thermal impedance is consistent with IBM's findings on the SiGe HBT devices [55],[56],[57]. The influence of RTH at all four ambient temperatures was discussed in Section 6.6.2 and identified as one of the main factors that strongly affected the accuracy of other parameters. The model fit of VBE steps versus VCE of each ambient temperature model is shown in Figures 7.5a, 7.6a, 7.7a and 7.8a. The corresponding model temperature at each bias point for the four ambient temperature output measurement results are shown in Figures 7.5b, 7.6b, 7.7b, and 7.8b.

Parameter RE. The saturation and quasi-saturation regions of the output's VBE response was used to extract the constant emitter resistance parameter, RE. Optimization of RE to the VBE response in these regions was performed in conjunction with optimization of RE to the AC data measurements of f_T versus collector current. The resulting values of RE for each of the four ambient temperature models are listed in Tables 7.1. The value of RE increased by less than 2Ω over the very wide temperature range. Although the increase in resistance was small the initial value of RE is large and any change in value required accurate fitting of the AC data. The large value of RE is attributed to the small active emitter area.

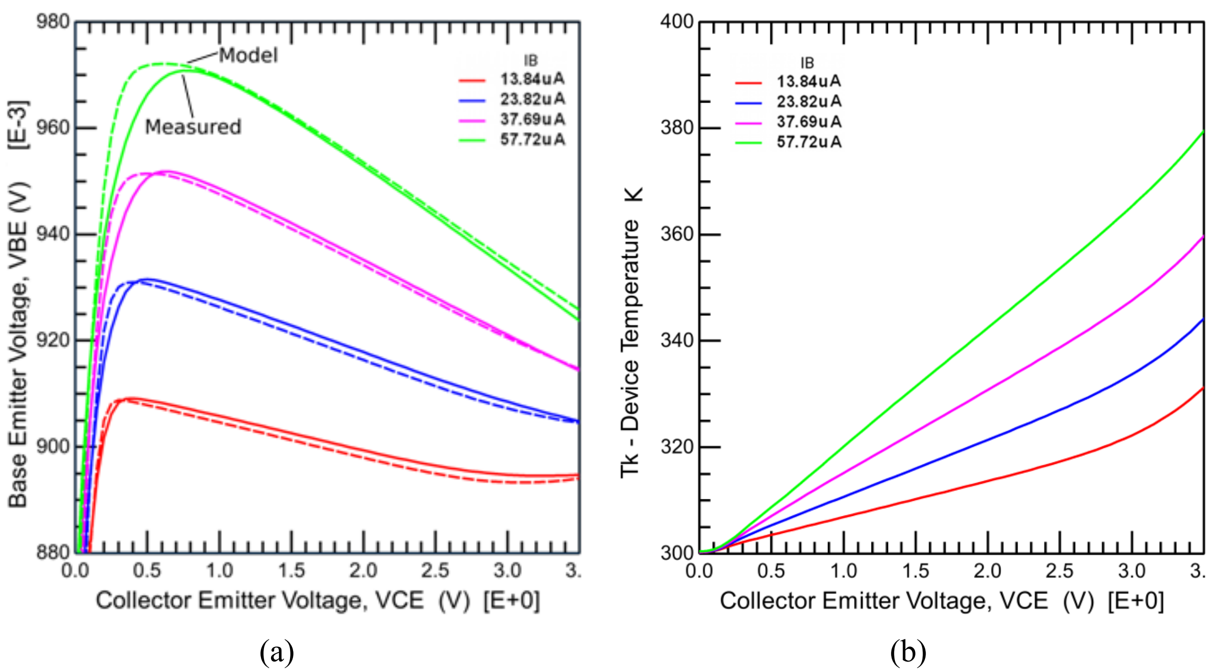

Figure 7.5 (a)VBE vs. VCE in 300K ambient temperature. Dashed lines are model simulation results and solid lines are measurement. (b)Model device temperature, Tk, at each output measurement bias point.

Model Parameter	300K Ambient Temperature	223K Ambient Temperature	162K Ambient Temperature	93K Ambient Temperature
RTH	5000 Ω	4542 Ω	3332 Ω	1500 Ω
RE	12.2 Ω	12.3 Ω	12.7 Ω	13.9 Ω

Table 7.1 Parameters, RTH and RE of the 300K ambient temperature model

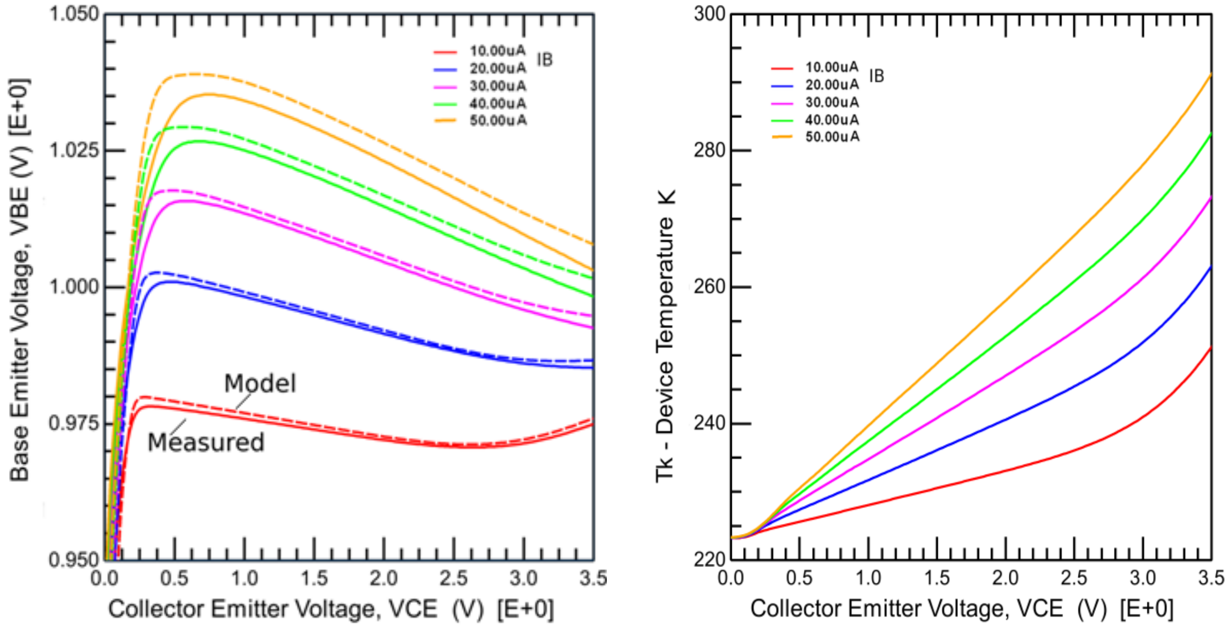

(a) (b)

Figure 7.6 (a)VBE vs. VCE in 223K ambient temperature. Dashed lines are model simulation results and solid lines are measurement. (b)Model device temperature, Tk, at each output measurement bias point.

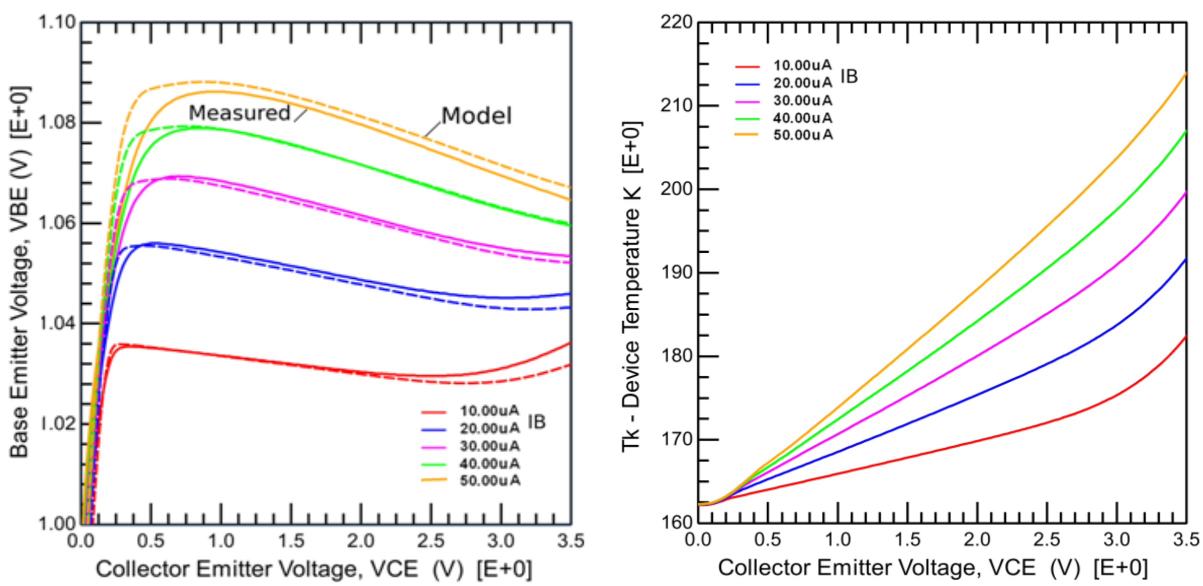

(a) (b)

Figure 7.7 (a)VBE vs. VCE in 162K ambient temperature. Dashed lines are model simulation results and solid lines are measurement. (b)Model device temperature, Tk, at each output measurement bias point.

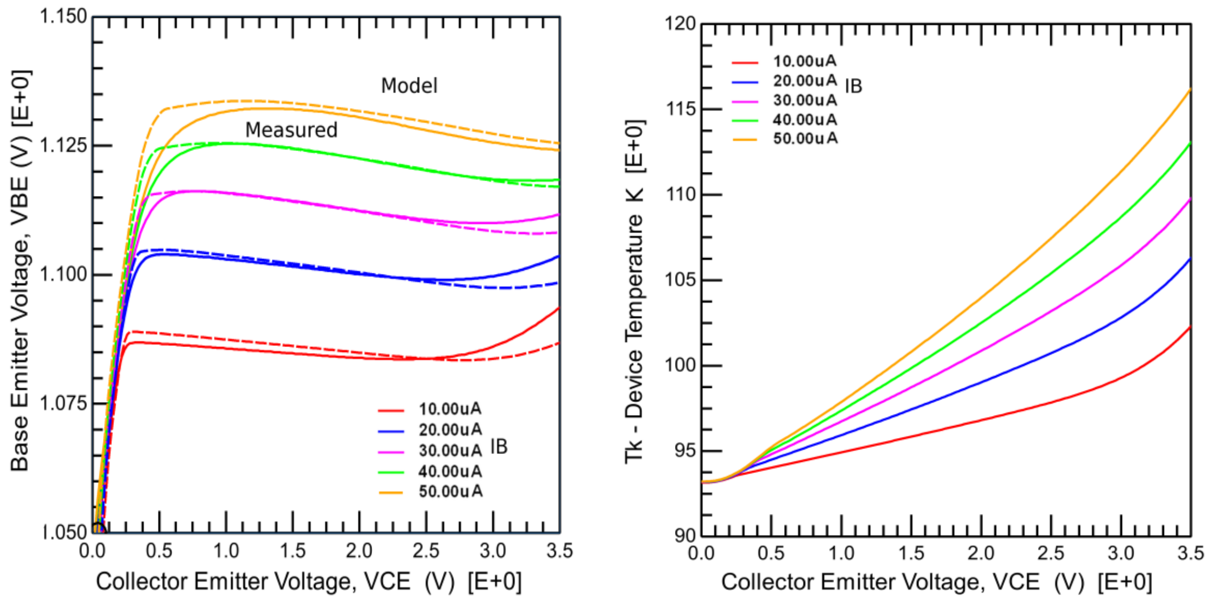

(a) (b)

Figure 7.8 (a)VBE vs. VCE, 93K ambient temperature. Dashed lines are model simulation results and solid lines are measurement. (b) Model device temperature, Tk, at each output measurement bias point.

7.1.3 Linear region of output characteristics optimized by SiGe base charge approach

The output characteristics in the linear region could not be modeled through parameter extraction by direct data techniques. But, an accurate fit of the full output curve range at cryogenic temperatures was possible with parameter optimization. The model parameters: DEG, VEF, VER and BF, were found to be very influential to the linear region of the output curves. The ambient temperature parameter values of each model at presented in Tables 7.2. By implementing the Mextram 504.7 model's SiGe base charge equations an accurate IC response was achievable at the cryogenic temperatures. The impact and use of the SiGe base charge approach to cryogenic parameter extraction approach was presented in Section 6.5. The approach required a joint effort of optimization and analysis of the contributors to the model's internal transfer current, I_N, defined in Equation (3.15) and repeated below.

$$I_N = \frac{I_f - I_r}{q_B} \tag{7.1}$$

The internal variable contributions of: forward current, I_f, and reverse current, I_r, and normalized base charge, q_B, of the output characteristics for each cryogenic temperature model are presented in Figures 7.9, 7.10, 7.11 and 7.12.

Model Parameter	300K Ambient Temperature	223K Ambient Temperature	162K Ambient Temperature	93K Ambient Temperature
DEG	41 mV	36.8 mV	32.8 mV	26.8 mV
VEF	151V	145V	141V	137.9V
VER	2.81 V	2.916 V	3.05 V	3.2 V
BF	244	328.4	453	1045

Table 7.2 Ambient temperature model parameters extracted from output characteristics

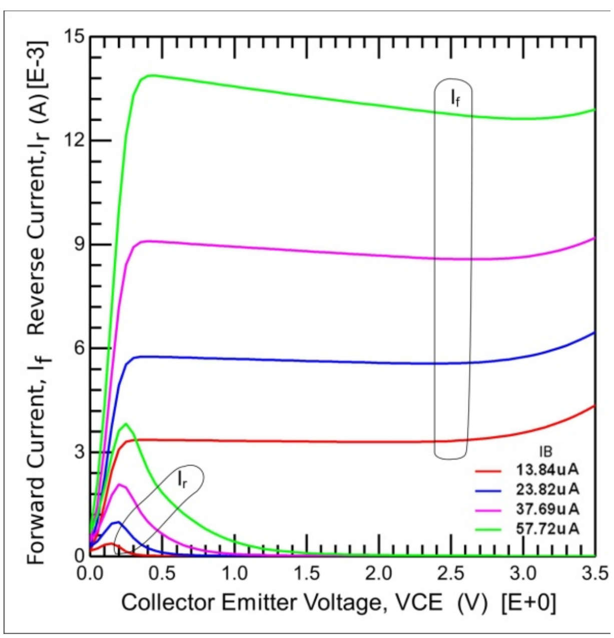

(a)

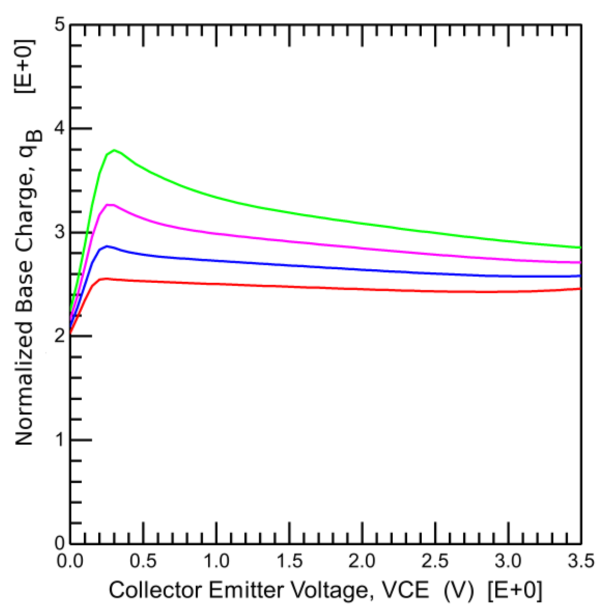

(b)

Figure 7.9 (a)Internal model variables, I_f and I_r, as a function of the output characteristics simulation. (b)Internal model variable of normalized base charge, q_B, as a function of the output characteristics simulation at an ambient temperature of 300K.

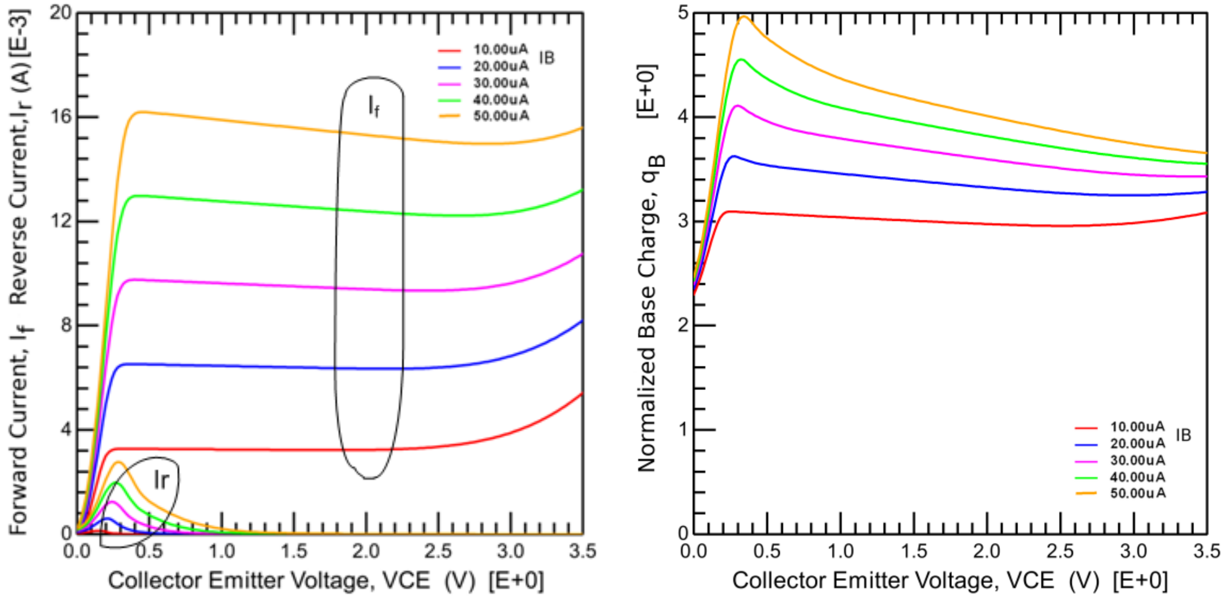

(a) (b)

Figure 7.10 (a)Internal model variables, I_f and I_r, as a function of the output characteristics simulation. (b)Internal model variable of normalized base charge, q_B, as a function of the output characteristics simulation at an ambient temperature of 223K.

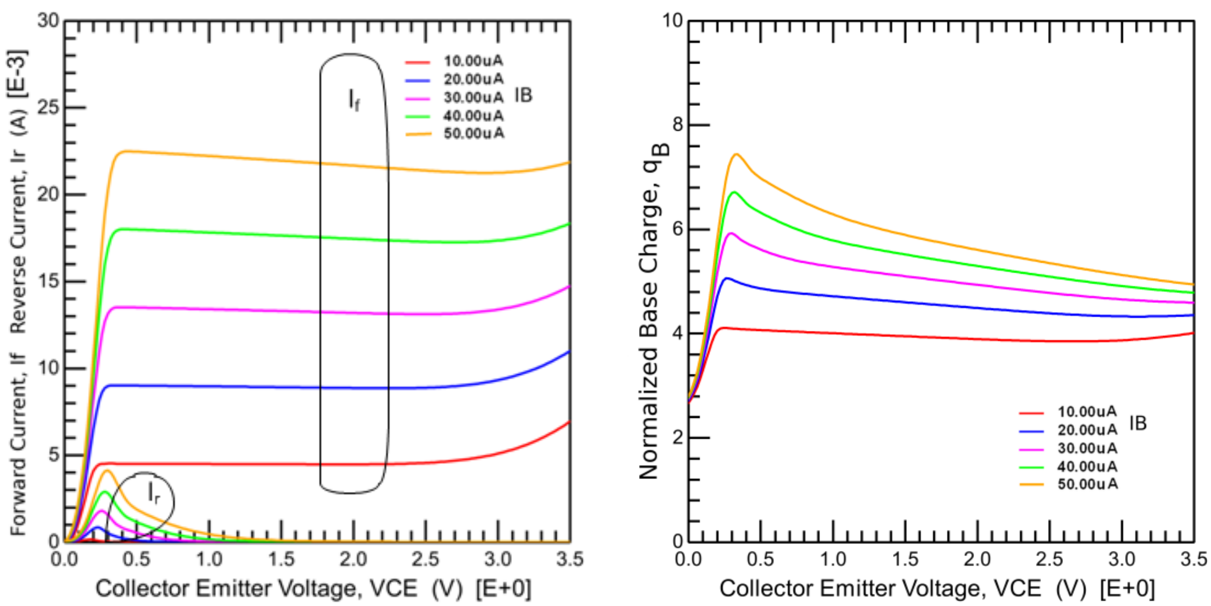

(a) (b)

Figure 7.11 (a)Internal model variables, I_f and I_r, as a function of the output characteristics simulation. (b)Internal model variable of normalized base charge, q_B, as a function of the output characteristics simulation at an ambient temperature of 162K.

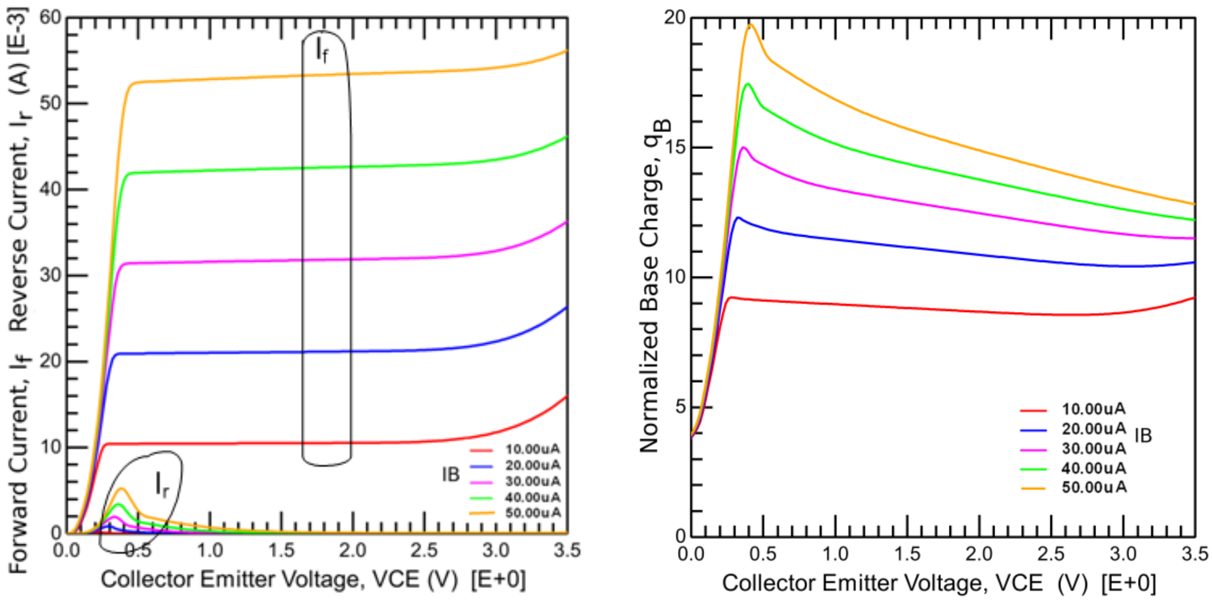

(a) (b)

Figure 7.12 (a)Internal model variables, I_f and I_r, as a function of the output characteristics simulation. (b)Internal model variable of normalized base charge, q_B, as a function of the output characteristics simulation at an ambient temperature of 93K.

Comparison of the four cryogenic temperature model I_f plots shows the dramatic increase in current from 12mA to 60mA and change in the current gradient of the linear region. The normalized base charge, q_B, value and trend also changed over temperature. The peak value of q_B, ranged from 4 at 300K to approximately 20 at 93K. The increase of q_B as temperature decreased illustrates the powerful influence of the SiGe bandgap narrowing term, DEG, decreasing and the reverse Early voltage, VER, increasing slightly. The impact of junction depletion voltages, SiGe bandgap narrowing effect, and the effective Early voltage values defined in $q_{B,}$ Equation (3.30), can be viewed in this one term. The impact of SiGe bandgap narrowing to modeling the output characteristics was discussed in Section 6.5. The extraction of the normalized base charge value as a function of DC bias and temperature gave the modeler the opportunity to fully monitor the influence of these parameters. During optimization, the value of q_B became too large if VER and DEG were not correctly balanced. Evaluating these effects during optimization of the collector current, IC, versus collector emitter voltage, VCE, output behavior was essential for an accurate fit of the full output voltage range.

7.1.4 Non-linear upper voltage range of the output measurement

The collector current exhibited breakdown behavior at the upper end of the output voltage range at all base bias levels and at all four ambient temperatures. This was modeled by the avalanche base current branch equations of the Mextram model defined in Section 3.2.6.3. The avalanche breakdown current is modeled with model parameters: WAVL and VAVL. The best fit of the non-linear region required optimization of these parameters. These model parameters were found to change as a function of ambient temperature at the lower temperatures. This dependence on temperature was incorporated into the SET model. These results differ from the standard Mextram model where direct data techniques are used to extract the avalanche model parameters. The two avalanche parameters, WAVL and VAVL are temperature independent in the standard Mextram 504.7 model. The avalanche model parameters of each of the four ambient temperatures are listed in Table 7.3.

Model Parameter	300K Ambient Temperature	223K Ambient Temperature	162K Ambient Temperature	93K Ambient Temperature
WAVL	245.1nm	245.1 nm	260nm	285nm
VAVL	0.800 V	0.800 V	0.400 V	0.100 V

Table 7.3 Avalanche model parameters of each ambient temperature model

The avalanche parameters shifting with temperature in the cryogenic temperature range was new. However, the optimization of the all the parameters influential in the higher output voltage range clearly concluded that these parameters had the dominate influence on collector current behavior in the breakdown region.

7.1.5 Saturation and quasi-saturation region of output characteristics, IC versus VCE

7.1.5.1 Saturation region

In the saturation region several effects are occurring at once. The base-collector junction is forward biased at the lowest VCE values. Therefore, the reverse parameters make a real contribution to the behavior of this region. Collector resistance is a dominating factor. The large impact that collector resistors have on the behavior of the collector current in the saturation region was discussed in Section 2.2. Finally the reverse Early voltage parameter, VER, has a tremendous influence on the collector current in the saturated region. Sensitivity analysis was done to determine the influence of each parameter. But the parameter VER had such an overwhelming influence that the weight of the other parameters could not be obtained and unique sensitivity approach was applied. Once the weighting of VER was determined the combination of parameters could be optimized to fit the saturation region.

Parameter NR. The reverse non-ideality factor, NR, was set to the value of NF in each ambient temperature model. It was found that a reverse non-ideality factor equivalent to the forward non-ideality factor was mandatory at the lower temperatures. Without the inclusion of NR there was an incorrect VCE offset present in the model.

Parameter VER. The effective reverse Early voltage parameter was the dominate parameter in the saturation operating region. The dominance of VER devalued the meaning of a basic sensitivity analysis. So VER was temporarily redefined by a factor of 10 and this temporary VER parameter was used in a sensitivity analysis to determine the weighting needed in the combination of parameter optimizations of the saturation region. Optimization of VER in the output measurement saturation region in combination with optimization of VER to the IB current of the mid-level Gummel measurement yielded a VER value that fit all DC measurements.

Parameter BRI. The extrinsic base current, I_{ex}, represents the ideal reverse base current branch described in Section 3.3.1. The reverse current gain parameter, BRI, in this model equation is has a strong influence on the collector current behavior in the saturation region. Optimization of BRI in the saturation region was the best method to determine the parameter value at each ambient temperature.

Parameters: IBR and VLR. The nonideal reverse base current, $I_{B3,}$ branch has a saturation current parameter, IBR and a crossover voltage parameter, VLR, which control the branch current relationship to the nodal voltage difference of VB1C1 as described in Section 3.3.2. The saturation current parameter has an influence on the collector current in the saturation region, so IBR was optimized in the saturation region at each temperature to determine the best value. Optimization of VLR indicated that it had minimal influence in quasi-saturation at the ambient temperatures. Therefore the value was set at 0.3V according to the recommendation of the Mextram standard parameter extraction procedures [35] for all ambient temperature models.

Parameters:RCC and RCBLI. These parameters have constant values that are not bias dependent. Each represents different regions of the external collector resistance. The sum of the two parameters equals the total constant external collector resistance, R_{Csat}, defined in Section 2.2. RCBLI is also influential in the behavior of the f_T versus IC response due to collector Miller effect response. This collector resistance is optimized to the data in the f_T region, ranging from the bias of ICmax to the upper bias limit. The value of RCBLI was determined by optimizing the both the DC output saturation region and the upper range of the AC data f_T response. The value of RCC is remaining component of the total collector saturation resistance.

7.1.5.2 Quasi-saturation region

The quasi-saturation behavior is defined by the Mextram epilayer model which is based on physical effects. The model equations are described in Section 3.2.5. The primary parameters of the collector epi-current model are the hot carrier current, IHC, variable collector resistance, RCV, space charge epilayer collector resistance, SCRCV, and epilayer smoothing parameter AXI. Two other parameters are utilized in the Mextram epilayer model; the diffusion voltage parameter, VDC, and the knee current parameter, IK. Typically these parameters are extracted from other measurement operating regions. However VDC and IK were found to have a strong influence in the quasi-saturation region of all four ambient temperature measurements which required optimizations.

Parameters: IHC, RCV, SCRCV, and AXI. These four parameters are the core of the epi-layer model equations for the epilayer current branch, I_{C1C2}. Typically they are extracted by equations based on physical relationships. However, optimization of these parameters was found to be the best method of obtaining an accurate fit in the quasi-saturation region. In Section 6.3 a comparison of calculations from the known physical characteristics to optimized values at 300K was made. The calculated parameter values could not support both DC and AC responses. The custom optimization was combined of two actions. One was the optimization of the parameters in the quasi-saturation region of the IC curves while simultaneously monitoring the internal model variable, I_{qs}. The current variable, I_{qs}, in Equation (3.61) defines the onset of quasi-saturation in the Mextram epilayer model equations. By monitoring the goodness of I_{qs} optimizations could be guided by physical analysis. The results were compatible with the AC response of the f_T curves.

Parameter VDC. The base-collector diffusion voltage parameter, VDC, value is typically defined by the physical calculation of Equation (3.56). However, all four ambient temperature models required optimization of VDC to fit its influence of both the DC and AC responses.

Parameter IK. The high level injection current parameter, IK, was found to have a significant influence on the behavior of the DC output curve quasi-saturation region and the higher current region of the AC f_T curves at all ambient temperature. Numerous iterations of optimizations of the DC and AC data were required. The Mextram implementation of the epilayer model which is based on physical effects reduces the influence IK as compared to the Gummel-Poon bipolar versions. However, optimizing IK accurately was found to critical to overall good fits.

Comparison of the model simulation to the measured data of the output measurement saturation and quasi-saturation region is detailed in the following plots. The measured data are symbols with each base bias current a defined color. The model simulation results are dash lines

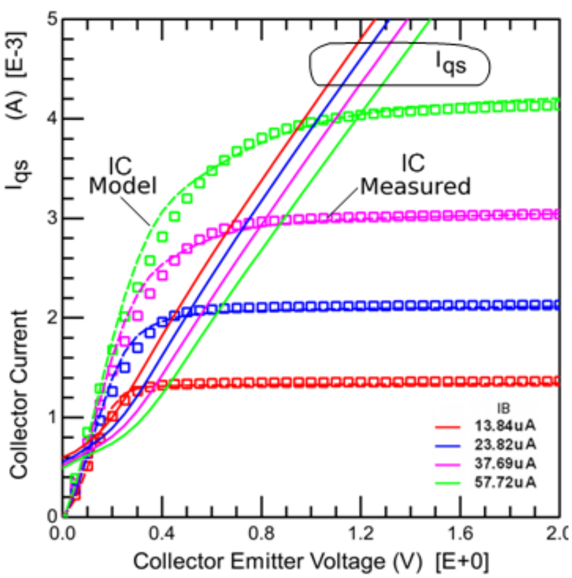

Figure 7.13 300K, saturation, quasi-saturation region of output measurement IC, I_{qs} vs. VCE. Measured data are symbols. Simulated results are dashed lines. Solid lines are the internal model variable, I_{qs}.

Model Parameter	300K Value
NR	1.0
VER	2.81 V
BRI	12.18
IBR	3.3E-18A
VLR	0.3V
RCC	41 Ω
RCBLI	20 Ω

Table 7.4 Saturation region model parameters, 300K

Model Parameter	300K Value
IHC	2.347 mA
RCV	108 Ω
SCRCV	301.4 Ω
AXI	0.2
VDC	0.8038 V
IK	17.69 mA

Table 7.5 300K quasi-saturation region model parameters

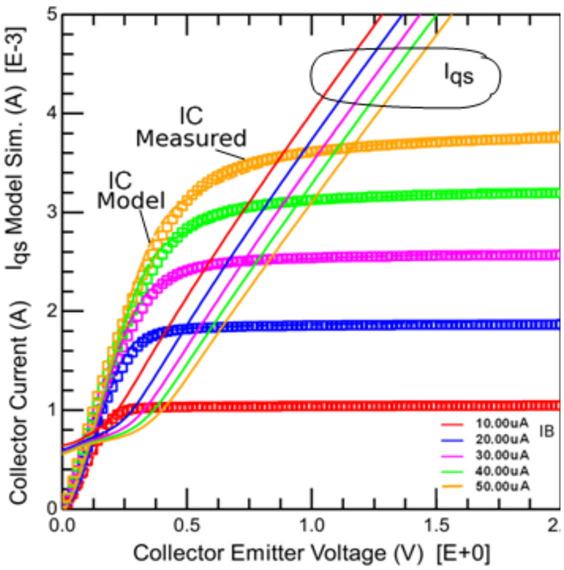

Figure 7.14 223K, saturation, quasi-saturation region of output measurement IC, I_{qs} vs. VCE. Measured data are symbols. Simulated results are dashed lines. Solid lines are the internal model variable, I_{qs}.

Model Parameter	223K Value
NR	1.0
VER	2.916 V
BRI	4.2
IBR	1.17E-26A
VLR	0.3V
RCC	60 Ω
RCBLI	20 Ω

Table 7.6 Saturation region model parameters, 223K

Model Parameter	223K Value
IHC	2.347 mA
RCV	115 Ω
SCRCV	301.4 Ω
AXI	0.2
VDC	0.880 V
IK	12.37 mA

Table 7.7 223K quasi-saturation region model parameters

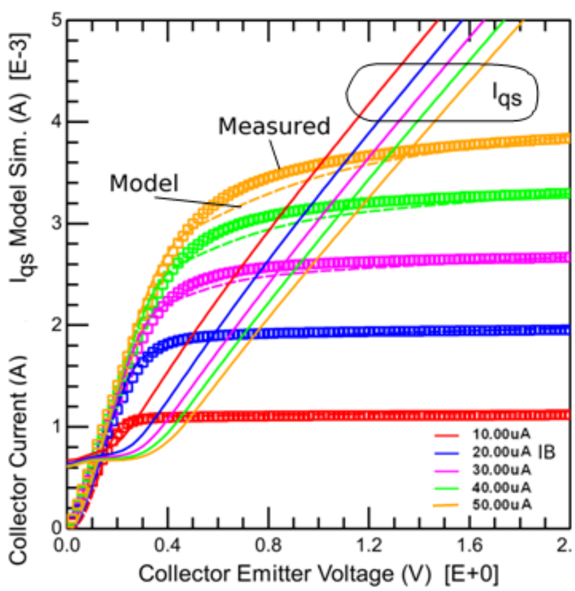

Figure 7.15 162K, saturation, quasi-saturation region of output measurement IC, I_{qs} vs. VCE. Measured data are symbols. Simulated results are dashed lines. Solid lines are the internal model variable, I_{qs}.

Model Parameter	162K Value
NR	1.04
VER	3.05 V
BRI	1.1
IBR	5.6E-35A
VLR	0.3V
RCC	67 Ω
RCBLI	30 Ω

Table 7.8 Saturation region model parameters, 162K

Model Parameter	162K Value
IHC	2.347 mA
RCV	125.3 Ω
SCRCV	350 Ω
AXI	0.2
VDC	0.945 V
IK	9.427 mA

Table 7.9 162K quasi-saturation region model parameters

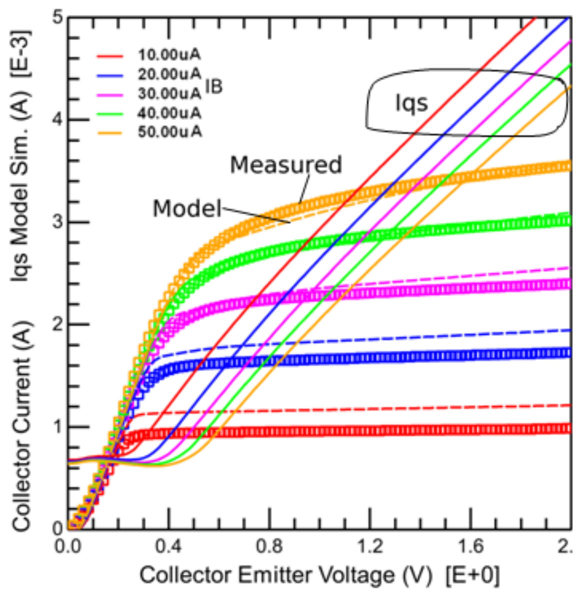

Figure 7.16 93K, saturation, quasi-saturation region of output measurement IC, I_{qs} vs. VCE. Measured data are symbols. Simulated results are dashed lines. Solid lines are the internal model variable, I_{qs}.

Model Parameter	93K Value
NR	1.10
VER	3.2 V
BRI	0.04
IBR	2.0E-55A
VLR	0.3V
RCC	110Ω
RCBLI	35 Ω

Table 7.10 Saturation region model parameters, 93K

Model Parameter	93K Value
IHC	2.347 mA
RCV	135.3 Ω
SCRCV	450 Ω
AXI	0.2
VDC	1.005 V
IK	5.0 mA

Table 7.11 93K quasi-saturation region model parameters

7.2 Ambient temperature model results in the DC linear operating region - Gummel measurements versus model simulations

Typically, several intrinsic transistor parameters are directly extracted from the Gummel measurements. However, this method of parameter extraction by direct data techniques, yielded inaccurate simulated model results when compared, i.e. "fitted" to measured data in the ambient temperature models. The Gummel measurements and characterizations of Chapters 5 and 6 could provide only the initial parameter values. The final values of intrinsic transistor parameters required custom optimization to the Gummel measurements at each ambient temperature. In fact, some of the intrinsic parameters strongly influenced the model equations of other measurements. This multiple measurement influence required that some model parameters be optimized to Gummel, as well as output and AC data. The model parameters extracted from the Gummel measurements are summarized in Table 7.12. The parameter optimizations are bound to the appropriate Gummel election injection operating regions: low-level, mid-level and high-level which were defined in Chapter 5 for each ambient temperature measurement. Parameters which strongly influenced the Gummel regions but were optimized to other measurements are indicated in Table 7.13. The model parameters which dominated or strongly influenced the various regions of the Gummel measurement are described below.

Parameters: NF, DEG, RTH. In Chapter 6, the significance to cryogenic modeling of three factors: implementation of a forward non-ideality factor parameter, utilization of the SiGe base charge equations, and the inclusion of the self-heating effects were defined. The behavior of the model equations representing these three factors are controlled by three model parameters: NF, DEG, and RTH. The importance of these parameters required that their values be defined before the final optimizations of the other model parameters. Each ambient temperature model utilizes the forward non-ideality factor parameter, NF. The NF values were extracted directly from Gummel measurements at the specific temperature, as defined in Chapter 5. The SiGe bandgap parameter, DEG, was determined by optimization, as described in the preceding section. The values of the thermal impedance parameter, RTH, used in the Mextram self-heating model were determined by optimization as defined in the preceding section. RTH was extracted from the output measurements' VBE response as VCE is swept across the linear region.

Once the three critical model parameters above were determined, the parameters which dominate the various Gummel measurement regions were extracted. They are grouped below by the three regions of the Gummel measurement.

Parameter	Description	Gummel Region of Influence		Additional Optimized Measurements and Region	
		Curve	Region	Measurement	Region
IBF	Saturation current of nonideal forward base current, I_{B2} branch	IB	low		
MLF	Non-ideality factor of nonideal forward base current, I_{B2} branch	IB	low		
IS	Saturation current	IC	mid		
BF	Current gain of ideal forward base current, I_{B1} branch	IB	mid		
VER	Reverse Early voltage at zero bias	IB	mid	Output	IC saturated
IK	High-level injection knee current	IC	mid, high	f_T	ICmax and beyond
				Output	IC saturated and linear
DVGBF	Forward BF bandgap delta	IC, IB	mid, high		
VGB	Base bandgap voltage Influences: VDE, IS	IC	mid, high		

Table 7.12 Model parameters which influence the intrinsic region

Parameters: IS, VER, BF. The mid-level electron injection region of the Gummel measurement has three parameters: IS, VER, and BF that are of primary influence to the model equations. The mid-level electron injection region had three parameters: IK, DVGBF, and VGB that were secondary influences on both the IC and IB curves. The parameters of secondary influence were optimization by weighting their optimization heavily toward the high-level injection region. The saturation current parameter, IS, was characterized in Chapter 5 and provided initial parameter values that were optimized. The inclusion of the SiGe bandgap effects in the base charge equations requires VER to be less physically relatable. Therefore, VER was optimized. It was found that VER had a strong influence on both the mid-level region of the Gummel IB curve and the saturated region of the output IC curve. VER was therefore optimized to both measurements until the best fit was reached. The DC current gain parameter, BF, was determined by optimization of the mid-level region of the Gummel IB curve. The DC current gain, β_F, was characterized in Chapter 5, but these values do not correspond to the model parameter BF. The SiGe bandgap effects significantly affect the values of BF. Each of the ambient temperature model parameters values: IS, VER, and BF are defined.

Parameters: IBF, MLF. The low-level electron injection region of the Gummel measurement had two parameters, saturation current of the nonideal forward base current, IBF and the nonideality factor, MLF, which are the primary influences to the model equations of that region in Equation (3.65). Low level effects were not present until the ambient temperature measurements of 93K. A small amount of base current leakage begins to occur at the lowest temperature, 93K. The device doesn't exhibit any low level IC leakage at any temperature modeled. Since the higher temperature measurements provided very little opportunity to accurately fit these parameters the modeling approach was to focus on the 93K fit and adjust the other ambient temperature models to be compatible with the 93K model. This approach allowed the value of MLF to be constant over temperature and IBF to vary as a function of temperature. The final ambient temperature model parameter values for IBF and MLF supported the standard Mextram behavior and temperature equation for parameter IBF.

Parameters: IK, VGB, DVGBF. The high-level electron injection region of the Gummel measurement has three parameters: forward knee current, IK, base bandgap voltage, VGB, and bandgap delta of forward current gain, DVGBF, that were of primary influence to the model equations. These three parameters were first optimized in the high-level injection region and then optimized further by including the mid-level injection region but with less numerical weight than the high-level injection region. Each ambient temperature had a different current gain, β_F, rolloff behavior in the high-level injection region. The effects and contributors changed as temperature decreased making this very difficult to accurately fit as temperature decreased. Several secondary effects had significant influences on both the base and current behavior. The significant contribution of self-heating modified the internal base-emitter voltage and had a large influence on the parameter fitting in the mid-level current range as well as the high-level current region. The increase in device temperature caused by self-heating also increased the contribution of the forward current gain bandgap parameter, DVBGF. The large parasitic resistances of the device influenced the base current and collector current behavior in both the mid-level and high-level current regions. These multiple influences in the two regions greatly decrease the ability to directly extract parameters from the specific measurement regions. Parameter optimization was needed to define the balance between operating regions.

The large resistances in the emitter, base, and collector regions produce voltage drops as the collector current, IC, and base current, IB, increased in the device. Resistive influences on both IC and IB were found in the mid-β_F range and high-injection current range of the Gummel measurements. All of the resistance parameters values were of significance amount, except the parameter representing the extrinsic region of the buried N^+ collector, RCBLX, which was defined as zero based on the device structure, in Section 6.3. Therefore, the resistive influence had to be accurate for each region for the model parameters to be correctly optimized. The resistances are also dependent on temperature. The self-heating effects of the device were significant, causing the device temperature, Tk, to increase during the Gummel measurement, thereby causing the resistance value to increase. Each of the resistances which were affected by the Gummel measurement behavior are listed in Table 7.13.

Parameter	Resistance region	Gummel Curve Influenced	Optimized Measurement and Operating Region	
			Measurement	Region
RE	Emitter, constant	IB	Output	VBE - linear region
			f_T	ICmax and beyond
RBC	External Base, constant	IB	f_T	ICmax and beyond
RBV	Intrinsic Base, varies with current, I_{B1B2} branch	IB	f_T	ICmax and beyond
RCC	External Collector, constant	IC	Output	IC saturated region
RCBLI	Intrinsic N^+ buried layer of collector beneath active transistor, constant	IC	Output	IC saturated region
			f_T	ICmax and beyond
RCV	Epilayer of collector varies with current I_{C1C2} branch	IC	Output	IC saturated region
			f_T	ICmax and beyond

Table 7.13 Resistance parameters influencing the Gummel measurements

Although, the Gummel measurement behavior is strongly influenced by the resistances the resistance parameter values could not be extracted accurately from the Gummel measurement. The resistance values were determined by optimizing the parameters to output and f_T measurements as indicated in Table 7.13 for each resistance parameter.

The sum total of these various parameter optimizations allowed a reasonable model fit of the device’s linear operating region for each ambient temperature. Additional custom fine tuning can improve the model accuracy of the Gummel measurements; however an increase in model error occurs in the device quasi-saturation, saturation or upper end of the voltage operating regions. The objective was to make an accurate model for all operating regions at each ambient temperature that would translate well to a single expansive temperature model, SET.

7.2.1 Four ambient temperature model results of Gummel IC measurements

The optimization approach utilizing the Gummel measurement was applied interactively with the optimization approaches of the other measurements discussed in this chapter. Repeated interactions improved the accuracy of the four ambient temperature model fits. The final model parameter set of each ambient temperature model was reached when a reasonable accuracy was achieved for all three measurement types. The final model results of the Gummel measurement in terms of current gain and collector current, IC, for all four ambient temperature models are presented in Figures 7.17, 7.18, 7.19, and 7.20. In the figures the blue dashed curves are the model simulations and the red solid curves are the measured data of the current gain, β_F, as a function of Log(IC). Included on the right vertical axis of the gain plots for each ambient temperature model is the device temperature, Tk, of the model at each collector current. Here the overall performance and accuracy of the four ambient temperature models can be seen by comparing the current gain of the model simulation to the measured data for the device's total dynamic collector current range. The RMS relative errors between model and measured current gain over the full dynamic IC range are summarized in Table 7.14 for each of the four ambient temperature models. The approach was to focus the fitting on in the IC range from 100uA to 2.5mA. This DC bias operating range coincidences with the bias range in which the small-signal gain is measureable. However, the DC gain is changing from the mid-level injection to high-level injection region in this bias range. In all four ambient temperature measurements the mid-level region is narrow and the high-level region is difficult to fit due to current gain rolloff behavior. The 93K ambient temperature model had the largest current gain error due to the

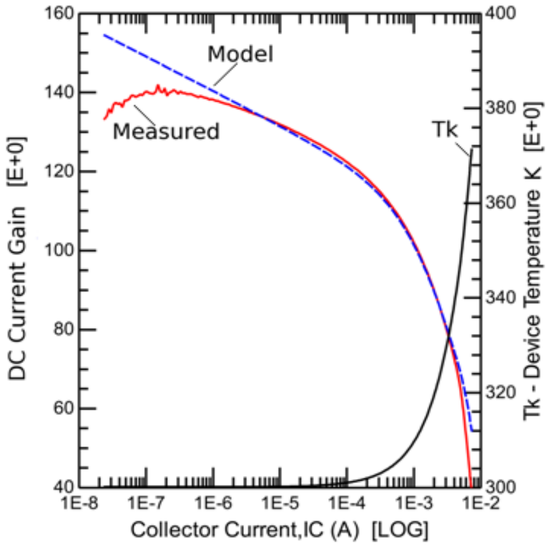

Figure 7.17 Model Simulation vs. Gummel Measurement, 300K. Left axis: Current Gain, β_f vs. Log(IC) at VBC= -1V. Solid line is measured data and dashed line is simulated results. Right axis: Device Temperature, Tk.

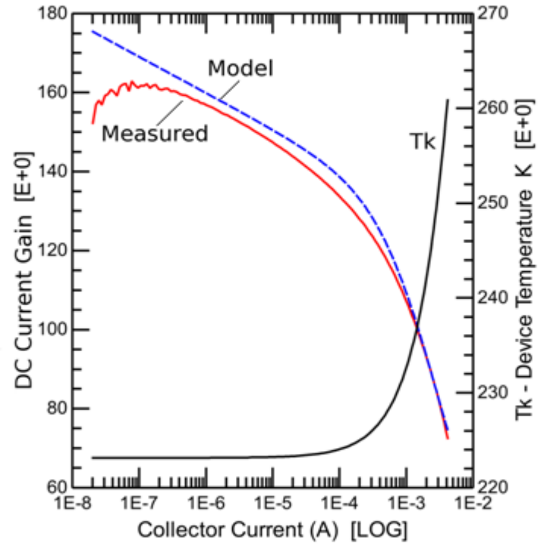

Figure 7.18 Model Simulation vs. Gummel Measurement, 223K. Left axis: Current Gain, β_f vs. Log(IC) at VBC= -1V. Solid line is measured data and dashed line is simulated results. Right axis: Device Temperature, Tk.

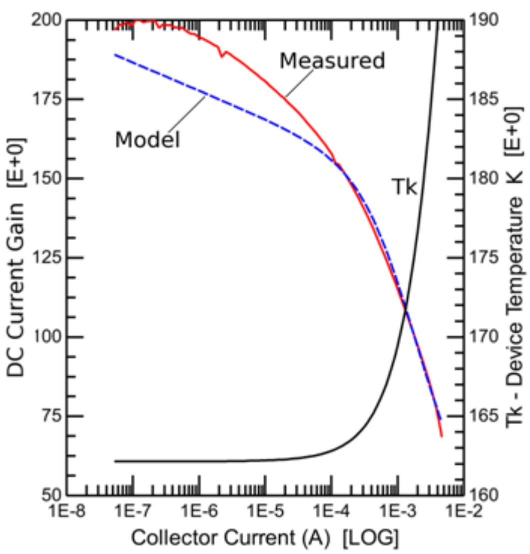

Figure 7.19 Model Simulation vs. Gummel Measurement, 162K. Left axis: Current Gain, β_f vs. Log(IC) at VBC= -1V. Solid line is measured data and dashed line is simulated results. Right axis: Device Temperature, Tk.

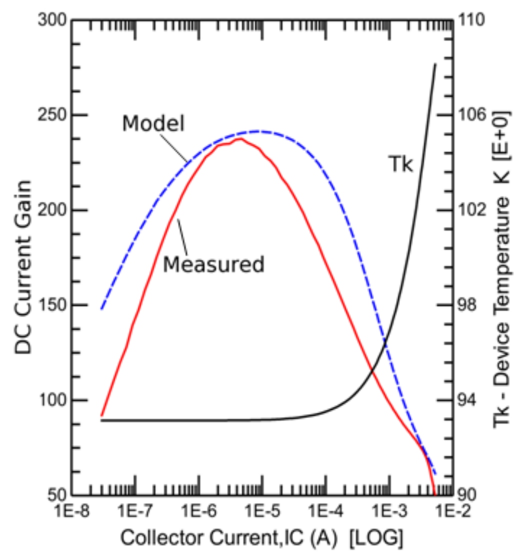

Figure 7.20 Model Simulation vs. Gummel Measurement, 93K. Left axis: Current Gain, β_f vs. Log(IC) at VBC= -1V. Solid line is measured data and dashed line is simulated results. Right axis: Device Temperature, Tk.

intense current gain peaking behavior which the model equations don't support well. The approach at 93K was to get the overall shape and behavior of the current gain curve and focus on minimizing the individual IC and IB curves.

Ambient Temperature	RMS Relative Fit Error of Current Gain	Fitted Model IC Range	Increase in Device Temperature During Measurement
300K	8.15%	30nA to 7.3mA	71.3 K
223K	3.73%	25nA to 4.1mA	38.0 K
162K	5.07%	58nA to 4.6mA	31.4 K
93K	21.45%		

Table 7.14 Ambient temperature model performance metrics: model error, IC dynamic range, and model predicted total device temperature rise during the Gummel measurement.

The self-heating effects during the Gummel measurements are most severe at the higher ambient temperatures as can be seen in the device temperature, Tk, summary plot of all four ambient temperature Gummel simulations in Figure 7.21.

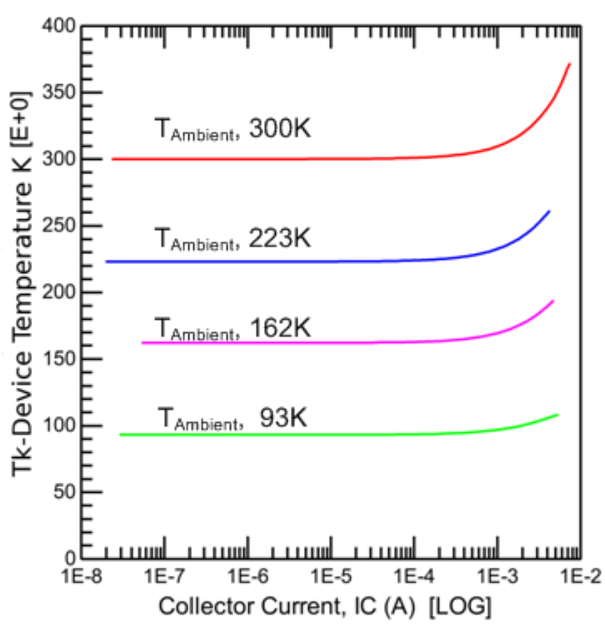

Figure 7.21 Summary the device temperature, Tk, as a function of collector current, for all four ambient temperature models in the Gummel measurement simulations in Figures: 7.17, 7.18, 7.19, and 7.20

The device temperature of the model at each Gummel measurement bias point, can be outputted from the Verilog code so that the full impact of self-heating can be considered. In an ambient temperature environment of 300K there was an increase of 71.3K degrees during the measurement. The model parameters which are dependent on an accurate thermal voltage, V_T, and base-emitter junction voltage would have been severely shifted if the standard method of direct data extraction followed by self-heating characterization had been applied.

7.2.2 Gummel measurement 300K, ambient temperature model results of VBE

Comparison of the Gummel measurement in terms of VBE applied voltage to 300K ambient temperature model simulation results completes the analysis of the DC linear operating region performance. Two Gummel plots: Log(IC, IB) versus VBE applied voltage and current gain, β_F, versus VBE applied voltage are shown in Figure 7.22 and Figure 7.23. The measured data are

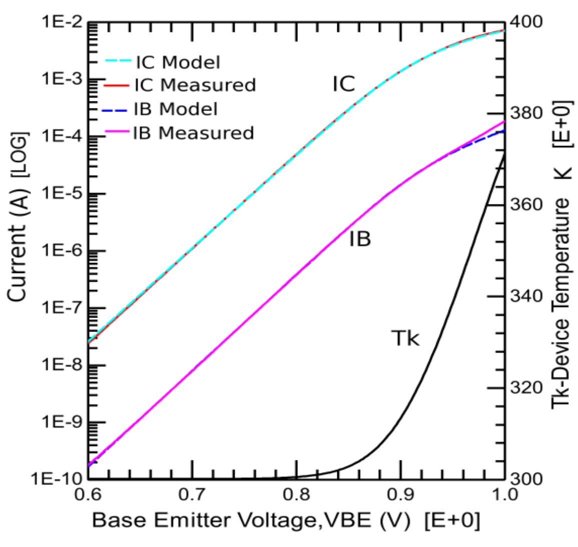

Figure 7.22 Model Simulation vs. Gummel Measurement, 300K. Left axis: Log(IC, IB) vs. VBE at VBC= -1V. Measured data are solid lines and simulated results are dashed lines. Right axis: device temperature, Tk.

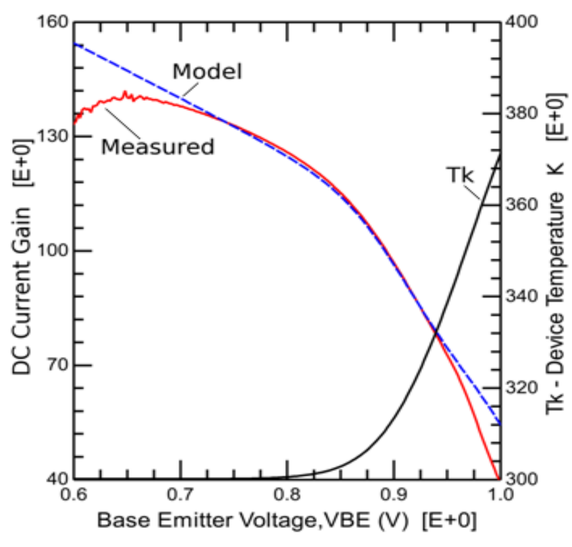

Figure 7.23 Model Simulation vs. Gummel Measurement, 300K. Left axis: Current Gain, β_f vs. VBE at VBC= -1V. Solid line is measured data and dashed line is simulated result. Right axis: device temperature, Tk.

solid lines and the model simulation results are dashed lines. The model device temperature is indicated on the right vertical axis. The model fits the IC curve well. The IC RMS relative model fit error was 3.1% over the full IC range. The model fit the IB curve well, with a RMS relative model fit error of 6.5%.

Table 7.15 summarizes the model parameters extracted at 300K from the Gummel measurement. The parameters were extracted in the manner described in the previous section. The lower limit of measurement resolution was 20pA set by the IB measurement. There is almost

Parameter	300K Ambient Value
IS	3.49E-18 A
IK	17.69 mA
NF	1.0
VER	2.81V
BF	244
IBF	1.34E-24 A
MLF	2.157
VGB	1.11V
DVGBF	10mV

Table 7.15 300K ambient temperature model parameters extracted from Gummel measurement.

no low-level injection region. Parameter optimization of the mid-level and high-level election injection regions was difficult due a limited mid-range of decreasing slope and a soft knee in the high-level injection region. The self-heating effects are clearly indicated by the behavior of the parasitic resistance parameters during the measurement.

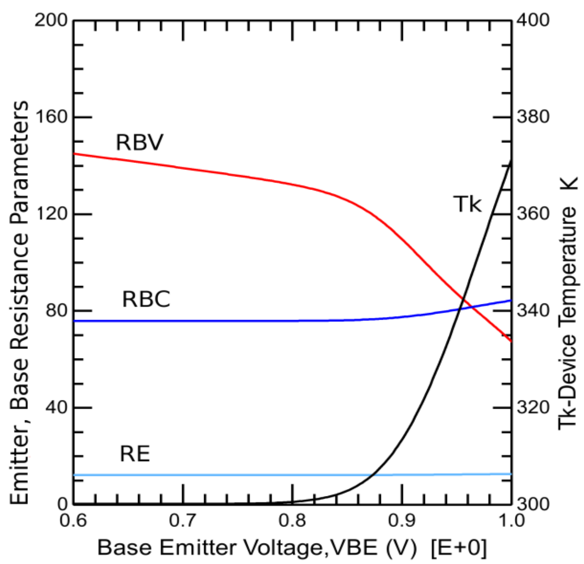

Figure 7.24 Base and Emitter Resistance Parameters, RBV, RBC, RE at each Gummel measurement bias point, 300K. Left axis: Resistance values. Right axis: device temperature, Tk.

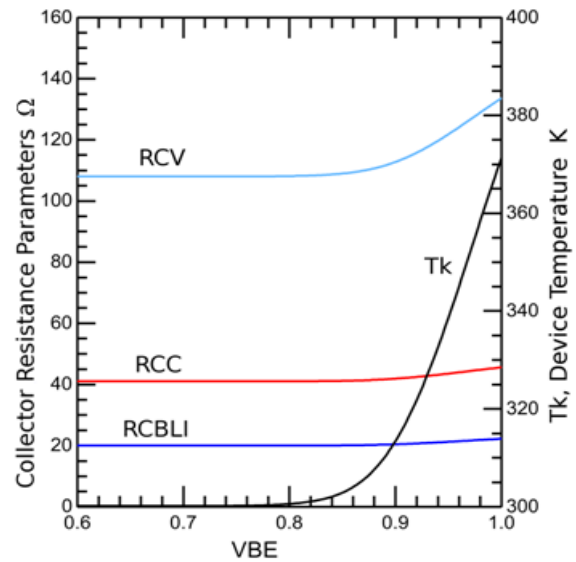

Figure 7.25 Collector Resistance Parameters, RCC, RCBLI, RCV at each Gummel measurement bias point, 300K. Left axis: Resistance values. Right axis: device temperature, Tk.

Figure 7.24 shows the increase in resistance of the constant extrinsic base resistor, RBC, and the constant emitter resistor, RE, as a function of Gummel measurements' VBE bias point. The variable base resistor, RBV, decreased due to current dependence. Figure 7.25 shows the increase of the collector resistance parameters: RCBLI, RCC and RCV.

7.2.3 Gummel measurement 223K, ambient temperature model results in terms of VBE

Analysis of the DC linear operating region performance utilized the 223K ambient temperature model and the DC Gummel measurement in terms of VBE. Two Gummel plots: Log(IC, IB) versus VBE applied voltage and current gain, β_F, versus VBE applied voltage are shown in Figure 7.26 and Figure 7.27. The measured data are solid lines and the model simulation results are dashed lines. The model device temperature is indicated on the right vertical axis. The model fits the IC curve well. The IC RMS relative model fit error was 4.3%

over the full IC range. The model fit the IB curve well, with a RMS relative model fit error of 2.0%.

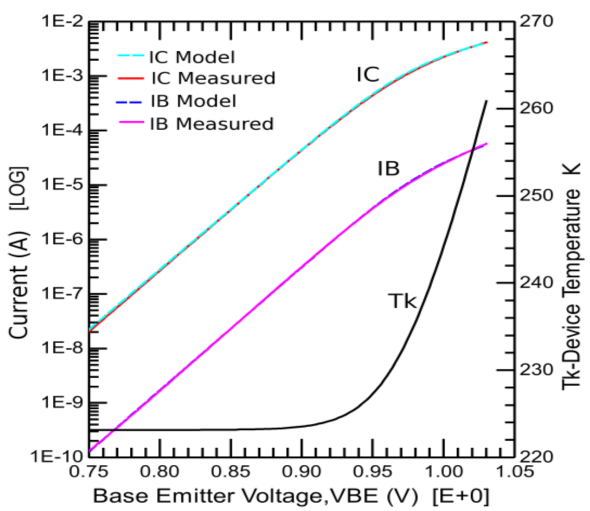

Figure 7.26 Model Simulation vs. Gummel Measurement, 223K. Left axis: Log(IC, IB) vs. VBE at VBC= -1V. Measured data are solid lines and simulated results are dashed lines. Right axis: device temperature, Tk.

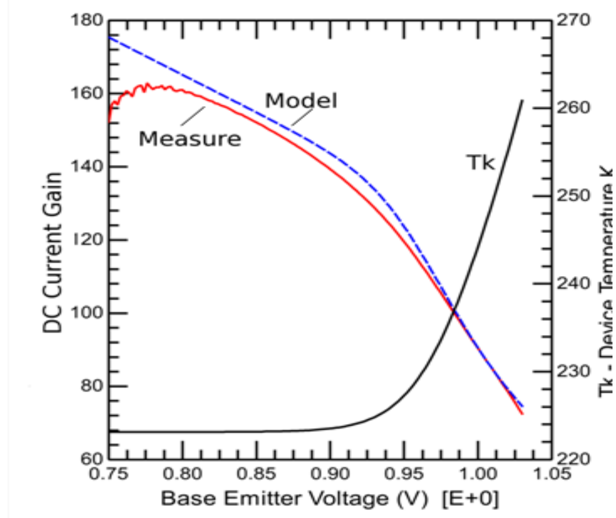

Figure 7.27 Model Simulation vs. Gummel Measurement, 223K. Left axis: Current Gain, β_f vs. VBE at VBC= -1V. Solid line is measured data and dashed line is simulated result. Right axis: device temperature, Tk.

Table 7.16 summarizes the model parameters extracted at 223K from the Gummel measurement. The parameters were extracted in the manner described in the Section 7.2.

Parameter	223K Ambient Temp. Model Value
IS	4.95E-25 A
IK	12.37 mA
NF	1.0
VER	2.916V
BF	328.4
IBF	2.79E-26 A
MLF	2.157
VGB	1.11V
DVGBF	10mV

Table 7.16 223K ambient temperature parameters extracted from the Gummel measurement

The Gummel data at the ambient temperature of 223K is similar in behavior to the 300K data. The gain rolloff of the low-level region is minor. The gain rolloff of the high-level region is very soft. The current gain increased as the temperature decreased but the VBE range for the mid-level current gain region is decreasing. Optimization of the model parameters was essential due to this behavior. Self-heating effects increased the parasitic resistances during the 223K Gummel measurements. Figure 7.28 shows the increase in resistance of the constant extrinsic base resistor, RBC, and the constant emitter resistor, RE, as a function of Gummel measurements' VBE bias point. The variable base resistor, RBV, decreased due to current dependence. Figure 7.29 shows the increase of the collector resistance parameters: RCBLI, RCC and RCV.

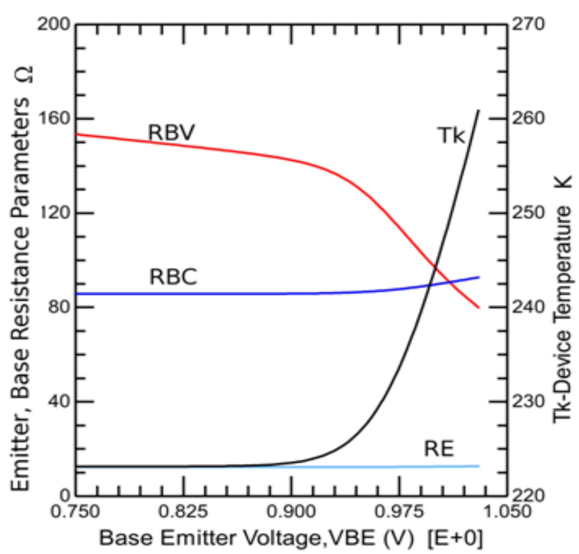

Figure 7.28 Base and Emitter Resistance Parameters, RBV, RBC, RE at each Gummel measurement bias point, 223K. Left axis: Resistance values. Right axis: device temperature, Tk.

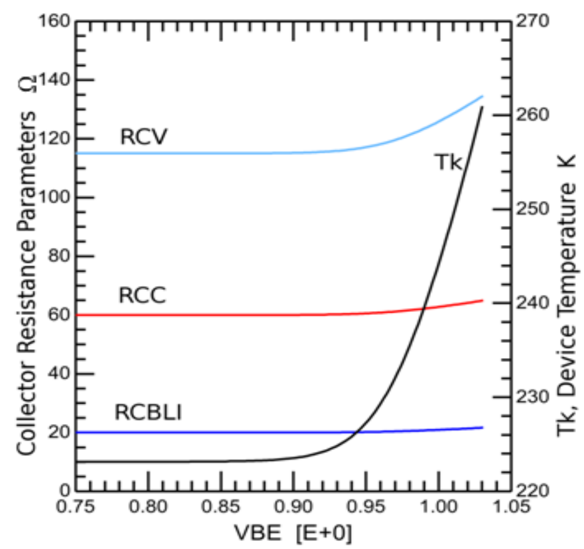

Figure 7.29 Collector Resistance Parameters, RCC, RCBLIX, RCV at each Gummel measurement bias point, 223K. Left axis: Resistance values. Right axis: device temperature, Tk.

7.2.4 Gummel measurement 162K, ambient temperature model results in terms of VBE

The 162K ambient temperature model simulation of the Gummel measurement in terms of VBE applied voltage completes the analysis of the model performance in the 162K DC linear operating state. This analysis was also used in parameter extraction by the described method of Section 7.2. Two Gummel plots: Log(IC, IB) versus VBE applied voltage and current gain, β_F, versus VBE applied voltage are shown in Figure 7.30 and Figure 7.31. The measured data are solid lines and the model simulation results are dashed lines. The model device temperature is indicated on the right vertical axis. The model fits the IC curve well in the mid-level region, but was less accurate in the very weak knee region of high-level injection. The IC RMS relative model fit error was 3.9% over the full IC range. The model fit the IB curve well, with a RMS relative model fit error of 6.9%.

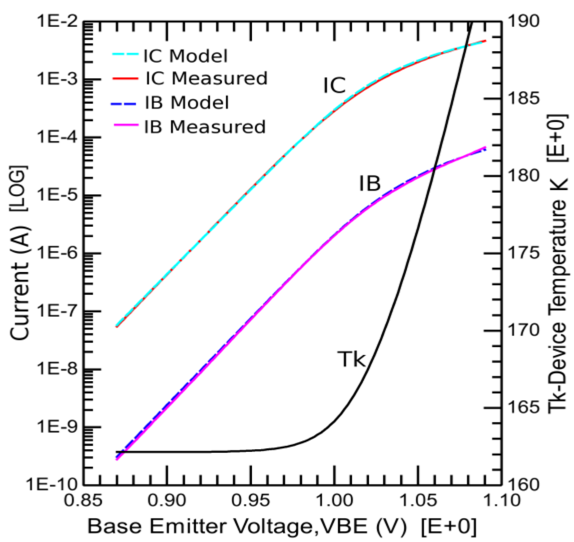

Figure 7.30 Model Simulation vs. Gummel Measurement, 162K. Left axis: Log(IC, IB) vs. VBE at VBC= -1V. Measured data are solid lines and simulated results are dashed lines. Right axis: device temperature, Tk.

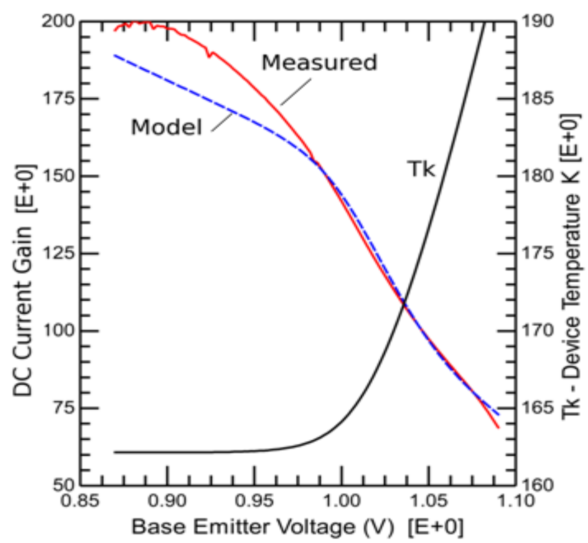

Figure 7.31 Model Simulation vs. Gummel Measurement, 162K. Left axis: Current Gain, β_f vs. VBE at VBC= -1V. Solid line is measured data and dashed line is simulated result. Right axis: device temperature, Tk.

Table 7.17 summarizes the model parameters extracted at 162K from the Gummel measurement. The parameters were extracted in the manner described in Section 7.2.

Parameter	162K Ambient Temp. Model Value
IS	1.41E-33 A
IK	9.427 mA
NF	1.04
VER	3.05V
BF	453
IBF	8.34E-29 A
MLF	2.157
VGB	1.11V
DVGBF	10mV

Table 7.17 162K ambient temperature parameters extracted from the Gummel measurement

The Gummel data at 162K had behavior similar to higher temperature measurements. One significant difference in the Gummel data at this cryogenic temperature had a non-ideality factor, NF, greater than the ideal value of 1. The lower limit of measured IC was 700nA because the IB curve was noisy below this bias point. The noisy data limits the knowledge of lower level injection behavior. The high level injection knee occurs at lower current levels than at higher temperatures. It was softer, less defined and not as well fitted as higher temperatures. . Self-heating effects increased the parasitic resistances during the 162K Gummel measurements. Figure 7.32 shows the slight increase in resistance of the constant extrinsic base resistor, RBC, and the constant emitter resistor, RE, as a function of Gummel measurements' VBE bias point. The variable base resistor, RBV, decreased due to current dependence. Figure 7.33 shows the increase of the collector resistance parameters: RCBLI, RCC and RCV.

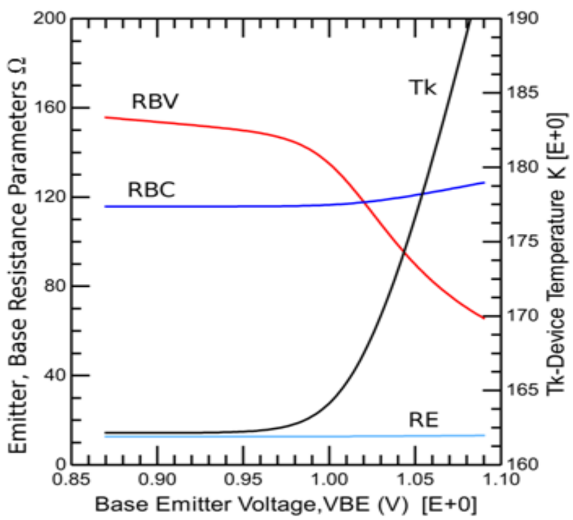

Figure 7.32 Base and Emitter Resistance Parameters, RBV, RBC, RE at each Gummel measurement bias point, 162K. Left axis: Resistance values. Right axis: device temperature, Tk

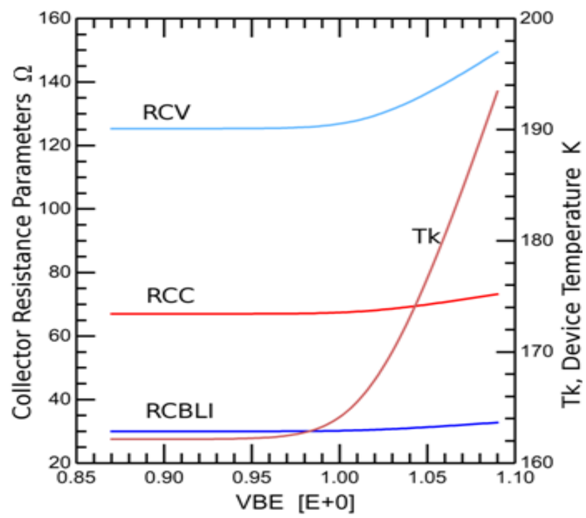

Figure 7.33 Collector Resistance Parameters, RCC, RCBLIX, RCV at each Gummel measurement bias point, 162K. Left axis: Resistance values. Right axis: device temperature, Tk.

7.2.5 Gummel measurement at ambient temperature 93K

The 93K ambient temperature model simulation of the 93K Gummel measurement in terms of VBE applied voltage completes the analysis of the model performance of DC linear operating region at 93K. Two Gummel plots: Log(IC, IB) versus VBE applied voltage and current gain, β_F, versus VBE applied voltage are shown in Figure 7.34 and Figure 7.35. The measured data are solid lines and the model simulation results are dashed lines. The model device temperature is indicated on the right vertical axis. The model fits the IC curve well in the mid range, but the soft knee of the IC curve as it transitions from mid to high-level was difficult to fit the model equations. The IC RMS relative model fit error was 13.8% over the full IC range. The model fit the IB curve well in the mid-level, but there was also difficulty with the soft knee present at the transition from mid to high-level injection. The IB curve had an RMS relative model fit error of 12.0% over the full IB model range.

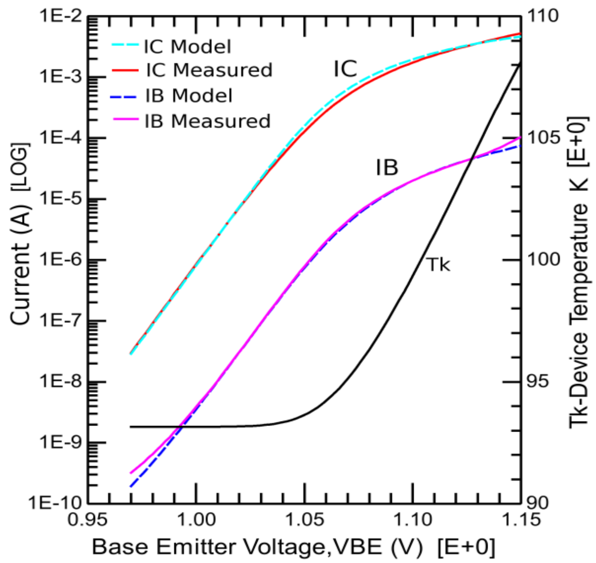

Figure 7.34 Model Simulation vs. Gummel Measurement, 93K. Left axis: Log(IC, IB) vs. VBE at VBC= -1V. Measured data are solid lines and simulated results are dashed lines. Right axis: device temperature, Tk.

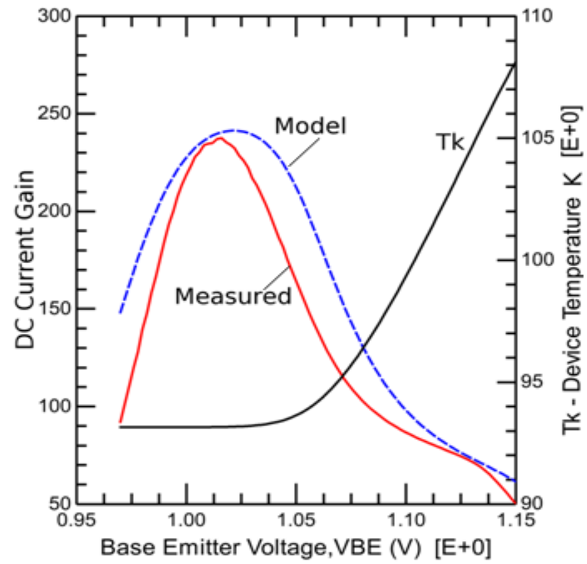

Figure 7.35 Model Simulation vs. Gummel Measurement, 93K. Left axis: Current Gain, β_f vs. VBE at VBC= -1V. Solid line is measured data and dashed line is simulated result. Right axis: device temperature, Tk.

Table 7.18 summarizes the model parameters extracted at 93K from the Gummel measurement. The parameters were extracted in the manner described in the previous section.

Parameter	93K Ambient Temp. Model Value
IS	2.08E-55 A
IK	5.0 mA
NF	1.1
VER	3.2V
BF	453
IBF	4.30E-35 A
MLF	2.157
VGB	1.11V
DVGBF	10mV

Table 7.18 93K ambient temperature parameters extracted from the Gummel measurement

The Gummel data at 93K is distinctly different in behavior as compared to the higher cryogenic temperature data. IB leakage at low bias points required low-level injection region parameters to be extracted. The severe low-level β_F rolloff influenced the parameter extractions of mid-level injection region as well. The dynamic IC range is less than a decade in the mid-level injection region. The ultra shallow mid-level region creates a severe β_F peaking effect because there is a severe rolloff in the high-level injection region. The DC current gain, $\beta_{F,}$ is decreasing in the operating region of common applications. The non-ideality factor, NF, continued to increase, going from 1.04 at 162K to 1.10 at 93K as the temperature decreased. The exponential relationship of NF with current makes the accuracy of the parameter value critical to the success of developing the model. The transition from mid to high-level injection is IC curve is non-typical. The measured data at 93K transitions rapidly in both directions from the mid-level. The Mextram bipolar model is not able to respond as sharply. The model equations for the low-level and high-level effects cannot transition from on to off in the VBE span of 5mV. Therefore the shape of the current gain curve is accurate but the exact values have a higher error than the upper ambient temperature models. Self-heating effects are decreasing as the cryogenic temperature decreases but the effect is not insignificant. Self-heating effects increased the parasitic resistances during the 93K Gummel measurements. Figure 7.36 shows the increase in resistance of the constant extrinsic base resistor, RBC, and the constant emitter resistor, RE, as a function of Gummel measurements' VBE bias point. The variable base resistor, RBV, decreased due to current dependence. Figure 7.37 shows the increase of the collector resistance parameters: RCBLI, RCC and RCV.

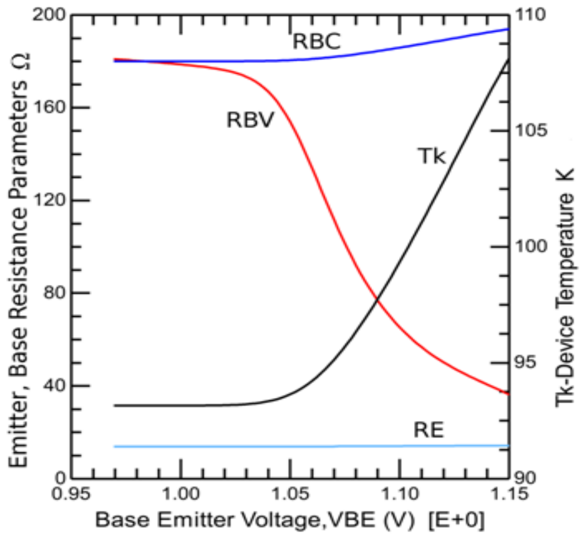

Figure 7.36 Base and Emitter Resistance Parameters, RBV, RBC, RE at each Gummel measurement bias point, 93K. Left axis: Resistance values. Right axis: device temperature, Tk

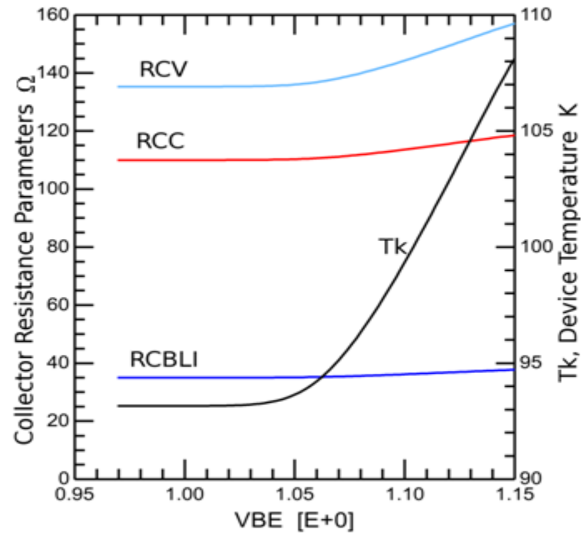

Figure 7.37 Collector Resistance Parameters, RCC, RCBLIX, RCV at each Gummel measurement bias point, 93K. Left axis: Resistance values. Right axis: device temperature, Tk.

7.3 Summary of AC measurements biased at VC= -1V

The device AC behavior at the four ambient temperatures was obtained from the S-parameter measurements. In Chapter 5, the S-parameters data was converted to H-parameters and Y-parameters, the pad metallization effects were removed and the device frequency response was presented in terms of cutoff frequency, f_T, versus collector current. The cutoff frequency, f_T, is defined as the frequency at which the small signal AC current gain is equal to one. The device frequency response as a function of collector current was used for model parameter extraction. The collector current, ICmax, is defined as the current at which the maximum or peak value of f_T occurs during the measurement. The AC measurements consist of biasing the device in the linear active region at a constant VBC of 1V and sweeping the base-emitter terminals over a range of VBE values as described in Chapter 5.

The AC measurements were used to extract the transit time model parameters and the junction capacitance parameters. The transit time parameters: TAUE, TAUB, TAUR, and MTAU are defined Chapter 3, as well as the capacitance parameters. The f_T response as a function of collector current was influenced by the high-current parameters and the quasi-saturation parameters described earlier in Sections 7.2 and 7.3. These two effects were included in each ambient temperature model. There were a large number of model parameters which influenced the f_T versus collector current. The parameters were organized by their dominant effects and region of influence which required complex and custom optimization at each ambient temperature point. The behavior over temperature was summarized after the model fits to the f_T curves. The group of parameters: CJE, XCJE, PE and VDE, influence the base-emitter junction effects of capacitance and voltage in optimizations. The group of parameters: CJC, XCJC, PC, MC and VDC, influence the base-collector junction effects of capacitance and voltage in optimizations. The transit time parameters: TAUB, TAUE, and MTAU have specific regions of influence, that affect the shape of the f_T curve, but as a group they as define the maximum value of f_T. The resistance group of parameters: RE, RBC, and RBV influence both the DC and AC behavior. The fitting of these parameters had to be a compromise between the optimum fit of both behaviors. The epilayer collector model of parameters: TEPI, IK, SCRCV, RCBLI and RCV had a strong influence on the high-level injection region of the f_T curve. However, this group of parameters also had a dominate influence on the quasi-saturation region of the output characteristics. Therefore, custom global optimizations of both DC output curves and f_T curves were fit simultaneously at each ambient temperature.

The resulting ambient temperature models fitted the measured f_T versus Log(IC) curves quite well, both in absolute value and curve contours. The model results of each ambient temperature model fit of f_T versus Log(IC) are shown in Figures 7.38, 7.39, 7.40 and 7.41 and the parameters values of each ambient temperature at defined in Table 7.19 through 7.22.

The 300K ambient temperature model was an excellent fit to the measured f_T response in Figure 7.38.

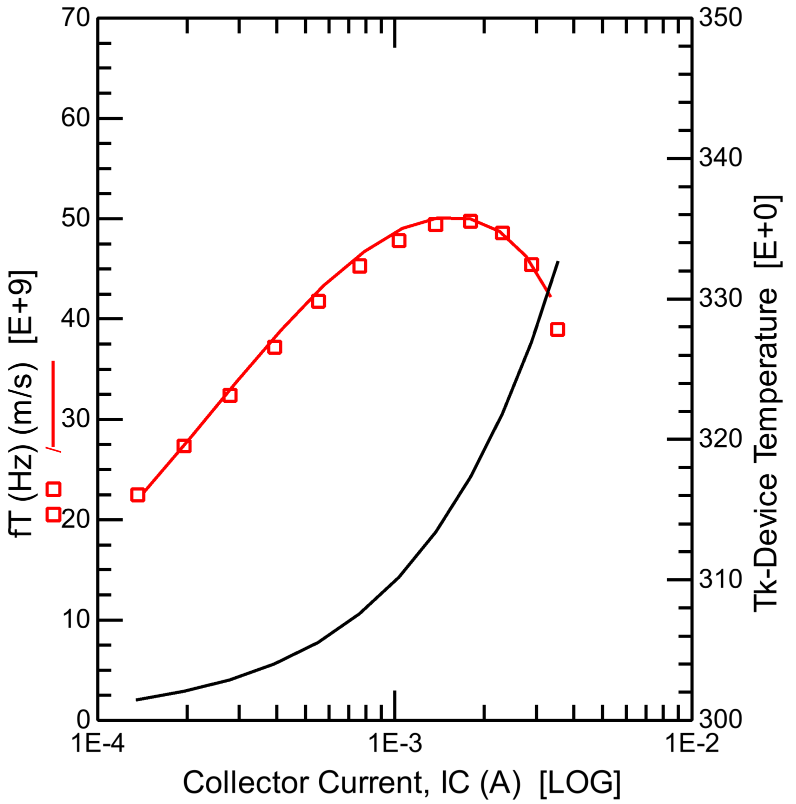

Figure 7.38 300K ambient temperature model comparison to measurement of f_T versus Log(Collector Current). Right axis: Model Device Temperature, Tk, at each measurement point.

Model Parameter	300K Value
CJE	10.96fF
XCJE	380m
PE	288.3m
VDE	909.3mV
CJC	5.913fF
XCJC	224.7m
MC	324.5m
PC	305.5m
TAUB	390.7fs
TAUE	213.8fs
MTAU	1.0
RE	12.2 Ω
RBC	75.85 Ω
RBV	180 Ω
TEPI	85.73ps
IK	17.69mA
SCRCV	301.4 Ω
RCBLIX	20 Ω
RCV	108 Ω
TAUR	150ps

Table 7.19 300K ambient model parameters from AC optimizations

At 300K, the high-level injection effects are well modeled by the epilayer collector equations. Also at 300K, the DC current response of Section 7.2.2 has a forward non-ideality factor, NF, of 1. The 300K, AC f_T response works well with a emitter charge non-ideality factor, MTAU, of 1.

The 223K ambient temperature model predicted a slightly higher fT of 4 to 5 GHz under low current conditions giving an error of 8 to 10% at low currents. The model f_T curve behavior was correct as was the peak f_T range.

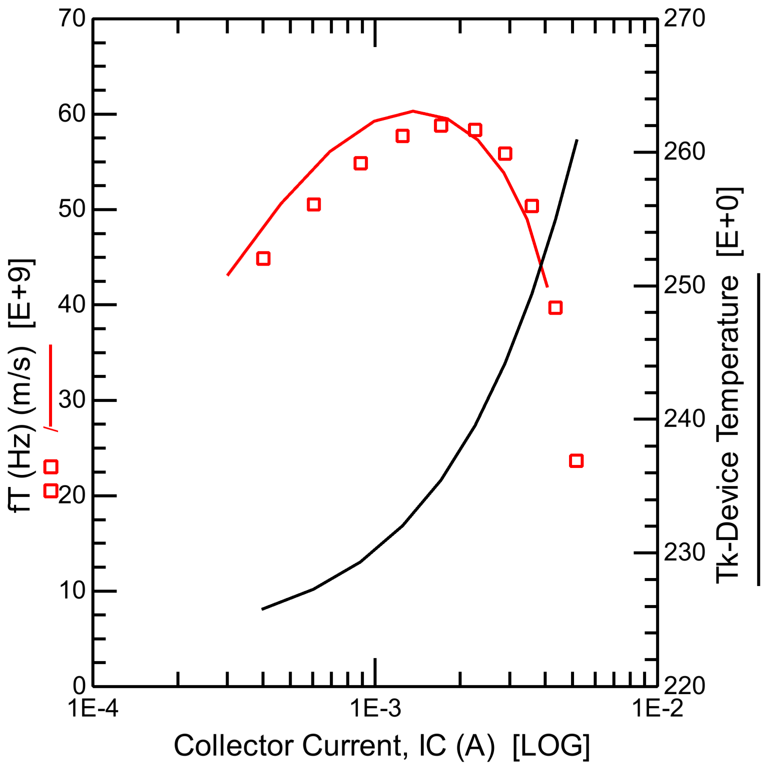

Figure 7.39 223K ambient temperature model comparison to measurement of f_T versus Log(Collector Current). Right axis: Model Device Temperature, Tk, at each measurement point.

Model Parameter	223K Value
CJE	10.73fF
XCJE	380m
PE	288.3m
VDE	978.0mV
CJC	5.787fF
XCJC	224.7m
MC	324.5m
PC	305.5m
TAUB	199.0fs
TAUE	169.0fs
MTAU	1.0
RE	12.3 Ω
RBC	85.8 Ω
RBV	200 Ω
TEPI	65.0ps
IK	12.37mA
SCRCV	301.4 Ω
RCBLIX	20 Ω
RCV	115 Ω
TAUR	150ps

Table 7.20 223K ambient model parameters from AC optimizations

The f_T response is increasing at 223K. The peak f_T has increased from 50 GHz at 300K to 60 GHz at 223K. The model represents the higher f_T by decreasing the transit times of the base and emitter, but the emitter charge non-ideality factor, MTAU, is still at 1. The DC current response for 223K also has a forward non-ideality factor, NF, of 1 in Section 7.2.3.

At 162K, the model fit is predicting slightly lower f_T values under low current conditions. The shape of the f_T curve is excellent and the model correctly predicted the peak f_T region.

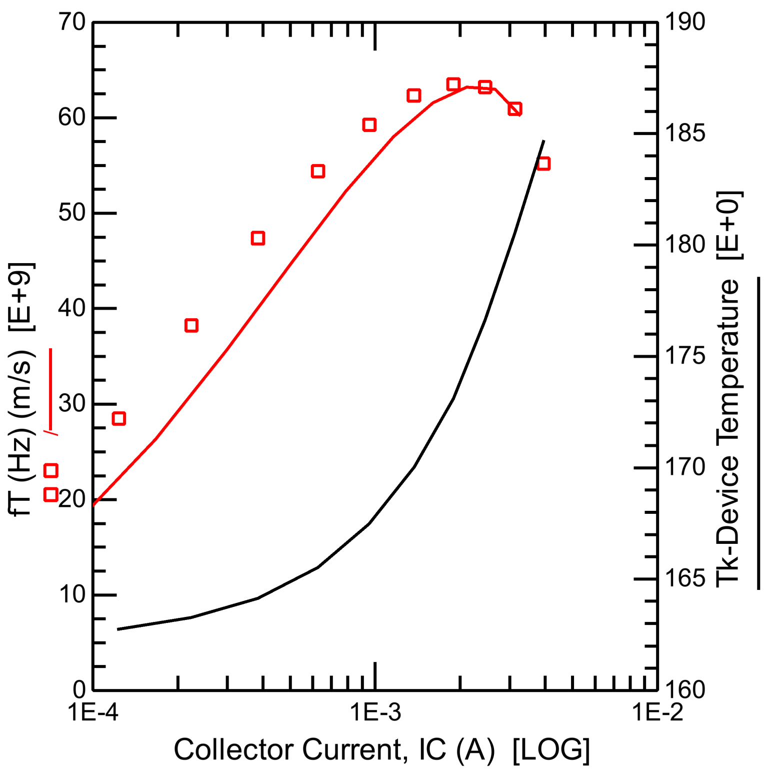

Figure 7.40 162K ambient temperature model comparison to measurement of f_T versus Log(Collector Current). Right axis: Model Device Temperature, Tk, at each measurement point.

Model Parameter	162K Value
CJE	10.58fF
XCJE	380m
PE	288.3m
VDE	1.024V
CJC	5.704fF
XCJC	224.7m
MC	324.5m
PC	305.5m
TAUB	125.8fs
TAUE	110.8fs
MTAU	2.7
RE	12.7 Ω
RBC	115.8 Ω
RBV	210 Ω
TEPI	45.7ps
IK	9.427mA
SCRCV	350 Ω
RCBLIX	30 Ω
RCV	125.3 Ω
TAUR	150ps

Table 7.21 162K ambient model parameters from AC optimizations

At 162K, the rate of increase in frequency response has decreased as compared to the amount of increase between 300K and 223K. The model represents the increase in f_T by decreasing both transit times again. However, at 162K the control over the peak f_T required the emitter charge non-ideality factor, MTAU, to increase from 1.0 to 2.7. In the DC current response at 162K, the forward non-ideality factor, NF, also increased from 1.0 to 1.04.

The 93K ambient model predicts the f_T behavior well in response to collector current. Overall the model predicts slightly lower f_T values but the error is approximately 5%.

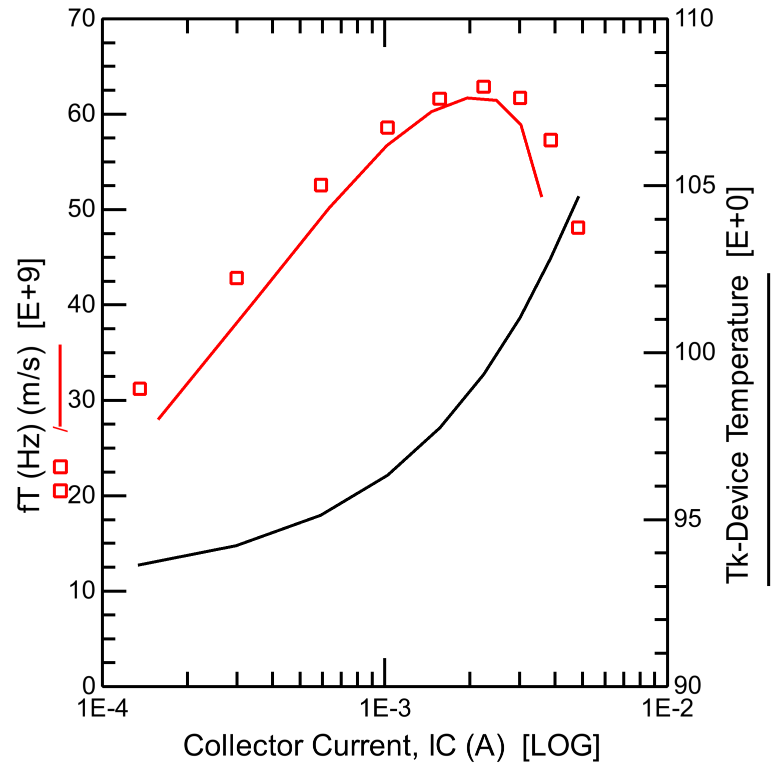

Figure 7.41 93K ambient temperature model comparison to measurement of f_T versus Log(Collector Current). Right axis: Model Device Temperature, Tk, at each measurement point.

Model Parameter	93K Value
CJE	10.44fF
XCJE	380m
PE	288.3m
VDE	1.076V
CJC	5.626fF
XCJC	224.7m
MC	324.5m
PC	305.5m
TAUB	90.0fs
TAUE	42.2fs
MTAU	5.0
RE	13.9 Ω
RBC	180 Ω
RBV	250 Ω
TEPI	25.7ps
IK	5.0mA
SCRCV	450 Ω
RCBLIX	35 Ω
RCV	135.3 Ω
TAUR	150ps

Table 7.22 93K ambient model parameters from AC optimizations

At 93K, the peak f_T did not increase as compared to the 162K values. However, model optimizations required the transit time to decrease and the non-ideality factor, MTAU, to increase to 5.0 for a good fit to be obtained. The DC current response at 93K also increased the forward non-ideality factor, NF, to 1.10.

Parameters: CJE, XCJE, PE, and VDE. The zero-biased, base-emitter depletion capacitance parameter, CJE, and the junction splitting parameter, XCJE, were optimized to the f_T behavior in the lower collector current regions. CJE decreased by approximately 0.5 fF over the entire temperature range. XCJE and PE are constant over temperature. The base-emitter diffusion voltage parameter, VDE, was determined initially from physical characteristics and then optimized in conjunction with CJE to the log-linear slope of the f_T response in order to finalize their values at each ambient temperature. VDE increases less than 200mV over the wide temperature range.

Parameters: CJC, VDC, XCJC, PC, MC. The zero-biased, base-collector depletion capacitance parameter, CJC, and the junction splitting parameter, XCJC, were optimized to the IC bias region where the f_T behavior was relatively flat in the 300K model. XCJC was maintained at a constant value over temperature. The collector diffusion voltage, VDC, was optimized in the DC quasi-saturation region initially. A second series of optimizations of VDC to both the DC quasi-saturation region and the high collector current region of the f_T curve finalized the value for each ambient temperature model. VDC increased by approximately 200mV over the temperature range. The collector modulation factor of base-collector junction capacitance parameters, MC, was determined by physical characteristics defined in Table 6.6. The base-collector junction grading coefficient parameter, PC, was determined from physical characteristics.

Parameters: TAUB, TAUE, MTAU. For ambient temperature models at 300K and 233K, the emitter charge non-ideality factor parameter, NF, was equal to one. The base transit time parameter, TAUB, and the emitter transit time parameter, TAUE, were optimized to the peak f_T region of the curve. At the lower temperatures of 162K and 93K, the value of MTAU increased from 2.7 to 5.0. All three parameters were optimized to fit the peak f_T region.

Parameter TAUR. Since there was no AC data measurements bias in the saturation region available TAUR was calculated from the physical relationship of TAUR being a scaled factor of TEPI [35] The initial values of TEPI were used for the calculation of TAUR at 150ps. All four ambient temperature models used this parameter value. TAUR represents the transistor saturation recovery time in a common-emitter configuration.

<u>Parameters: RE, RBC, and RBV</u>. The emitter resistance parameter, RE, was initially extracted from a DC optimization of the DC output response as described in Section 7.1. A second series of RE optimizations to both the DC and AC responses more accurately fit the influence of RE. The resistance parameters were optimized against the rising and falling slopes extending from the peak f_T region. RE tended to flatten the model response. RBC and RBV tended to cause rolloff.

<u>Parameters: TEPI, IK, SCRCV, RCBLI, RCV</u>. The epilayer collector transit time parameter, TEPI, was most influential to the f_T behavior beyond ICmax as f_T is decreasing and IC is increasing. This IC region is also controlled by the high injection knee current parameter, IK. The large collector current causes the collector resistance parameters: SCRCV, RCBLI, and RCV, to significantly influence the IC behavior, which thereby influences the f_T response beyond IK value. The quasi-saturation region collector resistance parameters, SCRCV and RCV, were initially determined by the DC optimizations methods described in Section 7.1. The saturation region collector resistance parameter, RCBLI was initially determined by the DC optimizations method of Section 7.1 as well. TEPI was then optimized in conjunction with the initial DC optimized parameter values of IK, SCRCV, RCBLI, and RCV. A second iteration of optimizations was done that included all five parameters to finalize the f_T versus IC response in the collector bias region of ICmax and above.

8 SET Model

Chapter 8 will complete the Single Expansive Temperature, SET model. The methodology defined in Section 1.1, and illustrated in Figure 1.3, was applied to develop the SET model parameters. The final SET model and fitted parameters produced simulated results which accurately represented the measured DC and AC electrical behaviors from room temperature, 300K, to the cryogenic temperature of 93K. The continuous SET model correlates well with the four ambient temperature measurements.

A key contributor to the development of the single expansive model was the full utilization of the capabilities of the industry standard Mextram 504.7 bipolar model [2]. The adaptation of the Mextram 504.7 strengths to this HBT device were discussed in Chapter 6: advanced bipolar process features, current calculations include the base SiGe bandgap reduction, self-heating, and expansion of the numerical range of the mathematical smoothing equations for optimum convergence. The cryogenic temperature implementation required limited modification of the standard 504.7 model in order to create the Cryo Mextram 504.7 model used to develop the four ambient temperature model parameter sets of Chapter 7.

In this chapter, the wide temperature range SET Mextram 504.7 model was completed through the use of the Cryo Mextram 504.7 model and the multiple temperature point model parameter sets. The ambient temperature models and measurements taken at Kelvin ambient temperatures, $T_{Ambient}$: 300K, 223K, 162K, and 93K were used to build the SET model. Parameter temperature equations were developed for the SET model when the standard 504.7 temperature equations [2] did not represent the ambient temperature parameter values over the wide temperature range. The new temperature equations were placed into the Cryo Mextram 504.7 model to create the Single Expansive Temperature, SET Mextram 504.7 model and the parameter values were extracted to best fit the entire expansive temperature range.

8.1 SET model development method of temperature equations and parameters

For the SET model, the parameter temperature equations of the Mextram 504.7 model were used as much as possible. However, the parameter temperature equations of the standard Mextram 504.7 were not able to represent all the parameters and electrical behavior over the extended temperature range from room temperature to cryogenic temperatures. It was discovered that the model parameters could be described by one of the three following behaviors:

- Over the full temperature range, the standard Mextram 504.7 temperature equation and its corresponding temperature model parameter describe the parameter's temperature behavior. (Section 8.2)
- Over the full temperature range, the temperature behavior of the parameter required a modified 504.7 temperature equation and newly defined temperature model parameter. (Section 8.3)
- Below a distinct temperature, defined in the SET model as TCRYO, the parameter's temperature behavior required a new parameter temperature equation and a newly defined temperature model parameter. (Section 8.4)

The approach taken in the development of the SET model parameter temperature equations and the SET parameter values is summarized in the organizational chart of Figure 8.1. The SET model is a modified version of the standard Mextram 504.7 code [2]. The SET code is only a modification of the original 504.7 code. The modifications are described in Chapters 6 and 8. The description of the standard Mextram 504.7 model and equations created by Phillips[34] and released by Delft University[2] was given in Chapter 3. This model summary provides a point of reference for the expansive temperature work and an understanding of the significant parameter interactions as a function of operating bias and temperature. Each Mextram 504.7 model parameter temperature equation was described in Section 3.6. In the 504.7 model electrical parameters are often controlled by a shared temperature parameter. The influence of each temperature parameter on the electrical model parameters were summarized in Tables 3.35 and 3.36.

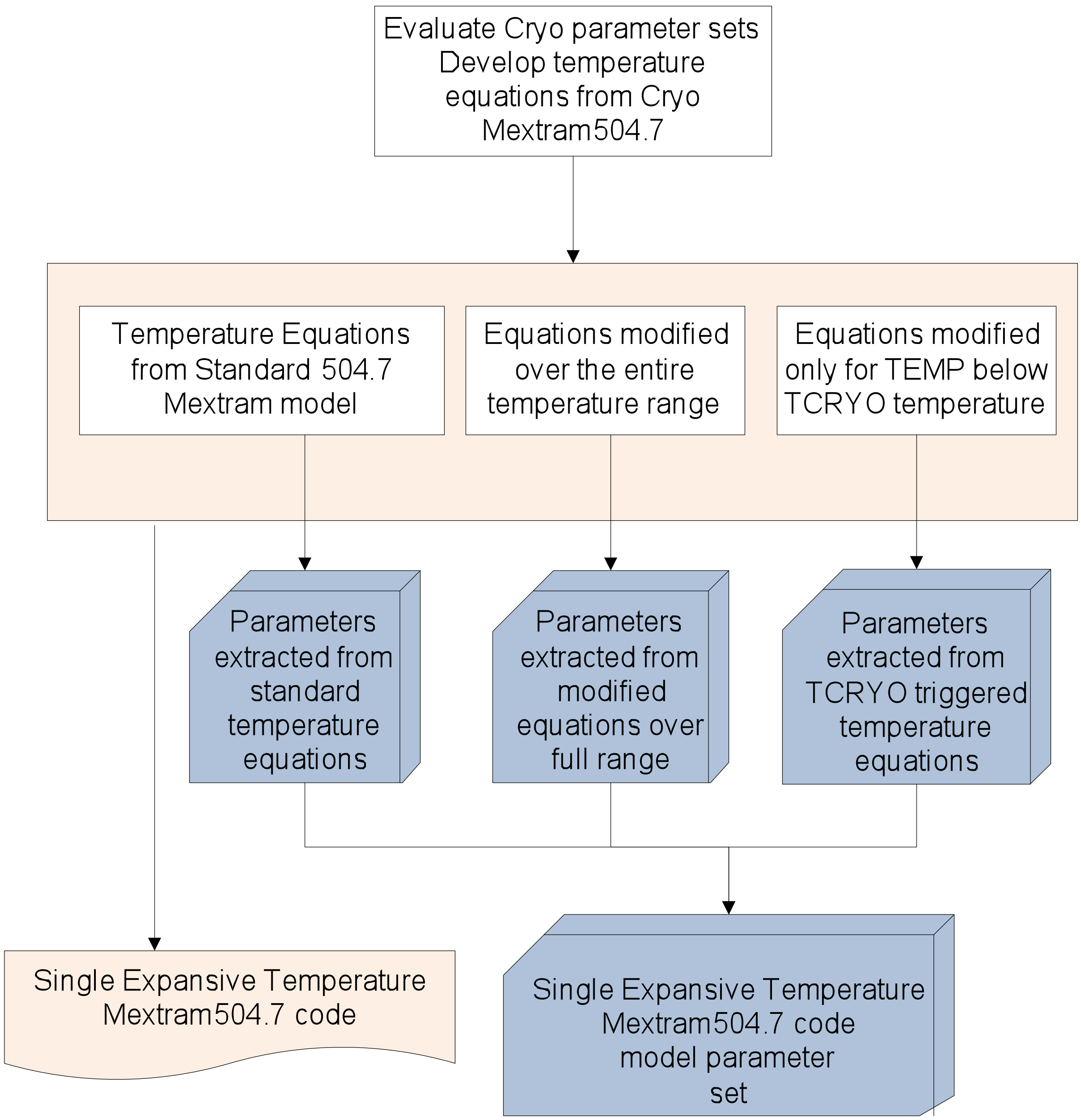

Figure 8.1 SET temperature equations and parameter development methodology

The SET model uses all of the temperature definitions of the Mextram 504.7 described in Chapter 3. These temperature definitions are summarized in Table 8.1 for quick reference. The SET reference temperature model parameter, TREF=27C, is 300K within the model.

Parameter/ Variable	Description	Function Within the Model	SET Value	Units
TEMP	Simulation temperature, equals ambient temperature, $T_{Ambient}$ 300K 223K 162K 93K	Simulation Parameter	27 -50 -111 -180	C
TREF	Model reference temperature parameter, 300K	Model Parameter	27	C
Tmodel	Model temperature converted to Kelvin Equation (3.2)	Internal Variable	300	K
Tk	Device temperature, total temperature of TEMP and self-heating temperature rise Equation (3.1)	Internal Variable		K
t_N	$\left(\frac{Tk}{Tmodel}\right)$, Temperature ratio Equation (3.3)	Internal Variable		
V_T	$\frac{k \cdot Tk}{q}$, Thermal voltage at Tk Equation (3.4)	Internal Variable		V
$\frac{1}{V_{\Delta T}}$	$\frac{q}{k}\left(\frac{1}{Tk}-\frac{1}{Tmodel}\right)$ Difference in thermal voltage between the device temperature and model temperature, Equation (3.4)	Internal Variable		$\frac{1}{V}$

Table 8.1 Temperature definitions of internal variables for SET model

The ambient temperature model parameter sets were fit to the Cryo Mextram 504.7 model as indicated in the SET development flowchart of Figure 1.3. In each of the four ambient temperature models, the model temperature reference parameter, TREF, was set equal to the ambient temperature simulation variable, TEMP. The self-heating effects were influential at each ambient temperature. Each ambient temperature model was fitted so that the electrical model parameters were extracted in conjunction with an accurate self-heating model contribution. Therefore, the device temperature, Tk, of the ambient temperature models correctly indicates the sum of the ambient temperature and the temperature increase due to self-heating. The temperature equations of the standard Mextram 504.7 model were able to correctly represent the self-heating effects of the four ambient temperature models [34],[13].

For the development of the SET model, the ambient temperatures, $T_{Ambient}$, was equated to the device temperature, Tk. Ambient temperature parameter values and the corresponding $T_{Ambient}$ are used to analyze the existing parameter temperature equations and develop new temperature relationships. The temperature equations are defined in terms of the temperature ratio, t_N, of Equation (3.3). Therefore in the SET temperature equation development, t_N is equated to the ratio, $\frac{T_{Ambient}}{300K}$. High accuracy was achieved in the ambient temperature model parameters of Chapter 7 due to the Mextram's self-heating model of internal power dissipation[13]. There was no self-heating influence in the resulting ambient temperature parameters. Therefore the ambient temperature parameters can be directly related to $\frac{T_{Ambient}}{300K}$. The SET temperature relationships can be determined by comparing the relationship of the parameter values to the corresponding ratio of $\frac{T_{Ambient}}{300K}$. Analysis using this approach was applied to each of the model parameters in Sections 8.2 and 8.3.

The temperature dependence of the standard 504.7 model parameters was derived from the temperature relationship of mobility, μ, and intrinsic carrier concentration, n_i. The relationship of mobility to temperature was defined in Equation (3.87). The relationship of intrinsic concentrations to temperature ratio, bandgap voltage, and thermal voltage change was defined in Equation (3.86). Both relationships are repeated below [13][35, 42]:

$$\mu \propto \frac{1}{t_n^A} \tag{8.1}$$

$$n_i^2 = n_{iREF}^2 t_N^3 \exp\left[-\frac{V_g}{V_{\Delta T}}\right] \tag{8.2}$$

A	Temperature coefficient defined by Klaussen mobility model [35, 39, 42], represented in Mextram 504.7 by temperature coefficient parameters in Table 3.10.
V_g	Bandgap voltage, represented in Mextram 504.7 by temperature bandgap voltage parameters in Table 3.11
n_{iREF}	Intrinsic carrier concentration at the reference temperature, 300K

8.2 Parameters temperature equations with standard Mextram 504.7 behavior

Analysis of ambient temperature parameters' behavior as a function of temperature determined the SET model parameter temperature equations. The behavior of several model parameters were found to fit the standard 504.7 parameter temperature equations across the full expansive temperature range and are listed in Tables 8.2 and 8.3.

The SiGe bandgap parameter behavior can be described by the standard Mextram 504.7 temperature equation. Most of the resistance model parameters were found to fit well using the standard 504.7 temperature equations over the wide temperature range Also, the junction diffusion voltage and capacitance parameters can be represented by the 504.7 standard parameter temperature equations. Some of reverse current parameters were found to work well with the standard 504.7 temperature equations [13]. The SET parameters utilizing the standard 504.7 parameter temperature equations and their associated temperature parameters are summarized in Table 8.2 and Table 8.3. Each of these ambient temperature parameters is analyzed and the final SET model parameters are reviewed in Sections 8.2.1 through 8.2.5.

Model parameter temperature equations which used the standard 504.7 temperature equations derived from the relationship of temperature to carrier mobility, Equation (8.1), are listed in Table 8.2. Each parameter has temperature dependence based on a unique temperature coefficient associated with the temperature ratio indicated by the SET temperature parameter in Table 8.2.

Temperature Equation Variable	Parameter Description	SET Parameter	SET Temperature Parameter
DEG_T	SiGe bandgap voltage	DEG	AQBO
RTH_T	Thermal impedance of self-heating	RTH	ATH
RE_T	Emitter resistance	RE	AE
RBC_T	External base resistance	RBC	AEX
RCC_T	External collector resistance	RCC	AC
RCCex_T	Internal buried N+ collector resistance	RCBLX	ACBL
RCV_T	Epilayer collector resistance at low currents	RCV	AEPI
TAUR_T	Reverse transit time	TAUR	
ISS_T	Saturation current of parasitic PNP	ISS	AS
IKS_T	Knee current of parasitic PNP	IKS	AS

Table 8.2 SET temperature adjusted parameters with a temperature coefficient dependence which were compatible with the standard 504.7 temperature equations

Model parameter temperature equations which used the standard 504.7 temperature equations derived from the relationship of temperature and bandgap voltages of Equation (8.2) are listed in Table 8.3. The exponential relationship of energy bandgap voltage and temperature in the intrinsic concentration influence the intrinsic junction descriptions. Each parameter in Table 8.3 has a temperature dependence defined by a unique junction bandgap voltage parameter or temperature adjusted diffusion voltage model parameter.

Temperature Equation Variable	Parameter Description	SET Parameter	SET Temperature Parameter
IBR_T	Saturation Current of nonideal reverse base current, I_{B3} branch	IBR	VGC
VDE_T	Base-Emitter diffusion voltage	VDE	VGB
CJE_T	Base-Emitter depletion capacitance	CJE	**VDE_T**
VDC_T	Base-Collector diffusion voltage	VDC	VGC
XP_T	Fraction of constant CJC	XP	**VDC_T**
CJC_T	Base-Collector depletion capacitance	CJC	**VDC_T**
VDS_T	Collector-Substrate diffusion voltage	VDS	VGS
CJS_T	Collector-Substrate depletion capacitance	CJS	**VDS_T**

Table 8.3 SET temperature adjusted parameters shifted by the bandgap voltage dependence to temperature

8.2.1 SiGe bandgap model parameter – DEG

For an accurate fit at the lower ambient temperatures, the use of the SiGe bandgap equations in the base charge calculation of current was found to be essential. The SiGe bandgap contribution to base charge allowed an accurate description of the full output operation range over the wide temperature range. The SiGe equation approach also influences the values of parameters: BF, VEF, and VER. Each of these ambient temperature parameter responses is included in the SET model as described in Section 8.3. The SiGe bandgap parameter, DEG, changed accurately with temperature in the SET model over the expansive temperature range. The temperature response of the standard 504.7 Mextram DEG bandgap parameter was described in Section 3.6.4 by the temperature adjusted parameter equation, **DEG_T** repeated in Equation (8.3) [2], [13].

$$\mathbf{DEG\_T} = \mathrm{DEG} \cdot t_N^{\mathrm{AQBO}} \tag{8.3}$$

Analysis of the ambient temperature DEG values indicated that Equation (8.3) would accurately fit the SET model simulation output results. Two parameters, DEG and AQBO, were extracted by fitting the ambient model values to the standard 504.7 temperature response of Equation (8.3).

The model temperature ratio, t_N, was equated to an ambient temperature versus SET model temperature ratio, $\frac{T_{Ambient}}{300K}$. The four ambient temperature DEG values listed in Table 7.2 were plotted versus the corresponding temperature ratio, $\frac{T_{Ambient}}{300K}$ in Figure 8.2. The DEG values were found to have a power series relationship with $\frac{T_{Ambient}}{300K}$ as seen by the parameter fit indicated by the solid line in Figure 8.2.

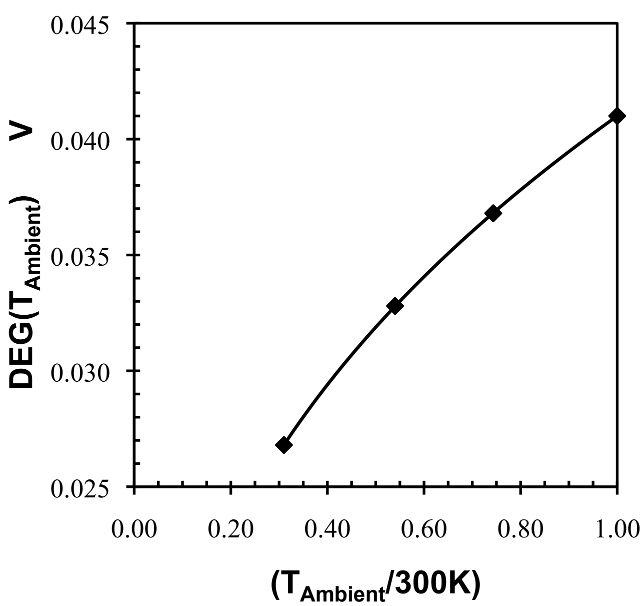

Figure 8.2 SET model extraction of SiGe bandgap model parameters. Equation (8.3) is the solid line and symbols are ambient values of DEG.

SET Model	
Parameter	Value
DEG	41mV
AQBO	363m

Table 8.4 SET Model parameters of DEG and AQBO

The values of DEG and AQBO extracted from this relationship are listed in Table 8.4. The parameter AQBO physically represents the intrinsic base region temperature coefficient under zero bias. In the standard 504.7 model AQBO, is shared by seven other model parameter temperature equations, as indicated in Table 3.35 [13]. Sharing of AQBO in the standard model was found not to be possible for the wide temperature range of the SET model. The importance of the SiGe bandgap effects to the base charge calculation was discussed in Chapter 6. The control and accuracy of DEG over the expansive temperature range required that the temperature coefficient parameter, AQBO, only support the SET model temperature equation of DEG. In particular, there was a very small region of optimization compatibility between parameter DEG and the forward and reverse Early parameters, VEF and VER. Therefore, utilizing one common temperature coefficient parameter for the temperature behavior of all three parameter over the expansive temperature SET model range was not possible. The Early voltage temperature equations were modified to have individual temperature coefficients added in the SET model which is discussed in Section 8.3.1.

8.2.2 Self-heating thermal impedance – RTH

Self-heating was very significant in the SiGe HBT modeled. Great attention was given to modeling the self-heating effects of each ambient temperature model. The standard 504.7 approach to modeling self-heating accounts for all power dissipation due to a thermal resistance parameter, RTH, contribution and a thermal capacitance parameter, CTH. The common self-heating model in 504.7 Mextram is described in Section 3.5. Temperature scaling of the two parameters in the standard 504.7 model is described in Section 3.6.7. CTH is temperature independent and RTH is temperature dependent. The standard 504.7 RTH temperature equation, **RTH_T**, is repeated in Equation (8.4) [2].

$$\mathbf{RTH\_T} = \mathrm{RTH} \cdot \left(\frac{T_{Ambient}}{TREF} \right)^{ATH} \tag{8.4}$$

For the SET model it was found that the standard 504.7 temperature equations were adequate for representing RTH and CTH. Equation (8.4) was used for the SET temperature equation, RTH_T. The SET equation, **RTH_T**, and the ambient temperature RTH values are plotted versus the ratio of $\frac{T_{Ambient}}{300K}$ in Figure 8.3. The ambient values are represented by symbols. The thermal resistance temperature equation, **RTH_T**, of Equation (8.4), is the solid line in Figure 8.3. The fit between the temperature equation ambient temperature RTH points was adequate. Evaluation of the model fits to the DC and AC measurements support that the SET model. The SET model error increases at 300K, but the output characteristics SET model simulations produce an excellent fit at 300K. However, the divergence of RTH from 223K to 300K indicates

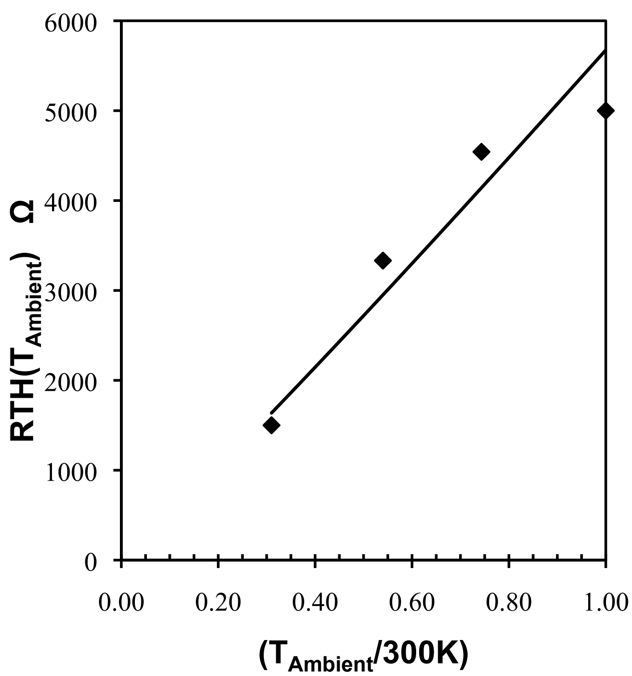

Figure 8.3 SET parameter extraction thermal impedance parameters. Equation 8.4 is the solid line and ambient temperature RTH values are the symbols.

SET Model	
Parameter	Value
RTH	5658Ω
ATH	1.107
CTH	241pF

Table 8.5 SET parameters RTH, ATH and CTH.

that a multi-section resistance approach might improve the ambient fit. Additional ambient temperature models in the higher temperature region would be required to pursue this research in the future. CTH remains temperature independent. The resulting SET model values of parameters, RTH ATH and CTH are shown in Table 8.5

8.2.3 Resistance parameters and their temperature behavior in SET model

The resistance parameters: RE, RBC, RCC, RCBLX and RCV, were found to respond to temperature by their respective standard Mextram 504.7 model temperature equations over the expansive temperature range. For the standard Mextram model, the parasitic resistance varies with temperature based on two physical principles:

- Resistance is inversely proportional to conductivity and therefore resistance is inversely proportional to charge carrier mobility.
- Mobility of charge carriers is inversely proportional to temperature.

The standard Mextram 504.7 temperature equations for each of the resistance parameters were described in Section 3.6.

8.2.3.1 Emitter resistance - RE

The emitter resistance of the Mextram model is a constant resistor value, RE, which varies only when the simulation temperature, TEMP, differs from the model reference temperature, TREF. The emitter resistance temperature equation, **RE_T**, of Equation (3.96) defines the variation of emitter resistance with temperature in the standard Mextram 504.7 model. A comparison of the temperature equation results to the ambient temperature RE values found that the standard 504.7 Mextram emitter resistance temperature equation, **RE_T**, does represents the RE parameter response over the expansive temperature range.

The SET model emitter resistance, **RE_T** corresponds to the standard 504.7 model Equation (3.96) and is defined below in Equation (8.5) [2].

$$\mathbf{RE\_T} = \mathrm{RE} \cdot t_N^{AE} \tag{8.5}$$

The SET model emitter resistance parameter, RE, and its temperature coefficient model parameter, AE, were determined from the RE values of the four ambient temperature models. The ambient temperature RE values are plotted versus the ratio of $\frac{T_{Ambient}}{300K}$ in Figure 8.4. The ambient values are represented by symbols. The emitter resistance temperature equation, **RE_T**, of Equation (8.5), is the solid line in Figure 8.4. The fit between the temperature

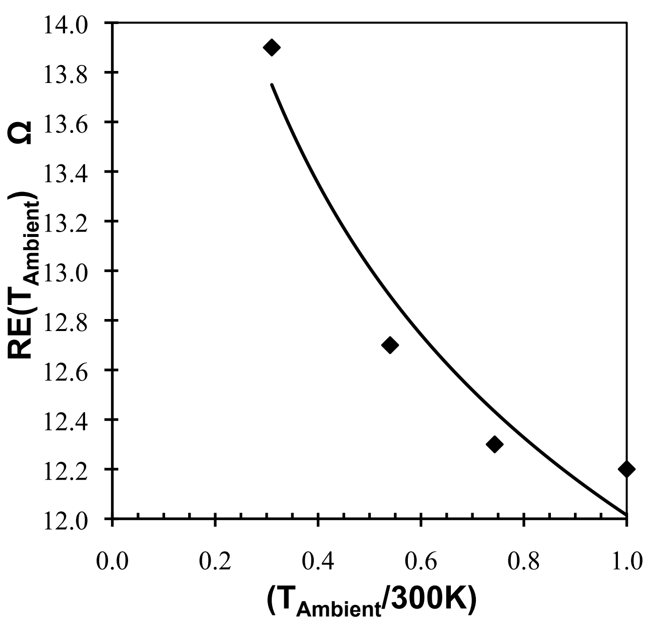

Figure 8.4 SET model extraction of emitter resistance model parameters, RE and AE. Equation (8.5) is the solid line and ambient temperature RE values are the symbols.

SET Model	
Parameter	Value
RE	12.02 Ω
AE	-0.115

Table 8.6 SET Model Parameters of RE and AE

equation ambient temperature RE points is satisfactory. The resulting SET model values of parameters, RE and AE are shown in Table 8.6. The fit of the SET model temperature equation to the ambient RE values has a fair degree of error. However, the dynamic range of the ambient RE values shifts over temperature by less than 15%. Therefore the effects of the differences between the SET model and ambient values had little impact on the DC and AC results.

8.2.3.2 External base resistance - RBC

The external base resistance of the Mextram model is a constant resistance, RBC. However, the value of RBC changes when the simulation temperature, TEMP, differs from the model reference temperature, TREF. The external base resistance temperature equation, **RBC_T**, of Equation (3.97) defines the dependence of external base resistance on temperature for the standard Mextram 504.7 model. A comparison of the **RBC_T** temperature equation results to the ambient temperature RBC values found that the standard 504.7 Mextram external base resistance temperature equation, **RBC_T**, accurately simulates the RBC parameter response over the full temperature range.

The SET model external base resistance temperature equation, **RBC_T**, corresponds to the standard Mextram 504.7 temperature Equation (3.97) and is defined in Equation (8.6) [2].

$$\mathbf{RBC\_T} = \mathrm{RBC} \cdot t_{N}^{AEX} \tag{8.6}$$

The SET model external base resistance parameter, RBC, and its temperature coefficient model parameter, AEX, were determined from the RBC values of the four ambient temperature models. The ambient temperature RBC values are plotted versus the ratio of $\frac{T_{Ambient}}{300K}$ in Figure 8.5. The ambient temperature RBC values are represented by markers. The external base resistance temperature equation, **RBC_T**, of Equation (8.6), is the solid line in Figure 8.5. The resulting SET model values of parameters, RBC and AEX are shown in Table 8.7.

The fit between the temperature equation ambient temperature RBC points is excellent. The SET model fit of the RBC temperature equation to the RBC ambient values was excellent and assisted in the good final DC and AC results.

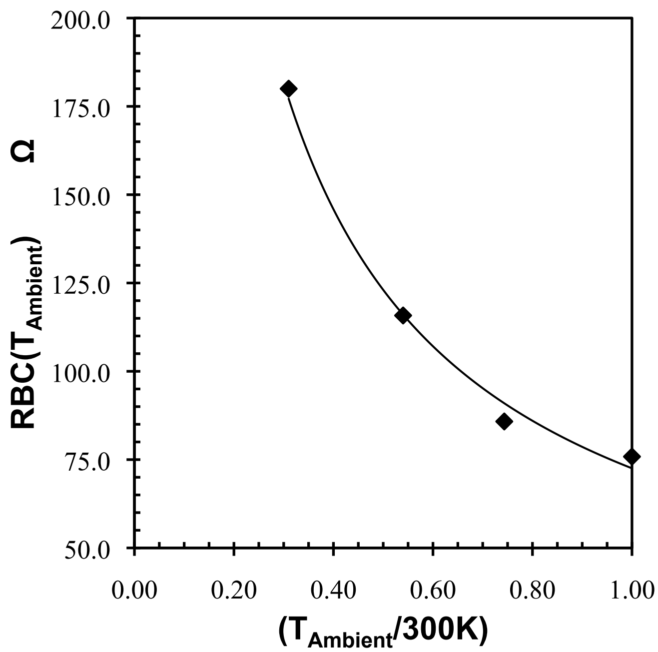

Figure 8.5 SET model extraction of external base resistance parameters, RBC and AEX. Equation (8.6) is the solid line. Ambient temperature RBC values are symbols.

SET Model	
Parameter	Value
RBC	75.85 Ω
AEX	-0.283

Table 8.7 SET model parameters of RBC and AEX

8.2.3.3 External collector resistance - RCC

The external collector resistance of the Mextram model is a constant resistance, RCC. The value of RCC only changes when the simulation temperature, TEMP, differs from the model reference temperature, TREF. The external collector resistance temperature equation, **RCC_T**, of Equation (3.99) defines the dependence of external collector resistance to temperature for the standard Mextram 504.7 model. A comparison of the **RCC_T** temperature equation results to the ambient temperature RCC values shows that the standard 504.7 Mextram external collector resistance temperature equation, **RCC_T**, accurately simulates the RCC parameter response over the full temperature range.

The SET model external collector resistance temperature equation, **RCC_T**, corresponds to the standard Mextram 504.7 temperature Equation (3.99) and is defined in Equation (8.7) [2].

$$\mathbf{RCC\_T} = \mathrm{RCC} \cdot t_N^{AC} \tag{8.7}$$

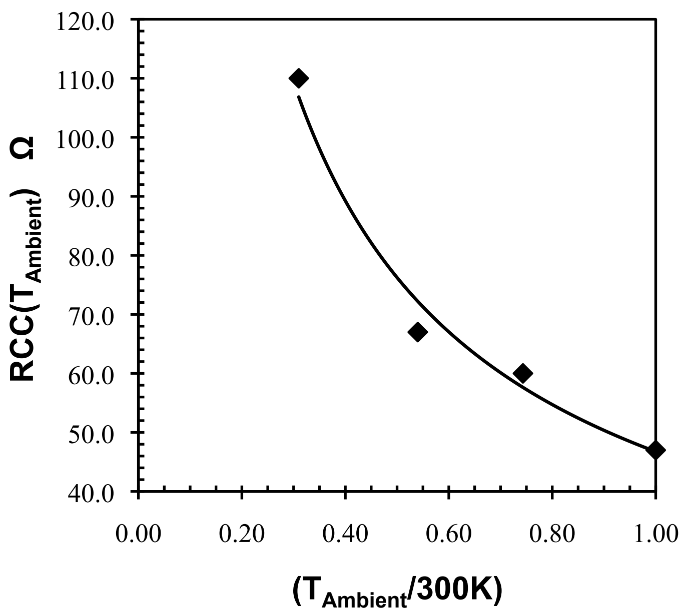

Figure 8.6 SET model extraction of external collector resistance parameters, RCC and AC. Equation (8.7) is the solid line and ambient temperature RBC values are symbols.

SET Model	
Parameter	Value
RCC	47Ω
AC	-0.706

Table 8.8 SET model parameters of RCC and AC

The SET model fit of the RCC temperature equation was excellent for all ambient values. The ambient value at 162K had a slight deviation of less than 6% error with the temperature equation, but this difference did not have an effect on the overall results of the SET model.

8.2.3.4 External buried layer collector resistance - RCBLX

The model release of the standard Mextram 504.7 added constant collector resistance branches to represent the external buried N^+ collector, RCBLX, and the internal buried N^+ collector region resistance, RCBLI. An extrinsic buried collector region was not present in the IBM SiGe BiCMOS process modeled. Therefore, RCBLX was set to zero in each ambient temperature model as detailed in Section 6.2. The SET model implemented the collector resistance in the same manner as the ambient temperature models as defined in Equation (8.8). The value for the RCBLX was set to zero and the corresponding temperature model parameter, ACBL was set to one. The SET values for external buried collector resistance as summarized in Table 8.9.

$$\mathbf{RCCex\_T} = \mathrm{RCBLX} \cdot t_N^{\mathrm{ACBL}} \tag{8.8}$$

SET Model	
Parameter	Value
RCBLX	0Ω
ACBL	1

Table 8.9 SET values for the external buried N^+ collector resistance, RCBLX and ACBL.

The intrinsic buried N^+ collector resistance, RCBLI, was significant to the high current region of the AC response in the ambient temperature models. The SET model temperature equations of RCBLI and the SET parameter values are defined in Section 8.4.6.

8.2.3.5 Low current collector epilayer resistance - RCV

The resistance of the N^- epilayer collector region changes with current flow through the collector. The physical behavior of the epilayer quasi-saturation effects was described in Section 2.3. The SET model does not deviate from the standard Mextram 504.7 model of the epilayer current description of Section 3.2.5. The epilayer current branch, I_{C1C2}, is defined by a low current constant resistance, RCV, and a high current space charged resistance, SCRCV. In the standard 504.7 parameter temperature equations, RCV is temperature dependent but SCRCV is temperature independent. It was found for the wide temperature range and at very low temperatures RCV resistance response could be described by the standard 504.7 temperature Equation (3.102). However, the temperature response of SCRCV did deviate from standard Mextram 504.7 definitions. The SET model temperature equation for SCRCV is described in Section 8.4.3.

The low current epilayer resistance, RCV, is a constant value which only varies when the simulation temperature, TEMP, differs from the model reference temperature, TREF. The epilayer collector resistance temperature equation, **RCV_T**, of Equation (3.102) defines the dependence of epilayer collector resistance to temperature for the standard Mextram 504.7 model. Comparison of the **RCV_T** temperature equation with the ambient temperature RCV values indicates the standard 504.7 Mextram temperature equation, **RCV_T**, will satisfactorily simulate the RCV parameter response over the full temperature range.

The SET model epilayer collector resistance temperature equation, **RCV_T**, corresponds to the standard Mextram 504.7 temperature Equation (3.102) and is defined in Equation (8.9) [2].

$$\mathbf{RCV\_T} = \mathrm{RCV} \cdot t_N^{\mathrm{AEPI}} \tag{8.9}$$

The SET model fit of **RCV_T**, Equation (8.9) did not produce an extremely accurate fit to the ambient RCV values in Figure 8.7. A more accurate fit would only have been accomplished by a more complex equation that was not defined in terms of a power series. A more complex equation would have deviated from the SET methodology of maintaining the relationships of resistance, carrier mobility and temperature. Maintaining the SET methodology was preferred because the SET extracted parameter values of Table 8.10 produced the best AC and DC results over all operating regions and temperatures.

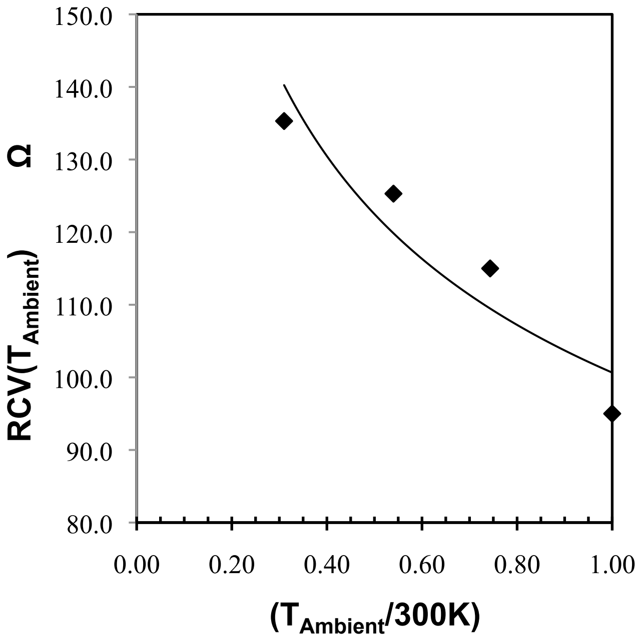

Figure 8.7 SET model extraction of variable epilayer collector resistance model parameters, , RCV and AEPI. Equation (8.9) is the solid line and ambient temperature RCV values are symbols.

SET Model	
Parameter	Value
RCV	100.7Ω
AEPI	-0.283

Table 8.10 SET model parameters of RCV and AEPI

8.2.4 Diffusion voltage and depletion capacitance parameter temperature equations

The standard 504.7 Mextram model representation of junction bias behavior was found to be essential to accurately fitting both the DC and AC response, over the wide temperature range. The SiGe HBT Early effects in the linear DC output operating region and the high current AC small signal behavior required advanced junction equations. The junction voltage equations described in Section 3.1.4.2 provided the necessary mathematical smoothing for the larger base-emitter junction voltages of the SiGe HBT at the very low temperature points. The junction voltages in the Mextram 504.7 are based on classic PN depletion junction theory. For each intrinsic bipolar PN junction, the diffusion voltage parameter is the built-in potential voltage of the junction. This classic PN junction physical relationship is defined by VD in Equation (8.10). In Mextram 504.7, the diffusion voltage parameter temperature equations are of the form of **VD_T,** described in Section 3.6.1 and repeated in Equation (8.10) [2].

$$\begin{aligned} VD &= V_T \ln\left[\frac{N_A N_D}{n_i^2}\right] \\ VD\_T &= -3V_T \cdot \ln\left[t_N\right] + V_d t_N + (1 - t_N) V_g \end{aligned} \qquad (8.10)$$

V_d	Diffusion voltage, represented in Mextram 504.7 by diffusion voltage parameters: VDE, VDC, and VDS.
V_g	Bandgap voltage, represented in Mextram 504.7 by bandgap voltage parameters: VGB, VGC, and VGS

In Equation (8.10) the temperature response was derived by applying the intrinsic concentration Equation (8.2). The diffusion voltage parameter temperature responses of the standard 504.7 model were found to support the SET model parameter temperature behavior. The wide temperature range caused significant shifts in junction voltage that required the diffusion voltage parameters, VDE, VDC, and VDS to also scale with temperature. Each junction diffusion voltage and its corresponding depletion capacitance parameters are defined in the following sections.

8.2.4.1 Base-emitter diffusion voltage and depletion capacitance - VDE and CJE

The base-emitter diffusion voltage, VDE, was defined and implemented in the model equations of Chapter 3. The value of VDE changes in the model simulations when the simulation temperature, TEMP, differs from the model reference temperature, TREF. The base-emitter diffusion voltage temperature equation, **VDE_T**, in the standard Mextram 504.7 model was derived by the method described in Equation (8.10). A comparison of the **VDE_T** temperature equation and the ambient temperature VDE values clearly indicated that the standard

504.7 Mextram base-emitter diffusion voltage temperature equation, **VDE_T**, accurately simulates the VDE parameter response over the full temperature range.

Therefore the SET model base-emitter diffusion voltage temperature equation, **VDE_T**, corresponds to the standard Mextram 504.7 temperature Equation (3.88) and is repeated in Equation (8.11) [2].

$$\mathbf{VDE\_T} = -3V_T \cdot \ln\left[t_N\right] + VDE \cdot t_N + (1 - t_N) \cdot VGB \tag{8.11}$$

The base-emitter bandgap parameter, VGB, was optimized to the DC and AC measurements. In the standard 504.7 model the base bandgap temperature parameter, VGB, is also used in the saturation current temperature equation, **IS_T**. During VGB optimizations it was discovered that the best fit of VGB for the diffusion voltage and depletion capacitance response created an error in the **IS_T** response to temperature. Therefore, in the SET model VDE and IS no longer share the base bandgap temperature parameter, VGB. The temperature response of IS required a new temperature equation and new temperature parameters to represent the values needed. The SET model approach to the temperature parameter equation, **IS_T,** is defined in Section 8.3.2.5.

The SET model base-emitter diffusion voltage parameter calculation, **VDE_T**, and the ambient temperature VDE values are plotted versus the ratio of $\frac{T_{Ambient}}{300K}$ in Figure 8.8. The ambient temperature VDE values are represented by markers. The base-emitter diffusion voltage temperature equation, **VDE_T**, of Equation (8.11), is the solid line in Figure 8.8. The final SET values for VDE and VGB are listed in Table 8.11. The SET model fit of the **VDE_T** temperature equation to the VDE ambient values was excellent, though the range

The base-emitter depletion capacitance parameter, CJE, has temperature response in the Mextram 504.7 as defined by Equation (3.92). The four ambient temperature CJE values were used to determine that the standard 504.7 response produced an excellent fit for the SET model as shown in Figure 8.9. Therefore, the SET model base-emitter depletion capacitance temperature equation, **CDE_T**, corresponds to the standard Mextram 504.7 temperature Equation (3.92) and is repeated in Equation (8.12) [2].

$$\mathbf{CJE\_T} = \mathrm{CJE} \cdot \left(\frac{\mathrm{VDE}}{\mathbf{VDE\_T}} \right)^{\mathrm{PE}} \tag{8.12}$$

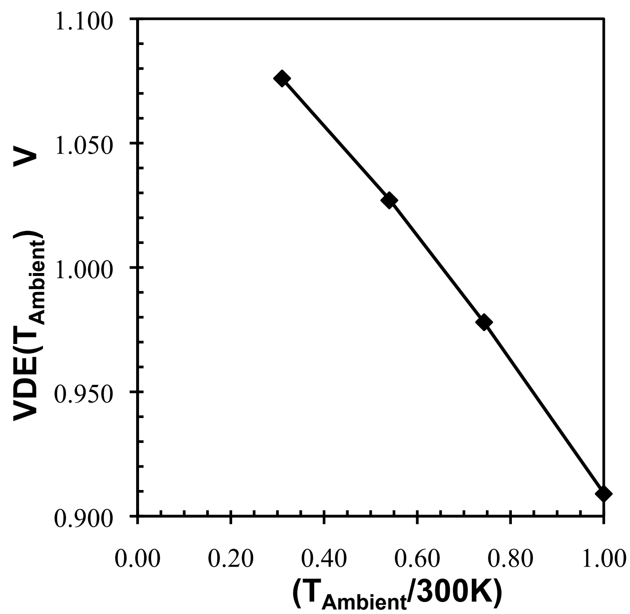

Figure 8.8 SET model extraction of base-emitter depletion voltage model parameters. Equation (8.11) is the solid line and ambient temperature VDE values are symbols

SET Model	
Parameter	Value
VDE	909.3mV
VGB	1.11V
CJE	10.96fF
PE	288.3m

Table 8.11 SET parameters of VDE, VGB, CJE, PE

The base-emitter grading factor parameter, PE, was independent of temperature. The final SET values for PE and CJE are listed in Table 8.11.

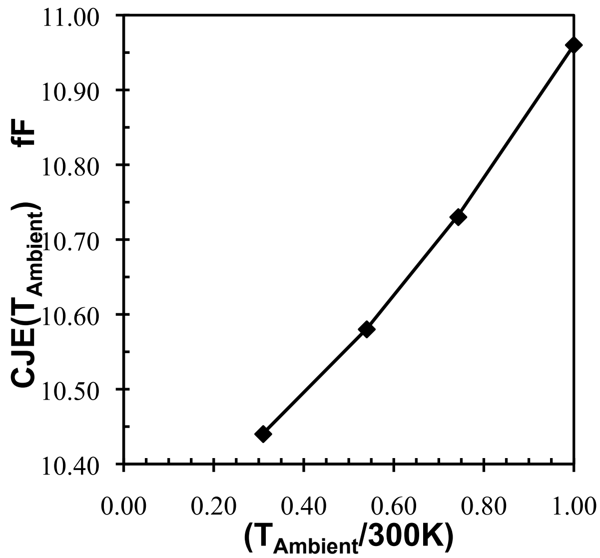

Figure 8.9 SET model extraction of CJE. Equation (8.12) is the solid line and ambient temperature VDE values are symbols

8.2.4.2 Base-collector diffusion voltage and depletion capacitance - VDC and CJC

The base-collector diffusion voltage, VDC, and temperature equation, **VDC_T**, were defined in Chapter 3. In model simulations, the value of VDC changes when the simulation temperature, TEMP, differs from the model reference temperature, TREF. The base-collector diffusion voltage temperature equation, **VDC_T**, in the standard Mextram 504.7 model was derived by the method described in Equation (8.10). A comparison of the **VDC_T** temperature equation and the ambient temperature VDC values showed that the standard 504.7 Mextram temperature equation accurately simulates the VDC parameter response over the full temperature range.

Therefore the SET model base-collector diffusion voltage temperature equation, **VDC_T**, does not differ from the standard Mextram 504.7 temperature Equation (3.89) and is repeated in Equation (8.13) [2].

$$\mathbf{VDC\_T} = -3V_T \cdot \ln\left[t_N\right] + VDC \cdot t_N + (1 - t_N) \cdot VGC \tag{8.13}$$

The collector bandgap voltage parameter, VGC, was optimized to produce a VDC response that best supported the DC and AC results. In the standard Mextram 504.7, the collector bandgap voltage parameter, VGC, is also shared in the temperature equation for the nonideal reverse base saturation current parameter, IBR. The temperature equation, **IBR_T**, and value of VGC are analyzed in Section 8.2.6. *It was determined that the VGC value optimized for the best VDC fit also yielded a good fit for the IBR temperature response*. Therefore, the standard 504.7 implementation of VGC worked well for the expansive temperature range of the SET model.

The SET model temperature equation, **VDC_T**, and the ambient temperature VDC values are plotted versus the ratio of $\frac{T_{Ambient}}{300K}$ in Figure 8.9. The ambient temperature VDC values are represented by markers. The base-collector diffusion voltage temperature equation, **VDC_T**, of Equation (8.13), is the solid line in Figure 8.10. The final SET values for VDC and VGC

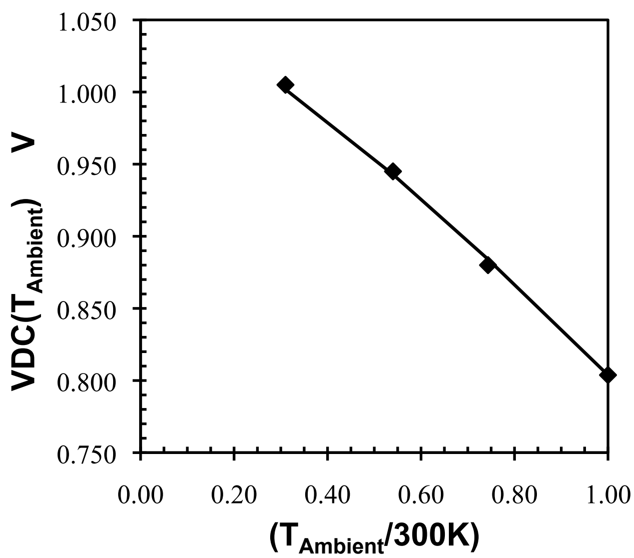

Figure 8.10 SET model comparison of solid line, Equation (8.13) and ambient temperature VDC values are symbols

SET Model	
Parameter	Value
VDC	803.8mV
VGC	1.05V
XP	351.1m
CJC	5.91fF
PC	305.5m

Table 8.12 SET parameters of VDC, VGC, CJC, XP, PC

are listed in Table 8.12. The SET model fit of the **VDC_T** temperature equation to the VDC ambient values was accurate.

The remaining depletion junction parameters, XP and CJC are scaled with temperature. Both model parameters are shifted by the change in the base-collector diffusion voltage, **VDC_T**. The standard Mextram 504.7 parameter temperature equations, **XP_T** and **CJC_T**, were compared to the ambient temperature XP and CJC values in Figures 8.11 and 8.12. Both parameter equations adequately represent the ambient values. The standard Mextram 504.7 temperature equations of (3.95) and (3.94) are used in the SET model temperature equations for XP and CJC [2].

$$\mathbf{XP\_T} = \frac{\mathrm{XP}}{\left[(1-\mathrm{XP})\cdot\left(\dfrac{\mathrm{VDC}}{\mathbf{VDC\_T}}\right)^{\mathrm{PC}} + \mathrm{XP}\right]} = \frac{\mathrm{XP}}{[\,\mathrm{CJC\_Scaling}\,]} \tag{8.14}$$

$$\mathbf{CJC\_T} = \mathrm{CJC}\cdot\left[(1-\mathrm{XP})\cdot\left(\frac{\mathrm{VDC}}{\mathbf{VDC\_T}}\right)^{\mathrm{PC}} + \mathrm{XP}\right] = \mathrm{CJC}\cdot[\,\mathrm{CJC\_Scaling}\,] \tag{8.15}$$

There is a slight difference between the SET model fit and the ambient temperature values of CJC and XP in Figures 8.11and 8.12. The error is less than 5% due to the small dynamic range of the values. This slight error did not affect the accuracy of SET model simulations.

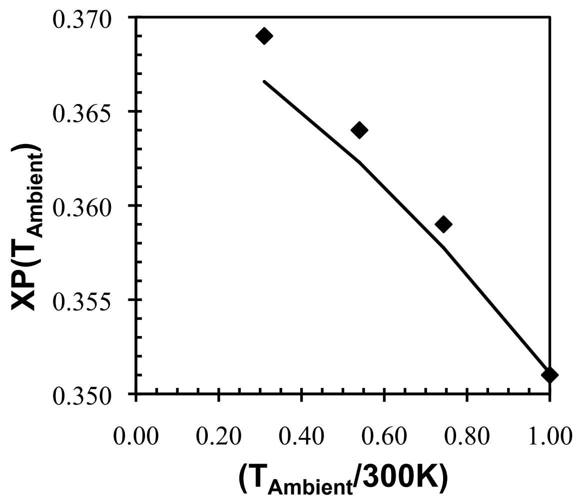

Figure 8.11 SET model of XP. Equation (8.14) is the solid line and ambient temperature XP values are symbols

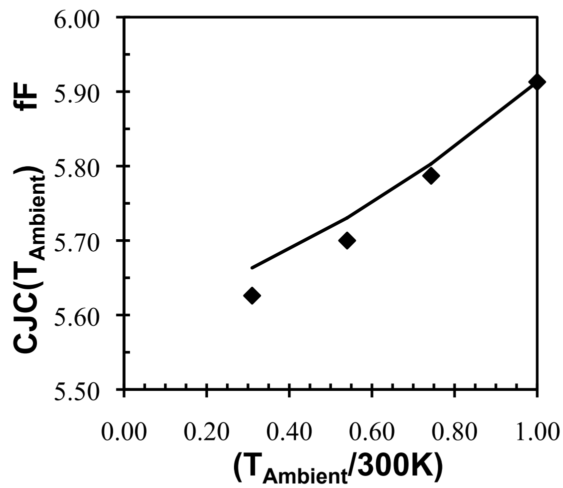

Figure 8.12 SET model of CJC. Equation (8.15) is the solid line and ambient temperature CJC values are symbols

8.2.4.3 Collector-substrate diffusion voltage and depletion capacitance - VDS and CJS

The collector-substrate diffusion voltage, VDS, and temperature equation, **VDS_T**, were defined in Chapter 3. The VDS parameter is defined at the model reference temperature, TREF and the value of VDS shifts according to the temperature equation, **VDS_T**, based on the simulation temperature, TEMP. The collector-substrate diffusion voltage temperature equation, **VDS_T**, in the standard Mextram 504.7 model was derived by the method described in Equation (8.10). A comparison of the **VDS_T** temperature equation and the ambient temperature VDS values indicated that the standard 504.7 Mextram temperature equation would adequately represent the VDC parameter response over the full temperature range.

Therefore, the SET model collector-substrate diffusion voltage temperature equation, **VDS_T**, does not differ from the standard Mextram 504.7 temperature Equation (3.90) and is repeated in Equation (8.16) [2].

$$\mathbf{VDS\_T} = -3V_T \cdot \ln\left[t_N\right] + VDS \cdot t_N + (1 - t_N) \cdot VGS \tag{8.16}$$

The substrate bandgap voltage, VGS, is shared by both the parameter temperature equation of VDS and ISS. The temperature response of the saturation current of the parasitic PNP parameter, ISS, is detailed in Section 8.2.6. The VGS value optimized for the SET model VDS response performed well in the ISS parameter temperature response. Therefore, the SET model used the standard 504.7 implementation and shared VGS in both **VDS_T** and **ISS_T**.

The SET model collector-substrate diffusion voltage parameter calculation, **VDS_T**, and the ambient temperature VDS values are plotted versus the ratio of $\frac{T_{Ambient}}{300K}$ in Figure 8.13. The ambient temperature VDS values are represented by symbols. The collector-substrate

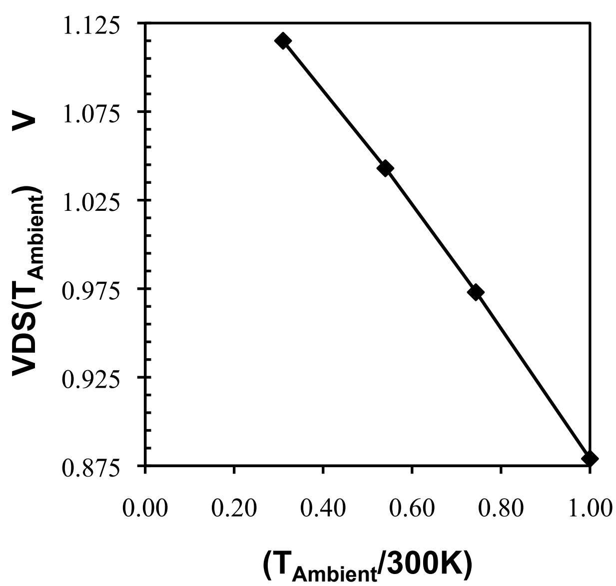

Figure 8.13 SET model extraction of base-emitter depletion voltage model parameters. Equation (8.16) is the solid line and ambient temperature VDS values are symbols

SET Model	
Parameter	Value
VDS	879mV
VGS	1.18V
CJS	0.66fF
PS	335.0m

Table 8.13 SET parameters of VDS, VGS, CJS, PS

diffusion voltage temperature equation, **VDS_T**, of Equation (8.16), is the solid line in Figure 8.13. The final SET values for VDC and VGC are listed in Table 8.13.

The standard Mextram 504.7 collector-substrate depletion capacitance parameter, CJS, and its temperature equation, **CJS_T,** were determined to produce an adequate wide temperature response. The SET model collector-substrate depletion capacitance temperature equation, **CDE_T**, corresponds to the standard Mextram 504.7 temperature Equation (3.93) and is repeated in Equation (8.17) [2].

$$\mathbf{CJS\_T} = \mathrm{CJS} \cdot \left(\frac{\mathrm{VDS}}{\mathbf{VDS\_T}} \right)^{\mathrm{PS}} \tag{8.17}$$

The SET model fit of **VDS_T** was an excellent fit to the ambient temperature VDS values. The final SET model fit of **CJS_T** diverged from the ambient temperature CJS values as seen in Figure 8.14. The final SET values of capacitance parameters were linked to the VDS parameter values as shown in the CJS_T temperature equation (8.17). The VDS influence to

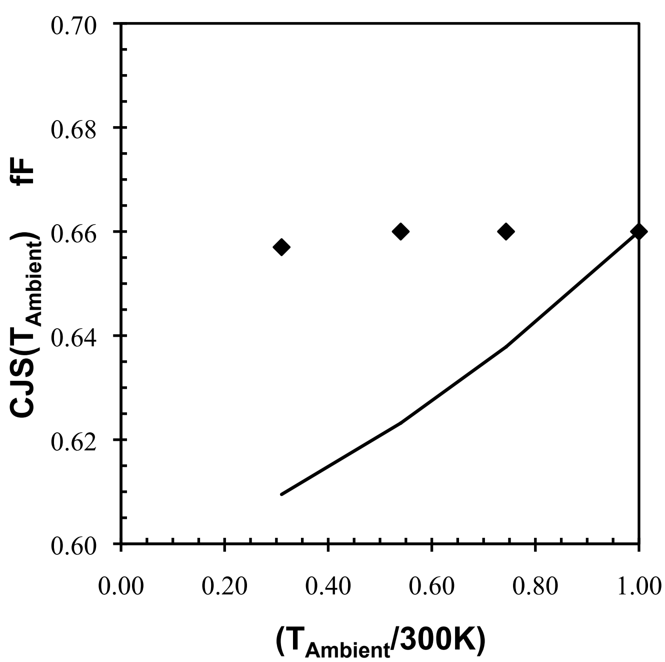

Figure 8.14 SET model extraction of collector-substrate depletion capacitance. Equation (8.17) is the solid line and ambient temperature VDS values are symbols

the SET model was more important to the other parameter interactions than the CJS term. Optimization approaches indicated that CJS was most accurate when less than 0.66fF. Therefore, the ambient temperature CJS values were held at approximately 0.66fF and the slight decrease in CJS due to lower temperatures were of minor importance to the overall DC and AC results.

8.2.5 Reverse transit time - TAUR

The temperature response of the reverse transit time parameter, TAUR, was not included in the SET model optimizations. The SET model used the standard Mextram 504.7 temperature equation (3.117) repeated here is equation (8.18) [2]. TAUR was defined as 150 pF.

$$\mathbf{TAUR\_T} = \mathrm{TAUR} \cdot \frac{(\mathbf{TAUB\_T} + \mathbf{TEPI\_T})}{(\mathrm{TAUB} + \mathrm{TEPI})} \tag{8.18}$$

8.2.6 Nonideal reverse base current model saturation current - IBR

The model parameter IBR is the saturation current for the nonideal reverse base current of branch, I_{B3}. The temperature response of IBR in the standard Mextram 504.7 was described in Chapter 3. An analysis of the ambient temperature IBR values indicated that the SET model required the same response as the standard Mextram temperature equation (3.111). The SET model temperature equation, **IBR_T** is repeated in Equation (8.19) [2]

$$\mathbf{IBR\_T} = \mathrm{IBR} \cdot t_N^2 \exp\left(-\frac{\mathrm{VGC}}{2V_{\Delta T}} \right) \tag{8.19}$$

The value of VGC was determined from the development of the base-collector diffusion voltage temperature response in Section 8.2.4.2. The SET value of IBR was optimized for the best fit of the ambient IBR values and a good fit of the saturated region of the DC output curves over the full temperature range. The final SET values produced a good fit between the SET model equation of **IBR_T** and the ambient temperature IBR values as shown in Figure 8.15.

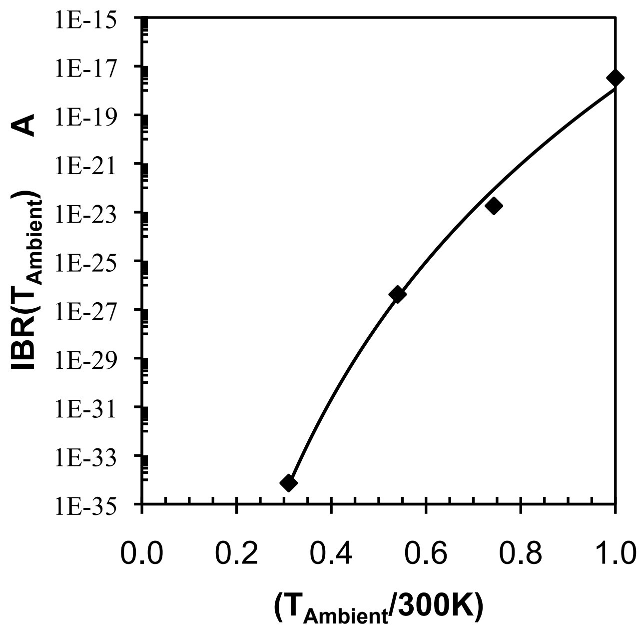

Figure 8.15 SET model extraction of nonideal reverse base saturation current, IBR. Equation (8.19) is the solid line and IBR values of the 4 ambient temperature models are symbols

SET Model	
Parameter	Value
VGC	1.05V
IBR	151.1E-18A

Table 8.14 SET parameters VGC and IBR

8.2.7 Saturation current of the parasitic PNP - ISS

The model parameter ISS is the saturation current of the parasitic PNP in the substrate current branch of I_{sub}. The standard Mextram 504.7 ISS temperature equation, **ISS_T**, was described in Chapter 3. The ambient temperature ISS values were found to be adequately represented by the standard Mextram temperature response of **ISS_T** as seen in Figure 8.16. The SET model temperature equation, **ISS_T** is the standard Mextram implementation of Equation

(3.111) and is repeated in Equation (8.20) [2]. The final SET values for VGS and ISS are listed in Table 8.15.

$$\mathbf{ISS\_T} = \mathrm{ISS} \cdot t_N^{(4-AS)} \cdot \exp\left(-\frac{\mathrm{VGS}}{V_{\Delta T}}\right) \tag{8.20}$$

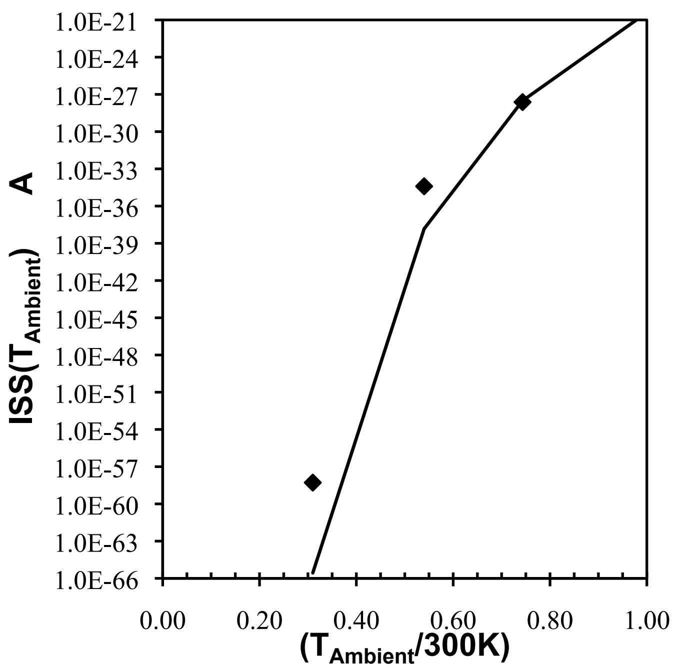

Figure 8.16 SET model extraction of parasitic PNP saturation current, ISS. Equation (8.20) is the solid line and 4 ambient temperature model ISS values are symbols

SET Model	
Parameter	Value
VGS	1.18V
ISS	3.94E-21A

Table 8.15 SET parameters VGS and ISS

8.2.8 High-level knee injection knee current of the parasitic PNP - IKS

The model parameter IKS is the high level injection knee current of the parasitic PNP in the substrate current branch of I_{sub}. The temperature response of IKS is described in the standard Mextram 504.7 summary of Chapter 3. The ambient parameter optimization of IKS found that it did not contribute in a meaningful manner. Therefore the value of IKS was set very large in the ambient models so that the substrate current, I_{sub}, did not contribute an incorrect amount of current. The relationship of the temperature adjusted IKS parameter in the I_{sub} current branch was defined in Equation (3.77). The standard Mextram temperature equation (3.113) was used in the SET model temperature equation, **IKS_T** and repeated in Equation (8.21) [2].

$$\mathbf{IKS\_T} = \mathrm{IKS} \cdot t_N^{(1-AS)} \left(\frac{\mathbf{IS\_T}}{\mathrm{IS}} \right) \left(\frac{\mathrm{ISS}}{\mathbf{ISS\_T}} \right) \tag{8.21}$$

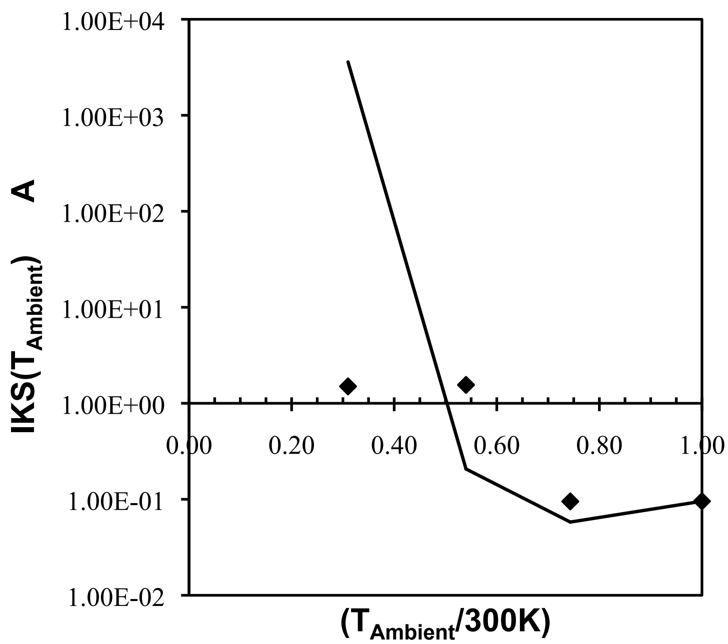

Figure 8.17 SET model extraction of the parasitic PNP contribution high-level injection knee current, IKS. Equation (8.21) is the solid line and ambient temperature IKS values are symbols.

8.3 Parameters with modified 504.7 temperature equations over the full temperature range

Each parameter in this section was determined to need a modification to its standard Mextram 504.7 parameter temperature equation, in order to fit the expansive temperature range of the SET model. The modified parameter temperature equations replaced the existing standard 504.7 equations for all temperatures from 300K to 93K. The model parameters with new parameter temperature equations defined for the expansive temperature range and the new SET parameters added to support their performance are listed in Table 8.16:

Model Parameter	Parameter Function	Original 504.7 Parameter Interacting with Temperature	Final SET Parameter Interacting with Temperature
VEF	Forward Early voltage	AQBO	CRYO_CVEF
VER	Reverse Early voltage	AQBO	CRYO_CVER
BF	Forward current gain	AE, AB, AQBO	CRYO_CBF
IBF	Forward base leakage current	MLF	CRYO_CIBF
IK	Forward knee current	AB	CRYO_CIK
BRI	Reverse current gain	none	CRYO_CBRI
RBV	Variable base resistance	AB, AQBO	CRYO_CRBV
TAUE	Emitter transit time	AB	CRYO_CTAUE
TAUB	Base transit time	AB, AQBO TAUB	CRYO_TAUB, CRYO_CTAUB
TEPI	Epilayer collector transit time	AS	CRYO_CTEPI

Table 8.16 SET model parameters with new parameter temperature equations and the new SET parameters to support the temperature equations.

The new parameter temperature equations and the SET parameter values of the model and temperature parameters are defined in the following sections.

8.3.1 Forward and reverse Early effects - VEF and VER

The ambient temperature values of VEF and VER behaved opposite of one another as temperature decreased. The forward Early voltage parameter, VEF, decreased as temperature decreased and the reverse Early voltage parameter, VER, increased slightly as temperature decreased. The SET model temperature equations, **VEF_T** and **VER_T**, needed to represent this Early effects behavior over the wide temperature range.

Development of the SET model Early effects temperature equations started with an evaluation of the suitability of the standard Mextram 504 model parameter temperature equations to represent the Early parameters over the expansive temperature range. The standard Mextram 504.7 equations for **VEF_T** and **VER_T** were described in Section 3.6.4. The standard forward Early voltage temperature equation, **VEF_T** is repeated in Equation (8.22). **VEF_T** is further represented in Equation (8.22) by grouping the base-collector depletion voltage influences into the term, CJC_Scaling [2].

$$\begin{aligned}\mathbf{VEF\_T} &= \mathrm{VEF}\cdot t_N^{\mathrm{AQBO}}\left[\left(1-\mathrm{XP}\right)\left(\frac{\mathrm{VDC}}{\mathbf{VDC\_T}}\right)^{\mathrm{PC}}+\mathrm{XP}\right]^{-1} \\ &= \mathrm{VEF}\cdot t_N^{\mathrm{AQBO}}\left[\quad \mathrm{CJC\_Scaling} \quad\right]^{-1}\end{aligned} \tag{8.22}$$

The standard reverse Early voltage temperature equation, **VER_T**, is repeated in Equation (8.23). The term, CJE_Effects, in Equation (8.23) identifies the base-emitter depletion voltage influences on **VEF_T** [2].

$$\begin{aligned}\mathbf{VER\_T} &= \mathrm{VER}\cdot t_N^{\mathrm{AQBO}}\left(\frac{\mathrm{VDE}}{\mathbf{VDE\_T}}\right)^{-\mathrm{PE}} \\ &= \frac{\mathrm{VER}\cdot t_N^{\mathrm{AQBO}}}{[\mathrm{CJE\_Effects}]}\end{aligned} \tag{8.23}$$

Optimizations of VER and VEF indicated that an accurate fit of the saturation region and the linear region of the output characteristics could not be achieved with the standard Mextram temperature equations. The standard Mextram 504.7 has a common temperature coefficient parameter, AQBO, in both **VEF_T** and **VER_T**. It was determined that a single temperature coefficient parameter controlling both forward and reverse behavior was unable to represent the ambient temperature Early parameter values over the expansive temperature range. Therefore both standard 504.7 Early effects temperature equations were modified for the SET model. In the SET Early effects temperature equations were changed by removing the shared temperature coefficient parameter, AQBO, and replacing it with individual temperature coefficient parameters, CRYO_CVEF and CRYO_CVER. The SET model forward Early voltage parameter temperature equation, **VEF_T**, is defined in Equation (8.24). The SET model reverse Early voltage parameter temperature equation, **VER_T**, is defined in Equation (8.25)

$$\mathbf{VEF\_T} = \mathrm{VEF} \cdot t_N^{\mathrm{CRYO\_CVEF}} \left[(1 - \mathrm{XP}) \left(\frac{\mathrm{VDC}}{\mathbf{VDC\_T}} \right)^{\mathrm{PC}} + \mathrm{XP} \right]^{-1} \tag{8.24}$$

$$\mathbf{VER\_T} = \mathrm{VER} \cdot t_N^{\mathrm{CRYO\_CVER}} \left(\frac{\mathrm{VDE}}{\mathbf{VDE\_T}} \right)^{-\mathrm{PE}} \tag{8.25}$$

Joint optimizations of both SET Early effects temperature equations, **VER_T** and **VEF_T** were used to investigate the relationship between the two individual temperature coefficient parameters. Through optimizations it was found that the best fit of model simulation to measured data, in the saturation and linear region, occurred when CRYO_CVEF and CRYO_CVER were of equal but opposite polarity.

The SET model **VEF_T** equation was analyzed by writing **VEF_T** in terms of the scaling effects due to the base-collector diffusion voltage as defined in Equation (8.26).

$$\mathbf{VEF\_T} \cdot [\ \mathrm{CJC\_Scaling}\ ] = \mathrm{VEF} \cdot t_N^{\mathrm{CRYO\_CVEF}} \tag{8.26}$$

Analysis of the VEF ambient temperature values and the SET **VEF_T** temperature equation were determined by plotting the $\text{VEF} \cdot [\text{CJC\_Scaling}]$ values and $\mathbf{VEF\_T} \cdot [\text{CJC\_Scaling}]$ versus the ratio of $\frac{T_{Ambient}}{300K}$ as shown in Figure 8.18. The ambient

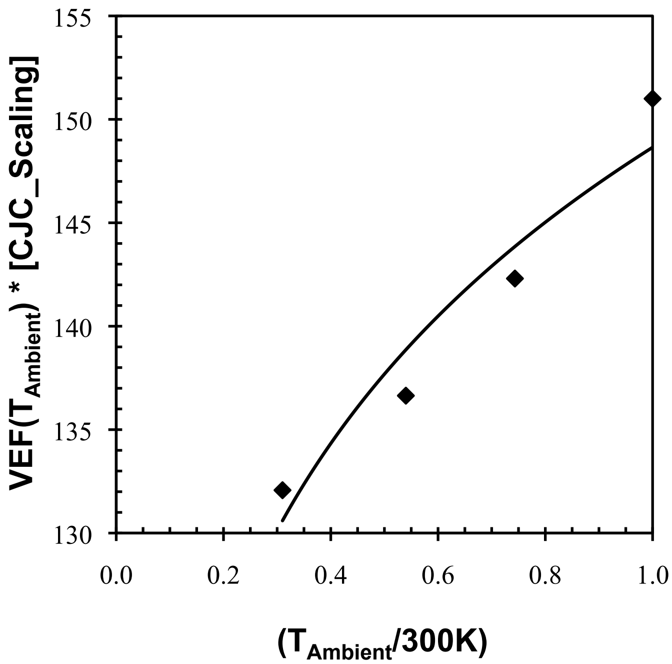

Figure 8.18 SET extraction of forward Early parameters. Equation (8.26) is the solid line and ambient temperature VEF·[CJC_Scaling] values are symbols

SET Model	
Parameter	Value
VEF	151V
CRYO_CVEF	111m
VER	2.82V
CRYO_CVER	-111m

Table 8.17 SET parameters of VEF, CRYO_CVEF, VER, CRYO_CVER

temperature values $\mathbf{VEF} \cdot [\text{CJC\_Scaling}]$ are represented by markers. The SET forward Early voltage equation term is the solid line in Figure 8.18.

The shape of the SET temperature equation, **VEF_T**, in Figure 8.18 was slightly concave, rather than the ambient temperature values being slight convex. However, the overall error of the equation fit to the ambient temperature values ranged from 3% to -2%. The final SET values for the individual temperature coefficient parameters were determined through a combination of output characteristics optimizations and the analysis of the temperature equations as compared to the ambient temperature Early parameters. The final SET values for VEF, CRYO_CVEF, CVEF, VER, and CRYO_CVER are listed in Table 8.17.

8.3.2 Forward current gain - BF

The forward current gain parameter, BF, shifts with temperature by the temperature equation, **BF_T**. The ambient temperature BF values are significantly larger than the measured forward current gain, β_F, values. The higher values are in part due to the use of the SiGe bandgap voltage terms in the current equations. The BF temperature equation for the SET model represent the effects of the SiGe equations as well as behavior of BF over a wide temperature range. The SET model was developed by analyzing the standard 504.7 implementation and then modifying the standard temperature equation.

The standard Mextram 504.7 model temperature equations are described in Section 3.6.5. The standard **BF_T** equation is repeated in Equation (8.27). The **BF_T** implementation includes temperature coefficient parameters and a bandgap voltage parameter. The total temperature coefficient is an equation of three parameters: AE, AB, and AQBO. Optimization of these three temperature coefficient parameters is limited since they are used in other parameter temperature equations. The forward current gain bandgap voltage parameter, DVGBF, is unique to the temperature equation, **BF_T.** DVGBF can be optimized by grouping the exponential relationship into a term, Bandgap_Effects, as indicated in the Equation (8.27) [2].

$$\mathbf{BF\_T} = BF \cdot t_N^{(AE-AB-AQBO)} \exp\left[\frac{-DVGBF}{V_{\Delta T}}\right]$$
$$= BF \cdot t_N^{(AE-AB-AQBO)} \cdot [Bandgap\_Effects] \qquad (8.27)$$
$$\text{where:}$$
$$[Bandgap\_Effects] = \exp\left[\frac{-DVGBF}{V_{\Delta T}}\right]$$

Analysis of the ambient temperature BF values determined that the total temperature coefficient value in Equation (8.27) could not be satisfied with the term (AE-AB-AQBO). Therefore, the SET model temperature equation for **BF_T** was a modified version of the standard Mextram 504.7 model, applicable over the full temperature range. The forward current gain parameter temperature equation of the SET model is defined in Equation (8.28).

$$\mathbf{BF\_T} = BF \cdot t_N^{CRYO\_CBF} \exp\left[\frac{-DVGBF}{V_{\Delta T}}\right] \qquad (8.28)$$

The development of the SET model **BF_T** equation and parameter extractions were determined by writing **BF_T** in terms of the Bandgap_Effects and a single temperature coefficient parameter as indicated in Equation (8.29).

$$\frac{\mathbf{BF\_T}}{[Bandgap\_Effects]} = BF \cdot t_N^{CRYO\_CBF} \qquad (8.29)$$

Analysis of the BF ambient temperature values and the SET **BF_T** temperature equation were determined by plotting the $\frac{BF}{[Bandgap\_Effects]}$ values and equation term,

$\frac{\mathbf{BF\_T}}{[\text{Bandgap\_Effects}]}$, versus the ratio of $\frac{T_{Ambient}}{300K}$ as shown in Figure 8.19. The ambient temperature $\frac{BF}{[\text{Bandgap\_Effects}]}$ values are represented by markers. The SET forward current gain temperature equation term is the solid line in Figure 8.19. Optimization of the SET temperature equation parameters, BF, DVGBF and CYRO_CBF was required. The final SET values for BF, DVGBF and CYRO_CBF are listed in Table 8.18.

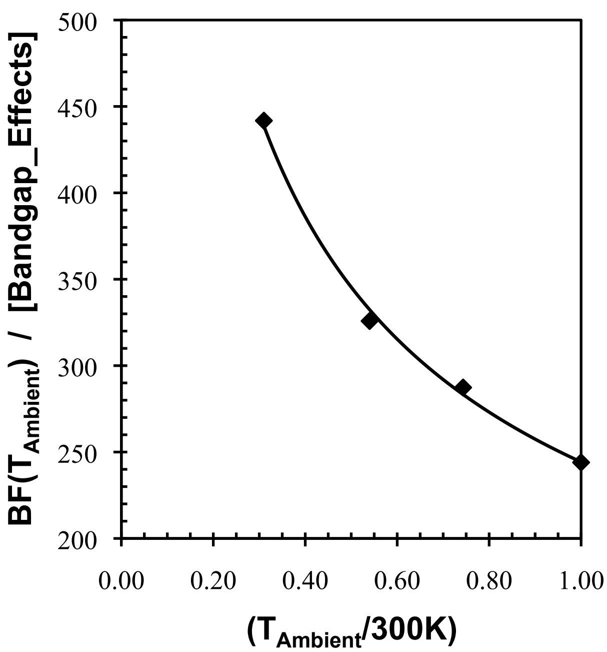

Figure 8.19 SET extraction of forward current gain parameters. Equation (8.29) is the solid line and ambient temperature BF/[Bandgap_Effects] values are symbols

SET Model	
Parameter	Value
BF	247
DVGBF	-10m
CRYO_CBF	-440m

Table 8.18 SET parameters BF, VDGBF and CRYO_CBF

The fit of the SET temperature equation to the ambient BF values was very good for wide dynamic range of the BF values.

8.3.3 Saturation current of forward nonideal base current - IBF

The SiGe HBT modeled has minimal base current leakage within the measurement resolution of the base current. Only at an ambient temperature of 93K is the base current leakage present in the Gummel measurements. In the ambient temperature base current summary plot of Figure 6.13 the base current at 93K indicates low-level leakage current is present. The nonideal forward base current branch, I_{B2}, represents the base leakage current at low base-emitter voltage bias in the Mextram model as described in Section 3.2.6. The nonideal forward base current saturation current parameter, IBF is directly proportional to I_{B2}, as defined in Equation (3.64). Therefore, modeling the IBF behavior over temperature in the SET model required the current to be a minimum value at the lower temperatures.

The parameter IBF shifts with temperature through the temperature equation, **IBF_T**. The standard Mextram 504.7 current temperature equations are described in Section 3.6.5. The standard 504.7 **IBF_T** temperature equation is repeated in Equation (8.30). Temperature change is controlled by a temperature coefficient and a bandgap voltage. However, optimization of the temperature coefficient is limited since it composed of an empirically derived equation, $\left[6-(2\cdot \mathrm{MLF})\right]$. The base-emitter recombination bandgap voltage parameter, VGJ, is unique to the temperature equation, **IBF_T.** VGJ can be optimized by grouping the exponential relationship into a term, Bandgap_Effects, as indicated in the Equation (8.30) [2].

$$\begin{aligned}\mathbf{IBF\_T} &= \mathrm{IBF}\cdot t_N^{[6-(2\cdot \mathrm{MLF})]}\exp\left[\frac{-\mathrm{VGJ}}{V_{\Delta T}\cdot \mathrm{MLF}}\right]\\ &= \mathrm{IBF}\cdot t_N^{[6-(2\cdot \mathrm{MLF})]}\cdot[\mathrm{Bandgap\_Effects}]\\ \text{where:}&\\ [\mathrm{Bandgap\_Effects}] &= \exp\left[\frac{-\mathrm{VGJ}}{V_{\Delta T}\cdot \mathrm{MLF}}\right]\end{aligned} \tag{8.30}$$

The limitations of the standard 504.7 temperature equation required a modification of Equation (8.30). The total temperature coefficient of $\left[6-(2\cdot \text{MLF})\right]$was replaced with a new temperature coefficient parameter, CRYO_CIBF. The new parameter is only assigned to the SET **IBF_T** equation, and therefore, the value is not restricted. The nonideal base saturation current parameter temperature equation of the SET model is defined in Equation (8.31).

$$\mathbf{IBF\_T} = \text{IBF}\cdot t_N^{\text{CRYO\_CIBF}} \exp\left[\frac{-\text{VGJ}}{V_{\Delta T}\cdot \text{MLF}}\right] \tag{8.31}$$

The development of the SET model **IBF_T** equation and parameter extractions were determined by writing **IBF_T** in terms of Bandgap_Effects and a single temperature coefficient parameter as indicated in Equation (8.32).

$$\frac{\mathbf{IBF\_T}}{[\text{Bandgap\_Effects}]} = \text{IBF}\cdot t_N^{\text{CYRO\_CIBF}} \tag{8.32}$$

Analysis of the IBF ambient temperature values and the SET **IBF_T** temperature equation were determined by plotting the $\frac{\text{IBF}}{[\text{Bandgap\_Effects}]}$ values and the equation term, $\frac{\mathbf{IBF\_T}}{[\text{Bandgap\_Effects}]}$, versus the ratio of $\frac{T_{\text{Ambient}}}{300\text{K}}$ as shown in Figure 8.20.

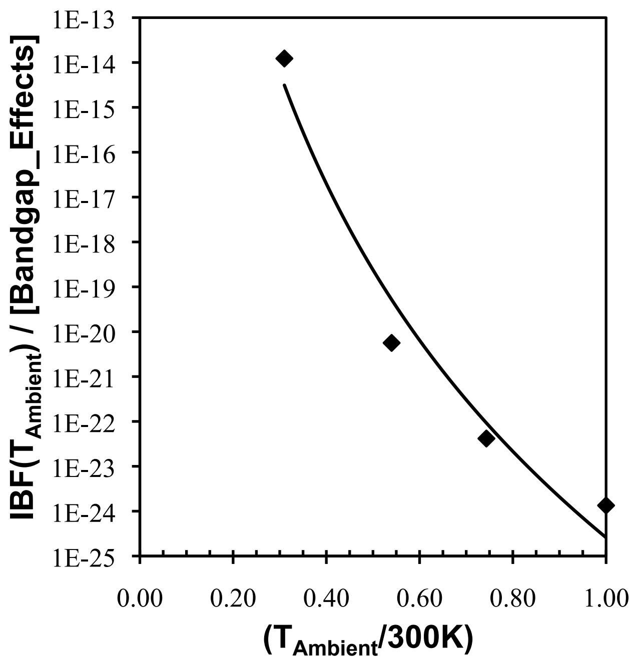

Figure 8.20 SET model of forward nonideal base saturation current parameters. Equation (8.32) is the solid line and the symbols are ambient temperature IBF/[Bandgap_Effects] values

SET Model	
Parameter	Value
IBF	1.34E-24A
VGJ	1.18V
MLF	2.157
CRYO_CIBF	-19.84

Table 8.19 SET parameters IBF, VGJ, MLF, CRYO_CIBF

The ambient temperature $\dfrac{\text{IBF}}{[\text{Bandgap\_Effects}]}$ values are represented by markers. The SET nonideal forward base saturation current temperature equation term is the solid line in Figure 8.20. Optimization of the SET temperature equation parameters, IBF, MLF, VGJ, and CYRO_CIBF was required. The final SET values are listed in Table 8.19.

8.3.4 Forward knee current - IK

The forward knee current parameter, IK, required a high degree of accuracy for the SET model temperature response. The optimization of IK was found to be very sensitive to a specific value at each ambient temperature. For the SiGe HBT modeled, IK was a primary influence during the ambient temperature optimizations of both DC measurements and AC measurements. The knee current had a strong influence on the DC gummel curve beginning in the mid-level injection region. In addition to a Gummel influence, IK exhibited current control of the higher current output curves and the high current region of the f_T versus IC curves during optimizations. Each final ambient IK value had to be accurately balanced with the best fit of all three measurements. The multiple measurement influence of IK over the expansive temperature range placed additional accuracy requirements on the SET model.

The first approach to fitting IK was to evaluate the standard 504.7 temperature equation. The standard Mextram 504.7 temperature equation**,** **IK_T**, was described in Section 3.6.5.and is repeated in Equation (8.33). The standard 504.7 **IK_T** equation relies on the temperature coefficient parameter AB to shift IK with temperature. However, AB is used with five other model parameter temperature equations in the standard 504.7. Multiuse of AB limited the ability to optimize the AB value for the accuracy needed in **IK_T** [2].

$$\mathbf{IK\_T} = \mathrm{IK} \cdot t_N^{(1-AB)} \tag{8.33}$$

The limitations of the standard 504.7 temperature equation required a modification of Equation (8.33). The total temperature coefficient of (1-AB) was replaced with a new coefficient parameter, CRYO_CIK. The new parameter is used only in the modified **IK_T** equation and the value is not restricted. The knee current parameter temperature equation of the SET model is defined in Equation (8.34).

$$\mathbf{IK\_T} = \mathrm{IK} \cdot t_N^{CRYO\_CIK} \tag{8.34}$$

Analysis of the ambient temperature IK values and development of the SET model knee current temperature parameters required the plotting of the SET model equation, **IK_T**, and the ambient temperature IK values versus the ratio of $\frac{T_{Ambient}}{300K}$ as shown in Figure 8.21.

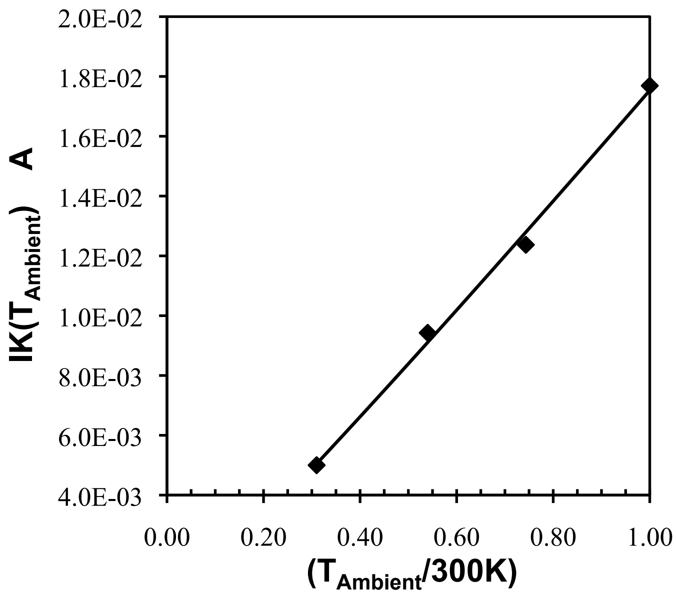

Figure 8.21 SET model extraction of forward knee current. Equation (8.34) is the solid line and ambient temperature IK values are symbols

SET Model	
Parameter	Value
IK	17.50mA
CRYO_CIK	1.063

Table 8.20 SET parameters IK, CRYO_CIK

The ambient temperature IK values are represented by markers. The SET knee current temperature equation, **IK_T**, of Equation (8.34), is the solid line in Figure 8.21. The final SET values for IK and CYRO_CIK are listed in Table 8.20.

8.3.5 Reverse current gain parameter - BRI

The reverse current gain parameter, BRI, was influential to the ambient temperature modeling of the saturated region of the output characteristics. The ambient values of BRI shifted from 15 to less than 1 as the temperature decreased. This range of BRI shift with temperature was required in the SET model parameter temperature equation, **BRI_T**. The SET model was developed by analyzing the standard 504.7 implementation and then modifying the standard temperature equation for the full temperature range.

The standard Mextram 504.7 model current gain temperature equation is described in Section 3.6.5. The standard 504.7 **BRI_T** equation is repeated in Equation (8.35). The shift in temperature of **BRI_T** is controlled by a bandgap voltage parameter. The reverse current gain bandgap parameter, DVGBR, is unique to the temperature equation, **BRI_T.** DVGBR can be optimized by grouping the exponential term, Bandgap_Effects, as indicated in the Equation (8.35) [2].

$$\begin{aligned} \mathbf{BRI\_T} &= \mathrm{BRI} \cdot \exp\left[\frac{-\mathrm{DVGBR}}{V_{\Delta T}}\right] \\ &= \mathrm{BRI} \cdot [\mathrm{Bandgap\_Effects}] \\ \text{where:} & \\ [\mathrm{Bandgap\_Effects}] &= \exp\left[\frac{-\mathrm{DVGBR}}{V_{\Delta T}}\right] \end{aligned} \tag{8.35}$$

Analysis of the ambient temperature BRI values determined that the DVGBR Bandgap Effects term did not shift BRI correctly over the full temperature range. The SET model reverse current gain was found to need a temperature relationship more like that of the forward current gain temperature equation. Therefore, the SET model temperature equation for **BRI_T** required the standard Mextram 504.7 temperature equation to be modified. The reverse current gain parameter temperature equation of the SET model is defined in Equation (8.36).

$$\mathbf{BRI\_T} = \mathrm{BRI} \cdot t_N^{\mathrm{CRYO\_CBRI}} \exp\left[\frac{-\mathrm{DVGBR}}{V_{\Delta T}}\right] \tag{8.36}$$

The SET model **BRI_T** equation and parameter extractions were determined by writing **BRI_T** in terms of the Bandgap_Effects term and a single temperature coefficient parameter as indicated in Equation (8.37).

$$\frac{\mathbf{BRI\_T}}{[\mathrm{Bandgap\_Effects}]} = \mathrm{BRI} \cdot t_N^{\mathrm{CRYO\_CBRI}} \tag{8.37}$$

Analysis of the BRI ambient temperature values and the SET **BRI_T** temperature equation were determined by plotting the $\frac{\mathrm{BRI}}{[\mathrm{Bandgap\_Effects}]}$ values and the $\frac{\mathbf{BRI\_T}}{[\mathrm{Bandgap\_Effects}]}$ equation versus the ratio of $\frac{T_{Ambient}}{300K}$ as shown in Figure 8.22. The ambient temperature

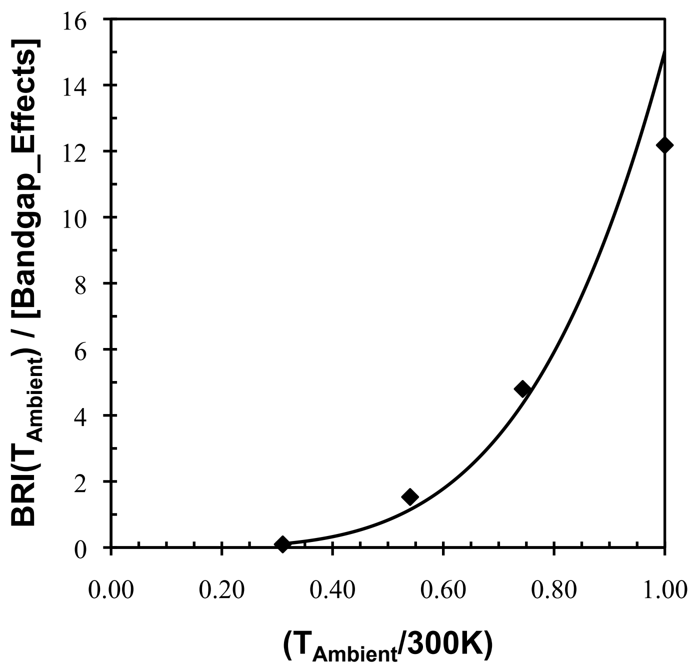

Figure 8.22 SET model extraction of reverse current gain parameters. Equation (8.37) is the solid line and the ambient temperature BRI/[Bandgap_Effects] values are symbols.

SET Model	
Parameter	Value
BRI	15.02
DVGBR	10.0mV
CRYO_CBRI	4.176

Table 8.21 SET parameters BRI, DVGBR, CRYO_CBRI

$\frac{\text{BRI}}{[\text{Bandgap\_Effects}]}$ values are represented by markers. The SET forward current gain temperature equation term is the solid line in Figure 8.22. Optimization of the SET temperature equation parameters, BRI, DVGBR and CYRO_CBRI was required. The final SET values for BRI, DVGBR and CYRO_CBRI are listed in Table 8.20.

8.3.6 Intrinsic base resistance - RBV

The ambient temperature values of the intrinsic base resistance parameter, RBV, shifted by approximately 75Ω over the expansive temperature range of the SET model in the SiGe HBT modeled. The intrinsic base resistance parameter temperature equation**, RBV_T**, must accurately represent this shift in resistance due to temperature change. The **RBV_T** equation of the standard Mextram 504.7 model was described in Section 3.6.3 and is repeated in Equation (8.38). In the standard 504.7 **RBV_T** equation, shifting the value of RBV with temperature depends on a total temperature coefficient derived from an equation of two temperature parameters: AB and AQBO. Both, AB and AQBO are used by several other model parameter temperature equations in the standard 504.7. The multiple use of AB and AQBO as well as the equation definition limited the ability to optimize the final temperature coefficient value.

$$\mathbf{RBV\_T} = \text{RBV} \cdot t_N^{(\text{AB}-\text{AQBO})} \tag{8.38}$$

The behavior of the ambient RBV values could not be represented by Equation (8.38). The limitations of the standard 504.7 temperature equation required a modification. The total temperature coefficient of (AB-AQBO) was replaced with a new coefficient parameter, CRYO_CRBV. The new temperature coefficient parameter is not shared in any other equations and is not restricted on value. The intrinsic base parameter temperature equation of the SET model is defined in Equation (8.39) [2].

$$\mathbf{RBV\_T} = \mathrm{RBV} \cdot t_N^{\mathrm{CRYO\_CRBV}} \tag{8.39}$$

Analysis of the ambient temperature RBV values and the development of the SET model intrinsic base resistance temperature parameters relied on a plotting of the SET model equation, **RBV_T**, and the ambient temperature RBV values versus the ratio of $\frac{T_{Ambient}}{300K}$ as shown in Figure 8.23. The ambient temperature RBV values are represented by markers. The SET intrinsic base resistance temperature equation, **RBV_T**, of Equation (8.40), is the solid line in Figure 8.23. The final SET values for RBV and CYRO_CRBV are listed in Table 8.22.

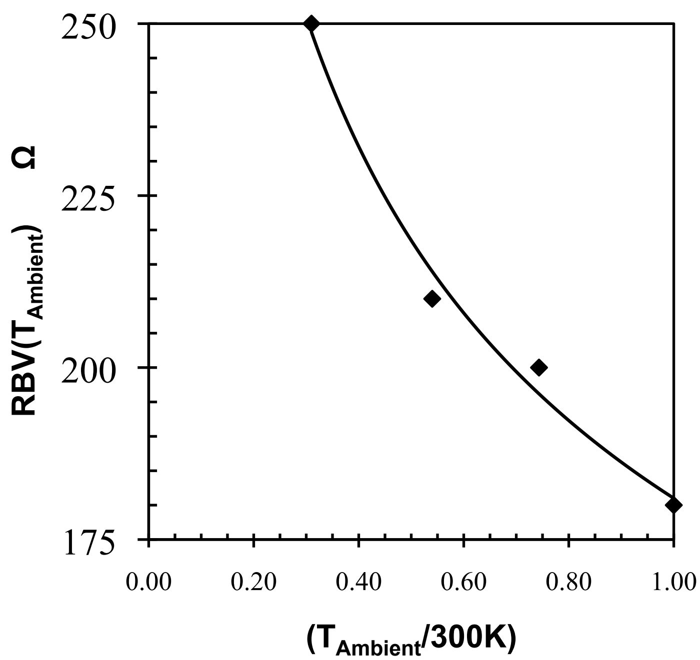

Figure 8.23 SET model extraction of intrinsic base resistance parameters. Equation (8.39) is the solid line and ambient temperature RBV values are symbols

SET Model	
Parameter	Value
RBV	181 Ω
CRYO_CRBV	-272m

Table 8.22 SET parameters RBV, CRYO_CRBV

8.3.7 Emitter transit time - TAUE

The emitter transit time parameter, TAUE, is the primary contributor to the emitter diffusion charge branch, Q_E, of the Mextram model. The behavior of Q_E, is described in Section 3.2.4.1.

Q_E is directly proportional to TAUE, and also has an exponential dependence on the emitter charge non-ideality parameter, MTAU. In the ambient temperature models, the frequency response of the small signal gain was very dependent upon Q_E. The peak value of the cutoff frequency, f_T, versus Log(IC) curves were dominated by the combination of TAUE and MTAU in the ambient temperature optimizations. Both parameters shifted with temperature. The temperature modeling of MTAU is detailed in Section 8.4.2. In the standard Mextram 504.7 model, TAUE shifts with temperature through the temperature equation, **TAUE_T.** The standard 504.7 implementation was described in Section 3.6.6. The standard 504.7 temperature equation, **TAUE_T,** is repeated in Equation (8.40). In the standard 504.7 **TAUE_T** equation, the value of TAUE depends on a total temperature coefficient derived from the equation, (AB-2). The value of AB is restricted since AB is shared by several other parameter temperature equations. Also, the equation limited the ability to optimize the final temperature coefficient value which produced the best **TAUE_T** response. The emitter charge difference bandgap voltage parameter, DVGTE, is unique to the temperature equation, **TAUE_T.** Therefore, DVGTE could be optimized by grouping the exponential term, Bandgap_Effects, as indicated in the Equation (8.40) [2].

$$\begin{aligned}\mathbf{TAUE\_T} &= \mathrm{TAUE} \cdot t_N^{(AB-2)} \cdot \exp\left[\frac{-\mathrm{DVGTE}}{V_{\Delta T}}\right] \\ &= \mathrm{TAUE} \cdot t_N^{(AB-2)} \cdot [\mathrm{Bandgap\_Effects}] \qquad (8.40)\end{aligned}$$

where:

$$[\mathrm{Bandgap\_Effects}] = \exp\left[\frac{-\mathrm{DVGTE}}{V_{\Delta T}}\right]$$

Analysis of the ambient temperature TAUE values determined that the total temperature coefficient value in Equation (8.40) was not supported by the term (AB-2). Therefore, the SET model temperature equation for **TAUE_T** became a modified version of the standard Mextram 504.7 model, applicable over the full temperature range. The emitter transit time parameter temperature equation of the SET model is defined in Equation (8.41).

$$\mathbf{TAUE\_T} = \mathrm{TAUE} \cdot t_N^{\mathrm{CRYO\_CTAUE}} \cdot \exp\left[\frac{-\mathrm{DVGTE}}{V_{\Delta T}}\right] \tag{8.41}$$

The SET model **TAUE_T** equation and parameter extractions were determined by writing the **TAUE_T** in terms of the Bandgap_Effects term and a single temperature coefficient parameter as indicated in Equation (8.42).

$$\frac{\mathbf{TAUE\_T}}{[\mathrm{Bandgap\_Effects}]} = \mathrm{TAUE} \cdot t_N^{\mathrm{CRYO\_CTAUE}} \tag{8.42}$$

Analysis of TAUE ambient temperature values and the SET **TAUE_T** temperature equation were determined by plotting the $\frac{\mathrm{TAUE}}{[\mathrm{Bandgap\_Effects}]}$ values and the $\frac{\mathbf{TAUE\_T}}{[\mathrm{Bandgap\_Effects}]}$ equation versus the ratio of $\frac{T_{\mathrm{Ambient}}}{300\mathrm{K}}$ as shown in Figure 8.24.

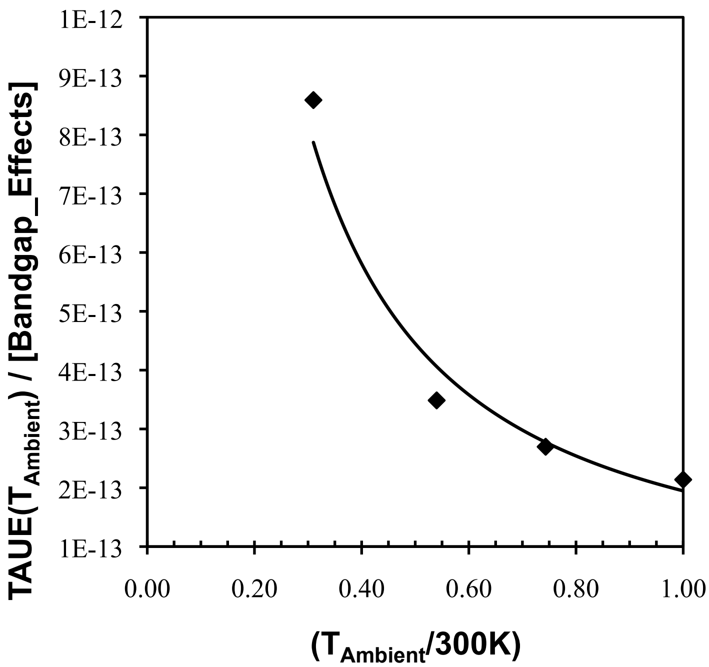

Figure 8.24 SET model extraction of emitter transit time parameters. Equation (8.37) is the solid line and the ambient temperature TAUE/[Bandgap_Effects] values are symbols

SET Model	
Parameter	Value
TAUE	200.1fs
DVGTE	35mV
CRYO_CTAUE	-1.23

Table 8.23 SET parameters TAUE, DVGTE, CRYO_CTAUE

The ambient temperature $\frac{\text{TAUE}}{[\text{Bandgap\_Effects}]}$ values are represented by markers. The SET emitter transit time temperature equation term is the solid line in Figure 8.24. The final SET values for TAUE, DVGTE and CYRO_CTAUE are listed in Table 8.22.

8.3.8 Base transit time - TAUB

The base transit time parameter, TAUB, is a direct proportional factor in both base diffusion charges branch, Q_{BE} and Q_{BC}, of the Mextram model. The diffusion charges are described in Section 3.2.4.2 of the standard 504.7 Mextram model. The optimization of all contributors to Q_{BE} and Q_{BC} were required during ambient model fitting of the f_T versus Log(IC) measurement responses. The ambient values of TAUB were optimized in sync with the emitter transit time parameter, TAUE, to maintain a consistent transit time balance as the ambient temperature decreases.

The base transit time parameter temperature equation**, TAUB_T**, therefore had to accurately represent the change in TAUB ambient temperature values across the expansive temperature range. The standard Mextram 504.7 **TAUB_T** equation was described in Section 3.6.6 and the equation repeated in Equation (8.43). The standard 504.7 **TAUB_T** equation, shifts the value of TAUB through a power law relationship with temperature which depends on a total temperature coefficient derived from an equation of two temperature parameters: AB and AQBO [2].

$$\mathbf{TAUB\_T} = \mathrm{TAUB} \cdot t_N^{(\mathrm{AQBO}+\mathrm{AB}-1)} \tag{8.43}$$

The standard 504.7 temperature equation of (8.43) was determined to be unable to represent the ambient temperature TAUB values and a new **TAUB_T** equation was developed. The SET model temperature equation, **TAUB_T**, is defined in Equation (8.44).

$$\mathbf{TAUB\_T} = \mathrm{CRYO\_TAUB} \cdot \exp(t_N \cdot \mathrm{CRYO\_CTAUB}) \tag{8.44}$$

The ambient temperature TAUB values were analyzed and the SET TAUB temperature parameters were extracted by plotting of the SET model equation, **TAUB_T**, and the ambient temperature TAUB values versus the ratio of $\frac{T_{\mathrm{Ambient}}}{300\mathrm{K}}$ as shown in Figure 8.25. The ambient temperature TAUB values are represented by markers. The SET base transit time temperature equation, **TAUB_T**, of Equation (8.44), is the solid line in Figure 8.25. A combination of this analysis and further parameter optimizations resulted in the final SET values for CRYO_TAUB and CYRO_CTAUB listed in Table 8.23.

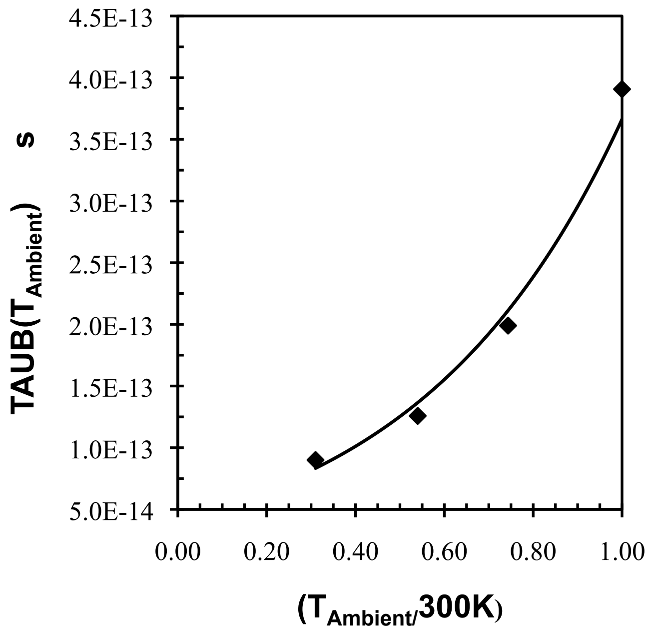

Figure 8.25 SET model extraction of base transit time parameters. Equation (8.44) is the solid line and the ambient temperature TAUB values are symbols

SET Model	
Parameter	Value
CRYO_TAUB	40fs
CRYO_CTAUB	2.132

Table 8.24 SET parameters CRYO_TAUB, CRYO_CTAUB

8.3.9 Epilayer transit time - TEPI

The diffusion charge of the epilayer collector region is represented by the charge branch, Q_{epi} as described in Section 3.2.4.3. The epilayer transit time parameter, TEPI, is directly proportional to Q_{epi} in the standard Mextram 504.7 definition of Q_{epi} defined in Equation (3.47). During optimization of the ambient temperature model parameters, the model parameters of the charge equation, Q_{epi}, controlled the fit of the cutoff frequency, f_T, versus Log(IC) curves beyond the peak f_T region. The epilayer transit time parameter, TEPI, had a strong influence on the ambient temperature model optimization of the cutoff frequency, f_T, curves in the high IC bias region.

TEPI shifts with temperature according to the temperature equation, **TEPI_T.** The standard 504.7 implementation of **TEPI_T** was described in Section 3.6.6. The temperature equation is repeated in Equation (8.45). The standard 504.7 temperature equation gives TEPI a temperature dependence described by a power law relationship. Control is determined by the temperature coefficient. However, the total temperature coefficient is an equation, (AEPI-1), which limits the ability to optimization the parameter's response to temperature. In the standard 504.7 implementation, AEPI is shared by other temperature equations thereby limiting the value of AEPI.

$$\mathbf{TEPI\_T} = \mathrm{TEPI} \cdot t_N^{(\mathrm{AEPI}-1)} \tag{8.45}$$

The limitations of the standard 504.7 temperature equation required a modification of Equation (8.45). The total temperature coefficient of (AEPI-1) was replaced by a new coefficient parameter, CRYO_CTEPI. The new parameter is used only in the modified **TEPI_T** equation and is therefore not restricted. The epilayer transit time temperature equation of the SET model is defined in Equation (8.46) [2].

$$\mathbf{TEPI\_T} = \mathrm{TEPI} \cdot t_N^{\mathrm{CRYO\_CTEPI}} \tag{8.46}$$

Analysis of the ambient temperature TEPI values and parameter extraction of the SET epilayer transit time temperature parameters required the plotting of the SET model equation, **TEPI_T**, and the ambient temperature TEPI values versus the ratio of $\frac{T_{\mathrm{Ambient}}}{300\mathrm{K}}$ as shown in Figure 8.26. The ambient temperature TEPI values are represented by markers. The SET epilayer transit time temperature equation, **TEPI_T**, of Equation (8.46), is the solid line in Figure 8.26. The final SET values for TEPI and CYRO_CTEPI are listed in Table 8.25.

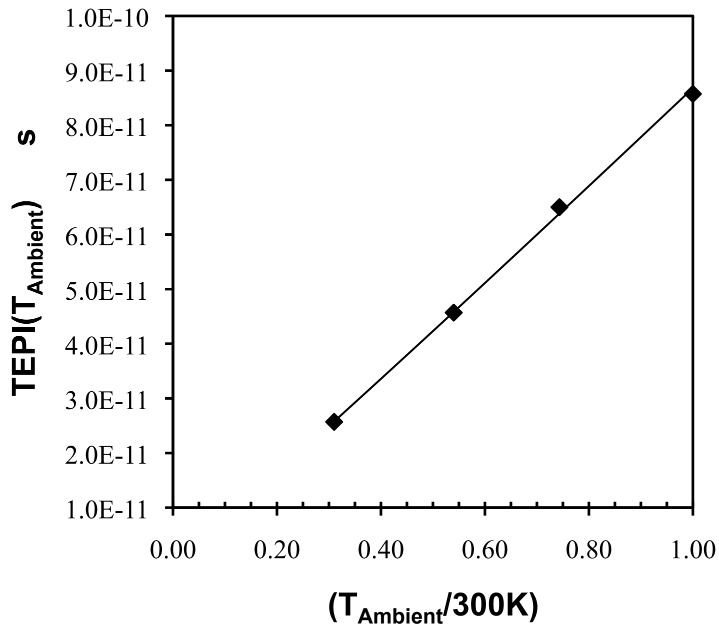

SET Model	
Parameter	Value
TEPI	85.73ps
CRYO_CTEPI	1.462

Table 8.25 SET parameters TEPI, CRYO_CTEPI

Figure 8.26 SET model extraction of epilayer transit time parameters. Equation (8.46) is the solid line and the ambient temperature TEPI values are symbols

8.4 Parameters modified below the cryogenic temperature parameter, TCRYO.

This section defines the parameters which required a new temperature equation below a certain temperature. The SET model parameter, TCRYO, was created to define the temperature at which the 504.7 parameter temperature behavior ends. For simulation temperatures below TCRYO another temperature equation represents the parameter. The use of the TCRYO temperature switch in the SET model was required due to the accuracy needed in the forward non-ideality factor parameter, NF, values.

The SET model parameters described in Section 8.4 utilized a switch between the unique temperature behaviors as illustrated in Figure 8.27.

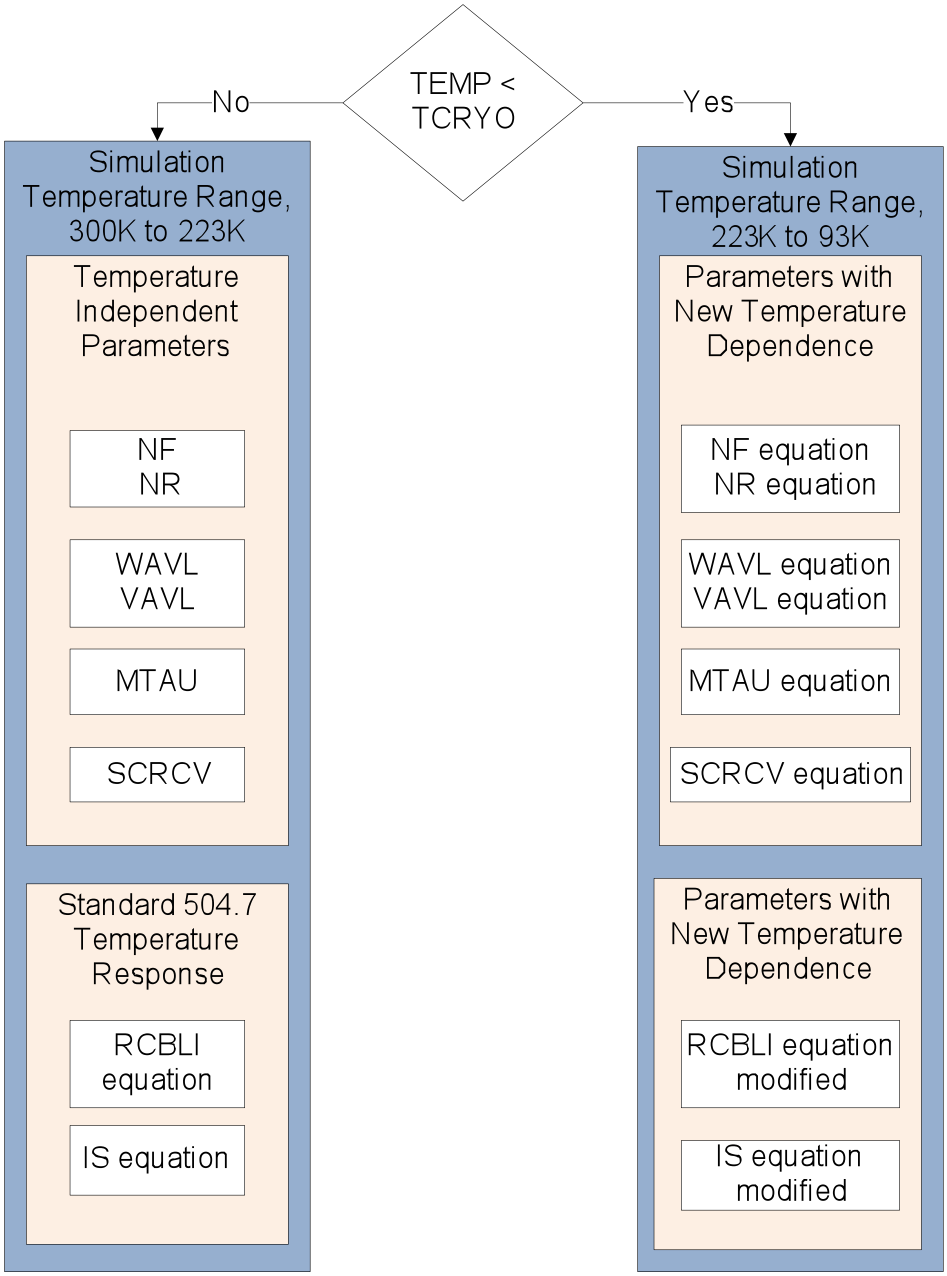

Figure 8.27 SET model parameters with temperature behavior defined by new temperature equations when simulation temperature, TEMP is less than the cryogenic temperature parameter, TCRYO.

From the ambient temperature model results of Chapter 7 six model parameters were identified with constant values till the simulation temperature of TCRYO. The forward and reverse non-ideality factor parameters, NF and NR are unique to the SET model. In the standard 504.7 model four of these parameters are defined as temperature independence. Therefore, the

SET model temperature behavior of these four parameters: WAVL, VAVL, MTAU, and SCRCV have constant values until simulation temperatures of TCRYO, but custom temperature equations below TCRYO. Two parameters, IS and RCBLI, were found to fit the standard 504.7 temperature equations until TCRYO and have modified temperature equations below TCRYO. Each parameter temperature equation and their associated parameter values are defined in the following sections.

8.4.1 Forward and Reverse Ideality Factors - NF and NR

The non-ideality factor parameters, NF and NR, were critical components in the development of the four ambient temperature models. The device characteristics of Chapter 5, defined the relationship of the forward non-ideality factor, NF, in the collector current, IC, and the IC behavior of the Gummel measurements across the wide temperature range. The value of NF was an essential first step in parameter extraction at each ambient temperature. The NF value was extracted in the mid-region of the Gummel measurements where the other parameters had less influence.

For simulation temperatures in the range from 300K to TCRYO, 223K, the forward non-ideality factor temperature response, **NF_T**, is defined by Equation (8.47) and the reverse non-ideality factor temperature response, **NR_T**, is defined by Equation (8.48) as a constant value.

$$\mathbf{NF\_T} = \mathrm{NF} \tag{8.47}$$

$$\mathbf{NR\_T} = \mathrm{NR} \tag{8.48}$$

For simulation temperatures less than TCRYO, 223K, both non-ideality factor parameters shift with temperature. Equation (8.49) defines **NF_T** and Equation (8.50) defines **NR_T**.

$$\mathbf{NF\_T} = CRYO\_NF \cdot t_N^{CRYO\_CNF} \tag{8.49}$$

$$\mathbf{NR\_T} = CRYO\_NR \cdot t_N^{CRYO\_CNR} \tag{8.50}$$

The ambient temperature model parameter optimizations were found to be very dependent upon the NF value. A change in NF after the other model parameters were fitted degraded the overall model fits of the DC and AC characteristics. The most accurate representation of the ambient temperature NF values required a switch between temperature behaviors. Analysis of the ambient temperature NF values and the resulting SET model forward non-ideality factor temperature equation is shown in Figure 8.28. The SET model equation is analyzed using $t_N = \frac{T_{Ambient}}{300K}$. The SET model equation, **NF_T**, and the ambient temperature NF values are plotted versus the ratio of $\frac{T_{Ambient}}{300K}$. The ambient temperature NF values are represented by symbols. The solid line in Figure 8.28 is the SET temperature equation, **NF_T**.

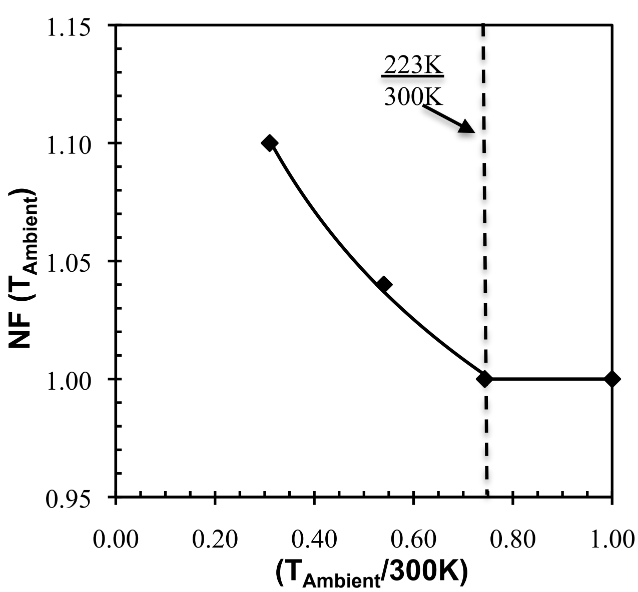

Figure 8.28 SET model extraction of non-ideality factor. SET equation NF_T is the solid line and the ambient temperature model NF values are symbols

SET Model	
Parameter	Value
CRYO_NF	0.9682
CRYO_CNF	-110m
CRYO_NR	0.9682
CRYO_CNR	-110m

Table 8.26 SET parameters CRYO_NF, CRYO_CNF, CRYO_NR, CRYO_CNR

NF_T for $T_{Ambient}$ temperatures at 223K and above is defined by Equation (8.47) and for $T_{Ambient}$ temperatures less than 223K, **NF_T** is defined by Equation (8.50). The use of the switch is indicated at $\frac{223K}{300K}$. Using this method provided the accuracy in NF values that was needed over the wide temperature range. Two new temperature parameters are defined for each non-ideality factor model parameter. The final SET values for CRYO_NF, and CYRO_CNF are listed in Table 8.26.

The development of the ambient models in Chapter 7 determined that the reverse non-ideality factor parameter, NR, must be equal to the NF. The NR pairing with NF was essential to preventing an unreal VCE saturation offset voltage effect. The SET model values for the reverse non-ideality factor temperature equations of (8.48) and (8.50) are listed in Table 8.26 as well.

8.4.2 Avalanche current – VAVL and WAVL

The collector current behavior in the breakdown voltage region of the output characteristics is described by the avalanche current branch, I_{avl}, of the Mextram model. The avalanche current model parameters, VAVL and WAVL, are temperature independent in the standard 504.7 model. However, it was found in the SiGe HBT modeled these two parameters shifted with temperature in the cryogenic temperature range. Therefore, the SET model has new parameter temperature equations for VAVL and WAVL. The ambient temperature value was constant until the cryogenic temperature, TCRYO, at 223K for both the avalanche voltage parameter, VAVL, and the epilayer collector effective width parameter, WAVL. Below TCRYO, the ambient values shifted with temperature as shown in Figures 8.29 and 8.30, respectively. The SET model temperature equations used a cryogenic temperature parameter, TCRYO, as a switch. The parameter temperature equation changed from a constant value, to an equation shifting the parameter with temperature when the simulation temperatures are less than TCRYO. For colder temperatures, the temperature response of both parameters was described by a power law relationship with a cryogenic parameter and coefficient parameter.

In the simulation temperature range from 300K to the cryogenic start temperature parameter, TCRYO, 223K, the SET model uses the parameter temperature equation, **VAVL_T** of Equation (8.51).

$$\mathbf{VAVL\_T} = \mathrm{VAVL} \tag{8.51}$$

The temperature behavior below the cryogenic temperature parameter, TCRYO defined in Equation (8.52) represents the temperature behavior below the cryogenic temperature parameter, TCRYO, for the avalanche voltage parameter VAVL.

$$\mathbf{VAVL\_T} = \mathrm{CRYO\_VAVL} \cdot t_N^{\mathrm{CRYO\_CVAVL}} \tag{8.52}$$

The parameter temperature equation, **WAVL_T**, in Equation (8.53) represents the temperature behavior above the cryogenic temperature parameter, TCRYO.

$$\mathbf{WAVL\_T} = \mathrm{WAVL} \tag{8.53}$$

For simulation temperatures below TCRYO, Equation (8.54) described **WAVL_T** in the SET model.

$$\mathbf{WAVL\_T} = \mathrm{CRYO\_WAVL} \cdot t_N^{\mathrm{CRYO\_CWAVL}} \tag{8.54}$$

The analysis of **VAVL_T** and **WAVL_T** used the same technique as was used in Section 8.4.1 for NF. The analysis of the ambient temperature model values of VAVL and WAVL were plotted against the resulting SET model temperature equations of **VAVL_T** and **WAVL_T** defined in Equations (8.51) through (8.54) and shown in Figures 8.29 and 8.30. The SET model equations were analyzed using $t_N = \frac{T_{Ambient}}{300K}$. The SET model equation, **VAVL_T**, and the ambient temperature model VAVL values are plotted versus the ratio of $\frac{T_{Ambient}}{300K}$. The ambient temperature VAVL values are represented by symbols. The solid line in Figure 8.29 is the SET temperature equation, **VAVL_T**. The SET model temperature parameters for VAVL are listed in Table 8.27.

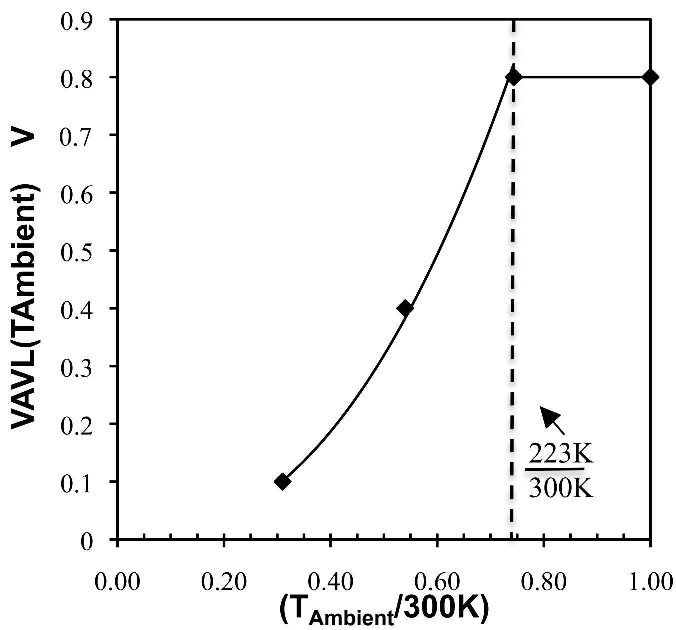

Figure 8.29 SET model extraction I_{avl} voltage parameters. The SET equation for VAVL_T is the solid line and the ambient temperature model VAVL values are symbols

SET Model	
Parameter	Value
CRYO_VAVL	1.671V
CRYO_CVAVL	2.391

Table 8.27 SET parameters CRYO_VAVL, CRYO_CVAVL

VAVL_T for $T_{Ambient}$ temperatures at 223K and above is defined by Equation (8.51) and for $T_{Ambient}$ temperatures less than 223K, **VAVL**_T is defined by Equation (8.52). The use of the switch is indicated at $\frac{223K}{300K}$.

The SET model equation, **WAVL_T**, and the ambient temperature model WAVL values are plotted versus the ratio of $\frac{T_{Ambient}}{300K}$. The ambient temperature WAVL values are represented by symbols. The solid line in Figure 8.30 is the SET temperature equation, **WAVL_T**. The SET model temperature parameters for WAVL are listed in Table 8.28.

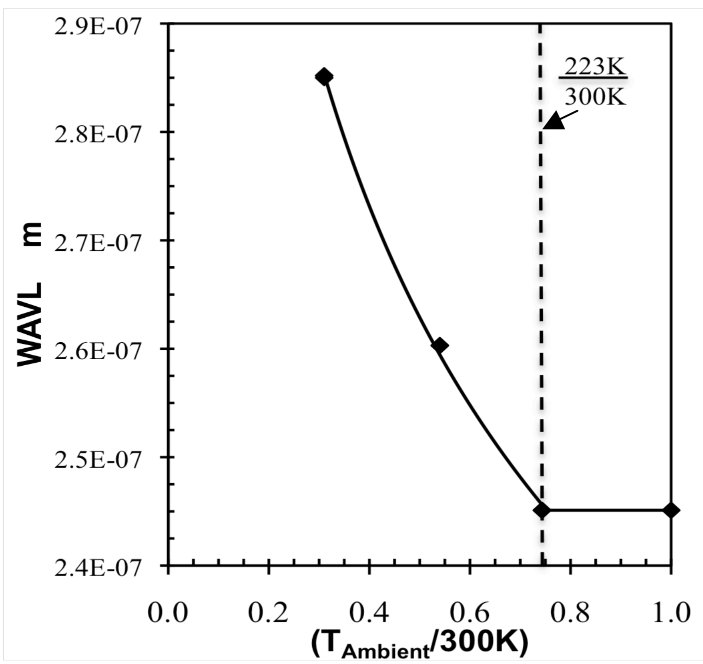

Figure 8.30 SET parameter extraction of I_{avl} effective width parameters. Equation (8.54) is the solid line and the ambient temperature WAVL values are symbols

SET Model	
Parameter	Value
CRYO_WAVL	200nm
CRYO_CWAVL	-172.0m

Table 8.28 SET parameters CRYO_WAVL, CRYO_CWAVL

WAVL_T for $T_{Ambient}$ temperatures at 223K and above is defined by Equation (8.53) and for $T_{Ambient}$ temperatures less than 223K, **WAVL_T** is defined by Equation (8.54). The use of the switch is indicated at $\frac{223K}{300K}$.

8.4.3 Non-ideality factor of emitter charge - MTAU

The emitter charge non-ideality factor parameter, MTAU, was a critical contributor in fitting the peak f_T response of the ambient temperature models as the temperature decreased. MTAU increased as temperature decreased. Typically, MTAU is fixed at one and the optimization of the emitter diffusion charge branch, Q_E, only involves the emitter transit time parameter, TAUE. In the standard 504.7 temperature equations TAUE shifts with temperature, but MTAU is temperature independent. The temperature response of TAUE required a modification of the 504.7 equation which is described in Section 8.3.7. Over the expansive temperature range, both parameters, TAUE and MTAU shifted with temperature. Therefore, a temperature equation for MTAU was created for the SET model. The ambient value of MTAU was constant until simulation temperatures were lower than TCRYO. The value of MTAU increased as temperatures decreased below TCRYO as shown in Figure 8.31. The MTAU temperature equation, **MTAU_T**, of Equation (8.55) is used in the SET model for simulation temperatures from 300K through 223K.

$$\mathbf{MTAU\_T} = \mathrm{MTAU} \tag{8.55}$$

Analysis of the ambient temperature MTAU values below 223K lead to the creation of an empirical relationship for **MTAU_T**, Equation (8.56), for simulation temperatures below TCRYO. Optimization of the corresponding temperature parameters in the empirical relationship produced a good fit in the SET model.

$$\mathbf{MTAU\_T} = \mathrm{CRYO\_FMTAU} \cdot t_N + \mathrm{CRYO\_MTAU} \tag{8.56}$$

The same analysis technique used in creating the non-ideality factor temperature equations of Section 8.4.1 was used for **MTAU_T**. The analysis of the ambient temperature model values of

MTAU were plotted against the resulting SET model temperature equations of **MTAU_T** defined in Equations (8.55) and (8.56) in Figures 8.31. The SET model equations were analyzed using $t_N = \frac{T_{Ambient}}{300K}$. The SET model equation, **MTAU_T**, and the ambient temperature model MTAU values are plotted versus the ratio of $\frac{T_{Ambient}}{300K}$ in Figure 8.31. The ambient temperature MTAU values are represented by symbols. The solid line in Figure 8.31 is the SET temperature equation, **MTAU_T**.

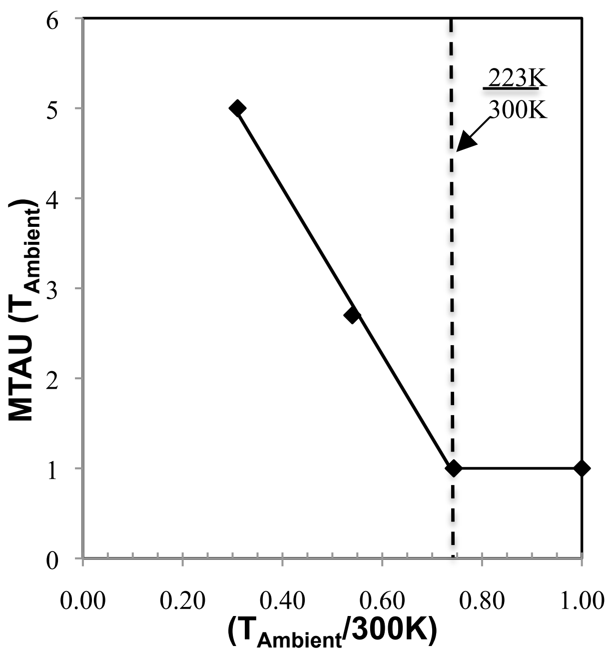

Figure 8.31 SET model of nonideal emitter charge factor parameters. The SET equation MTAU_T is a solid line, ambient temperature MTAU values are symbols

SET Model	
Parameter	Value
MTAU	1
CRYO_MTAU	7.811
CRYO_FMTAU	-9.248

Table 8.29 SET parameters MTAU, CRYO_CMTAU, CRYO_FMTAU

MTAU_T for $T_{Ambient}$ temperatures at 223K and above is defined by Equation (8.55) and for $T_{Ambient}$ temperatures less than 223K, **MTAU_T** is defined by Equation (8.56). The use of the switch is indicated at $\frac{223K}{300K}$. The final SET values for MTAU, CRYO_MTAU, and CYRO_FMTAU are listed in Table 8.31.

8.4.4 Epilayer collector resistance - SCRCV

The physical structure of the epilayer collector region results in the resistance changing with current flow through the collector as defined by quasi-saturation in Section 2.3. The standard Mextram 504.7 model of the epilayer current, described in Section 3.2.5, was developed to accurately represent the quasi-saturation effects of most advanced bipolar process technologies. In the standard 504.7 model the epilayer current branch, I_{C1C2}, consists of a low current constant resistance, RCV, and a high current space charged resistance, SCRCV. RCV has temperature dependent described in Section 3.6.3. SCRCV is temperature independent in the standard 504.7 model.

For the SET model the RCV temperature response, **RCV_T**, followed the standard 504.7 temperature equation. The SET **RCV_T** analysis and parameter extraction was detailed in Section 8.2.3.5. *But the ambient temperature SCRCV values were not constant over the expansive temperature range.*

Therefore, in the SET model a parameter temperature response, **SCRCV_T**, had to be created for SCRCV. The ambient values of SCRCV were constant until simulation temperatures were lower than TCRYO. The value of SCRCV increased as temperatures decreased below TCRYO as shown in Figure 8.32. The SCRCV temperature equation, **SCRCV_T**, of Equation (8.57) represent constant values of SCRCV in the SET model for simulation temperatures from 300K through 223K.

$$\mathbf{SCRCV\_T} = \mathrm{SCRCV} \qquad (8.57)$$

Analysis of the ambient temperature SCRCV values below 223K indicated that SCRCV has a power law relationship with temperature. The temperature response for **SCRCV_T**, is defined in Equation (8.58), for simulation temperatures below TCRYO.

$$\mathbf{SCRCV\_T} = \mathrm{CRYO\_SCRCV} \cdot t_N^{\mathrm{CRYO\_CSCRCV}} \tag{8.58}$$

Again the same analysis technique used for **SCRCV_T** as was used in NF. The ambient temperature model values of SCRCV were plotted against the resulting SET model temperature equations of **SCRCV_T** defined in Equations (8.57) and (8.58) in Figures 8.32. The SET model equations were analyzed using $t_N = \dfrac{T_{Ambient}}{300K}$.

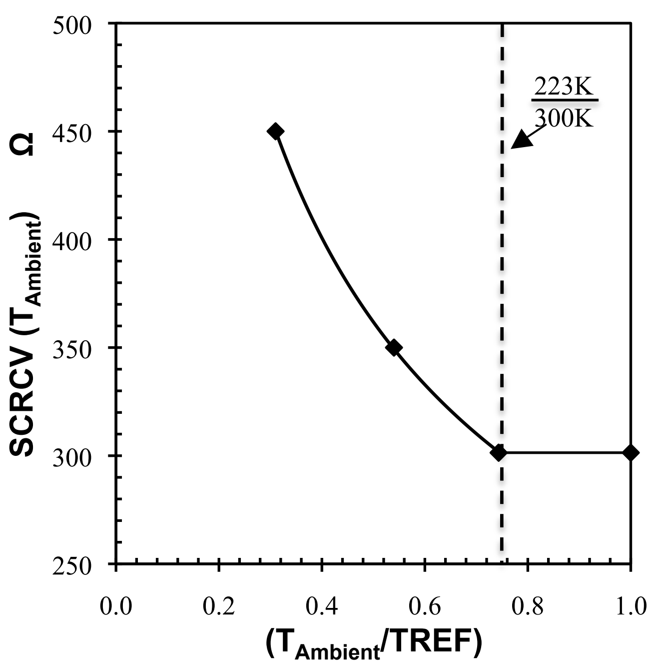

Figure 8.32 SET extraction of space charge resistance parameters. Equation (8.58) is the solid line and the ambient temperature SCRCV values are symbols

SET Model	
Parameter	Value
CRYO_SCRCV	263.5Ω
CRYO_CSCRCV	-0.458

Table 8.30 SET parameters CRYO_SCRCV, CRYO_CSCRCV

The SET model equation, **SCRCV_T**, and the ambient temperature model SCRCV values are plotted versus the ratio of $\frac{T_{Ambient}}{300K}$. The ambient temperature SCRCV values are represented by symbols. The solid line in Figure 8.30 is the SET temperature equation, **SCRCV_T**. **SCRCV_T** for $T_{Ambient}$ temperatures at 223K and above is defined by Equation (8.57) and for $T_{Ambient}$ temperatures less than 223K, **SCRCV_T** is defined by Equation (8.58). The use of the switch is indicated at $\frac{223K}{300K}$. The final SET values for CRYO_SCRCV, and CYRO_CSCRCV are listed in Table 8.30.

8.4.5 Saturation current - IS

The saturation current parameter, IS, a dominant contributor to the transfer current, I_N, and therefore the collector current. In the standard 504.7 model IS has a temperature response, **IS_T**, which was described in Section 3.6.5. The standard temperature equation is repeated in Equation (8.59) [2].

$$\mathbf{IS\_T} = IS \cdot t_N^{(4-AB-AQBO+DAIS)} \exp\left[\frac{-VGB}{V_{\Delta T}}\right] \tag{8.59}$$

Analysis of the ambient IS values over the expansive temperature range determined that the standard 504.7 temperature equation did adequately represent the IS parameter response in the temperature range from 300K to 223K. However, at simulation temperatures less than TCRYO it was determined from the ambient temperature IS values that a different temperature equation was needed. For simulation temperatures below TCRYO a new IS temperature equation, **IS_T**, was created in the SET model as defined in Equation (8.60).

$$\mathbf{IS\_T} = IS \cdot t_N^{CRYO\_CIS} \cdot \exp\left[\frac{CRYO\_VGB}{V_{\Delta T}}\right] \tag{8.60}$$

In the SET model equation, **IS_T**, the standard 504.7 empirical temperature coefficient equation of $(4 - AB - AQBO + DAIS)$ was replaced with SET parameter, CRYO_CIS, of Equation (8.61). Also, in the SET definition of **IS_T** the base bandgap voltage parameter, VGB, was replaced with a new cryogenic base bandgap voltage parameter, CRYO_VGB, which is defined in Equation (8.62).

The SET model IS temperature coefficient parameter, CRYO_CIS, was created by optimizing the Equations (8.60) to the ambient temperature IS values.

$$CRYO\_CIS = CRYO\_ISO \cdot t_N^{CRYO\_CISO} \tag{8.61}$$

The SET parameters, CRYO_ISO and CRYO_CISO, were optimized in Equation (8.61) using fitted results of Equation (8.60). A good fit of these internal CRYO_CIS parameters was determined by analyzing Figure 8.33. The SET model variable, CRYO_CIS, in Equation (8.61), and the optimized values of CRYO_CIS from Equation (8.60) were plotted versus the ratio of $\frac{T_{Ambient}}{300K}$. The CRYO_CIS optimized values from Equation (8.60) are represented by markers. The fitted results of CRYO_CIS in Equation (8.61), is the solid line in Figure 8.33. The final SET values for CRYO_ISO, and CYRO_CISO are listed in Table 8.31.

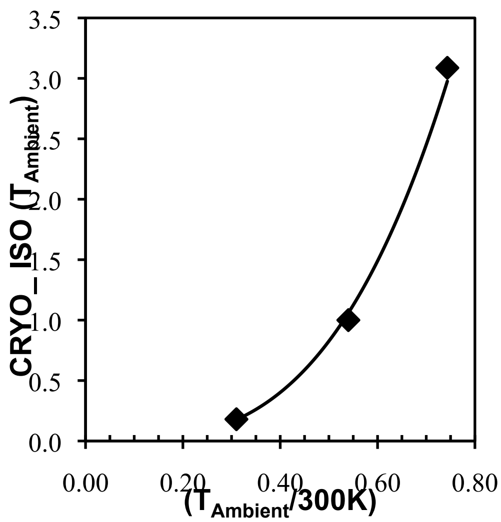

Figure 8.33 SET model of saturation current parameters. Equation (8.61) is the solid line and the CRYO_CIS values from Equation (8.60) are symbols

SET Model	
Parameter	Value
CRYO_ISO	7.761
CRYO_CISO	3.232

Table 8.31 SET parameters CRYO_ISO, CRYO_CISO

For the SET model below TCRYO, 223K, IS shifts with temperature by **IS_T** of Equation (8.60) with a new base bandgap voltage parameter, CRYO_VGB defined in Equation (8.62).

$$CRYO\_VGB = CRYO\_VGB\_VOLTAGE \cdot t_N^{CRYO\_CVGB} \quad (8.62)$$

The ambient values for CRYO_VGB were taken from Equation (8.60). The values of the internal CRYO_VGB parameters in Equation (8.62), are parameters: CRYO_CVGB and CRYO_CVGB_VOLTAGE. These internal parameters were optimized by fitting CRYO_VGB of Equation (8.62) to the values of CRYO_VGB in Equation (8.60).

The SET model variable, CRYO_VGB, in Equation (8.62), and the optimized values of CRYO_VGB from Equation (8.60) were plotted versus the ratio of $\frac{T_{Ambient}}{300K}$. The CRYO_VGB optimized values from Equation (8.60) are represented by markers. The fitted result of CRYO_VGB in Equation (8.62), is the solid line in Figure 8.34. The final SET values were extracted from the fit of Equation (8.62) in Figure 8.34. CRYO_CVGB, and CYRO_CVGB_VOLTAGE are listed in Table 8.32.

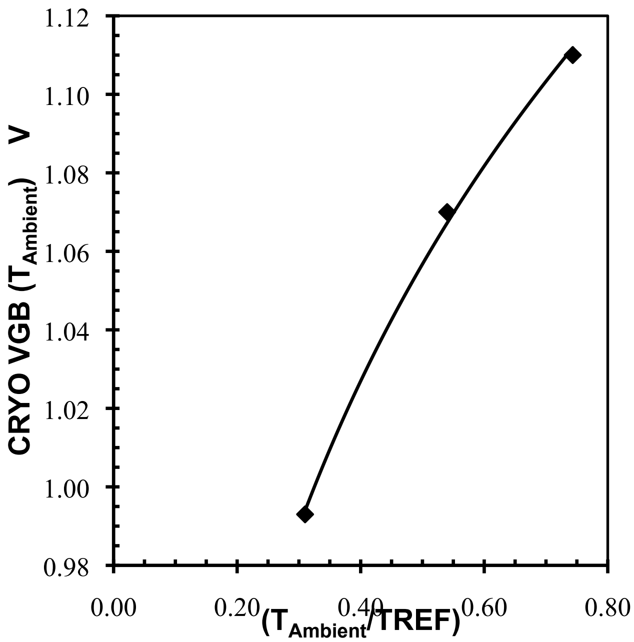

Figure 8.34 SET model extraction of saturation current bandgap voltage parameters. Equation (8.62) is the solid line and the CRYO_VGB values from Equation (8.60) are symbols

SET Model	
Parameter	Value
CRYO_CVGB	128.2m
CRYO_CVGB_VOLTAGE	1.155V

Table 8.32 SET parameters CRYO_VGB, CRYO_CVGB_VOLTAGE

The ability of the two **IS_T** equations to be compatible at the TCRYO switch was evaluated by plotting the **IS_T** equation over the full temperature range in Figure 8.35 versus the ambient temperature model IS values. The fit of the new SET **IS_T** equation was excellent as compared to the extracted IS values at each ambient temperature model.

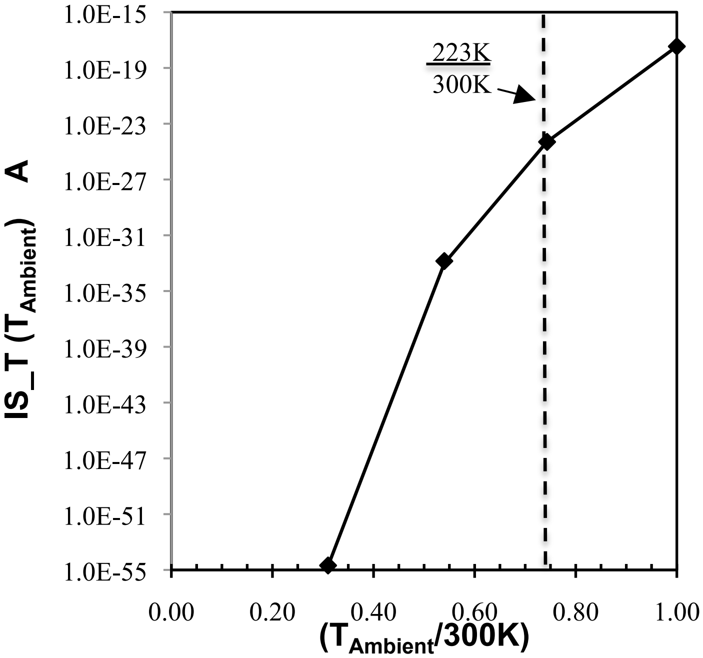

Figure 8.35 The SET model temperature equation IS_T across the full temperature range as compared to the ambient temperature model IS values.

8.4.6 Intrinsic N^+ buried collector resistance - RCBLI

The intrinsic N^+ buried collector resistance parameter, RCBLI, was influential to the optimizations of the ambient temperature models in the high current region of the f_T versus Log(IC) curves. The ambient temperature RCBLI values increased as temperature decreased when the simulation temperature were below TCRYO. The temperature response of RCBLI for the standard 504.7 temperature equation, **RCCin_T**, was defined in Section 3.6.5.and is repeated in Equation (8.63) [2].

$$\mathbf{RCCin\_T} = \mathrm{RCBLI} \cdot t_N^{\mathrm{ACBL}} \tag{8.63}$$

The ambient temperature RCBLI values could not be represented by the standard 504.7 temperature equation. A different parameter temperature approach was required. The value of RCBLI was constant until below the temperature of TCRYO. Therefore the SET model temperature equation used the cryogenic temperature parameter, TCRYO, as switch to go from a constant resistance value, RCBLI, to power law relationship between resistance and temperature. a new coefficient parameter, CRYO_CRCBLI. In the simulation temperature range from 300K to TCRYO of 223K, the SET model used a constant value defined by Equation (8.64).

$$\mathbf{RCCin\_T} = \mathrm{RCBLI} \tag{8.64}$$

The SET model temperature equation, **RCCin_T**, for simulation temperatures below the value of TCRYO are defined by Equation (8.65).

$$\mathbf{RCCin\_T} = \mathrm{CRYO\_RCBLI} \cdot t_{N}^{\mathrm{CRYO\_CRCBLI}} \tag{8.65}$$

Analysis of the ambient temperature RCBLI values and development of the SET model intrinsic N^{+} buried collector resistance temperature parameters required the plotting of the SET model equation, **RCCin_T**, and the ambient temperature RCBLI values as shown in Figure 8.36.

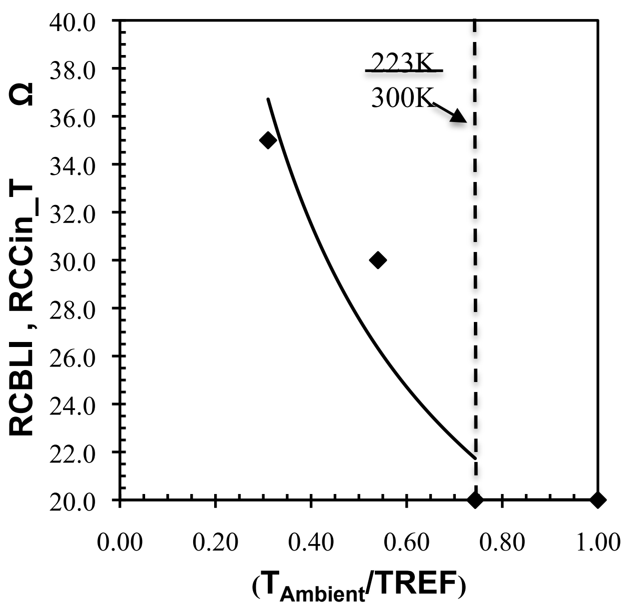

Figure 8.36 SET extraction of intrinsic buried collector resistance parameters. SET equation RCCin_T is the solid line and the ambient temperature RCBLI values are symbols

SET Model	
Parameter	Value
RCBLI	20Ω
CRYO_RCBLI	18.19Ω
CRYO_CRCBLI	-0.600

Table 8.33 SET parameters RCBLI, CRYO_RCBLI, CRYO_CRCBLI

The SET model equation, **RCCin_T**, and the ambient temperature model RCBLI values are plotted versus the ratio of $\frac{T_{Ambient}}{300K}$. The ambient temperature RCBLI values are represented by symbols. The solid line in Figure 8.36 is the SET temperature equation, **RCCin_T**. For $T_{Ambient}$ temperatures at 223K and above **RCCin_T** is defined by Equation (8.64) and for $T_{Ambient}$ temperatures less than 223K, **RCCin_T** is defined by Equation (8.65). The use of the switch is indicated at $\frac{223K}{300K}$. The final SET values for RCBLI, CRYO_RCBLI, and CYRO_CRCBLI are listed in Table 8.33.

8.5 SET Model Simulation Results - DC and AC fits

The behavior of the electrical model parameters over the temperature range of 300K to 93K often differed from the expected standard 504.7 parameter temperature equations. The SET model parameter temperature equations which used standard 504.7 temperature equations are detailed in Section 8.2. The model parameters which required unique and individual temperature parameters for their temperature equations are described in Section 8.3. Finally those SET model parameters which required completely new temperature equations are described in Section 8.4. In all there were 36 model parameters that shifted with temperature in the SET model. There were a total of 30 new model temperature parameters created in the definitions of the new parameter temperature equations for the wide temperature range modeling of the SET model.

The SET model is the compilation of all of the new parameter equations in this chapter and the CRYO_504.7 model equations. The SET model was simulated with the extracted model parameters values for a final verification of the SET model fit over the expansive temeperaure range of 300K to 93K. The final SET model parameter set is listed in Appendix C. The new parameter temperature equations and their corresponding values complete the development of the SET model and parameter values.

The following comparison of the measurement characteristics to the SET model simulations verifies the success of creating one model and parameter values to represent the SiGe HBT over a expansive temperature range. The output characteristics of the four ambient temperatures are compared to a corresponding SET model simulation in Figures 8.37 through 8.40.

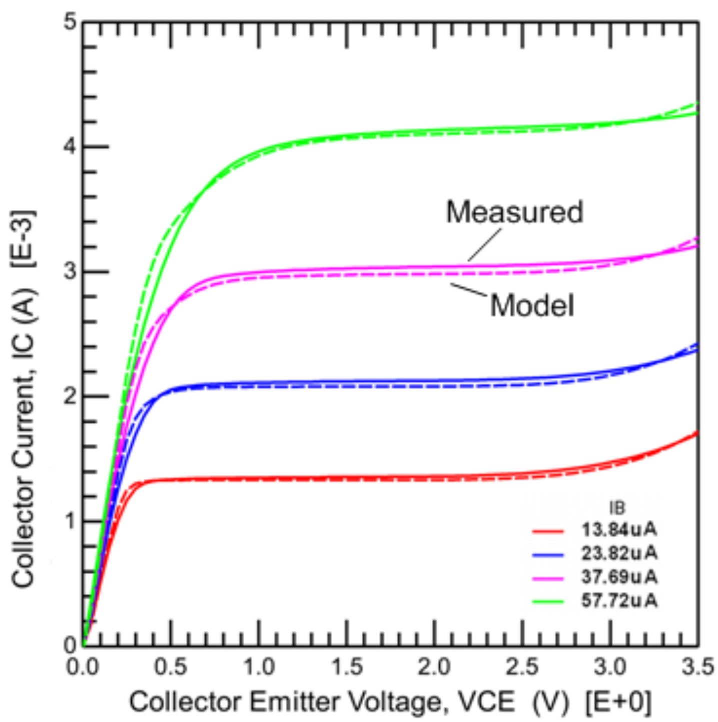

Figure 8.37 Output characteristics at 300K. Measured ambient data is solid line and SET model simulation is the dashed line.

The SET model simulation of output characteristics at 300K was an excellent fit with the ambient temperature measurement in Figure 8.37.

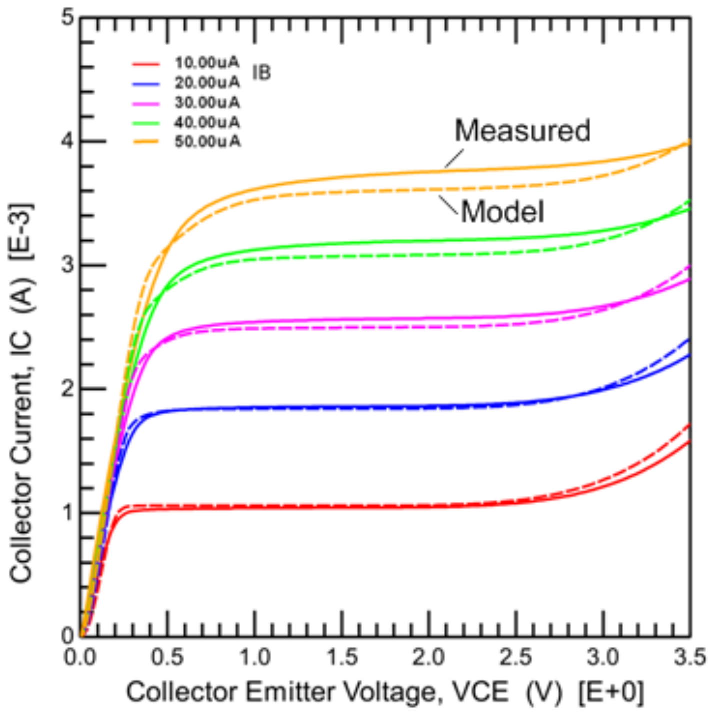

Figure 8.38 Output characteristics at 223K. . Measured ambient data is solid line and SET model simulation is the dashed line.

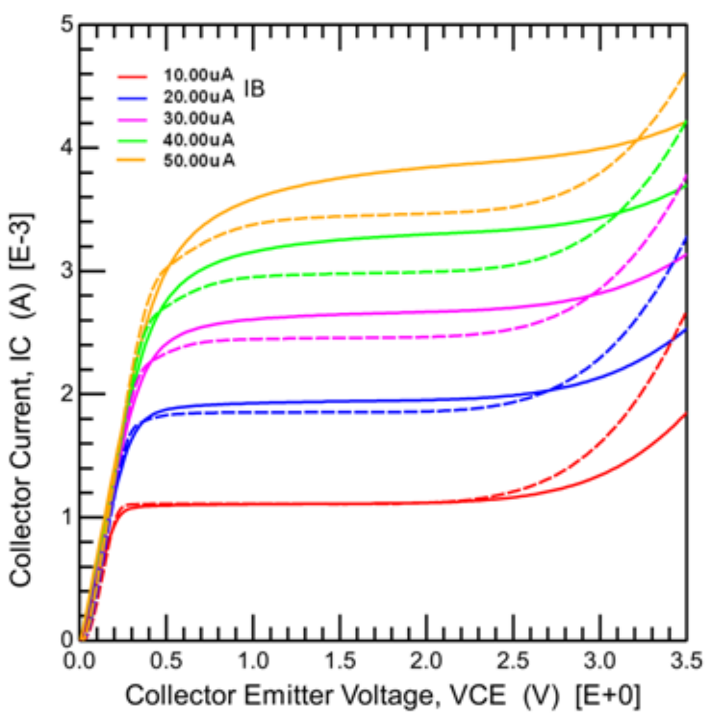

Figure 8.39 Output characteristics 162K. Measured ambient data is solid line and SET model simulation is the dashed line.

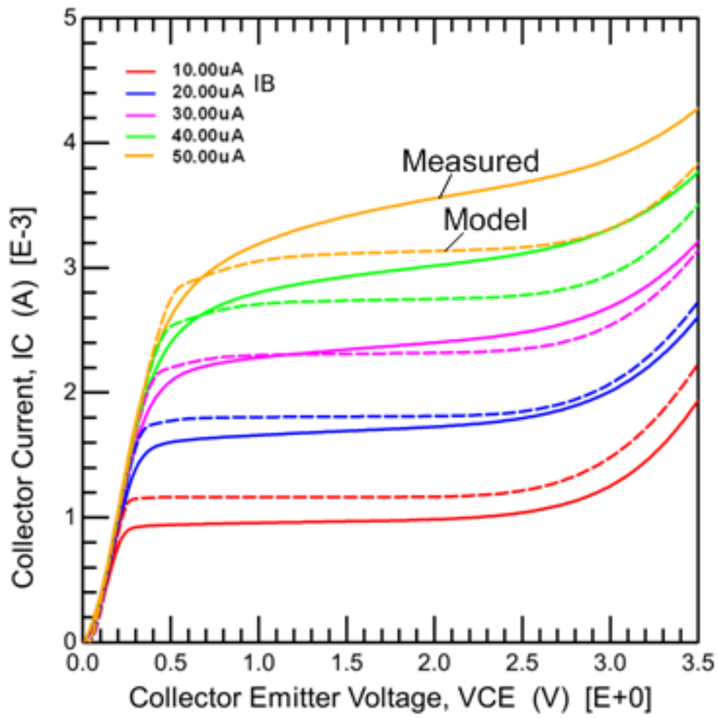

Figure 8.40 Output characteristics at 93K. Measured ambient data is solid line and SET model simulation is the dashed line.

The fit of the SET model to measured data is excellent at 300K and 223K. The output characteristics of the highest base bias current are slightly off at 162K. The 93K output characteristics have a larger error at the highest base bias current. This error is due to the rapidly changing DC current gain at high bias levels as shown in Figure 8.44, of the 93K Gummel.

The SET model fit of the Gummel measurements illustrates the difficulty that any model faces in accurately fitted the high-level injection region of operation. The comparison of SET model simulations to Gummel measurements at all four ambient temperatures are presented in Figures 8.40 through 8.47. The fit of the SET model to measured data for the DC current gain versus Log(IC) curves are presented in Figures 8.40 through 8.43. The linear region Gummel measurements are also compared by the classic Log(IC) and Log(IB) versus VBE in Figures 8.44 through 8.47.

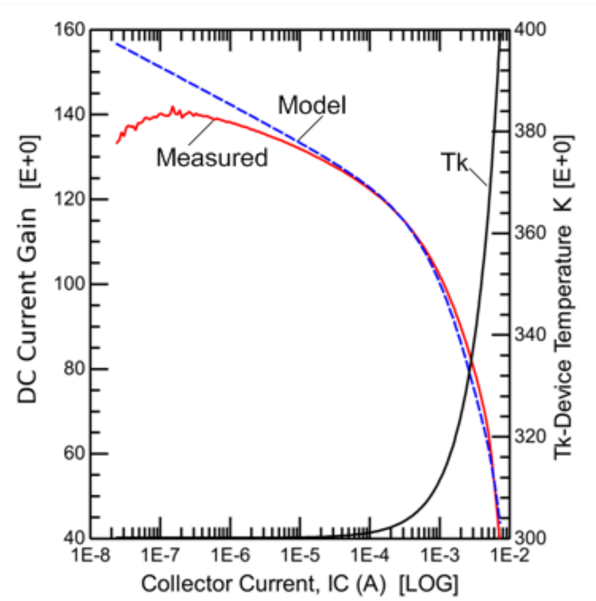

Figure 8.41 SET Model Simulation vs. Gummel Measurement, 300K. Left axis: Current Gain, β_f vs. Log(IC) at VBC= -1V. Solid line is measured data and dashed line is simulated results. Right axis: Device Temperature, Tk.

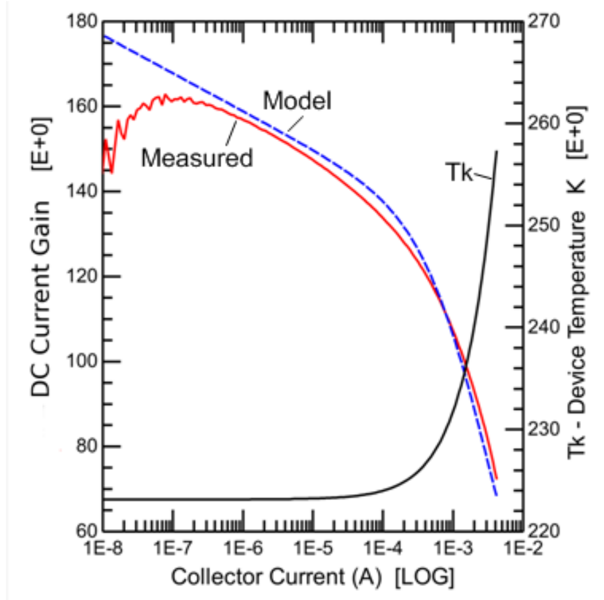

Figure 8.42 SET Model Simulation vs. Gummel Measurement, 223K. Left axis: Current Gain, β_f vs. Log(IC) at VBC= -1V. Solid line is measured data and dashed line is simulated results. Right axis: Device Temperature, Tk.

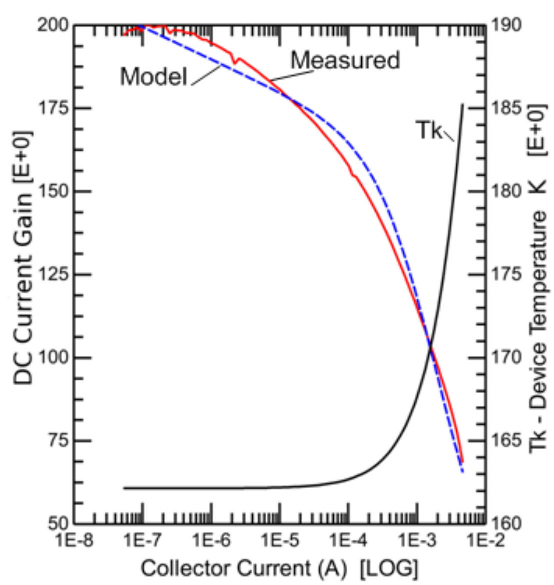

Figure 8.43 SET Model Simulation vs. Gummel Measurement, 162K. Left axis: Current Gain, β_f vs. Log(IC) at VBC= -1V. Solid line is measured data and dashed line is simulated results. Right axis: Device Temperature, Tk.

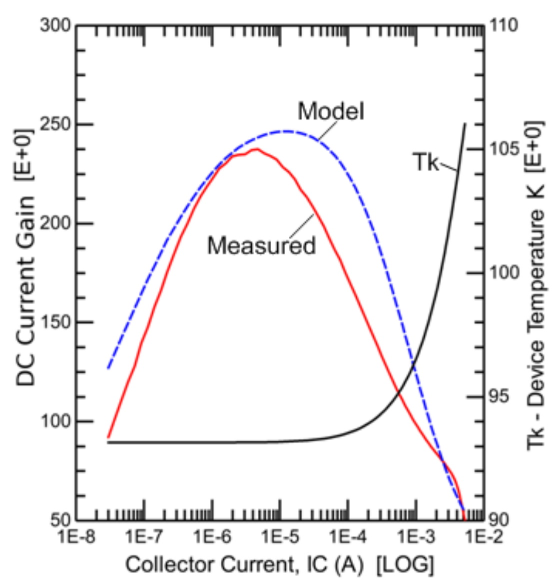

Figure 8.44 SET Model Simulation vs. Gummel Measurement, 93K. Left axis: Current Gain, β_f vs. Log(IC) at VBC= -1V. Solid line is measured data and dashed line is simulated results. Right axis: Device Temperature, Tk.

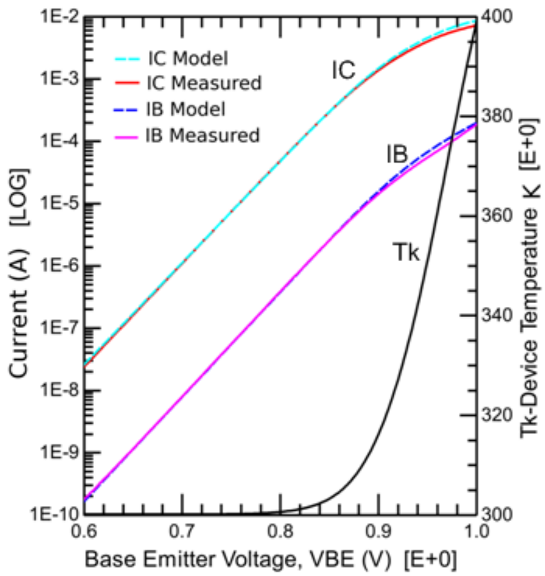

Figure 8.45 SET Model Simulation vs. Gummel Measurement, 300K. Left axis: IC and IB vs. VBE. Solid line is measured data and dashed line is simulated results. Right axis: Device Temperature, Tk.

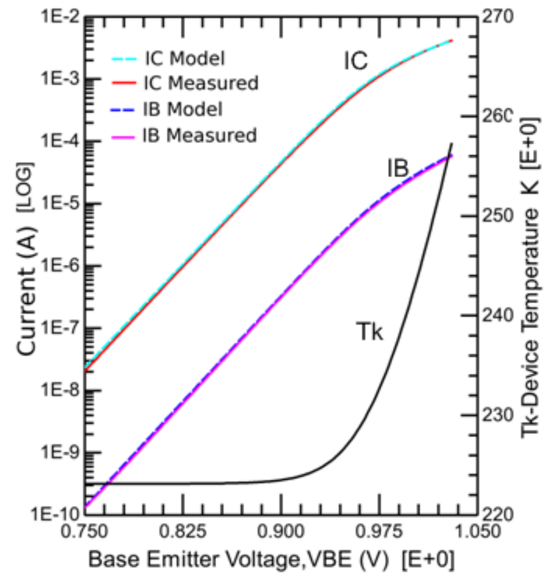

Figure 8.46 SET Model Simulation vs. Gummel Measurement, 223K. Left axis: IC, IB vs. VBE. Solid line is measured data and dashed line is simulated results. Right axis: Device Temperature, Tk.

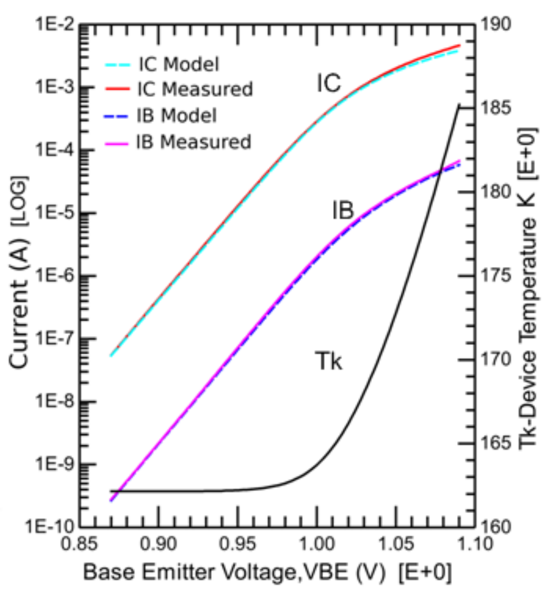

Figure 8.47 SET Model Simulation vs. Gummel Measurement, 162K. Left axis: IC, IB vs. VBE. Solid line is measured data and dashed line is simulated results. Right axis: Device Temperature, Tk.

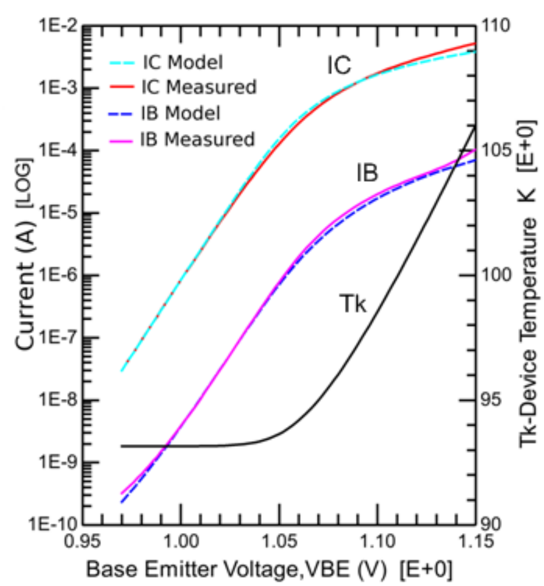

Figure 8.48 SET Model Simulation vs. Gummel Measurement, 93K. Left axis: IC, IB vs. VBE. Solid line is measured data and dashed line is simulated results. Right axis: Device Temperature, Tk.

The SET model simulations of Figures 8.40 through 8.43 demonstrate an excellent fit from 300K to 162K in the collector current range of 100uA to 3mA. However, the narrow peak shaped DC current gain curve at 93K is much more difficult to fit. The various physical influences overlap the three distinct carrier injection regions to such a large extent that equation representation becomes limited. The regions of IC and IB which are challenged by the characteristics of the HBT are also clearly present in Figure 8.47. The Gummel fits very well throughout the entire range of 0.1μA through quasi-saturation which covers 5.5 decades of current range for IC and IB. The total RMS relative fit error of current gain ranged from 8.02% at 300K to 13.0% at 93K as indicated in Table 8.34.

The device temperature, Tk, is plotted as a function of bias in all Gummel characteristic plots of Figures 8.40 through 8.48. The device temperature includes the ambient temperature and the increase in temperature due to self-heating. The device temperature of all SET model simulations as a function of the collector current in the ambient temperature Gummel characteristics is plotted in Figure 8.49. The device temperature increase of each ambient temperature Gummel measurement is summarized in Table 8.34.

Ambient Temperature	RMS Relative Fit Error of Current Gain	Fitted Model IC Range	Increase in Device Temperature During Measurement
300K	8.02%	30nA to 7.3mA	99.2 K
223K	8.90%	25nA to 4.1mA	34.2 K
162K	7.91%	58nA to 4.6mA	23.1 K
93K	13.0%	29nA to 5.1mA	12.9 K

Table 8.34 SET model performance metrics: model error, IC dynamic range and model predicted total device temperature increase during the Gummel measurement.

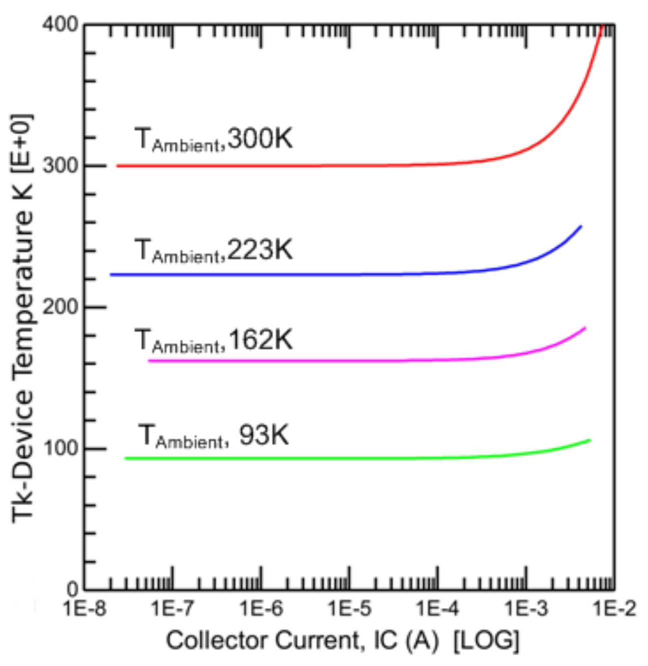

Figure 8.49 Total device temperature predicted by SET model as a function of collector current in a Gummel measurement.

The AC characteristics of the SET model were evaluated by comparing the f_T versus Log(IC) simulation results for the four ambient measurements in Figures 8.50 through 8.53.

The SET model simulation fitted extremely well at 300K when compared to the measured f_T of Figure 8.50. At 223K the SET model saw a temperature shift of 67K yet the f_T simulation results were almost the same as the "at temperature" ambient temperature model fit of Figure 7.39 in Chapter 7. At 162K, the SET model must correctly represent a 138K decrease in ambient simulation temperature. A comparison at 162K of the SET model simulation in Figure 8.51 to the "at temperature" ambient model f_T simulation of Figure 7.40 shows very similar results. At the lowest measured cryogenic temperature, 93K both the SET model simulated results and the ambient temperature simulation have similar shapes. However, the SET model has slightly higher error at the higher IC bias conditions.

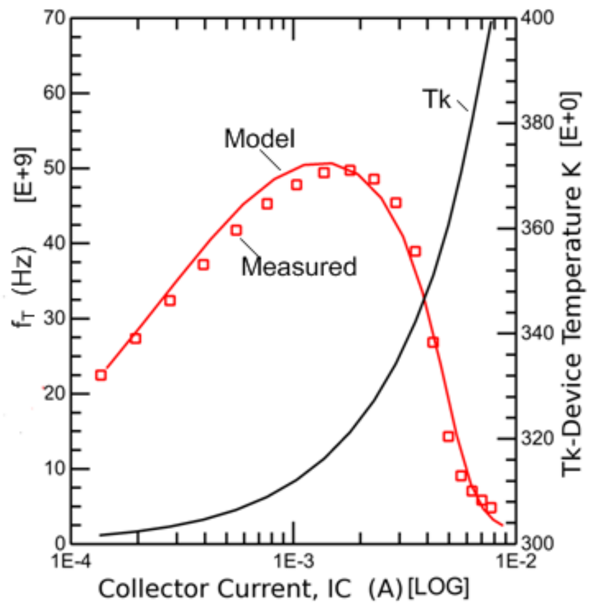

Figure 8.50 SET Model Simulation vs. Gummel Measurement, 300K. Left axis: f_T vs. Log(IC). Symbols are measured data and solid line is simulated results. Right axis: Device Temperature, Tk.

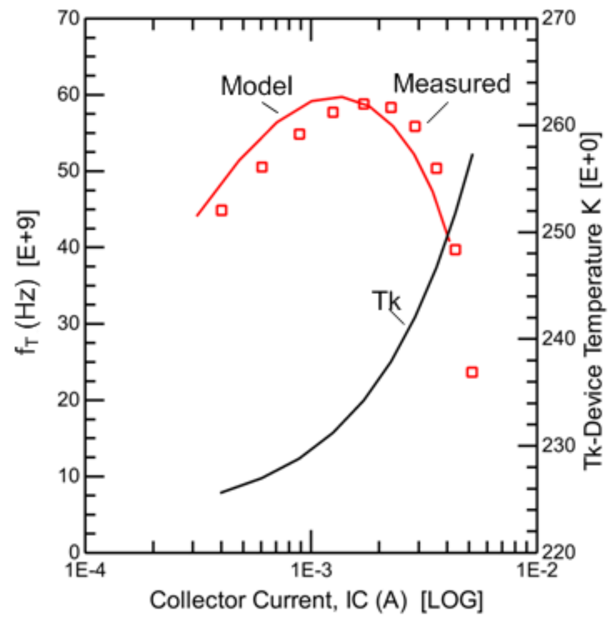

Figure 8.51 SET Model Simulation vs. Gummel Measurement, 223K. Left axis: f_T vs. Log(IC). Symbols are measured data and solid line is simulated results. Right axis: Device Temperature, Tk..

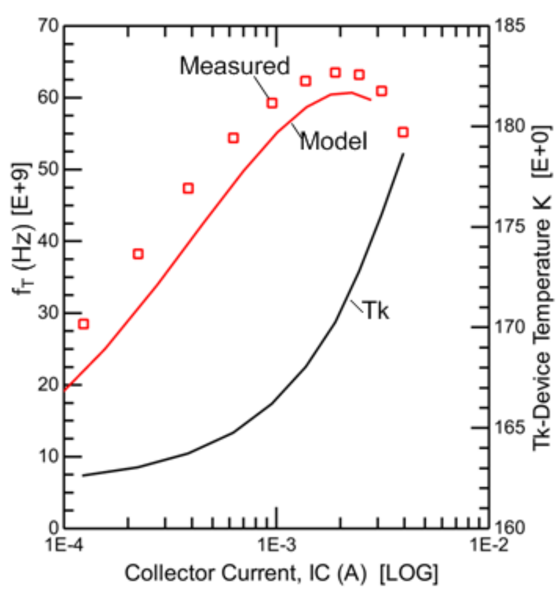

Figure 8.52 SET Model Simulation vs. Measurement, 162K. Left axis: f_T vs. Log(IC). Symbols are measured data and solid line is simulated results. Right axis: Device Temperature, Tk.

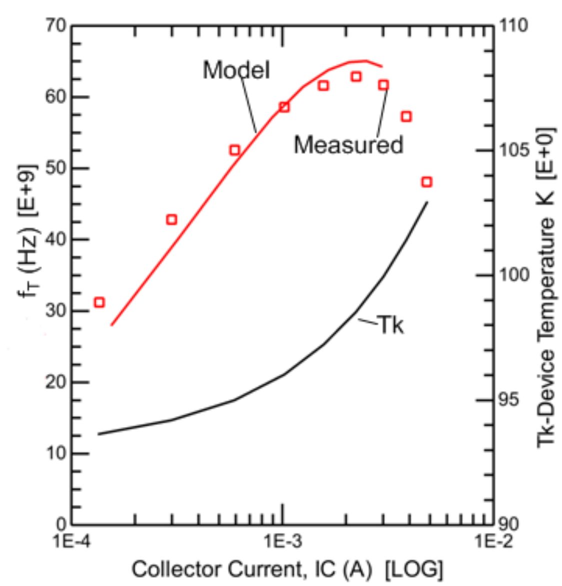

Figure 8.53 SET Model Simulation vs. Measurement, 93K. Left axis: f_T vs. Log(IC). Symbols are measured data and solid line is simulated results. Right axis: Device Temperature, Tk..

All four temperature simulations of the SET model represented the f_T characteristics reasonably well. The SET model fit of f_T at each ambient temperature point was very similar to the ambient model fits in Chapter 7. The peak f_T was fitted well as temperature decreased. The challenge to both the SET models and the ambient temperature models was the rapid f_T rolloff in the high current injection region. This fitting problem corresponds to the limits of fitting the DC current gain rolloff in the high level injection region. The rapid rolloff of current gain at 93K is attributed to heterojunction barrier effects in the SiGe HBT device [52].

Overall, the SET model succeeds in fitting the DC and AC characteristics in the linear operation region. The SET model is able to accurately represent the SiGe HBT model over the full output operating region. Quasi-saturation, significant Early voltage effects and non-linear collector current behavior at the upper VCE voltage range are well represented with the SET model and parameter set from the 300K to 93K.

8.6 Circuit Simulation with SET models

A preliminary circuit design simulation using multiple placements of the SET HBT model was evaluated to determine how well the SET model performed in a complex simulation environment. In this initial analysis, testing for non-convergence instances over the wide temperature range was the primary concern. Therefore, DC and AC simulations at the upper and lower limit of the temperature range were performed. Also, an assessment of the circuit simulation performance at these temperatures was evaluated.

The circuit simulation chosen was a video differential amplifier based on the classic UA733 differential amplifier [58]. The frontend stage of a UA733 simulated with the SET model was composed of a differential input amplifier with a pair of emitter follower output drivers as shown in Figure 8.54. The resistance value of the mirror reference resistor of 2005Ω was chosen to bias the differential input at approximately 2mA. Thus, 1mA is the optimal f_T bias point for each of the differential transistors. The Q1 and Q2 quiescent collector bias potential was set at 2.5V with the input swinging symmetrically about ground. At 300K, the output swing is about 0.75V as shown in Figures 8.55 and 8.56. At this output voltage the quiescent output current of the drivers is 1.2mA each.

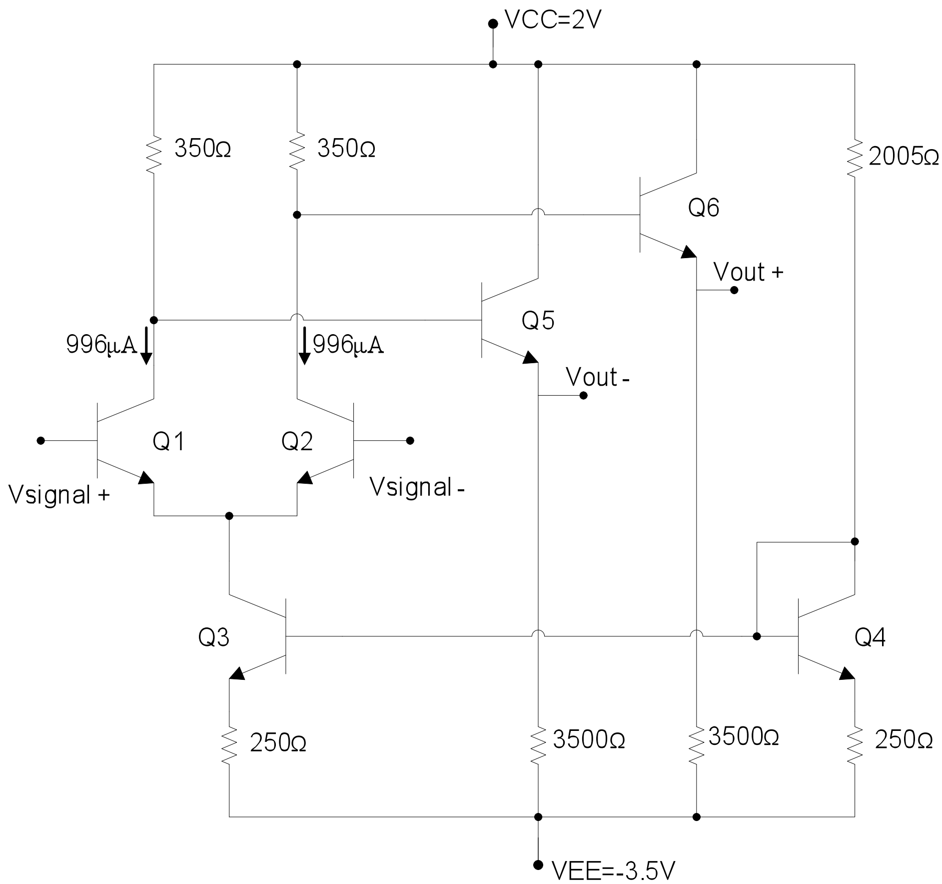

Figure 8.54 Video Differential Amplifier with SET Models

All simulations showed no non-convergence or discontinuity in the video differential amplifier with 6 single expansive temperature, SET, models and 7 bias resistors at either the DC or AC simulations. The DC transfer curves at each temperature, 300K and 93K, were symmetrical as shown in Figures 8.55, 8.56, 8.59 and 8.60. The transfer range of a ±60mV input differential signal is summarized in Table 8.35.

	DC Transfer Simulation PP Vsignal -60mV to 60mV	
	300K	93K
Vout-	1.07V to 0.46V	0.92V to 0.25V
Vout+	0.46V to 1.07V	0.25V to 0.92V

Table 8.35 Summary of DC and AC simulated performance of Video Differential Amplifier with SET Models

The AC voltage gain at 300K was 7.5 and with a -3dB=10 GHz as shown in Figure 8.XX. The 300K phase is plotted in Figure 8.XX. The simulation is agreement with the standard design rule of thumb that the -3dB point is approximately 20% of the SiGe HBT, f_T, 50 GHz at 300K.

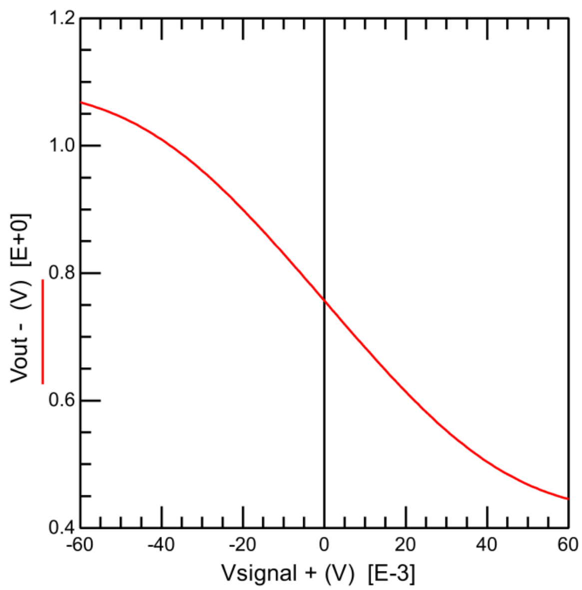

Figure 8.55 Transfer curve of Vout-, at 300K

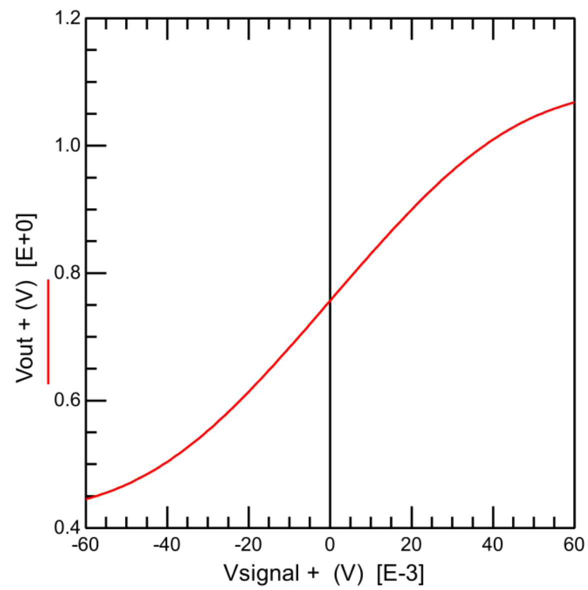

Figure 8.56 Transfer curve of Vout +, at 300K

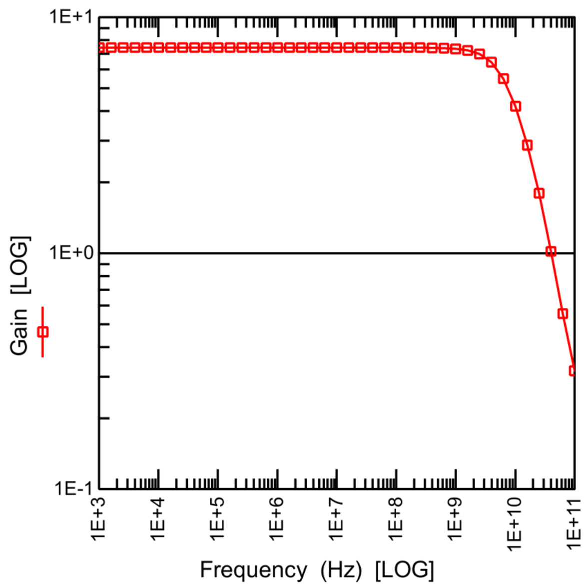

Figure 8.57 AC Voltage Gain, at 300K

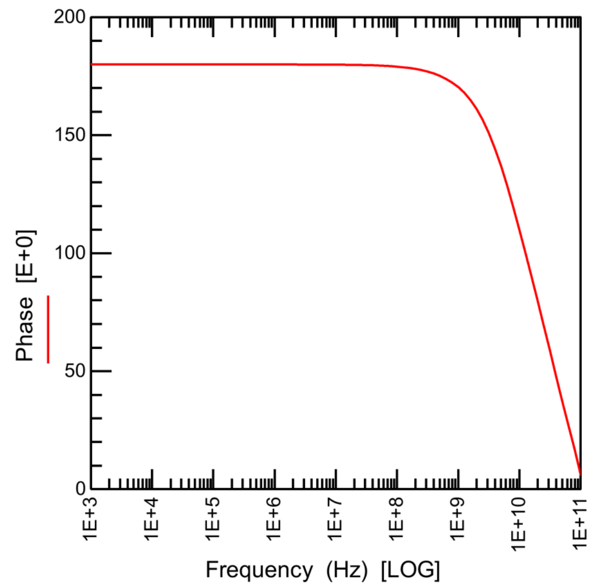

Figure 8.58 Phase, at 300K

The simulation at 93K, had a AC voltage gain of 12 and -3dB=10 GHz as shown in Figure 8.61 and the phase is plotted in Figure 8.62.

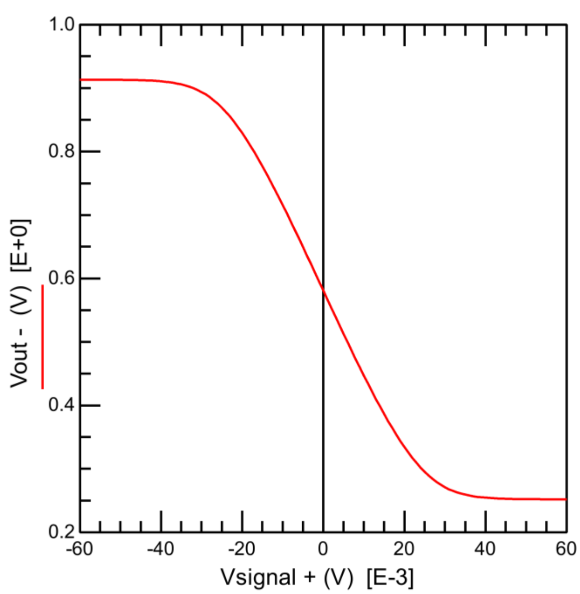

Figure 8.59 Transfer curve of Vout-, at 93K

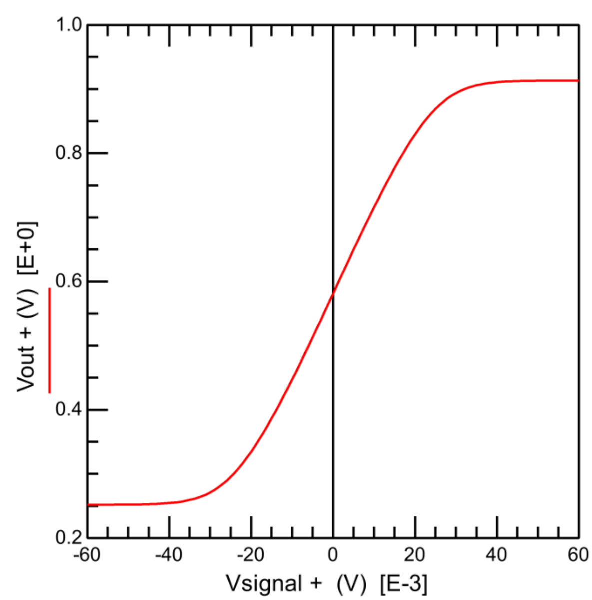

Figure 8.60 Transfer curve of Vout+, at 93K

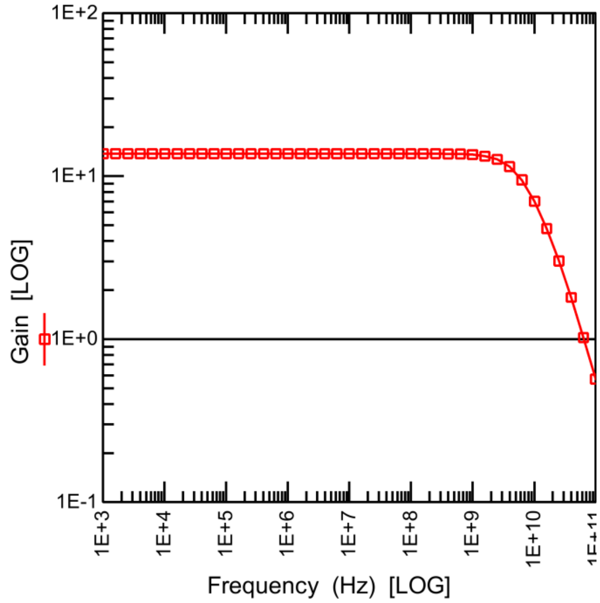

Figure 8.61 AC Voltage Gain, at 93K

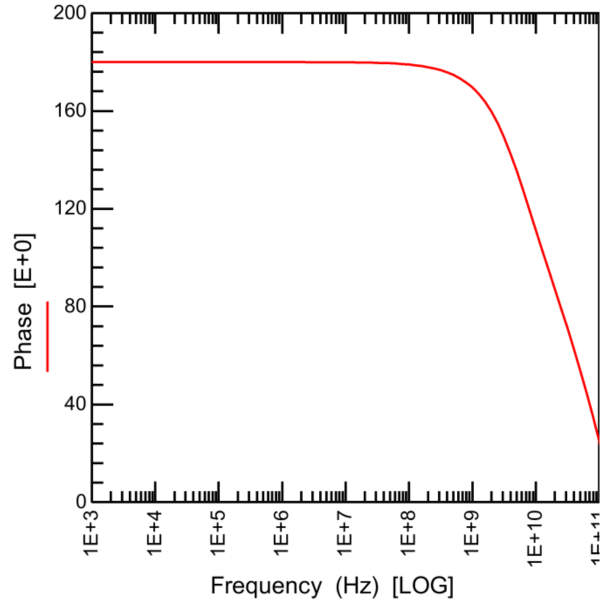

Figure 8.62 Phase, at 93K

9 Summary and Future Work

The goal of this dissertation was to create a compact SiGe HBT model that represents the DC and AC behavior over an expansive temperature range. The temperature range of this project is from 300K, room temperature to 93K, cryogenic temperature. Therefore, a single expansive temperature, SET, model was created, capable of representing the full forward operating range of the DC output characteristics, the wide dynamic current range of the Gummel linear operating region, and the AC response of the device.

The standard Mextram 504.7 bipolar model has advanced technology features which were needed in successfully modeling the device electrical performance over the complete expanded temperature range. Mextram features utilized for the SiGe HBT included the: SiGe current equations, intrinsic and extrinsic region distinctions and the voltage bias dependence on forward and reverse Early effects. The Mextram 504.7 release also included a separation of the buried collector resistance from the external collector contact resistance. This resistance separation is designed to improve the f_T response in the high level injection region.

The development of the single compact bipolar model and parameter set which represented electrical performance over a wide temperature range was divided into two parts.

1^{st} Part - The standard Mextram 504.7 model was modified to function correctly at ambient temperatures, "at temperature," in the cryogenic temperature range. This research effort created the modified model, CRYO_504.7, used to develop model parameters values at four ambient temperature points: 300K, 223K, 162K and 93K. Each model parameter group had a model temperature, TREF, equal to the simulated ambient temperature, $T_{Ambient}$. The four ambient temperature models/parameter groups were created by developing new parameter extraction techniques.

2^{nd} Part – The SET model was developed by modifying and creating parameter temperature equations to represent the expansive temperature range in the modified model, CRYO_504.7. The ambient temperature model parameter sets provided the parameter response over the full temperature range. The final SET parameter temperature equations and parameter values were derived through a combination of parameter optimizations and equation fitting of the ambient parameters.

9.1 Accomplishments

9.1.1 1^{st} Part. Development of the Mextram 504.7 cryogenic version model and four ambient temperature model parameter value groups

Four, "at temperature", ambient temperature model parameter groups were developed and fitted to measured data with the cryogenic temperature Mextram model, CRYO_504.7. DC and AC over-temperature measurements of the SiGe HBT single device were provided by Georgia Tech. The packaged DC device modeling structure was measured in a cryostat environment and the AC device modeling structure was measured on-wafer in a custom cryogenic probe station. Dr. John Cressler's research group took all measurements at the Georgia Tech lab in Atlanta, Georgia.

It was discovered that the standard Mextram 504.7 model was incapable of operating correctly at cryogenic temperatures. A modified version, CRYO_504.7, was created which expanded the numerical abilities of the standard Mextram model. It was discovered that the standard Mextram model was unable to generate current when the model temperature, TREF, or the simulated ambient temperature, $T_{Ambient}$ were less than 145 ^{o}C. Also, non-ideality factor model parameters were added to current equations with exponential relationships to junction voltages.

The unique, ambient temperature model parameter sets were extracted to accurately represent the complete the full collector-emitter voltage range from 0 to 3.5V of the SiGe HBT. SiGe HBT models were developed which accurately represented the full DC output characteristics operation region which ranged from room temperature, 300K, down to 93K, the lowest measured cryogenic ambient temperature. The DC performance of the full output operating range was correctly represented in all four ambient temperature models. The model accurately represented the saturation region, quasi-saturation region, the linear region, and nonlinear behavior of the upper voltage range of the output characteristics. The models also accurately represented the linear operating regions of the DC Gummel measurements and the AC small signal response of the cutoff frequency, f_T versus collector current. Accurate modeling of the full DC output characteristics voltage range at cryogenic temperatures has not been demonstrated before.

New parameter extraction approaches were developed to support the cryogenic temperature modeling. Parameter optimizations were typically more successful as the ambient temperatures decreased than parameter calculations based on physical process relationships used in the standard Mextram extraction routines. The self-heating effects of the small active area SiGe HBT model were extremely high at 300K. The thermal resistance at 300K was greater than 5000Ω. The self-heating effects decreased as temperature decreased. Therefore, an accurate model of the self-heating contributions had to be included in all ambient temperature parameter extractions. Otherwise parameter values would be a combination of operating effects and self-heating effects. The self-heating model and parameters were initially fitted and all parameters extractions were derived based on simulations which included the self-heating contribution.

Two new parameters, the forward and reverse non-ideality factors, were added to the standard Mextram 504.7 model to adjust the exponential relationship between current and junction voltages as ambient temperatures decreased. Non-ideality factors were common in previous bipolar models for the representation of process properties and limitations. However, in the standard Mextram model the non-ideality factors were discontinued as bipolar processing capability improved. The return of non-ideality factors for cryogenic bipolar modeling has been implemented by at least two other research groups [59],[60] In the approach taken by one research group, an equation for NF over temperature was accurate for the mid-level injection region and collector currents of approximately 1uA. At higher current levels, where the HBT is more typically operated, 100uA to 2mA, the accuracy of the collector current fit decreases. This, causes over compensation in other parameter extractions, such as the intrinsic base resistance of over 10,000 ohms at 93K and the variable epilayer collector resistance of approximately 10,000 ohms at 93K.

The forward non-ideality factor, NF, was found to be a dominant parameter with a strong influence on parameters typically extracted in the mid-level and high-level injection regions of the Gummel measurement. Therefore, extraction techniques were developed to optimize the mid-level and high injection parameters in synchronization with NF. NF was extracted accurately from the collector current in the Gummel measurement by individually defining the optimum mid-level injection region where it was a primary influence.

The tremendous importance of the reverse non-ideality factor, NR, in parameter extraction was discovered during optimization of the DC output characteristics, saturation region. A non-real collector-emitter voltage offset was present in the model simulations when NR was undefined in the current voltage relationship equations involving the base-collector junctions. Through optimization it was determined that the value of NR must be of equal value to NF to eliminate current inaccuracy and voltage offsets in the saturation region. Therefore, the numerical values of NF and NR were accurately determined at each temperature.

New extraction techniques were developed for parameters which were influential in the AC response and in the high current region. New parameter interactions at cryogenic temperatures were found during AC modeling through optimization. It was discovered that the addition of non-ideality factors for DC characteristics at cryogenic temperatures caused the model's AC small-signal current gain response to decrease drastically. As NF and NR increased in value above one, the parameters which typically influenced AC gain became unresponsive. The emitter diffusion charge branch, Q_E, is a major contributor to total transit time and therefore the frequency response of the small-signal current gain. Q_E is derived by calculating the emitter hole density. It was found that the inclusion of non-ideality factors modified the electron density of current equations without equally adjusted the emitter charge contribution. Custom parameter optimization of the emitter charge non-ideality factor parameter, MTAU, was found to provide accurate AC small signal current gain response at cryogenic temperatures. The standard parameter extraction methods relied on physical relationships based on process technology information and simple direct data extractions which became inaccurate as the ambient temperatures decreased. Custom optimization of the electrical performance as ambient temperatures decreased were found to be the more successful method of extracting model parameter sets.

Accurate model fits of the DC output characteristics at cryogenic temperature were accomplished by using the SiGe bandgap voltage contribution to Early effects, parameter DEG, in the base charge equations. However, the influence of SiGe effects on the base is not physically relatable to other Mextram parameters. A new extraction technique was created using the model's internal variables to determine the interaction or optimum values for the SiGe parameter, DEG, and the parameters representing current, gain, and Early effects. The parameters were optimized to the response of the normalized base charge, q_B, and transfer current variables, I_f and I_r. Monitoring the internal variables provided the control needed to accurately fit the measured output characteristics of collector current as a function of collector-emitter voltage.

The accuracy of the ambient temperature models was critical to creating the SET model temperature equations. The four ambient temperature parameter groups were optimized with the same unique approaches, but customization to the changing performance behavior at each temperature.

9.1.2 2nd Part. A single expansion temperature, SET, model and parameter set created for a SiGe HBT operating over a wide temperature range

The objective of this work was completed with the creation of the single expansive temperature, SET, model. This new version of Mextram 504.7 is capable of representing the full operating range of the SiGe HBT modeled over a wide and extreme temperature range. The SET model parameter groups for this small area SiGe HBT was extracted to produce a good fit to measured data across the wide cryogenic temperature range. The SET model, combined with the extracted SET model parameter set was successful in representing the electrical behavior of IBM5AM (0.5μm x 2.5μm) high performance SiGe HBT from room temperature, 300K, to the cryogenic temperature of 93K.

This single expansive temperature model was designed to represent the all operating regions of the DC output characteristics for the SiGe HBT over temperature. The SET model represents the HBT from VCE=0V through saturation, quasi-saturation, and linear operating regions, up to the breakdown region of VCE=3.5V. The upper limit voltage of 3.5V was selected to maintain a 50% limit of maximum linear region collector current, thereby avoiding damage to the small area HBT device. The SET model reference temperature is 300K and through the model parameter temperature equations it is able to simulate DC and AC performance down to 93K.

The advanced technology features of the standard Mextram 504.7 model require a total of 78 model parameters of which 30 model parameters shift with temperature. In the standard 504.7 model, these 30 parameters have parameter temperature shifting equations. There are a total of 17 temperature model parameters that are shared by the 30 parameter temperature equations. The standard 504.7 approach was to minimize the number of temperature parameters. The SET model created is a modified version of the industry standard Mextram 504.7 bipolar model but with a significantly less temperature parameters sharing.

The SET model temperature equations and parameter values were developed by comparing each model parameter's response in the four ambient temperature models with the corresponding standard 504.7 parameter temperature equation results. Often the ambient model parameter response indicated that modification or new temperature equations were required for wide temperature ranges. It was determined that sharing temperature parameters among electrical model parameters was not accurate for simulations over expansive temperature ranges.

It was found that 36 model electrical parameters shifted with temperature across the wide and extreme temperature range. This was at odds with the standard Mextram 504.7 model that only supported 30 electrical parameters with temperature equations. For the SET model, 30 new model temperature parameters were created to provide more individual control of the parameter temperature shifting. Of the 36 model electrical parameters that shifted with temperature in the expansive temperature range, 18 model parameters were found to shift according standard temperature equations using the existing temperature parameters. An additional 9 model parameters required new temperature coefficient parameters in the existing temperature equation to allow unique parameter control of temperature shifting. Also, 5 model parameters required both new temperature equations and new temperature parameters to support parameter response to temperature. An finally, there were 4 model parameters which had been defined in the standard 504.7 model as temperature independent were found to shift with temperature across the much wider and colder temperature range of the SET model. Temperature equations and temperature parameters were created to define these new parameter temperature relationships.

The development of additional temperature parameters and modifications of the standard Mextram 504.7 parameter temperature equation in the SET model provided the freedom needed to model bipolar transistors, particularly SiGe HBT over a wider temperature range. The total number of model parameters rose to 110 for the SET model from the original standard 504.7 model total number of 78. The parameter extraction techniques were developed for the SiGe HBT, SET model parameter through a combination of optimization and analysis of the ambient temperature model parameter sets.

The DC and AC model fits to measured data of the SET model and parameter set clearly indicate the capability of this new version of Mextram for use in expansive temperatures ranges at cryogenic temperatures. The DC output characteristics results were accurate across all regions and temperature. The 93K output characteristics were more difficult to fit at the highest base current bias levels due to high level injection current gain rolloff. The DC Gummel characteristics represent a large dynamic collector current range in the linear operating region. The SET model total RMS error across the Gummel collector current range only varied from 8% at 300K to 13% at 93K. The SET model AC response across the expansive temperature range, fit well with measurements in the f_T versus collector current behavior. So in conclusion, modeling of the SiGe heterojunction bipolar transistor electrical performance over expansive temperature ranges at cryogenic temperatures is possible through the use of this new single expansive temperature, SET, model.

9.2 Future Research Suggestions

The sharp and rapid rolloff of current gain and f_T at high-level injection collector current is attributed to heterojunction barrier effects that are inherit to SiGe HBT's. This effect became more severe at temperatures below 223K. The capability is currently not present in the Mextram model to represent this behavior. Future work to accurately modeling the DC and AC performance rolloff at high-level carrier injection would greatly benefit cryogenic bipolar modeling.

The quasi-saturation region of the DC output characteristics is complex. The collector epilayer current equations in the quasi-saturation region were found to become less responsive to parameter optimization in the cryogenic temperature range. The reverse Early voltage effects became more dominating in the saturation and quasi-saturation as temperature decreased. Future work could include investigating the relationship of the collector epilayer model and the Early voltage effects in the SiGe HBT as temperature decreases.

The focus of this work was on a minimum sized active area device. The area and periphery relationships between intrinsic and extrinsic regions of a small structure tend to be skewed. Future work might include applying the SET model approach of a modified Mextram model to larger area devices or arrayed devices. The standard physical relationships are more likely to apply and possibly a less intense optimization approach would work well. The circuit applications for very small area SiGe HBT's are limited as compared to the larger area SiGe

HBT's. The accuracy available with the SET model temperature equations could improve the modeling capability of other HBT types for extreme temperature circuit applications.

The model exhibited no convergence problems in the DC and AC simulations of the modeling test structure configurations during model development. However, convergence issues are a common problem in cold temperature circuit simulations in the commercial temperature range. As the simulation temperatures decreases into the cryogenic temperature range these convergence issues are exacerbated. Possible future work could include applying the SiGe HBT to complex circuit configurations to evaluate the convergence issues of cryogenic bipolar models and bipolar circuits operating at cryogenic temperatures.

References

[1] J. D. Cressler, "Using SiGe HBT technology for extreme environment electronics," in *Bipolar/BiCMOS Circuits and Technology Meeting, 2005. Proceedings of the,* 2005, pp. 248-251.

[2] Delft University of Technology, "Mextram Level 504.7 Code," http://mextram.ewi.tudelft.nl/, 2012.

[3] "IBM Specialty Foundry SiGe BiCMOS " IBM, 2012.

[4] J. Dunn, D. L. Harame, A. J. Joseph, S. A. St. Onge, N. B. Feilchenfeld, L. Lanzerotti, B. Orner, E. Gebreselasie, J. B. Johnson, D. D. Coolbaugh, R. Rassel and M. Khater, "SiGe BiCMOS trends - today and tomorrow," in *Custom Integrated Circuits Conference, 2006. CICC '06. IEEE,* 2006, pp. 695-702.

[5] O. Kegege, M. Barlow, A. Mantooth and R. Ulrich, "Mission optimization and tradeoffs of using SiGe based electronics for a cryogenic environment rover mission," in *Aerospace Conference, 2010 IEEE,* 2010, pp. 1-6.

[6] B. O. Woods, H. A. Mantooth and J. D. Cressler, "SiGe HBT compact modeling for extreme temperatures," in *Semiconductor Device Research Symposium, 2007 International,* 2007, pp. 1-2.

[7] "IBM SiGE 5AM BiCMOS process," IBM, Inc, 2004.

[8] D. L. Harame, E. F. Crabbe, J. D. Cressler, J. H. Comfort, J. Y. -. Sun, S. R. Stiffler, E. Kobeda, J. N. Burghartz, M. M. Gilbert, J. C. Malinowski, A. J. Dally, S. Ratanaphanyarat, M. J. Saccamango, W. Rausch, J. Cotte, C. Chu and J. M. C. Stork, "A high performance epitaxial SiGe-base ECL BiCMOS technology," in *Electron Devices Meeting, 1992. IEDM '92. Technical Digest., International,* 1992, pp. 19-22.

[9] J. D. Cressler, "Everything you always wanted to know about the SiGe HBT... but were afraid to ask," in *Bipolar/BiCMOS Circuits and Technology Meeting Short Course Notes,* Minneapolis, MN, 1999.

[10] I. E. Getreu, *Modeling the Bipolar Transistor.* Beaverton, Or: Tektronix, 1979.

[11] P. Ashburn, *SiGe Heterojunction Bipolar Transistors.* Hoboken, NJ: John Wiley & Sons, 2003.

[12] J. M. Early, "Effects of Space-Charge Layer Widening in Junction Transistors," *Proceedings of the IRE,* vol. 40, pp. 1401-1406, 1952.

[13] J. C. J. Paasschens, W. J. Kloosterman and R. van der Toorn, *Model Derivation of Mextram 504: The Physics Behind the Model.* Koninklijke Philips Electronics N.V., 2005.

[14] C. T. Kirk Jr., "A theory of transistor cutoff frequency (fT) falloff at high current densities," *Electron Devices, IRE Transactions on,* vol. 9, pp. 164-174, 1962.

[15] G. M. Kull, L. W. Nagel, Shiuh-Wuu Lee, P. Lloyd, E. J. Prendergast and H. Dirks, "A unified circuit model for bipolar transistors including quasi-saturation effects," *Electron Devices, IEEE Transactions on,* vol. 32, pp. 1103-1113, 1985.

[16] J. C. J. Paasschens, W. J. Kloosterman and R. J. Havens, *Parameter Extraction for the Bipolar Transistor Model Mextram Level 504.* Koninklijke Philips Electronics N.V., 2001.

[17] J. J. Ebers and J. L. Moll, "Large-Signal Behavior of Junction Transistors," *Proceedings of the IRE,* vol. 42, pp. 1761-1772, 1954.

[18] H.K. Gummel and H.C. Poon, "An integral chrage control model of bipolar transistors," *Bell Sys. Techn. J.,* vol. May-June, pp. 827-825, 1970.

[19] D. L. Harame and B. S. Meyerson, "The early history of IBM's SiGe mixed signal technology," *Electron Devices, IEEE Transactions on,* vol. 48, pp. 2555-2567, 2001.

[20] P. R. Gray, *Analysis and Design of Analog Integrated Circuits.* New York: Wiley, 2009.

[21] D. L. Harame, J. H. Comfort, J. D. Cressler, E. F. Crabbe, J. Y. Sun, B. S. Meyerson and T. Tice, "Si/SiGe epitaxial-base transistors. I. Materials, physics, and circuits," *Electron Devices, IEEE Transactions on,* vol. 42, pp. 455-468, 1995.

[22] J. C. J. Paasschens, W. J. Kloosterman, R. J. Havens and H. C. De Graaff, "Improved modeling of output conductance and cut-off frequency of bipolar transistors," in *Bipolar/BiCMOS Circuits and Technology Meeting, 2000. Proceedings of the 2000,* 2000, pp. 62-65.

[23] P. Ashburn, D. J. Roulston and C. R. Selvakumar, "Comparison of experimental and computed results on arsenic- and phosphorus-doped polysilicon emitter bipolar transistors," *Electron Devices, IEEE Transactions on,* vol. 34; 34, pp. 1346-1353, 1987.

[24] L. E. Kay and T. Tang, "Monte Carlo calculation of strained and unstrained electron mobilities in Si1-xGex using an improved ionized-impurity model," *J. Appl. Phys.,* vol. 70, pp. 1483, 8, 1991.

[25] D. L. Harame, J. H. Comfort, J. D. Cressler, E. F. Crabbe, J. Y. Sun, B. S. Meyerson and T. Tice, "Si/SiGe epitaxial-base transistors. II. Process integration and analog applications," *Electron Devices, IEEE Transactions on,* vol. 42, pp. 469-482, 1995.

[26] B. El-Kareh, S. Balster, W. Leitz, P. Steinmann, H. Yasuda, M. Corsi, K. Dawoodi, C. Dirnecker, P. Foglietti, A. Haeusler, P. Menz, M. Ramin, T. Scharnagl, M. Schiekofer, M. Schober, U. Schulz, L. Swanson, D. Tatman, M. Waitschull, J. W. Weijtmans and C. Willis, "A 5V complementary-SiGe BiCMOS technology for high-speed precision analog circuits," in

Bipolar/BiCMOS Circuits and Technology Meeting, 2003. Proceedings of the, 2003, pp. 211-214.

[27] R. Payne, M. Corsi, D. Smith, Tien-Ling Hsieh and S. Kaylor, "A 16-Bit 100 to 160 MS/s SiGe BiCMOS Pipelined ADC With 100 dBFS SFDR," *Solid-State Circuits, IEEE Journal of,* vol. 45, pp. 2613-2622, 2010.

[28] D. L. Harame, D. C. Ahlgren, D. D. Coolbaugh, J. S. Dunn, G. G. Freeman, J. D. Gillis, R. A. Groves, G. N. Hendersen, R. A. Johnson, A. J. Joseph, S. Subbanna, A. M. Victor, K. M. Watson, C. S. Webster and P. J. Zampardi, "Current status and future trends of SiGe BiCMOS technology," *Electron Devices, IEEE Transactions on,* vol. 48, pp. 2575-2594, 2001.

[29] L. Nagel, "SPICE2: A computer program to simulate semiconductor circuits," University of California, Berkeley, Tech. Rep. Memorandum No. ERL-M520, May, 1975.

[30] J. L. Moll and I. M. Ross, "The Dependence of Transistor Parameters on the Distribution of Base Layer Resistivity," *Proceedings of the IRE,* vol. 44, pp. 72-78, 1956.

[31] H. C. de Graaff and W. J. Kloosterman, "New formulation of the current and charge relations in bipolar transistor modeling for CACD purposes," *Electron Devices, IEEE Transactions on,* vol. 32, pp. 2415-2419, 1985.

[32] M. Schroter and H. -. Rein, "Investigation of very fast and high-current transients in digital bipolar IC's using both a new compact model and a device simulator," *Solid-State Circuits, IEEE Journal of,* vol. 30, pp. 551-562, 1995.

[33] C. C. McAndrew, J. A. Seitchik, D. F. Bowers, M. Dunn, M. Foisy, I. Getreu, M. McSwain, S. Moinian, J. Parker, D. J. Roulston, M. Schroter, P. van Wijnen and L. F. Wagner, "VBIC95, the vertical bipolar inter-company model," *Solid-State Circuits, IEEE Journal of,* vol. 31, pp. 1476-1483, 1996.

[34] R. van der Toorn, J. C. J. Paasschens and W. J. Kloosterman, *The Mextram Bipolar Transistor Model Level 504.7.* Delft University of Technology, 2008.

[35] J. C. J. Paasschens, W. J. Kloosterman and R. J. Haven, *Parameter Extraction for the Bipolar Transistor Model Mextram Level 504.* Koninklijke Philips Electronics N.V., 2001.
[36] Compact Modeling Council, http://www.gias.org/index.asp, 2012.

[37] M. Schroter, "Hicum model definition," http://www.iee.et.tu-dresden/de/iee/eb/hic_new/hic_intro.html, 2012

[38] P. Deixler, H. G. A. Huizing, J. J. T. M. Donkers, J. H. Klootwijk, D. Hartskeerl, W. B. de Boer, R. J. Havens, R. van der Toorn, J. C. J. Paasschens, W. J. Kloosterman, J. G. M. van Berkum, D. Terpstra and J. W. Slotboom, "Explorations for high performance SiGe-heterojunction bipolar transistor integration," in *Bipolar/BiCMOS Circuits and Technology Meeting, Proceedings of the 2001,* 2001, pp. 30-33.

[39] D. B. M. Klaassen, "A unified mobility model for device simulation—I. Model equations and concentration dependence," *Solid-State Electronics,* vol. 35, pp. 953-959, 7, 1992.
[40] A. G. Chynoweth, "Ionization Rates for Electrons and Holes in Silicon," *Physical Review,* vol. 109, pp. 1537-1540, 1958.

[41] J. C. J. Paasschens, W. J. Kloosterman and R. van der Toorn, *The Mextram Bipolar Model Level 504.6.* Koninklijke Philips Electronics N.V., 2005.

[42] D. B. M. Klaassen, "A unified mobility model for device simulation—II. Temperature dependence of carrier mobility and lifetime," *Solid-State Electronics,* vol. 35, pp. 961-967, 7, 1992.

[43] M. Mierzwinski, P. O'Halloran and B. Troyanovsky, "Developing and releasing compact models using verilog-A," in 2008.

[44] Agilent Technologies Inc, "IC-CAP, Device Modeling Software," http://www.home.agilent.com/en/pc-1297149/ic-cap-device-modeling-software-measurement-control-and-parameter-extraction?nid-34268.0.00&cc=US&Ic=eng, 2012.

[45] Agilent Technologies Inc, "ADS, Advanced Design System, Software," http://www.home.agilent.com/en/pc-1297113/advanced-design-system-ads, 2012.

[46] NASA Exploration Technology Development Program, http://www.nasa.gov/exploration/technology/, 2012.

[47] J. D. Cressler, "Silicon-germanium as an enabling IC technology for extreme environment electronics," in *Aerospace Conference, 2008 IEEE,* 2008, pp. 1-7.

[48] F. Sischka, "The ICCAP characterization basics handbook," Agilent Technologies, Inc, Munich, Germany, Tech. Rep. 18.10.00, 2000.

[49] "Calibration tools: Achieving consistent parameter extraction for advanced RF devices," Cacade Microtech, Inc, Beaverton, OR, Tech. Rep. CALTOOL-AN-0612, 2012.

[50] "S-parameter design," Agilent Technologies, Inc, Tech. Rep. AN 154, 2006.

[51] G. Gonzalez, *Microwave Transistor Amplifiers : Analysis and Design.* Englewood Cliffs, N.J: Prentice-Hall, 1984.

[52] J. D. Cressler and N. Guofu, *Silicon-GermaniumHeterojunction Bipolar Transistors.* Norwood, MA: Artech House, Inc, 2003.

[53] R. van der Toorn, J. J. Dohmen and O. Hubert, "Distribution of the collector resistance of planar bipolar transistors: Impact on small signal characteristics and compact modeling," in *Bipolar/BiCMOS Circuits and Technology Meeting, 2007. BCTM '07. IEEE,* 2007, pp. 184-187.

[54] J. C. J. Paasschens and R. van der Toorn, *Introduction to and Usage of the Bipolar Transistor Model Mextram.* Koninklijke Philips Electronics N.V., 2002.

[55] Jae-Sung Rieh, K. M. Watson, F. Guarin, Zhijian Yang, Ping-Chuan Wang, A. J. Joseph, G. Freeman and S. Subbanna, "Reliability of high-speed SiGe heterojunction bipolar transistors under very high forward current density," *Device and Materials Reliability, IEEE Transactions on,* vol. 3, pp. 31-38, 2003.

[56] J. Rieh, J. Johnson, S. Furkay, D. Greenberg, G. Freeman and S. Subbanna, "Structural dependence of the thermal resistance of trench-isolated bipolar transistors," in *Bipolar/BiCMOS Circuits and Technology Meeting, 2002. Proceedings of the 2002,* 2002, pp. 100-103.

[57] J. Rieh, D. Greenberg, B. Jagannathan, G. Freeman and S. Subbanna, "Measurement and modeling of thermal resistance of high speed SiGe heterojunction bipolar transistors," in *Silicon Monolithic Integrated Circuits in RF Systems, 2001. Digest of Papers. 2001 Topical Meeting on,* 2001, pp. 110-113.

[58] *Fairchild Linear Integrated Circuits Data Book.* Fairchild, Inc, 1971.

[59] J. C. Bardin, "Silicon-Germanium Heterojunction Bipolar Transistors for Extremely Low-Noise Applications," *Ph. D Dissertation,* 2009.

[60] Lan Luo, Ziyan Xu, Guofu Niu, P. S. Chakraborty, Peng Cheng, D. Thomas, K. Moen, J. D. Cressler, M. Mudholkar and H. A. Mantooth, "Wide temperature range compact modeling of SiGe HBTs for space applications," in *System Theory (SSST), 2011 IEEE 43rd Southeastern Symposium on,* 2011, pp. 110-113.

Appendix A: Glossary

Physical constants and transistor physics terms:

q	Magnitude of electron charge, (C)
k	Boltzmann constant (eV/K)
T	Temperature (K)
W_B	Intrinsic base width of quasi-neutral base at bias (nm)
W_E	Neutral emitter width (nm)
W_C	Base-collector depletion region width (nm)
A_E	Active emitter area (um^2)
N_{dE}	Electron donor concentration in the emitter (cm^{-3})
D_{pE}	Diffusion coefficient of holes in the emitter (cm^2/s)
N_C	Constant density of states in the conduction band of Si (cm^{-3})
N_V	Constant density of states in the valence band of Si (cm^{-3})
$\bar{N}_C$	Average density of states in the conduction band of SiGe (cm^{-3})
$\bar{N}_V$	Average density of states in the valence band of SiGe (cm^{-3})
D_{nB}	Constant diffusion coefficient of electrons in the base of Si (cm^2/s)
$\bar{D}_{nB}$	Average diffusion coefficient of electrons in the base of SiGe (cm^2/s)
N_{aB}	Hole concentration in the neutral base, constant base doping assumed(cm^{-3})
x	Position in the base, the emitter side is 0 and W_B is the collector side (nm)
$N_{AB}(x)$	Doping concentration as a function of distance, x, within the base (cm^{-3})
$D_{nB}(x)$	Diffusion coefficient as function of distance, x, within the base (cm^2/s)
$n_{iB}(x)$	Intrinsic carrier concentration as a function of distance, x, within the base (cm^{-3})
n_{i0}	Intrinsic carrier concentration of the undoped Si base (cm^{-3})
ΔE_{gb}	Bandgap narrowing due to heavy doping in the emitter (eV)
Q_B	Charge of the intrinsic base region
Q_E	Charge of the emitter region
Q_C	Charge of the base-collector depletion region
v_{sat}	Base-collector saturation drift velocity due high electric field (cm/s)

SiGe bandgap terms:

$\Delta E_{g,Ge}$(grade)	total Germanium influenced bandgap narrowing across neutral base region:
$\Delta E_{g,Ge}(x=0)$	Germanium influenced bandgap narrowing at the emitter- neutral base interface.
$\Delta E_{g,Ge}(x=W_b)$	Germanium influenced bandgap narrowing at the neutral base-collector interface.

Collector, epilayer collector, knull theory and physical terms:

VBC(external)	External base-collector voltage, VBC, defined as nodes B and C. Total voltage is the sum of the base-collector junction voltage and the voltage drops across the various collector regions
VBC(internal)	Internal base-collector junction voltage, V_{B2C2}, between metallurgical interface of base and N- collector epilayer, defined at nodes B2 and C2
R_{epi}	N^- collector epilayer variable resistance. Voltage drop, V_{C1C2}, is due to R_{epi}.
R_{buried}	N^+ buried collector constant resistance. Voltage drop $V_{C1C}$is due to R_{buried}.
W_{epi}	Total thickness of the N^- collector epilayer
x=0	Base-collector epilayer interface, the epilayer edge is referenced to 0
$x=W_{epi}$	Interface of the N- epilayer collector layer and N+ buried collector layer, the end of the epilayer and defined as W_{epi}
N_{epi}	Effective collector epilayer doping concentration
n_i	Collector intrinsic concentration
$x=x_i$	Injection layer thickness measured from the base-collector interface into the N^- epilayer
p_0	Hole density at base/collector epilayer interface, normalized with respect to N_{epi}
V_{B2C2}	Voltage across base/collector epilayer junction
p_W	Hole density at epilayer/N^+ buried collector interface, normalized with respect to N_{epi}
V_{B2C1}	Total voltage drop from the base-N^- collector epilayer interface to the N^-epilayer-N^+ buried layer interface. Sum of voltages, V_{B2C2}, the base-collector epilayer junction and V_{C1C2}, the voltage drop across the N^- epilayer.

Depletion junction terms:

C_0	Depletion capacitance at zero bias
V_D	Diffusion voltage
p	Grading coefficient
V	Applied (branch) voltage
V_j	Junction voltage which is an(adjusted) branch voltage
V_F	Switching voltage to engage constant C
V_{ch}	Numerical voltage to avoid singularity capability
V_{j0}	Adjusted junction voltage at V=0, $V_j(V=0)$
a	Constant capacitance factor

Mextram 504.7 temperature terms:

Tk	Device Temperature at each bias point
TEMP	Simulation Temperature
ΔT	Self-Heating Temperature Shift
DTA	Parameter, Location specific temperature shift
Tmodel	Model Temperature K
TREF	Parameter, Model Temperature C
V_g	Bandgap voltage
t_N	Ratio of device temperature, Tk, to model temperature, Tmodel as defined in equation (3.3)
n_{iREF}	Intrinsic concentration at the reference temperature

Mextram 504.7 base charge terms:

Q_{B0}	Total base charge at zero bias
Q_{tE}	Base-emitter depletion charge
Q_{tC}	Base-collector depletion charge
Q_{BE}	Base-emitter diffusion charge
Q_{BC}	Base-collector diffusion charge
q_1	Normalized base charge due to Early effect, from equation (3.23)
n_0	Normalized electron density at emitter edge of the neutral base region, defined in equation (3.44)
n_B	Normalized electron density at collector edge of the neutral base region,defined in equation (3.44)

Mextram 504.7 collector epilayer model terms:

$\frac{x_i}{W_{epi}}$	Ratio of the thickness of the injection layer, x_i, to the width of the total collector epilayer, W_{epi}
p_0	Hole density at base/collector epilayer interface, normalized with respect to N_{epi}
p_0^*	Hole density at base/collector epilayer interface, normalized with respect to N_{epi}
p_W	Hole density at epilayer/N^+ buried collector interface, normalized with respect to N_{epi}
N_{epi}	Effective collector epilayer doping concentration (cm^{-3})
N_{ref}	NPN reference concentration of epilayer(9.7E16 cm^{-3})
μ_{min}	Maximum mobility of collector epilayer (52 cm^2/Vs)
μ_{max}	Maximum mobility of collector epilayer (1417 cm^2/Vs)
W_{epi}	Thickness of collector epilayer layer (nm)
q	Elemental charge (1.609E-19 C)
ε	Dielectric constant of collector epilayer (1.036E-10 C/Vm)
n_i	Collector intrinsic concentration (cm^{-3})
ν_{sat}	Saturation velocity of collector epilayer (8.0E4 m/s)

Mextram 504.7 Avalanche current model:

A_n	Avalanche coefficient, NPN value =7.05E07 m^{-1}
B_n	Critical electric field, NPN value =1.23E08 m^{-1}
E_m	Maximum electric field
x_d	Depletion layer thickness base-collector epilayer interface
λ_D	Interception point in the collector where the extrapolated electric field is zero
V_{AVL}	Voltage describing the derivative of the electric field at low currents
W_{AVL}	Effective thickness of collector epilayer layer for avalanche

Appendix B: Ambient Temperature Model Parameters

Model Parameter	93K	162K	223K	300K
LEVEL	504	504	504	504
TREF	-180	-111	-50	27
DTA	0	0	0	0
EXMOD	0	0	0	0
EXPHI	1	1	1	1
EXAVL	0	0	0	0
IS	2.08E-55	1.41E-33	4.95E-25	3.492a
NF	1.1	1.04	1	1
NR	1.1	1.04	1	1
IK	5.000m	9.427m	12.37m	17.69m
VER	3.2	3.05	2.916	2.81
VEF	137.9	141	145	151
BF	1.045K	453	328.4	244
IBF	4.30E-35	8.34E-29	2.79E-26	1.34E-24
MLF	2.157	2.157	2.157	2.157
XIBI	0	0	0	0
BRI	40.00m	1.1	4.2	12.18
IBR	2.00E-55	5.60E-35	1.17E-26	3.300a
VLR	300.0m	300.0m	300.0m	300.0m
XEXT	0	0	0	0
WAVL	285.0n	260.0n	245.1n	245.1n
VAVL	100.0m	400.0m	800.0m	800.0m
SFH	800.0m	800.0m	800.0m	800.0m
RE	13.9	12.7	12.3	12.2
RBC	180	115.8	85.8	75.85
RBV	250	210	200	180
RCC	110	67	60	41
RCBLI	35	30	20	20
RCBLX	0	0	0	0
RCV	135.3	125.3	115	108
SCRCV	450	350	301.4	301.4
IHC	2.347m	2.347m	2.370m	2.347m
AXI	200.0m	200.0m	200.0m	200.0m
CJE	10.44f	10.58f	10.73f	10.96f
VDE	1.076	1.027	978.0m	909.3m
PE	288.3m	288.3m	288.3m	288.3m
XCJE	380.4m	380.0m	380.0m	380.0m
AJE	2	2	2	2
CBEO	0	0	0	0

CJC	5.626f	5.704f	5.787f	5.913f
VDC	1.005	945.0m	880.0m	803.8m
PC	305.5m	305.5m	305.5m	305.5m
XP	369.0m	364.0m	359.0m	351.1m
MC	324.5m	324.5m	324.5m	324.5m
XCJC	224.5m	224.7m	224.7m	224.7m
CBCO	0	0	0	0
MTAU	5	2.7	1	1
TAUE	42.20f	110.8f	169.0f	213.8f
TAUB	90.00f	125.8f	199.0f	390.7f
TEPI	25.70p	45.70p	65.00p	85.73p
TAUR	150.0p	150.0p	150.0p	150.0p
DEG	26.80m	32.80m	36.80m	41.00m
XREC	0	0	0	0
AQBO	363.0m	363.0m	363.0m	363.0m
DAIS	0	0	0	0
AE	200.0m	200.0m	200.0m	200.0m
AB	800.0m	800.0m	800.0m	800.0m
AEX	500.0m	500.0m	500.0m	500.0m
AEPI	1	1	1	1
AC	500.0m	500.0m	500.0m	500.0m
ACBL	500.0m	500.0m	500.0m	500.0m
DVGBF	10.00m	10.00m	10.00m	10.00m
DVGBR	-10.00m	-10.00m	-10.00m	-10.00m
VGB	1.1	1.1	1.11	1.11
VGC	1.1	1.1	1.1	1.1
VGJ	1.18	1.18	1.18	1.18
DVGTE	35.00m	35.00m	35.00m	35.00m
AF	2	2	2	2
KF	20.00p	20.00p	20.00p	20.00p
KFN	5.000u	5.000u	5.000u	5.000u
ISS	5.19E-59	3.94E-35	2.39E-28	3.94E-21
IKS	1.5	1.554	95.00m	95.40m
CJS	657.0a	660.0a	660.0a	660.0a
VDS	1.115	1.043	973.0m	879.0m
PS	335.0m	335.0m	335.0m	335.0m
VGS	1.18	1.18	1.18	1.18
AS	2	2	2	2
ATH	1.28	1.2	1.2	1.2
RTH	1.500K	3.332K	4.542K	5.000K
CTH	241.0p	241.0p	241.0p	241.0p

Appendix C: SET Model Parameters

SET Model Parameter	Value
LEVEL	504
TREF	27
DTA	0
EXMOD	0
EXPHI	1
EXAVL	0
TCRYO	-50
CRYO_ISO	7.761
CRYO_CISO	3.232
CRYO_NF	968.2m
CRYO_CNF	-110.0m
CRYO_NR	968.2m
CRYO_CNR	-110.0m
CRYO_CIK	1.063
CRYO_CVER	-111.0m
CRYO_CVEF	111.0m
CRYO_CBF	-440.0m
CRYO_CIBF	-19.84
CRYO_CBRI	4.176
CRYO_WAVL	200.0n
CRYO_CWAVL	-172.0m
CRYO_VAVL	1.671
CRYO_CVAVL	2.391
CRYO_CRBV	-272.0m
CRYO_RCBLI	18.19
CRYO_CRCBLI	-600.0m
CRYO_SCRCV	263.5
CRYO_CSCRCV	-458.0m
CRYO_MTAU	7.811
CRYO_FMTAU	-9.248
CRYO_CTAUE	-1.23
CRYO_TAUB	40.00f
CRYO_CTAUB	2.132
CRYO_CTEPI	1.462
CRYO_CVGB	128.2m
CRYO_VGB_VOLTAGE	1.155
IS	3.490a
NF	1
NR	1

IK	17.50m
VER	2.82
VEF	151
BF	247
IBF	1.34E-24
MLF	2.157
XIBI	0
BRI	15.02
IBR	151.1a
VLR	300.0m
XEXT	0
WAVL	245.1n
VAVL	800.0m
SFH	800.0m
RE	12.02
RBC	75.85
RBV	181
RCC	47
RCBLI	20
RCBLX	0
RCV	100.7
SCRCV	301.4
IHC	2.347m
AXI	200.0m
CJE	10.96f
VDE	909.3m
PE	288.3m
XCJE	380.0m
AJE	2
CBEO	0
CJC	5.913f
VDC	803.8m
PC	305.5m
XP	351.1m
MC	324.5m
XCJC	224.7m
CBCO	0
MTAU	1
TAUE	200.1f
TAUB	390.7f
TEPI	85.73p

TAUR	150.0p
DEG	41.00m
XREC	0
AQBO	363.0m
DAIS	250.0m
AE	-115.0m
AB	800.0m
AEX	-762.0m
AEPI	-283.0m
AC	-706.0m
ACBL	1
DVGBF	-10.00m
DVGBR	10.00m
VGB	1.11
VGC	1.05
VGJ	1.18
DVGTE	35.00m
AF	2
KF	20.00p
KFN	5.000u
ISS	3.94E-21
IKS	1.554
CJS	660.0a
VDS	879.0m
PS	335.0m
VGS	1.18
AS	2
ATH	1.107
RTH	5.658K
CTH	241.0p

Appendix D: SET Model code

Filename	Contribution	SET Model File
bjt504t.va	Module	bjt504tcryo.va
frontdefine.inc	Model constants	Same, but modified
parameters.inc	Model parameters	Same,but modified
variables.inc	Internal variables	Same, but modified
tscaling.inc	Parameter temperature equations	tscaling_cryo.inc, New code added to existing Mextram 504.7 file
evaluate.inc	Mextram model equations	evaluate_cryo.inc, New code added to Mextram 504.7 file

bjt504tcryo.va

The SET Verilog module is a modification of the Mextram 504.7 module, bjt504t

```
`include "frontdef.inc"
`define  SELFHEATING
`define  SUBSTRATE

module bjt504tcryova (c, b, e, s, dt);

  // External ports
     inout c, b, e, s, dt;

     electrical e, b, c, s;
     electrical dt;

  // Internal nodes
     electrical e1, b1, b2, c1, c2, c3, c4;
     electrical noi; // For correlated noise implementation

`include "parameters.inc"
`include "variables.inc"
`include "opvars.inc"

analog begin

`include "initialize.inc"
`include "tscaling_cryo.inc"
`include "evaluate_cryo.inc"
`include "opinfo.inc"

// The following can be used to print OP-info to std out:
// `include "op_print.inc"
```

end // analog

endmodule

frontdefine.inc

The following was redefined in the file frontdefine.inc:

```
// Numerical, physical and model constants
`define TEN_M40 1.0e-150
`define TEN_M07 1.0e-47
```

Parameters.inc

`Pre-factor of the recombination part of Ib1

1	TCRYO = -50.0 from [-273.0:inf)	Cryo temperature range begins below this value
2	CRYO_ISO = 7.0 from (0.0:inf)	Cryo value of IS coefficient equation CRYO_CIS
3	CRYO_CISO = 3.0 from (0.0:inf)	Temperature coeff. of IS coefficient equation CRYO_CIS
4	CRYO_NF = 1.0	Cryo ideality factor of ideal forward base voltage of B2E1
5	CRYO_CNF = 1.0	Temperature coeff. of cryo ideality factor of ideal forward base voltage of B2E1
6	CRYO_NR = 1.0	Cryo ideality factor of ideal reverse base voltage of B2C2
7	CRYO_CNR = 1.0	Temperature coeff. of cryo ideality factor of ideal reverse base voltage of B2C2
8	CRYO_CIK = 1.0	Temperature coefficient of IK,replaces 1-AB
9	CRYO_CVEF = 0.3	Temperature coefficient of VEF,replaces AQBO
10	CRYO_CVER = 0.3	Temperature coefficient of VER,replaces AQBO
11	CRYO_CBF = -2.0	Temperature coefficient of BF,replaces AE-AB-AQBO
13	CRYO_CIBF = -20.0	Temperature coefficient of IBF,replaces 6.0-2.*MLF
14	CRYO_CBRI = 1.5	Temperature coefficient of BRI equation
15	CRYO_WAVL = 1.0	Cryo value of WAVL equation
16	CRYO_CWAVL = 1.0	Temperature coefficient of cryo WAVL equation
17	CRYO_VAVL = 1.0	Cryo value of the VAVL, voltage determining curvature of avalanche current

18	CRYO_CVAVL = 1.0	Temperature coefficient of the voltage determining curvature of avalanche current
19	CRYO_CRBV = 0.5	Temperature coefficient of the RBV,replaces AB-AQBO
20	CRYO_RCBLI = 10	Cryo value of RCBLI equation
21	CRYO_CRCBLI = 10	Temperature coefficient of cryo RCBLI equation
22	CRYO_SCRCV = 1250.0	Cryo value of SCRCV space charge resistance of the epilayer
23	CRYO_CSCRCV = 1	Temperature coefficient of cryo scrcv space charge resistance of the epilayer
24	CRYO_MTAU = 1.0	Temperature constant for cryo MTAU shift in emitter transit time
25	CRYO_FMTAU = 1.0	Temperature factor for cryo MTAU shift in emitter transit time
26	CRYO_CTAUE = -1.2	Temperature coefficient of the TAUE, replaces AB-2
27	CRYO_TAUB = 1.0e-15	Cryo TAUB value for exp behavior of the TAUB
28	CRYO_CTAUB = 1.0	Temperature coefficient of the TAUB in exp eqn, replaces AQBO+AB-1 in pow eqn
29	CRYO_CTEPI = 1.0	Temperature coefficient of the TEPI, replaces AEPI-1
30	CRYO_CVGB = 1	Temperature coefficient of the band-gap voltage of the base
31	CRYO_VGB_VOLTAGE = 1.17	Cryo fitted band-gap voltage of the base for IS_T temperature eqn

variables.inc

```
//Variables for ideality factors added BOW 2010
real NFinv;
real NRinv;
// Added, CRYO temperature variables - BOW 2010:
real Trcryo;
real CRYO_VGB;
real CRYO_CIS;
real NF_T;
real NR_T;
real MTAU_T;
real VAVL_T;
real WAVL_T;
real SCRCV_T, SCRCV_TM;
```

tscaling_cryo.inc

```
// Temperature scaling of parameters

//Added cryo temperature parameter - defines cryo temp scaling - BOW 2010
   Trcryo = TCRYO +  `C2K;
   // Temperature variables
   Trk = TREF + `C2K;


//Added CRYO_CRBV,Changed RBV_T from AB-AQBO
   RBV_T = RBV * pow(tN, CRYO_CRBV);


//Added CRYO_CBF,Changed BF_T from AE-AB-AQBO - BOW 2010
   BF_T  = BF  * pow(tN, CRYO_CBF) * exp(-DVGBF * VdtINV);
//Added CRYO_CBF,Changed BF_T from AE-AB-AQBO - BOW 2010
   BRI_T = BRI * pow(tN, CRYO_CBRI) * exp(-DVGBR * VdtINV);

   // Currents and voltages
if (Tk < Trcryo)
 begin
//Added for cryo: NF_T  and NR_T equations - BOW 2010
   NF_T = CRYO_NF * pow(tN, CRYO_CNF);
   NR_T = CRYO_NR * pow(tN, CRYO_CNR);

//Added for cryo: VAVL_T equation - BOW 2010
   VAVL_T = CRYO_VAVL * pow(tN, CRYO_CVAVL);
   WAVL_T = CRYO_WAVL * pow(tN, CRYO_CWAVL);

//Cryo range IS_T eqn
//Added parameters CRYO_VGB_VOLTAGE, CRYO_CVGB for IS_T eqn - BOW 2010

//changed VGB to cryo calculated variable,CRYO_VGB_IS
   CRYO_VGB = CRYO_VGB_VOLTAGE *  pow(tN, CRYO_CVGB);

//replaced coefficient 4.0 - AB - AQBO + DAIS with CRYO_CIS equation
   CRYO_CIS = CRYO_ISO * pow(tN,CRYO_CISO);

//IS_T equation for cryo range
   IS_T  = IS  * pow(tN,CRYO_CIS) * exp(-CRYO_VGB * VdtINV);

//Added for cryo: MTAU_T equation - BOW 2010
   MTAU_T = CRYO_FMTAU * tN + CRYO_MTAU;
```

```
// Addced cryo SCRCV_T effects - BOW 2010
   SCRCV_T = CRYO_SCRCV * pow(tN,CRYO_CSCRCV);

// Addced cryo RCCin_T effects - BOW 2010
   RCCin_T = CRYO_RCBLI * pow(tN,CRYO_CRCBLI);
 end
else
 begin
   NF_T = NF;
   NR_T = NR;
   WAVL_T = WAVL;
   VAVL_T = VAVL;
   IS_T  = IS  * pow(tN,4.0 - AB - AQBO + DAIS) * exp(-VGB * VdtINV);
   MTAU_T = MTAU;
   SCRCV_T = SCRCV;
   RCCin_T = RCBLI * pow(tN, ACBL);
  end



//Added CRYO_IK,Changed IK_T from 1-AB –
```

evaluate_cryo.inc

This is the Mextram 504.7 evaluate.inc, but modified for the SET model:

```
// Evaluate model equations

begin  // Currents and sharges
// Nodal biases

   Vb2c1 = TYPE * V(b2, c1);
   Vb2c2 = TYPE * V(b2, c2);
   Vb2e1 = TYPE * V(b2, e1);
   Vb1e1 = TYPE * V(b1, e1);
   Vb1b2 = TYPE * V(b1, b2);
`ifdef SUBSTRATE
   Vsc1  = TYPE * V(s,  c1);
`endif
   Vc1c2 = TYPE * V(c1, c2);
   Vee1  = TYPE * V(e,  e1);
   Vbb1  = TYPE * V(b,  b1);
   Vbe   = TYPE * V(b,  e);
   Vbc   = TYPE * V(b,  c);


/* RvdT, 03-12-2007, voltage differences
```

```
 associated with distributed parasitic collector.
 Evaluated taking values of resistances into account:
 in case of vanishing resistance corresponding node
 is not addressed: */

if (RCBLX > 0.0)
 begin
  if (RCBLI > 0.0)
    begin
     Vc4c1 = TYPE * V(c4, c1);
     Vc3c4 = TYPE * V(c3, c4);
    end
   else
    begin
     Vc4c1 = 0 ;
     Vc3c4 = TYPE * V(c3, c1);
    end
 end
else
 begin
  if (RCBLI > 0.0)
    begin
     Vc4c1 = TYPE * V(c4, c1);
     Vc3c4 = 0 ;
    end
   else
    begin
     Vc4c1 = 0 ;
     Vc3c4 = 0 ;
    end
 end

   Vb1c4 = Vb1b2 + Vb2c2 - Vc1c2 - Vc4c1 ;
   Vcc3  = - Vbc + Vbb1 + Vb1c4 - Vc3c4 ;
   Vbc3  = Vbc + Vcc3 ;

`ifdef  SUBSTRATE
Vsc4 = Vsc1 - Vc4c1 ;
Vsc3 = Vsc4 - Vc3c4 ;
`endif

NFinv = 1.0 / NF_T;

NRinv = 1.0 / NR_T;
// Exponential bias terms
// Modiftied for cryo - added NR parameter
```

```
   `expLin(eVb2c2,Vb2c2 * VtINV * NRinv)
// Modified for cryo - added NF parameter
   `expLin(eVb2e1,Vb2e1 * VtINV *  NFinv)
   `expLin(eVb1e1,Vb1e1 * VtINV * NFinv)
   `expLin(eVb1c4,Vb1c4 * VtINV * NRinv)
   `expLin(eVb1b2,Vb1b2 * VtINV)
   `expLin(eVbc3,Vbc3  * VtINV * NRinv)
`ifdef SUBSTRATE
   `expLin(eVsc1,Vsc1  * VtINV)
`endif

   `expLin(eVbc3VDC,(Vbc3  - VDC_T) * VtINV * NRinv)
   `expLin(eVb1c4VDC,(Vb1c4 - VDC_T) * VtINV * NRinv)
   `expLin(eVb2c2VDC,(Vb2c2 - VDC_T) * VtINV * NRinv)
   `expLin(eVb2c1VDC,(Vb2c1 - VDC_T) * VtINV * NRinv)

// Governing equations

   // Epilayer model

   K0 = sqrt(1.0 + 4.0 * eVb2c2VDC);
   Kw = sqrt(1.0 + 4.0 * eVb2c1VDC);
   pW = 2.0 *  eVb2c1VDC / (1.0 + Kw);

   if (pW < `TEN_M40) pW = 0;
   Ec = Vt * (K0 - Kw - ln((K0 + 1.0) / (Kw + 1.0)) );
   Ic1c2 =  (Ec + Vc1c2) / RCV_TM;

   if (Ic1c2 > 0.0) begin

     `linLog(tmpV,Vb2c1,100.0);
     Vqs_th = VDC_T + 2.0 * Vt *
            ln(0.5 * Ic1c2 * RCV_TM * VtINV + 1.0) - tmpV;
     eps_VDC = 0.2 * VDC_T;
     `max_hyp0(Vqs, Vqs_th, eps_VDC);
     Iqs = Vqs * (Vqs + IHC_M * SCRCV_TM) / (SCRCV_TM * (Vqs + IHC_M * RCV_TM));

     Ic1c2_Iqs = Ic1c2 / Iqs;
     `max_logexp(alpha1, Ic1c2_Iqs, 1.0, AXI);
     alpha = alpha1 / (1.0 + AXI * ln(1.0 + exp(-1.0 / AXI)));
     vyi = Vqs / (IHC_M * SCRCV_TM);
     yi = (1.0 + sqrt(1.0 + 4.0 * alpha * vyi * (1.0 + vyi))) /
          (2.0 * alpha * (1.0 + vyi));

     xi_w = 1.0 - yi / (1.0 + pW * yi);
      gp0 = 0.5 * Ic1c2 * RCV_TM * xi_w * VtINV;
```

```
      gp0_help = 2.0 * gp0 + pW * (pW + gp0 + 1.0);
      gp02 = 0.5 * (gp0 - 1.0);
      sqr_arg = gp02 * gp02 + gp0_help;
      if (gp0 >= 1.0)
        p0star =  gp02 + sqrt(sqr_arg);
      else
        p0star = gp0_help / (sqrt(sqr_arg) - gp02);

      if (p0star < `TEN_M40) p0star = 0.0;
      eVb2c2star = p0star * (p0star + 1.0) * exp(VDC_T * VtINV * NRinv);
       Vb2c2starInside = Vt * ln(eVb2c2star);

      B1 = 0.5 * SCRCV_TM * (Ic1c2 - IHC_M);
      B2 = SCRCV_TM * RCV_TM * IHC_M * Ic1c2;
      Vxi0 = B1 + sqrt(B1 * B1 + B2);
      Vch = VDC_T * (0.1 + 2.0 * Ic1c2 / (Ic1c2 + Iqs));
      Icap = IHC_M * Ic1c2 / (IHC_M + Ic1c2);
      Icap_IHC = IHC_M / (IHC_M + Ic1c2);

// Section if Ic1c2 is = or < 0
    end else begin

      p0star = 2.0 * eVb2c2VDC / (1.0 + K0);
      eVb2c2star = eVb2c2;
      if ((abs(Vc1c2) < 1.0e-5 * Vt) ||
         (abs(Ec) < `TEN_M40 * Vt * (K0 + Kw)))
        begin
          pav = 0.5 * (p0star + pW);
          xi_w = pav / (pav + 1.0);
        end

      else
        begin
          xi_w = Ec / (Ec + Vb2c2 - Vb2c1);
        end

      Vxi0 = Vc1c2;
      Vch = 0.1 * VDC_T;
      Icap = Ic1c2;
      Icap_IHC = 1.0 - Icap / IHC_M;

    end

    // Effective emitter junction capacitance bias
```

```
Vfe = VDE_T * (1.0 - pow(AJE , -1.0 / PE));
a_VDE = 0.1 * VDE_T;
`min_logexp(Vje, Vb2e1, Vfe, a_VDE);

Vte = VDE_T / (1.0 - PE) * (1.0 - pow(1.0 - Vje / VDE_T, 1.0 - PE)) +
    AJE * (Vb2e1 - Vje);

// Effective collector junction capacitance bias

Vjunc = Vb2c1 + Vxi0;
bjc = (`AJC - XP_T) / (1.0 - XP_T);
Vfc = VDC_T * (1.0 - pow(bjc, -1.0 / PC));
`min_logexp(Vjc, Vjunc, Vfc, Vch);
fI = pow(Icap_IHC, MC);
Vcv = VDC_T / (1.0 - PC) * (1.0 - fI * pow(1.0 - Vjc / VDC_T, 1.0 - PC)) +
     fI * bjc * (Vjunc - Vjc);
Vtc = (1.0 - XP_T) * Vcv + XP_T * Vb2c1;


// Transfer current

If0 = 4.0 * IS_TM / IK_TM;
f1 =  If0 * eVb2e1;
n0 =  f1 / (1.0 + sqrt(1.0 + f1));
f2 =  If0 * eVb2c2star;
nB =  f2 / (1.0 + sqrt(1.0 + f2));

if (DEG == 0.0)
    q0I = 1.0 + Vte / VER_T + Vtc / VEF_T;
else
  begin
    termE = (Vte / VER_T + 1.0) * DEG_T * VtINV;
    termC = -Vtc / VEF_T * DEG_T * VtINV;
    q0I = (exp(termE) - exp(termC)) /
         (exp(DEG_T * VtINV) - 1.0);
  end

`max_hyp0(q1I, q0I, 0.1);
qBI = q1I * (1.0 + 0.5 * (n0 + nB));

Ir = IS_TM *  eVb2c2star;
If = IS_TM * eVb2e1;
In = (If - Ir) / qBI;


// Base and substrate current(s)
```

```
  Ibf0 = IS_TM / BF_T;
  if (XREC == 0.0)
    Ib1 = (1.0 - XIBI) * Ibf0 * (eVb2e1 - 1.0);
  else
    Ib1 = (1.0 - XIBI) * Ibf0 * ((1.0 - XREC) * (eVb2e1 - 1.0) +
        XREC * (eVb2e1 + eVb2c2star - 2.0) * (1.0 + Vtc / VEF_T));

  Ib1_s = XIBI * Ibf0 * (eVb1e1 - 1.0);
  `expLin(tmpExp,Vb2e1 * VtINV / MLF)
  Ib2 = IBF_TM * (tmpExp - 1.0) + GMIN * Vb2e1;
  `expLin(tmpExp,0.5 * Vb1c4 * VtINV)
  Ib3 = IBR_TM * (eVb1c4 - 1.0) /
      (tmpExp + exp(0.5 * VLR * VtINV)) +
      GMIN  * Vb1c4;



 // Iex, Isub (XIex, XIsub)

  g1 = If0 * eVb1c4;
  g2 = 4.0 * eVb1c4VDC;
  nBex = g1 / (1.0 + sqrt(1.0 + g1));
  pWex = g2 / (1.0 + sqrt(1.0 + g2));
  Iex = (1.0 / BRI_T) * (0.5 * IK_TM * nBex - IS_TM);

`ifdef SUBSTRATE
  Isub = 2.0 * ISS_TM * (eVb1c4 - 1.0) /
       (1.0 + sqrt(1.0 + 4.0 * (IS_TM / IKS_TM) * eVb1c4));
//   Isf =  ISS_TM * (eVsc1 - 1.0);
    Isf = 1.0e-25;
`endif

  XIex =0.0;

`ifdef SUBSTRATE
  XIsub = 0.0;
`endif



  if (EXMOD == 1)
   begin

    Iex =   Iex *  Xext1;
```

```
`ifdef SUBSTRATE
     Isub  = Isub * Xext1;
`endif

     Xg1 = If0 * eVbc3;
     XnBex = Xg1 / (1.0 + sqrt(1.0 + Xg1));
     XIMex = XEXT * (0.5 * IK_TM * XnBex - IS_TM) / BRI_T;

`ifdef SUBSTRATE
     XIMsub = XEXT * 2.0 * ISS_TM * (eVbc3 - 1.0) /
              (1.0 + sqrt(1.0 + 4.0 * IS_T / IKS_T * eVbc3));
     Vex_bias = XEXT * (IS_TM / BRI_T + ISS_TM) * RCCxx_TM;
`else
     XIMsub = 0.0;
     Vex_bias = XEXT * (IS_TM / BRI_T) * RCCxx_TM;
`endif

     Vex = Vt * (2.0 - ln( Vex_bias * VtINV));
     vdif = Vbc3 - Vex;
     `max_hyp0(VBex, vdif, 0.11);

     Fex = VBex /(Vex_bias + (XIMex + XIMsub) * RCCxx_TM + VBex);
     XIex = Fex * XIMex;

`ifdef SUBSTRATE
     XIsub = Fex * XIMsub;
`endif
    end
   else
    begin
     Fex = 0;
     XnBex = 0 ;
    end

   // Variable base resistance

   q0Q = 1.0 + Vte / VER_T + Vtc / VEF_T;
   `max_hyp0(q1Q, q0Q, 0.1);
   qBQ = q1Q * (1.0 + 0.5 * (n0 + nB));

   Rb2 = 3.0 * RBV_TM / qBQ;
   Ib1b2 =  (2.0 * Vt * (eVb1b2 - 1.0) + Vb1b2) / Rb2;


   // Weak-avalanche current
```

```
Iavl = 0.0;
Gem  = 0.0;
if ((Ic1c2 > 0.0) && (Vb2c1 < VDC_T)) begin

  dEdx0 = 2.0 * VAVL_T / (WAVL_T * WAVL_T);
  sqr_arg = (VDC_T - Vb2c1) / Icap_IHC;
  xd = sqrt(2.0 * sqr_arg / dEdx0);
  if (EXAVL == 0.0)
    Weff = WAVL_T;
  else
    begin
      xi_w1 = 1.0 - 0.5 * xi_w;
      Weff = WAVL_T * xi_w1 * xi_w1;
    end
  Wd = xd * Weff / sqrt(xd * xd + Weff * Weff);
  Eav = (VDC_T - Vb2c1) / Wd;
  E0 = Eav + 0.5 * Wd * dEdx0 * Icap_IHC;

  if (EXAVL == 0)
    Em = E0;
  else
    begin
      SHw = 1.0 + 2.0 * SFH * (1.0 + 2.0 * xi_w);
      Efi = (1.0 + SFH) / (1.0 + 2.0 * SFH);
      Ew = Eav - 0.5 * Wd * dEdx0 * (Efi - Ic1c2 / (IHC_M * SHw));
      sqr_arg = (Ew - E0) * (Ew - E0) + 0.1 * Eav * Eav * Icap / IHC_M;
      Em = 0.5 * (Ew + E0 + sqrt(sqr_arg));
    end

  EmEav_Em = (Em - Eav) / Em;
  if (abs(EmEav_Em) > `TEN_M07)
    begin
      lambda = 0.5 * Wd / EmEav_Em;
      Gem = An / BnT * Em * lambda *
          (exp(-BnT / Em) - exp(-BnT / Em * (1.0 + Weff / lambda)) );
    end
  else
    Gem = An * Weff * exp(-BnT / Em);

  Gmax = Vt / (Ic1c2 * (RBC_TM + Rb2)) +  qBI / BF_T +
        RE_TM / (RBC_TM + Rb2);
  Iavl = Ic1c2 * Gem  / (Gem +Gem / Gmax + 1.0);
end
```

```
`ifdef SELFHEATING
   // Power dissipation

  if (eVb2c2star > 0.0)
      Vb2c2star = Vt * ln(eVb2c2star);
   else
      Vb2c2star = Vb2c2;
// RvdT 03-12-2007, modified power equation due to distribution collector resistance

   power =  In * (Vb2e1 - Vb2c2star) +
          Ic1c2 * (Vb2c2star - Vb2c1) -
          Iavl  * Vb2c2star +
          Vee1  * Vee1  / RE_TM +
          Vcc3  * Vcc3  * GCCxx_TM +
          Vc3c4 * Vc3c4 * GCCex_TM +
          Vc4c1 * Vc4c1 * GCCin_TM +
          Vbb1  * Vbb1  / RBC_TM +
          Ib1b2 * Vb1b2 +
          (Ib1 + Ib2) * Vb2e1 +
          Ib1_s * Vb1e1 +
`ifdef SUBSTRATE
          (Iex + Ib3) * Vb1c4 + XIex  * Vbc3 +
            Isub * (Vb1c4 - Vsc4) +
           XIsub * (Vbc3 - Vsc3) +
            Isf * Vsc1;
`else
          (Iex + Ib3) * Vb1c4 + XIex * Vbc3;
`endif

`endif



   // Charges

   Qte = (1.0 - XCJE) * CJE_TM * Vte;
   `min_logexp(Vje_s, Vb1e1, Vfe, a_VDE);
   Qte_s = XCJE * CJE_TM * (VDE_T / (1.0 - PE) *
         (1.0 - pow(1.0 - Vje_s / VDE_T, 1.0 - PE)) +
          AJE * (Vb1e1 - Vje_s));

   Qtc = XCJC * CJC_TM * Vtc;
   Qb0 = TAUB_T * IK_TM;
   Qbe_qs = 0.5 * Qb0 * n0 * q1Q;
   Qbc_qs = 0.5 * Qb0 * nB * q1Q;
```

```
  a_VDC = 0.1 * VDC_T;
  `min_logexp(Vjcex, Vb1c4, Vfc, a_VDC);
  Vtexv = VDC_T / (1.0 - PC) * (1.0 - pow(1.0 - Vjcex / VDC_T, 1.0 - PC)) +
        bjc * (Vb1c4 - Vjcex);
  Qtex = CJC_TM * ((1.0 - XP_T) * Vtexv + XP_T * Vb1c4) *
       (1.0 - XCJC) * (1.0 - XEXT);

  `min_logexp(XVjcex, Vbc3, Vfc, a_VDC);
  XVtexv = VDC_T / (1.0 - PC) * (1.0 - pow(1.0 - XVjcex / VDC_T, 1.0 - PC)) +
         bjc * (Vbc3 - XVjcex);
  XQtex = CJC_TM * ((1.0 - XP_T) * XVtexv + XP_T * Vbc3) *
        (1.0 - XCJC) * XEXT;

`ifdef SUBSTRATE
  a_VDS = 0.1 * VDS_T;
  Vfs = VDS_T * (1.0 - pow(`AJS , -1.0 / PS));
  `min_logexp(Vjs, Vsc1, Vfs, a_VDS);
  Qts = CJS_TM * (VDS_T / (1.0 - PS) *
      (1.0 - pow(1.0 - Vjs / VDS_T, 1.0 - PS)) +  `AJS * (Vsc1 - Vjs));
`endif

  Qe0 = TAUE_T * IK_TM * pow(IS_TM / IK_TM, 1.0 / MTAU_T);
  `expLin(tmpExp,Vb2e1 / (MTAU_T * Vt))
  Qe = Qe0 * (tmpExp - 1.0);

  Qepi0 = 4.0 * TEPI_T * Vt / RCV_TM;
  Qepi = 0.5 * Qepi0 * xi_w * (p0star + pW + 2.0);

  Qex = TAUR_T * 0.5 * (Qb0 * nBex + Qepi0 * pWex) / (TAUB_T + TEPI_T);
  XQex = 0.0;

  if (EXMOD == 1) begin

    Qex = Qex * (1.0 - XEXT);
    Xg2 = 4.0 * eVbc3VDC;
    XpWex = Xg2 / (1.0 + sqrt(1.0 + Xg2));
    XQex = 0.5 * Fex * XEXT * TAUR_T *
         (Qb0 * XnBex + Qepi0 * XpWex) / (TAUB_T + TEPI_T);

  end

  Qb1b2 = 0.0;
  if (EXPHI == 1)
    begin
      dVteVje = pow(1.0 - Vje / VDE_T, -PE) - AJE;
```

```
        Vb2e1Vfe = (Vb2e1 - Vfe) / a_VDE;
        if (Vb2e1Vfe < 0.0)
          dVjeVb2e1 = 1.0 / (1.0 + exp(Vb2e1Vfe));
        else
          dVjeVb2e1 = exp(- Vb2e1Vfe) / (1.0 + exp(- Vb2e1Vfe));

        dVteVb2e1 = dVteVje * dVjeVb2e1 + AJE;
        dQteVb2e1 = (1.0 - XCJE) * CJE_TM * dVteVb2e1;

        dn0Vb2e1 = If0 * eVb2e1 * VtINV * (0.5 / sqrt(1.0 + f1));
        dQbeVb2e1 = 0.5 * Qb0 * q1Q * dn0Vb2e1;

        dQeVb2e1 = (Qe + Qe0) / (MTAU_T * Vt);

        Qb1b2 = 0.2 * Vb1b2 * (dQteVb2e1 + dQbeVb2e1 + dQeVb2e1);

        Qbc = Qbe_qs / 3.0 + Qbc_qs;
        Qbe = 2.0 * Qbe_qs / 3.0;
      end
    else
      begin
        Qbe = Qbe_qs;
        Qbc = Qbc_qs;
      end
// Add branch current contributions

   // Static currents
   I(c1, c2) <+ TYPE * Ic1c2;
   I(c2, e1) <+ TYPE * In;
   I(b1, e1) <+ TYPE * Ib1_s;
   I(b2, e1) <+ TYPE * (Ib1 + Ib2);
`ifdef SUBSTRATE
   I(b1, s)  <+ TYPE * Isub;
   I(b,  s)  <+ TYPE * XIsub;
   I(s,  c1) <+ TYPE * Isf;
`endif
   I(b1, b2) <+ TYPE * Ib1b2;
   I(b2, c2) <+ TYPE * (-1.0 * Iavl);
   I(e,  e1) <+ TYPE * Vee1 / RE_TM;
   I(b,  b1) <+ TYPE * Vbb1 / RBC_TM;

`ifdef SELFHEATING
   // Electrical equivalent for the thermal network
   I(dt) <+ V(dt) / RTH_Tamb_M;
   I(dt) <+ ddt(CTH_M * V(dt));
   I(dt) <+ -1.0 *  power;
```

```
`endif

   // Electrical equivalent for the correlated noise
   I(noi, e1)    <+ V(noi, e1);
   cor_exp_1 = sqrt(1.0 + 2.0 * Gem) * V(noi,e1);
   I(b2, e1) <+ cor_exp_1;
   cor_exp_2 = (2.0 + 2.0 * Gem) / sqrt(1.0 + 2.0 * Gem) * V(noi, e1);
   I(e1, c2) <+ cor_exp_2;

   // Dynamic currents
   I(b2, e1) <+ ddt(TYPE * (Qte + Qbe + Qe));
c_current_Qbe = Qbe;
c_current_Qe = Qe;
c_current_Qte = Qte;
$fstrobe(file_Qbe,"%e",c_current_Qbe);
$fstrobe(file_Qe,"%e",c_current_Qe);
$fstrobe(file_Qte,"%e",c_current_Qte);


   I(b1, e1) <+ ddt(TYPE * (Qte_s));
   I(b2, c2) <+ ddt(TYPE * (Qtc + Qbc + Qepi));
`ifdef SUBSTRATE
   I(s,  c1) <+ ddt(TYPE * Qts);
`endif
   I(b1, b2) <+ ddt(TYPE * Qb1b2);
   I(b,   e) <+ ddt(TYPE * CBEO_M * Vbe);
   I(b,   c) <+ ddt(TYPE * CBCO_M * Vbc);

   end  // Currents and charges


/* RvdT, Delft Univ. Tech. 03-12-2007.
Distribution of parasitic collector resistance.
This construct supports the case
RCBLI = 0.0 and or RCBLX = 0.0 .
It is up to the compiler to adjust the circuit topology
and perform a node-collapse in such cases. */
if (RCBLX > 0.0)
 begin
  I(b,  c3) <+ TYPE * XIex;
  I(c,  c3) <+ TYPE * Vcc3  * GCCxx_TM ;
  I(b,  c3) <+ ddt(TYPE * (XQtex + XQex));
  if (RCBLI > 0.0)
   begin
     I(c4, c1) <+ TYPE * Vc4c1 * GCCin_TM;
     I(b1, c4) <+ TYPE * (Ib3 + Iex);
```

```
    I(c3, c4) <+ TYPE * Vc3c4 * GCCex_TM ;
    I(b1, c4) <+ ddt(TYPE * (Qtex + Qex));
   end
  else
   begin
    V(c4, c1) <+ 0.0 ;
    I(b1, c1) <+ TYPE * (Ib3 + Iex);
    I(b1, c1) <+ ddt(TYPE * (Qtex + Qex));
    I(c3, c1) <+ TYPE * Vc3c4 * GCCex_TM ;
   end
 end
else
 begin
  V(c3, c4) <+ 0 ;
      if (RCBLI > 0.0)
         begin
           I(b,  c4) <+ TYPE * XIex;
           I(c,  c4) <+ TYPE * Vcc3  * GCCxx_TM ;
           I(c4, c1) <+ TYPE * Vc4c1 * GCCin_TM;
           I(b1, c4) <+ TYPE * (Ib3 + Iex);
           I(b1, c4) <+ ddt(TYPE * (Qtex + Qex));
           I(b,  c4) <+ ddt(TYPE * (XQtex + XQex));
         end
      else
         begin
           I(b,  c1) <+ TYPE * XIex;
           I(c,  c1) <+ TYPE * Vcc3  * GCCxx_TM ;
           V(c4, c1) <+ 0.0 ;
           I(b1, c1) <+ TYPE * (Ib3 + Iex);
           I(b1, c1) <+ ddt(TYPE * (Qtex + Qex));
           I(b,  c1) <+ ddt(TYPE * (XQtex + XQex));
           I(c3, c1) <+ TYPE * Vc3c4 * GCCex_TM ;
         end
 end

 $fstrobe(file_Vbb1,"%e",Vbb1);
 $fstrobe(file_Vb1b2,"%e",Vb1b2);
// $fstrobe(file_Vb2e1,"%e",Vb2e1);
 $fstrobe(file_Vb2c2,"%e",Vb2c2);
 $fstrobe(file_Vc1c2,"%e",Vc1c2);

// Small signal equivalent circuit conductances and resistances

ddxgx     = - ddx(In, V(e1));      // Forward transconductance
ddxgy     = - ddx(In, V(c2));      // Reverse transconductance
```

```
ddxgz     = - ddx(In, V(c1));      // Reverse transconductance

ddxsgpi   = - ddx(Ib1_s, V(e))
          - ddx(Ib1_s, V(e1));   // Conductance sidewal b-e junction
ddxgpix   = - ddx(Ib1+Ib2, V(e1)); // Conductance floor b-e junction

ddxgpiy   = - ddx(Ib1, V(c2));  // Early effect on recombination base current
ddxgpiz   = - ddx(Ib1, V(c1));  // Early effect on recombination base current

ddxgmux   =  ddx( Iavl, V(e1)); // Early effect on avalanche current limitting
ddxgmuy   =  ddx( Iavl, V(c2)); // Conductance of avalanche current
ddxgmuz   =  - ddx(- Iavl, V(c1));   // Conductance of avalanche current

// Conductance extrinsic b-c current :
ddxgmuex  =   ddx(Iex+Ib3, V(e))
          + ddx(Iex+Ib3, V(b1))
          + ddx(Iex+Ib3, V(b2))
          + ddx(Iex+Ib3, V(e1))
          + ddx(Iex+Ib3, V(c2));

ddxxgmuex = ddx(XIex, V(b)) ; // Conductance extrinsic b-c current

ddxgrcvy  =  - ddx(Ic1c2, V(c2)); // Conductance of epilayer current
ddxgrcvz  =  - ddx(Ic1c2, V(c1));  // Conductance of epilayer current

ddxrbv    = 1.0 / (- ddx(Ib1b2, V(b2)) - ddx(Ib1b2, V(c2)));  // Base resistance

ddxgrbvx  = - ddx(Ib1b2, V(e)) - ddx(Ib1b2, V(e1)); // Early effect on base resistance
ddxgrbvy  = - ddx(Ib1b2, V(c2)); // Early effect on base resistance

ddxgrbvz  = - ddx(Ib1b2, V(c1)); // Early effect on base resistance

ddxre     = RE_TM;  // Emiter resistance
ddxrbc    = RBC_TM; // Constant base resistance
ddxrcc    = RCCxx_TM; // Collector Contact resistance
ddxrcblx  = RCCex_TM; // Extrinsic buried layer resistance
ddxrcbli  = RCCin_TM; // Extrinsic buried layer resistance


`ifdef SUBSTRATE
ddxgs     = ddx(Isub, V(b)) + ddx(Isub, V(b1));  // Conductance parasitic PNP transitor
ddxxgs    = ddx(XIsub, V(b)) ; // Conductance parasitic PNP transistor
ddxgsf    = ddx(Isf, V(s)) ;   // Conductance substrate failure current
`endif
```

```
// Small signal equivalent circuit capacitances
ddxscbe   = - ddx(Qte_s, V(e)) - ddx(Qte_s, V(e1)); // Capacitance sidewall b-e junction

ddxcbex   = - ddx(Qte + Qbe + Qe, V(e1)) ;          // Capacitance floor b-e junction

ddxcbey   = - ddx(Qbe, V(c2)); // Early effect on b-e diffusion junction

ddxcbez   = - ddx(Qbe, V(c1)); // Early effect on b-e diffusion junction

ddxcbcx   = - ddx(Qbc, V(e)) - ddx(Qbc, V(e1)); // Early effect on b-c diffusion junction


ddxcbcy   =  - ddx(Qtc + Qbc + Qepi, V(c2)); // Capacitance floor b-c junction
ddxcbcz   =  - ddx(Qtc + Qbc + Qepi, V(c1)); // Capacitance floor b-c junction

// Capacitance extrinsic b-c junction :
ddxcbcex  =   ddx(Qtex + Qex,V(e))
          + ddx(Qtex + Qex,V(b1 ))
          + ddx(Qtex + Qex,V(b2))
          + ddx(Qtex + Qex,V(e1))
          + ddx(Qtex + Qex,V(c2)) ;

// Capacitance extrinsic b-c junction :
ddxxcbcex =  ddx(XQtex + XQex, V(b)) ;

ddxcb1b2  = - ddx(Qb1b2, V(b2)) - ddx(Qb1b2, V(c2));  // Capacitance AC current crowding

ddxcb1b2x =  - ddx(Qb1b2, V(e)) - ddx(Qb1b2, V(e1));  // Cross-capacitance AC current
crowding
ddxcb1b2y =  - ddx(Qb1b2, V(c2));  // Cross-capacitance AC current crowding
ddxcb1b2z =  - ddx(Qb1b2, V(c1)) ;  // Cross-capacitance AC current crowding

`ifdef SUBSTRATE
ddxcts    = ddx(Qts, V(s)) ; // Capacitance s-c junction
`endif

// Approximate small signal equivalent circuit
bowdydx = (ddxgx - ddxgmux)           / (ddxgrcvy + ddxgmuy - ddxgy);
bowdydz = (ddxgz - ddxgrcvz - ddxgmuz) / (ddxgrcvy + ddxgmuy - ddxgy);
bowgpi  = ddxsgpi + ddxgpix + ddxgmux + ddxgpiz + ddxgmuz +
      (ddxgpiy + ddxgmuy) * (bowdydx + bowdydz);
ddxgm   = (ddxgrcvy * (ddxgx - ddxgmux +                // Transconductance
         ddxgz - ddxgmuz) - ddxgrcvz *
        (ddxgy - ddxgmuy)) / (ddxgrcvy + ddxgmuy - ddxgy);
ddxbeta = ddxgm / bowgpi;                               // Current amplification
```

```
ddxgout = ((ddxgy - ddxgmuy) * ddxgrcvz -                 // Output conductance
        (ddxgz - ddxgmuz) * ddxgrcvy) /
        (ddxgrcvy + ddxgmuy - ddxgy);
ddxgmu  = ddxgpiz + ddxgmuz + (ddxgpiy + ddxgmuy) * bowdydz + // Feedback
transconductance
        ddxgmuex + ddxxgmuex;
ddxrb   = RBC_TM + ddxrbv;                          // Base resistance
ddxrc   = ddxrcc + ddxrcblx + ddxrcbli;              // Collector resistance
ddxcbe  = ddxcbex + ddxscbe + ddxcbcx +              // Base-emitter capacitance
        (ddxcbey + ddxcbcy) * bowdydx + CBEO_M;
ddxcbc  = (ddxcbey + ddxcbcy) * bowdydz + ddxcbcz +      // Base-collector capacitance
         ddxcbcex + ddxxcbcex + CBCO_M;


// Quantities to describe internal state of the model
bowgammax = (ddxgpix + ddxgmux - ddxgrbvx) * ddxrbv;
bowgammay = (ddxgpiy + ddxgmuy - ddxgrbvy) * ddxrbv;
bowgammaz = (ddxgpiz + ddxgmuz - ddxgrbvz) * ddxrbv;
bowgbfx   =  ddxgpix + ddxsgpi * (1.0 + bowgammax);
bowgbfy   =  ddxgpiy + ddxsgpi * bowgammay;
bowgbfz   =  ddxgpiz + ddxsgpi * bowgammaz;

// RvdT March 2008:
bowalpha_ft  = (1.0 + (ddxgrcvy * bowdydx * ddxrc) +
          (ddxgx + bowgbfx + (ddxgy + bowgbfy) * bowdydx) * RE_TM)/
          (1.0 - (ddxgrcvz + ddxgrcvy * bowdydz) * ddxrc -
          (ddxgz + bowgbfz + (ddxgy + bowgbfy) * bowdydz) * RE_TM);

bowrx = pow((ddxgrcvy * bowdydx + bowalpha_ft * (ddxgrcvz + ddxgrcvy * bowdydz)), -1);
bowrz = bowalpha_ft * bowrx;
bowry = (1.0 - ddxgrcvz * bowrz) / ddxgrcvy;
bowrb1b2 = bowgammax * bowrx + bowgammay * bowry + bowgammaz * bowrz;
bowrex = bowrz + bowrb1b2 - ddxrcbli;
bowxrex = bowrex + RBC_TM * ((bowgbfx + ddxgmux) * bowrx + (bowgbfy + ddxgmuy) *
bowry +
      (bowgbfz + ddxgmuz) * bowrz) - ddxrcbli - ddxrcblx;

bowtaut = ddxscbe * (bowrx + bowrb1b2) + (ddxcbex + ddxcbcx) * bowrx + (ddxcbey +
ddxcbcy) *
        bowry + (ddxcbez + ddxcbcz) * bowrz + ddxcbcex * bowrex + ddxxcbcex * bowxrex +
        (CBEO_M + CBCO_M) * (bowxrex - RCCxx_TM);

ddxft = 1.0 / (2.0 * `PI * bowtaut); // Good approximation for cut-off frequency
ddxiqs = Iqs;                   // Current at onset of quasi-saturation
ddxxiwepi = xi_w;               // Thickness of injection layer
ddxvb2c2star = Vb2c2star;        // Physical value of internal base-collector bias
```

```
// Small signal equivalent circuit conductances and resistances

$strobe("ddxgx     : ",  ddxgx   ) ; // Forward transconductance

$strobe("ddxgy     : ",ddxgy   ) ; // Reverse transconductance
$strobe("ddxgz     : ",ddxgz   ) ; // Reverse transconductance
$strobe("ddxsgpi   : ",ddxsgpi   ) ; // Conductance sidewal b-e junction
$strobe("ddxgpix   : ",ddxgpix   ) ; // Conductance floor b-e junction

$strobe("ddxgpiy   : ",ddxgpiy   ) ; // Early effect on recombination base current
$strobe("ddxgpiz   : ",ddxgpiz   ) ; // Early effect on recombination base current

$strobe("ddxgmux   : ",ddxgmux   ) ; // Early effect on avalanche current limitting
$strobe("ddxgmuy   : ",ddxgmuy   ) ; // Conductance of avalanche current
$strobe("ddxgmuz   : ",ddxgmuz   ) ; // Conductance of avalanche current
$strobe("ddxgmuex  : ",ddxgmuex   ) ; // Conductance extrinsic b-c current
$strobe("ddxxgmuex : ",ddxxgmuex   ) ; // Conductance extrinsic b-c current

$strobe("ddxgrcvy  : ",ddxgrcvy   ) ; // Conductance of epilayer current
$strobe("ddxgrcvz  : ",ddxgrcvz   ) ; // Conductance of epilayer current

$strobe("ddxrbv    : ",ddxrbv   ) ; // Base resistance

$strobe("ddxgrbvx  : ",ddxgrbvx   ) ; // Early effect on base resistance
$strobe("ddxgrbvy  : ",ddxgrbvy   ) ; // Early effect on base resistance
$strobe("ddxgrbvz  : ",ddxgrbvz    ) ; // Early effect on base resistance
$strobe("ddxre     : ",ddxre   ) ; // Emiter resistance
$strobe("ddxrbc    : ",ddxrbc   ) ; // Constant base resistance
$strobe("ddxrcc    : ",ddxrcc   ) ; // Collector Contact resistance
$strobe("ddxrcblx  : ",ddxrcblx   ) ; // Extrinsic buried layer resistance
$strobe("ddxrcbli  : ",ddxrcbli   ) ; // Extrinsic buried layer resistance


`ifdef SUBSTRATE
$strobe("ddxgs     : ", ddxgs   ) ; // Conductance parasitic PNP transitor
$strobe("ddxxgs    : ", ddxxgs  ) ; // Conductance parasitic PNP transistor
$strobe("ddxgsf    : ", ddxgsf  ) ; // Conductance substrate failure current
`endif

// Small signal equivalent circuit capacitances
$strobe("ddxscbe   : ", ddxscbe    ) ; // Capacitance sidewall b-e junction
$strobe("ddxcbex   : ", ddxcbex    ) ; // Capacitance floor b-e junction
$strobe("ddxcbey   : ", ddxcbey   ) ; // Early effect on b-e diffusion junction
$strobe("ddxcbez   : ", ddxcbez   ) ; // Early effect on b-e diffusion junction
$strobe("ddxcbcx   : ", ddxcbcx   ) ; // Early effect on b-c diffusion junction
```

```
$strobe("ddxcbcy   : ",  ddxcbcy  ) ; // Capacitance floor b-c junction
$strobe("ddxcbcz   : ", ddxcbcz   ) ; // Capacitance floor b-c junction
$strobe("ddxcbcex  : ", ddxcbcex  ) ; // Capacitance extrinsic b-c junction
$strobe("ddxxcbcex : ", ddxxcbcex ) ; // Capacitance extrinsic b-c junction
$strobe("ddxcb1b2  : ", ddxcb1b2    ) ; // Capacitance AC current crowding
$strobe("ddxcb1b2x : ", ddxcb1b2x   ) ; // Cross-capacitance AC current crowding
$strobe("ddxcb1b2y : ", ddxcb1b2y   )      ; // Cross-capacitance AC current crowding
$strobe("ddxcb1b2z : ", ddxcb1b2z   ) ; // Cross-capacitance AC current crowding
$strobe("ddxcts    : ", ddxcts   ) ; // Capacitance s-c junction

// Approximate small signal equivalent circuit
$strobe("ddxgm   : ",  ddxgm     ) ; // Transconductance
$strobe("ddxbeta : ", ddxbeta     ) ; // Current amplification
$strobe("ddxgout : ", ddxgout     ) ; // Output conductance

$strobe("ddxgmu  : ",  ddxgmu      ) ; // Feedback transconductance
$strobe("ddxrb   : ",  ddxrb      ) ; // Base resistance
$strobe("ddxrc   : ",  ddxrc       ) ; // Collector resistance
$strobe("ddxcbe  : ",   ddxcbe      ) ; // Base-emitter capacitance
$strobe("ddxcbc       : ", ddxcbc         ) ; // Base-collector capacitance

//quanitites to describe internal state of the model
$strobe("ddxft        : ", ddxft          ) ; // Good approximation for cut-off frequency
$strobe("ddxiqs       : ", ddxiqs         ) ; // Current at onset of quasi-saturation
$strobe("ddxxiwepi    : ", ddxxiwepi      ) ; // Thickness of injection layer
$strobe("ddxvb2c2star : ", ddxvb2c2star   ) ; // Physical value of internal base-collector bias


// Noise sources

`NOISE begin

  // Thermal noise
  common = 4.0 * `KB * Tk;
  powerREC = common / RE_TM;  // Emitter resistance
  powerRBC = common / RBC_TM; // Base resistance
 // RvdT, 03-12-2007: distributed collector resistance
  powerRCCxx = common * GCCxx_TM; // Collector resistance
  powerRCCex = common * GCCex_TM; // Collector resistance
  powerRCCin = common * GCCin_TM; // Collector resistance
  powerRBV = common / Rb2 * (4.0 * eVb1b2 + 5.0) / 3.0; // Variable base resistance

  // Collector current shot noise
  powerCCS = 2.0 * `QQ * (If + Ir) / qBI;

  // Forward base current shot noise and 1/f noise
```

```
  powerFBCS = 2.0 * `QQ * (abs(Ib1) + abs(Ib2));
  powerFBC1fB1 = (1.0 - XIBI) * pow((abs(Ib1) / (1 - XIBI)), AF) * KF_M;
  exponentFBC1fB2 = (2.0 * (MLF - 1.0)) + (AF * (2.0 - MLF));
  powerFBC1fB2 = KFN_M * pow(abs(Ib2), exponentFBC1fB2);

 // Emitter-base sidewall current shot and 1/f noise
  powerEBSCS = 2.0 * `QQ * abs(Ib1_s);
  if (XIBI == 0)
     powerEBSC1f = 0.0;
  else
     powerEBSC1f = KF_M * XIBI * pow((abs(Ib1_s / XIBI)), AF);

 // Reverse base current shot noise and 1/f noise
  powerRBCS = 2.0 * `QQ * abs(Ib3);
  powerRBC1f = KF_M * pow(abs(Ib3), AF);

  // Extrinsic current shot noise and 1/f noise
  powerExCS = 2.0 * `QQ * abs(Iex);
  powerExC1f = KF_M * (1 - (EXMOD * XEXT)) *
             pow((abs(Iex) / (1 - (EXMOD * XEXT))), AF);
  powerExCSMOD = 2.0 * `QQ * abs(XIex) * EXMOD;
  if (XEXT == 0.0)
     powerExC1fMOD = 0.0;
  else
     powerExC1fMOD = KF_M * EXMOD * XEXT * pow((abs(XIex) / XEXT), AF);

`ifdef SUBSTRATE
  // Substrate current shot noise (between nodes B1 and S, resp. B and S)
  powerSubsCS_B1S = 2.0 * `QQ * abs(Isub);
  powerSubsCS_BS  = 2.0 * `QQ * abs(XIsub);
`endif


  // Noise due to the avalanche
//   twoqIavl = KAVL * 2.0 * `QQ * Iavl;
   twoqIavl  = KAVL*Gem*powerCCS;
  powerCCS_A  = powerCCS + twoqIavl * (3.0 + 2.0 * Gem
             - (2.0 + 2.0 * Gem)*(2.0 + 2.0 * Gem)/(1.0 + 2.0 * Gem) );

  // Add noise sources
  I(e, e1)   <+ white_noise(powerREC);          // "emitter resistance"
  I(b, b1)   <+ white_noise(powerRBC);          // "base resistance"

  I(b1, b2)  <+ white_noise(powerRBV);          // "variable baseresistance"

  I(noi, e1) <+ white_noise(twoqIavl);          // "avalanche"
```

```
   I(c2, e1)  <+ white_noise(powerCCS_A);         // "col_emi_shot"
   I(b2, e1)  <+ white_noise(powerFBCS);         // "bas_emi_forw"

   I(b2, e1)  <+ flicker_noise(powerFBC1fB1, 1);  // "bas_emi_forw"
   I(b2, e1)  <+ flicker_noise(powerFBC1fB2, 1);  // "bas_emi_forw"
   I(e1, b1)  <+ white_noise(powerEBSCS);        // "emi_bas_side"
   I(e1, b1)  <+ flicker_noise(powerEBSC1f, 1);   // "emi_bas_side"
   I(b1, c1)  <+ white_noise(powerRBCS);         // "bas_col_reve"
   I(b1, c1)  <+ flicker_noise(powerRBC1f, 1);    // "bas_col_reve"
   I(b1, c1)  <+ white_noise(powerExCS);         // "Ext_bas_col"
   I(b1, c1)  <+ flicker_noise(powerExC1f, 1);    // "Ext_bas_col"
   I(b, c1)   <+ white_noise(powerExCSMOD);      // "Ext_bas_col"
   I(b, c1)   <+ flicker_noise(powerExC1fMOD, 1); // "Ext_bas_col"
`ifdef SUBSTRATE
   I(b1, s)   <+ white_noise(powerSubsCS_B1S);    // "bas_sub_current"
   I(b, s)    <+ white_noise(powerSubsCS_BS);     // "bas_sub_current"
`endif

/* RvdT, Delft University of Technology 03-12-2007,
Noise voltage associated with distributed parasitic collector.
In case of vanishing resistance corresponding node
is not addressed: */

 // RvdT, 31-01-2007: distributed collector resistance

if (RCBLX > 0.0)
 begin
  if (RCBLI > 0.0)
    begin /* all branches exist */
      I(c,  c3)  <+ white_noise(powerRCCxx); // "collector plug resistance"
      I(c3, c4)  <+ white_noise(powerRCCex); // "extrinsic collector BL resistance"
      I(c4, c1)  <+ white_noise(powerRCCin); // "intrinsic collector BL resistance"
    end
   else
    begin  /* only Rcblx exists */
      I(c,  c3)  <+ white_noise(powerRCCxx); // "collector plug resistance"
      I(c3, c1)  <+ white_noise(powerRCCex); // "extrinsic collector BL resistance"
    end
 end
else
 begin
  if (RCBLI > 0.0)
    begin   /* only Rcbli exists */
      I(c,  c4)  <+ white_noise(powerRCCxx); // "collector plug resistance"
      I(c4, c1)  <+ white_noise(powerRCCin); // "intrinsic collector BL resistance"
    end
```

```
  else
   begin /* neither Rcblx nor Rcbli exists */
     I(c,  c1)  <+ white_noise(powerRCCxx); // "collector plug resistance"
   end
 end


end // Noise sources
```

Index

ΔE_{gb}	11	24	Emitter bandgap voltage narrowing for graded-heavily doped base (cm^{-3})
D_{nb}	24	24	Diffusion coefficient on electrons in the base (cm^2/s)
$D_{nB}(x)$	49	49	Within base, diffusion coefficient as a function of distance x
$\bar{D}_{nb}$	39	39	Average diffusion coefficient of electron in base
D_{pe}	24	24	Diffusion coefficient on holes in the emitter (cm^2/s)
DTA	60		Parameter, location specific temperature change for TREF
DVGBF	61		Parameter, bandgap delta of forward current gain
DVGBR	61		Parameter, bandgap delta of reverse current gain
DVGTE	61		Parameter, emitter charge difference bandgap voltage
E_m	94	94	Maximum electric field
f_T	12		Small signal cutoff frequency
G_B	49	49	Gummel number
g_m	11		Transistor transconductance
I_{avl}	54		Avalanche current threshold
IB	8	24	Base terminal current
I_{B1}	54		Base emitter current ideal diode
I_{B1B2}	54		Base current variable resistance
I_{B2}	54		Current non ideal base emitter diode
I_{B3}	54		Current non ideal base collector diode
IBF	57		Parameter, saturation current of nonideal forward base current I_{B2} branch
IBF_T	92	92	Temperature adjusted saturation current of nonideal forward base current
IBR	57		Parameter, saturation current of nonideal reverse base current I_{B3} branch
IBR_T	98	98	Temperature adjusted saturation current of nonideal reverse base current
IC	8	24	Collector terminal current
I_{C1C2}	86		Collector current epilayer resistance
ICCR	22	49	Integrated charge control relationship by Gummel-Poon Used in the Mextram Model
IE	8		Emitter terminal current
Iepi(Kull)	33	33	Kull's onset current
I_{ex}	54		Current extrinsic base collector
IHC	58		Parameter, hot carrier current in epilayer I_{C1C2} branch
IK	57		Parameter, high level injection knee current
IK_T	85	85	Temperature adjusted high injection knee current
IKS	57		Parameter, high level injection knee current parasitic PNP transistor
IKS_TM	99	99	Temperature adjusted Knee current of parasitic PNP
I_N	48	48	Transfer current from emitter to collector
I_{qs}	87	90	Quasi-saturation current

I_S, IS	11	24	Junction saturation current
IS_T	71	110	temperature adjusted saturation current
I^S_{B1}	54		Sidewall current ideal base emitter diode
I_{SF}	54		Current substrate failure
ISS	57		Parameter, saturation current of parasitic PNP transistor
ISS_T	99	112	Temperature adjusted saturation current on NPN
I_{SUB}	54		Current substrate
K	11	11	Boltzman constant (eV/K)
KAVL	61		Parameter, flag to activate white noise due to avalanche
KF	61		Flicker noise coefficient for ideal base
KFN	61		Flicker noise coefficient for non ideal base current
λ_D	94	94	Intercept point in the collector where the extrapolated electric field is zero
MC	59		Parameter, collector current modulation factor for base collector depletion capacitance
MLF	57		Parameter, non-ideality factor of nonideal forward base current I_{B2} branch
MTAU	58		Parameter, non-ideality factor of emitter charge
n_0	73	85	Normalized electron density at emitter edge of neutral base
N_{AB}	24	24	Hole acceptor concentration in the neutral base (cm^{-3})
$N_{AB}(x)$	49	49	Within base, doping concentration as a function of distance x
n_b	73	85	Normalized electron density at collector edge of neutral base region
N_C	39	39	Constant density (probability) of state in the conduction band of SiGe
$\bar{N}_C$	39	39	Average density (probability) of state in the conduction band of SiGe
N_{de}	24	24	Electron donor concentration in the emitter (cm^{-3})
N_{epi}	31	31	Effective collector doping concentration
n_{i0}	24	24	Intrinsic concentration of undoped Si (cm^{-3})
$n_{iB}(x)$	49	49	Within base, intrinsic carrier concentration as a function of distance x
N_V	39	39	Constant density (probability) of state in the valence band of SiGe
$\bar{N}_V$	39	39	Average density (probability) of state in the valence band of SiGe
PE	59		Parameter, grading coefficient of emitter base depletion cap
PC	59		Parameter, grading coefficient of collector base depletion cap
p_o	32	32	Base to N- epilayer interface hole density
PS	59		Parameter, grading coefficient of collector substrate depletion cap
p_w	32	33	Hole density at epilayer interface to buried collector

q	11		Magnitude of electron charge
q_0^Q	74	74	Normalized base charge neglecting diffusion charge (only Early effects)
q_1	73	73	Normalized base charge due to Early effect with zero protection
Q_{B0}	72	72	Charge of the intrinsic base region at zero bias
Q_{B1B2}	54		Charge AC current crowding
Q_{BC}	54		Charge base collector diffusion
Q_{BCO}	54		Charge base collector overlap
Q_{BE}	54		Charge base emitter diffusion
Q_{BEO}	54		Charge base emitter surface overlap
Q_C	25	25	Charge of the base-collector depletion region
Q_E	25	25	Charge of the emitter region
Q_E	54		Charge emitter
Q_{epi}	54		Charge collector epilayer diffusion
Q_{ex}	54		Charge extrinsic base collector depletion
Q_{te}^S	54		Charge sidewall base emitter depletion
Q_{tC}	54		Charge base collector depletion
Q_{tE}	54		Charge base emitter depletion
Q_{tex}	54		Charge extrinsic base collector depletion
Q_{tS}	54		Charge collector substrate depletion
R_B	12		Base region parasitic resistance
RBC	54		Parameter, base contact resistance
RBC-T	97		Temperature adjusted constant resistance of external base
R_{buried}	29		N+ buried collector resistance, V_{C1C2} due to R_{buried}
RBV_T	95	95	Temperature adjusted low current resistance of intrinsic base I_{B1B2} branch
R_C	12		Collector region parasitic resistance
RCBL1	54		Intrinsic buried collector resistance
RCBLX	54		Parameter, extrinsic buried collector resistance
RCC	54		Parameter, collector contact resistance
RCCEX_T	97		Temperature adjusted constant resistance of extrinsic N+ buried layer under extrinsic region
RCCin_T	97		Temperature adjusted constant resistance of intrinsic N+ buried layer
RCC_T	97		Temperature adjusted constant resistance of external collector
R_{Csat}	28		Saturated collector resistance
RCV	58		Parameter, low current resistance of epilayer I_{C1C2} branch
RCV_T	86	109	Temperature adjusted epilayer Ohmic resistance
R_E	12		Emitter region parasitic resistance
RE	54		Parameter emitter resistance
RE_T	96	108	Temperature adjusted constant resistance of emitter

R_{epi}	29		N- collector epilayer variable resistance V_{C1C2} due to R_{epi}
r_o	13		Hybrid-π collector emitter output resistance
r_π	13		Hybrid-π base-emitter input resistance
RTH	60		Parameter, thermal resistance of self heating effects
r_μ	13		Hybrid-π collector base shunt resistance
SCRCV	58		Parameter space charge resistance of epilayer IC1C2 branch
SFH	57		Parameter, spreading factor of the avalanche current
SiGe HBT	1		Silicon-Germanium heterojunction bipolar transistor
T	11		Device temperature (Kelvin)
$T_{Ambient}$	34		Environmental or ambient temp, not device temperature
τ_C	25	25	Collector transit time
τ_B	25	25	Base transit time
TAUB	58		Parameter, transit time of base charge
TAUB_T	85	112	Temperature adjusted base transit time
τ_E	25	25	Emitter transit time
TAUE	58		Parameter, minimum transit time of emitter charge
TAUE_T	84	112	Temperature adjusted minimum emitter layer transit time
τ_F	12		Forward transit time
τ_R	12		Reverse transit time
TAUR	59		Parameter, reverse transit time
TEPI	58		Parameter, transit time of the epilayer
TEPI_T	86	113	Temperature adjusted collector epilayer transit time
t_N	63		Ratio of device temperature to reference temperature (deg Kelvin)
TREF	60		Parameter, model reference temperature
VAVL	57		Parameter, voltage describing the curvature of the avalanche current I_{avl} branch
VB	8		Base terminal potential
VB2E1	71	71	Base emitter voltage between B2 and E1
VBC	8		Base-collector terminal voltage
VBE	8		Emitter-base terminal voltage
V_C	33	33	Kull's critical voltage of the injections layer's electric field
VC	8		Collector terminal potential
VDC	59		Parameter, built in diffusion voltage of base collector
VDC_T	80	81	Temperature adjusted base collector diffusion voltage
VDE	59		Parameter, built in diffusion voltage of base emitter
VDE_T	79	79	Temperature adjusted base emitter diffusion voltage
VDS	59		Parameter, built in diffusion voltage of collector substrate
VDS_T	99	99	Temperature adjusted collector substrate built in voltage
VE	8		Emitter terminal potential
VEF	57		Parameter, forward Early voltage at zero bias
VEF_T	75	110	Temperature adjusted forward Early voltage
VER	57		Parameter, reverse Early voltage at zero bias
VER_T	75	110	Temperature adjusted reverse Early voltage
VGB	60		Parameter, base bandgap voltage

VGC	60		Parameter, collector bandgap voltage
VGJ	60		Parameter, base emitter recombination bandgap voltage
VGS	60		Parameter, substrate bandgap voltage
VLR	57		Parameter, crossover voltage on nonideal reverse base current I_{B3} branch
V_{qs}	90	90	Quasi-saturation voltage
vsat	33	33	Kull's injection layer saturation velocity
V_T	31	31	Thermal voltage at temperature T
WAVL	57		Parameter, effective width of the collector epilayer for avalanche current I_{aval} branch
W_B	24	24	Intrinsic base width (nm)
W_{B0}	9		Neutral base region width
W_{BC}	9		Base-collector layer thickness
W_C	25	25	Base-collector depletion region width (nm)
WE	9		Neutral emitter region thickness
W_E	24	24	Intrinsic emitter width (nm)
W_{epi}	32		Thickness of the entire N-epilayer collector layer
x_d	93	93	Depletion layer thickness base collector epilayer interface
XI_{ex}	54		Split current of extrinsic base collector
XP	59		Parameter, action of the base collector depletion capacitance that is constant at zero bias
XP_T	81	108	Temperature adjusted ration of depletion layer thickness to epilayer at zero bias
XQ_{ex}	54		Factor charge extrinsic base collector depletion
XQ_{tex}	54		Factor charge extrinsic base collector depletion
XREC	57		Parameter, factor of base recombination by SiGe base